Fakultät für Chemie
Zentralinstitut für Katalyseforschung - Catalysis Research Center
Lehrstuhl für Technische Chemie II

Investigation and Understanding of Unsupported Ni-Mo-W Sulfides for Hydrotreating

Dipl. Chem. Jennifer Hein

Vollständiger Abdruck der von der Fakultät für Chemie der Technischen Universität München zur Erlangung des akademischen Grades eines

Doktors der Naturwissenschaften (Dr. rer. nat.)

genehmigten Dissertation.

Vorsitzender: Univ.-Prof. Dr. K. Köhler

Prüfer der Dissertation:

1. Univ.-Prof. Dr. J. A. Lercher
2. Prof. Dr. M. Tromp, Ph.D.
   (Univ. Amsterdam / Niederlande)

Die Dissertation wurde am 01.09.2015 bei der Technischen Universität München eingereicht und durch die Fakultät für Chemie am 12.10.2015 angenommen.

Für einen ganz besonderen Menschen

Sascha Nagy

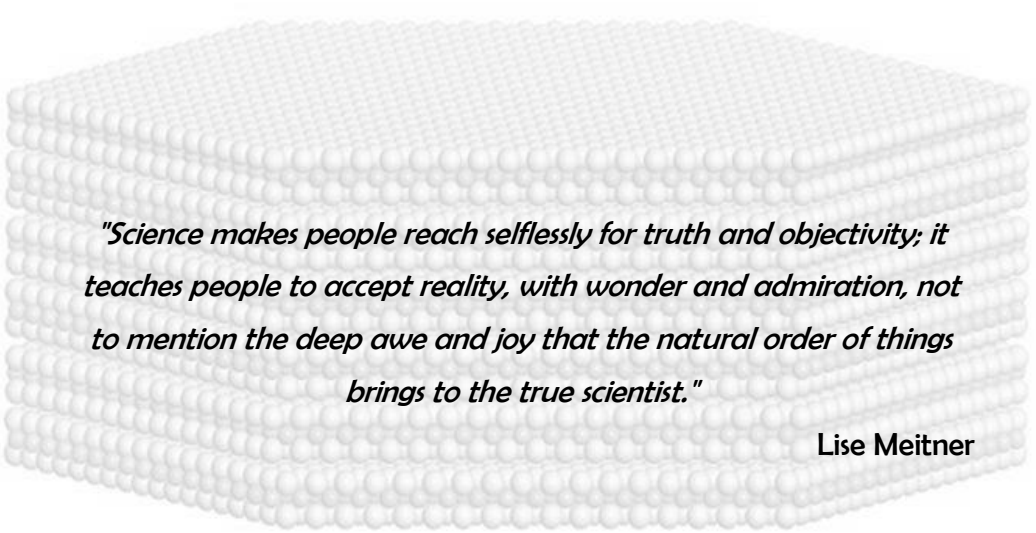

"Science makes people reach selflessly for truth and objectivity; it teaches people to accept reality, with wonder and admiration, not to mention the deep awe and joy that the natural order of things brings to the true scientist."

Lise Meitner

Acknowledgements

.....it's over now! This exciting journey through the chemistry and application of transition metal sulfides reaches its end. I really enjoyed my research, had ups and downs and learned a lot throughout the last five years. However, I finally succeeded, which would never have happened without the help, support, guidance and friendship of many different people. Therefore, it is time to say how much I appreciated all these people, their work and deeds.

First of all, I acknowledge my doctoral adviser Prof. Johannes A. Lercher. Thanks a lot for all the opportunities, I had in your team, the scientific discussions, the knowledge and experiences I gained on a scientific and personal level and also for the great PhD topic, which you offered me. This exciting topic is directly connected to my industry partner, the Chevron Energy Technology Company. I am thankful not only for the financial support, but also for this great cooperation. My special thanks goes to Dr. Alexander Kuperman for being a motivating and valuable member of the "scientific board" throughout my whole project. I also appreciated the work and fruitful discussions with Dr. Jinyi Han and Dr. Theo Maesen, thanks for the nice and informative days in Richmond.

The greatest team ever - The Sulfur-Sub-Group! I am glad that I was a part of it. Essential for the nice team spirit were my supervisor, Dr. Oliver Y. Gutiérrez and my favorite "sulfur-girl" Eva Schachtl. Oliver, it was a pleasure to work, discuss and grow with you. Thanks a lot that you had always time for me, that you worked so hard in my stuff and that you always found a way to explain even disappointing results. My dear Eva, thanks for being a great colleague, laboratory and equipment-sharing partner and friend, thanks for the scientific and problem solving discussions and for the great time spent together all over the world. I wish you both and your families all the best and much success in your future careers. I also acknowledge Dr. Ana Hrabar, you were the one who brought me in contact with the TMS. Thanks for preparing the project, for my smooth start in Munich and for being a friend.

I further thank Prof. Andreas Jentys, for your honest and direct manner from the very first moment, for your critical reviews as well as for your general support and provided knowledge not only in the matter of spectroscopy. Prof. Roel Prins, Prof. Moniek Tromp, Prof. Matthias Bauer and Prof. Gary Haller are acknowledged. All these great scientist I met on my way and I am thankful for all the fruitful discussions, the valuable input, the critical reviews and the patient answering of all my questions. I am also grateful to Prof. Thomas Weber and Dr. Hendrik Dathe for their support and understanding in the final stage of my thesis.

Furthermore, I am thankful to several colleagues within the group, but especially I would like to mention Dipl.-Ing. Xaver Hecht, the "set-up whisperer", who provides the best technical support and trained me very well, and Stefanie Saibold, who is the priceless base of the success of the whole group. Furthermore, my thanks goes to Bettina Federmann and Ulrike Sanwald, who excellently manage all administrative and financial issues in the back.

Dr. Marianne Hanzlik, Ph.D. Hui Shi and Elisabeth Hanrieder are acknowledged for their patience during TEM measurements and the great images. The SEM and HR-SEM measurements were performed by Dipl.-Ing. Martin Neukamm and Dipl.-Min. Katia Rodewald, to whom I am as well very grateful. I also appreciate the work of Ulrike Ammari in the Microanalytical Laboratory of the TU München and of Marc Schönberger and Michael Wanninger, who designed and built high-quality set-ups always in a reliable and fast manner. My thanks goes as well to Ph.D. Pinhong Xu and Ph.D. Robert Colby from the PNNL in Richland for the STEM and SHIM measurements and all the efforts they put in my samples and during our stay at the PNNL.

No XAS data set, without synchrotrons, well aligned beamlines and enthusiastic beamline scientists, therefore I acknowledge the light source facilities DORIS III at DESY(member of the Helmholtz Association, Germany), the ESRF (Grenoble, France) and ALBA (Barcelona, Spain) for the provision of beam time as well as the HASYLAB staff at DESY (beamline X1), especially Dipl.-Ing. Mathias Hermann, Dr. Adam Webb and Dr. Michael Murphy, the DUBBLE staff at ESRF, namely, Dr. Dipanjan Banerjee and Dr. Sergey Nikitenko and the CLAESS staff Dr. Laura Simonelli, Dr. Carlo Marini and Dr. Wojciech Olszewski for all their great support and their spent time during weekends and nights.

Additionally, I thank all my highly motivated bachelor, master and exchange students for their help: Marian Rötzer, Julia Thammer, Robert Kick, Moritz Schreiber, Thomas Kleiner, Julia Rieb, Stefan Haslinger, Andreas Ehrmaier, Thomas Kandler, Elke Herrmann, Fatma Meltem Aygüler, Robert Kender, Sabine Zacherl and Santiago Stalin Guerra Salcedo.

My colleagues and friends Dr.-Ing. Stefanie Simson, Monica Markovits, Dr. Robin Kolvenbach, Dr. Stefan Schallmoser and Dr. John Ahn are sincerely acknowledged; you guys became my first address in scientific and non-scientific concerns and enabled an inspiring and productive working atmosphere in the office. I am also thankful to Dr. Sarah Maier, Claudia Himmelsbach, Dr.-Ing. Christian Gärtner, Linus Schulz, Sebastian Foraita and Stanislav Kasakov. You all created a feel-good atmosphere at university, on conferences, at beamlines and after work, which was always very important for me.

Und letztendlich gibt es einige Menschen in meinem privaten Umfeld, denen ich gerne danken möchte und was mich nun dazu veranlasst in Deutsch weiter zu schreiben.

Ich möchte mich bei Jeannine, Andi, Kathi, Tom, Moni, Iulius, Steffi, Eva und Felix bedanken. Ihr wurdet zu sehr guten Freunden in München und habt mir das Heimatgefühl ein Stück näher gebracht. Außerdem geht mein Dank auch an Anne, Diana, Manu, Nine, Jule, Robert, Alex und Sven. Ihr habt bewiesen, dass Freundschaft weder an Orten noch an Zeiten gebunden ist.

Bei meinem Bruder Jeffrey Hein möchte ich mich bedanken, du hast von klein auf dazu beigetragen, dass ich unerschrocken und hoch motiviert neuen Dinge entgegen gehe. Dann möchte ich mich bei meinen tollen Schwiegereltern Birgit und Árpád Nagy bedanken; für eure fortwährende Unterstützung und allgegenwärtige positive Grundeinstellung. Einen Dank richte ich auch an meine lieben Großeltern, Anita und Arnold Hein, Ursula Parnitzke und Heinz Granzow, von denen leider nicht mehr alle das Ende meiner Promotion miterleben können, dennoch ich war mir eures Zuspruchs immer bewusst.

Ein ganz besonderer Dank geht selbstverständlich an meine großartigen Eltern, Barbara und Jörg Hein. Erst durch euren Glauben und Vertrauen in mich, durch eure aufmunternden Worte und euren stetigen Beistand aber auch durch die Werte, die ihr mir mit auf den Weg gegeben haben, durch eure Lebenseinstellung und aufgrund eurer offenen und verständnisvollen Art, habe ich jede Chance in meinem Leben genutzt und bin ich überhaupt erst bis hier gekommen.

Und schlussendlich möchte ich den einen ganz besonderen Menschen in meinem Leben danken. Schon seit mehreren Jahren bist du für mich da, bist nie von meiner Seite gewichen und hast immer meine Begeisterung und Aufopferung für die Wissenschaft respektiert, verstanden und unterstützt - Sascha, du bist und bleibst mein "Lieblingsmensch"!

Abstract

Unsupported Ni-Mo, Ni-W and Ni-Mo-W catalysts consist of stacks of $Mo(W)S_2$ slabs decorated by Ni at the edges and NiS_x crystals. In NiMoW materials, intralayer Mo-W sulfide slabs are present. All materials were active in the removal of S and N from model compounds. The composition does not affect the reaction pathway but the degree of Mo-W alloying, direct interaction with Ni, and morphology determined the activity

Ungeträgerte Ni-Mo, Ni-W und Ni-Mo-W Katalysatoren bestehen aus NiS_x Kristallen und $Mo(W)S_2$. In kleineren Konzentrationen wird Ni an den Rändern der $Mo(W)S_2$ Schichten eingebaut. Mo und W können gemeinsam in einer Schicht der Sulfide vorliegen. Bei der hydrierenden Eliminierung von N und S aus Modellverbindungen waren alle Katalysatoren aktiv. Die Aktivität wurde durch die Synergie zwischen Ni, Mo und W beeinflusst, die sowohl Morphologie als auch die Oberflächenzusammensetzung bestimmte.

Table of Contents

Acknowledgements I
Abstract V
Chapter 1 1
General Introduction - The Motivation 1
1. The Relevance of Transition Metal Sulfides 2
2. The Importance of Hydrotreating 3
3. The Scope of the Thesis 7
Chapter 2 9
Transition Metal Sulfides versus Hydrotreating - The Background 9
1. The Chemistry of Nickel, Molybdenum and Tungsten 10
1.1. The Transition Metals Ni, Mo and W 10
1.2. Selected Compounds of Ni, Mo and W 12
2. Heterogeneous Catalysis in Hydrotreating 24
2.1. Hydrodenitrogenation 24
2.2. Hydrodesulfurization 29
2.3. Hydrotreating Catalysts and Their Active Sites 32
Chapter 3 42
γ-Al_2O_3-supported and unsupported (Ni)MoS_2 for hydrodenitrogenation of quinoline in the presence of dibenzothiophene 42
1. Abstract 44
2. Introduction 44
3. Results 45
4. Discussion 61
5. Conclusions 68
6. Experimental Section 69
Chapter 4 75
Physicochemical characterization of unsupported Ni-Mo-W oxides 75
1. Preparation and Characterization Techniques 76
2. Results and Discussion 80
3. Conclusions 109
Chapter 5 112
Distribution of metal cations in Ni-Mo-W sulfide catalysts 112
1. Abstract 114

2. Introduction 114
3. Experimental Part 115
4. Results and Discussion 117
5. Conclusions 138
Chapter 6 141
Physicochemical characterization and hydrotreating activity of unsupported Ni-Mo-W sulfide catalysts 141
1. Introduction 142
2. Experimental Part 142
3. Results 146
4. Conclusions 168
Chapter 7 171
Summary and Final Conclusions 171
1. Concluding Summary 172
2. Abschließende Zusammenfassung 178
References 186
Appendices 196
1. A 1 - Support Chapter 3 197
2. A 2 - Support Chapter 5 203
3. A 3 - Support Chapter 6 224
Short Curriculum Vitae of Jennifer Hein 238
Publications and Conference Contributions 239

Chapter 1

General Introduction - The Motivation

1. The Relevance of Transition Metal Sulfides

The investigation and research in the field of solid state transition metal sulfides (TMS) is triggered by their unique structures and properties resulting in a high variety of applications. Especially, the two-dimensional layered graphene analogon, the metal disulfides MoS_2 and WS_2 are of interest.[1] These semiconducting materials applied as bulk materials[2], supported[3] or as ultrathin[4] or exfoliated layers[5] are widely used in catalytic hydrotreating of crude oil[6-8] and biomass derived feeds[9-10], photocatalysis and electrochemistry[11-13] or as lubricants[14]. MoS_2 and WS_2 are isomorph and consist of stacked sulfur-metal-sulfur layers, which creates three-dimensional crystals. It is found that the stacking degrees influence the band structure and a transition from a indirect to a direct optical band gap is observed with decreasing stacking degree of MoS_2.[15] Moreover, the edges of these stacked layers are discussed as active sites in hydrotreating reactions.[6, 16] That means, for optoelectronic devices few or single layer materials are the main requirement, whereas for heterogeneous catalysts a high concentration of edge sites is needed addressing stacking degree as well as particle size and shape.

For different applications as well as for research purpose, also mixed TMS are of interest. For instance, bimetallic mixtures of layered TMS were under investigation, mainly Mo-W disulfide systems.[17-20] And although MoS_2 and WS_2 are comparable in terms of structure and properties, they are just rarely found in the same compound in nature. The central question is how Mo and W are dispersed within a mixed disulfide material on the atomic level. There are three possible scenarios. The first possibility would be a mechanical mixture, where both phases are present next to each. Moreover, an interlayer mixture of $Mo_{1-x}W_xS_2$ ($0 \leq x \leq 1$) crystals with different stacking sequences of [MoS_2] and [WS_2] could be feasible or Mo and W could be atomic mixed in one sulfide layer. In this so called intralayer $Mo_{1-x}W_xS_2$ mixture, Mo and W could be either appear as perfect homogeneous solid solution (alloy-like) or they could be distributed randomly, i.e. bulk pure phases are next to mixed disulfide phases. In literature, just a few studies address this question since it is not straightforward to gain an answer for such mixture of isostructural phases. With X-ray diffraction (XRD) very small shifts of the reflections between MoS_2 and WS_2 phases would be visible, if both appear as large single crystals in a mechanical mixture. However, if the pure phase domains are too small XRD would fail and just an averaged result is obtained. In this case, transmission electron microscopy coupled with energy dispersive X-ray spectroscopy as well as Raman spectroscopy could be helpful to differentiate between a real and a mechanical mixture. But the distinction between an intra or interlayer mixture is much more complicate and techniques with atomic resolution are needed. Thomazeau et al. used extended X-ray absorption fine structure (EXAFS) at the Mo K-edge and W L_{III}-edge since this method gives

an insight in the local coordination geometry of the metals.[21] Dumcenco et al. could visualize by STEM-ADF that random alloying occurs in $Mo_{1-x}W_xS_2$ single layers.[22]

The addition of promoters like Ni or Co to MoS_2 and WS_2 is increasing the activity for catalytic hydrogenation and nitrogen and sulfur removal from hydrocarbons. Several structural and kinetic studies for bimetallic, mainly supported, TMS catalysts exists using different hydrotreating reactions and conditions[23-26] and analytical tools[27-28], like electron microscopy[16, 29-32], Mößbauer spectroscopy[33], theoretical calculations[34-36], or X-ray absorption spectroscopy[37-42]. However, in recent years, the complexity of hydrotreating catalysts was increased by the investigation of highly active unsupported trimetallic sulfide materials, containing Mo, W and Ni.[2] For these trimetallic systems just a few publications can be found in literature,[10, 43-49] and even less EXAFS studies.[50-51] Moreover, up to know no full characterization of these complex bulk trimetallic systems exists in literature. Consequently, it is worth to combine the two most powerful techniques for sulfides, i.e. EXAFS and electron microscopy to investigate unsupported multimetallic sulfides to gain a deeper understanding.

2. The Importance of Hydrotreating

Hydrotreating is one of the key processes of crude oil conversion to more valuable products in the oil refining industry, as can be seen in Figure 1. 1. Hydrotreating, hydrogenation and hydrocracking are hydroprocessing reactions, where organic compounds are converted with hydrogen under high pressure, elevated temperatures and usually in presence of a heterogeneous catalyst. During hydrotreating, heteroatoms like sulfur, nitrogen, oxygen and metals are removed from hydrocarbons commonly in the presence of Co or Ni promoted MoS_2 supported on γ-alumina. The removal of heteroatoms is required because of process related, ecological and economical reasons.

In respect to the refinery process, heteroatoms have to be removed since they poison the used catalysts in the subsequently process steps, such as catalytic reforming and cracking catalyzed by noble metals and acid catalysts like zeolites (Figure 1. 1). Furthermore, heteroatom containing molecules tend to coke formation, which is undesired in all process steps. The quality, i.e. the heteroatom content in crude oil depends strongly on the geographical origin, the source/type of crude oil and on the boiling point of the feedstock.

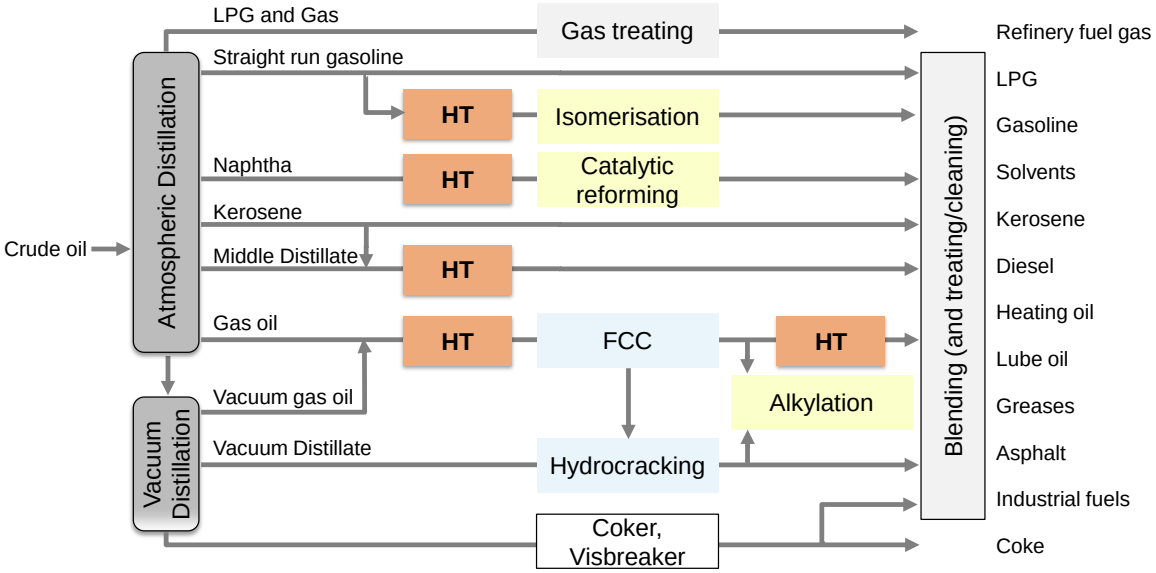

Figure 1. 1. Simplified flow diagram of an industrial refinery showing the main processes from crude oil to the final products. The application of hydrotreating (HT) in several process steps indicates its importance (FCC: fluid catalytic cracking).

For instance, so-called unconventional high viscous heavy feedstocks like tar sands or oils sands have much higher heteroatom content. Therefore, the sulfur content could vary between 0.1 - 7 wt.%, the nitrogen content is typically between 0.4 - 1.8 wt.% and metals (V, Ni) have concentrations between 1 - 1200 ppm.[52] The highest heteroatom content is found in the asphaltene fraction of crude oil. Asphaltenes are aggregates of divers poly-cyclic and poly-aromatic molecules with aliphatic chains including pyrrolic, pyridinic, mercaptane and thiophene structures, as presented in Figure 1. 2.[53]

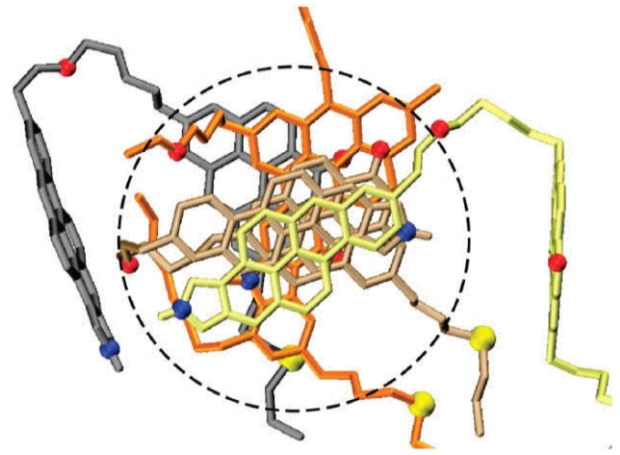

Figure 1. 2. Aggregate of organic molecules in water representing one possible asphaltene structure, taken from Ref. [53]. Each molecule is represented by a different color, whereas N, O, and S are shown with blue, red, and yellow circles, respectively.

Under consideration of the concentration range of heteroatoms in crude oil, the complete removal of sulfur is apparently the most important one. However, nitrogen compounds inhibit

the sulfur removal and are much more challenging to remove. Nitrogen compounds are less reactive and require higher hydrogen partial pressures during conversion than sulfur compounds and the C-N bond is stronger than the C-S bond (C-N 306 kJ/mol and C=N 616 kJ/mol versus C-S 272 kJ/mol and C=S 536 kJ/mol).[52] Therefore, not every sulfur removal catalyst is also active in nitrogen removal.

From the ecological perspective, the heteroatoms have to be removed since they are converted into air polluting oxides, like SO_x and NO_x, during fuel combustion. These gases are associated with climate change causing acid rain, smog, global warming or affecting the ozone layer next to health and life quality related issues.[54] Comparable to the refinery processes, sulfur also influences other technologies, which control e.g. vehicle emissions of CO, NO_x, hydrocarbons and particles (dust). Therefore, the reduction of sulfur especially in fuels is a key for the overall reduction of emissions.[55] As a consequence, the majority of the nations have defined sulfur limits for transportation fuels and agreed timelines for further reductions, which is presented in Figure 1. 3.[54, 56]

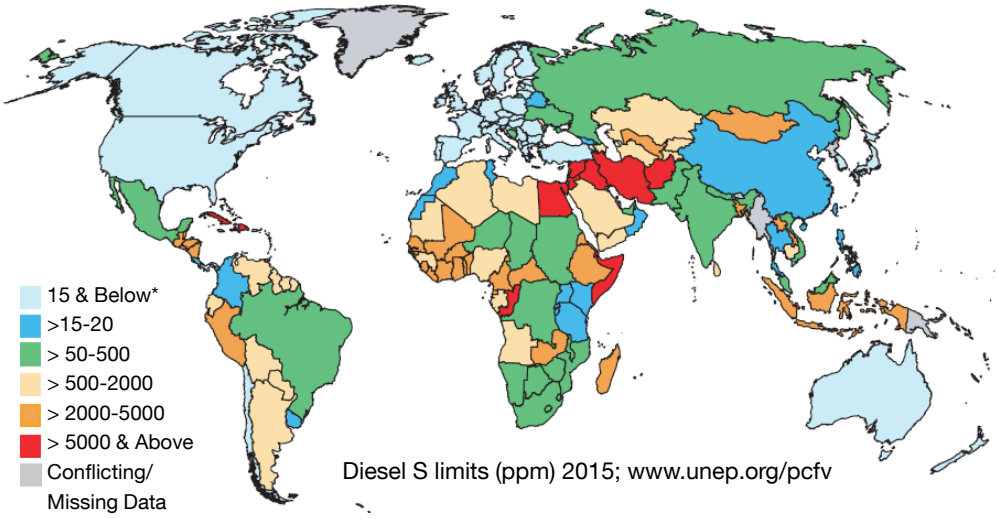

S limits, ppm	Fuel	US	EU	China	Russia	India	Brazil	Mexico
2010	Diesel	15	10	2000	500	350	1800	500
	Gasoline	30	10	150	500	150	1000	150
2015	Diesel	15	10	50	50	350	500	500
	Gasoline	30	10	50	10	150	50	150
2020	Diesel	15	10	10	10	50	10	15
	Gasoline	10	10	10	10	50	50	30

Figure 1. 3. The world map shows the diesel fuel sulfur limits in ppm of 2010 indicated by different colors.[54] Additionally in the table, the timeline for the adopted diesel and gasoline sulfur limits (in ppm) of selected countries are presented from 2010 to 2020.[56]

The world map shows the nationwide legal sulfur limits for diesel fuel to date (06/2015), which indicates that almost all nations have already sulfur limits below 500 ppm. Moreover, the listed timeline shows that a reduction below 50 ppm sulfur is aspired by 2020. The sulfur

limits for gasoline are even lower. These trends show that there is an increasing demand for clean transportations fuels and for an improved fuel quality.

This demand for clean fuels affects of course the refineries, which have to meet with their produced fuels the very low sulfur limits. Additionally, higher amounts of fuels have to be provided since the total world energy demand increases, which can be seen in Figure 1. 4. Oil currently contributes to the global primary energy sources to one third[57]. In accordance to the new policies scenario of the world energy outlook (WEO) 2012, the share of oil will decline by around 4 % in 2035.[58] However, in 2035 oil will be still the most widely used energy source (share of 27 %). On the other hand, the refineries are confronted with a depletion of natural crude oil resources, which increases the conversion need of heavy and unconventional feedstocks with high heteroatom contents. Consequently, hydroprocessing in the refineries has to become more efficient and highly active hydrotreating catalysts are required to meet the increasing energy demand and the low legal sulfur limits. The increased demands are also reflected in the global catalyst market. Between 2014 and 2019, a compound annual growth rate of 4 % for the refinery catalyst market is expected, which is dominated by hydrotreating catalysts with a market share of 35 % (sources: marketsandmarkets.com 11/2014; Catalyst Group Resources 06/2014 and The Freedonia Group 12/2014).

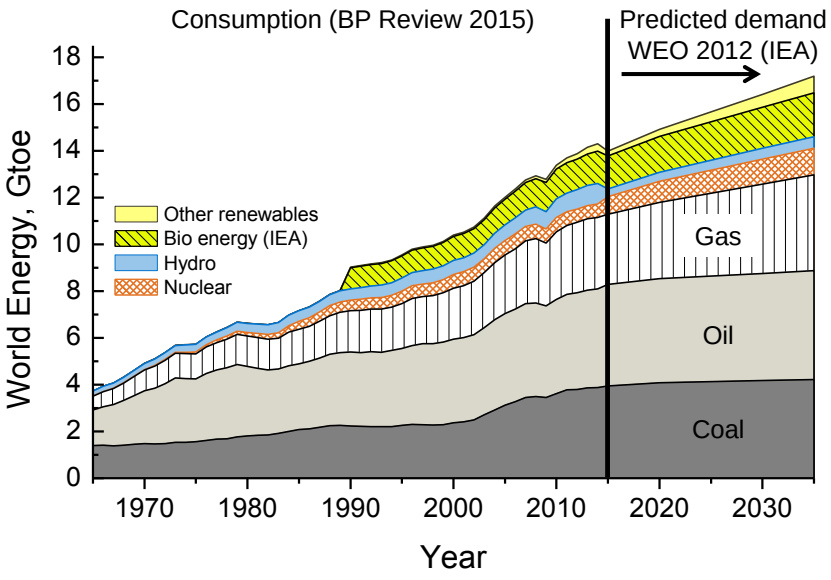

Figure 1. 4. World energy consumption by fuel from 1965 to 2014 (BP Statistical Review of World Energy 2015; June 2015)[57] and predicted demand until 2035 (World Energy Outlook 2012 of IEA)[58] in giga tonnes oil equivalent (Gtoe). The data for bio energy were taken from the WEO 2012 (IEA).

However, the current global situation and the predicted developments in terms of energy demand and strict environmental regulations highlight not only the commercial relevance of hydrotreating, but also the importance of research in and development and understanding of hydrotreating and its catalysts. Thus, even more than 100 years of investigation of transition

metal sulfides for fuel production and the development of large scale crude oil processing,[8] hydrotreating and transition metal sulfide catalysts are still of interest and require continuous improvement.

3. The Scope of the Thesis

Motivated by the need of highly active hydrotreating catalysts for conventional and heavy feedstocks as well as by the promising properties and wide applications of transition metal sulfides, the target of the current PhD thesis is the investigation of multimetallic sulfide catalysts for hydrotreating applications. Tasks accomplished in this work are exploration of suitable synthesis procedures, detailed physicochemical characterization, and kinetic studies using relevant methods and techniques.

The emphasis is put on unsupported formulations containing Ni, Mo, and W for hydrodenitrogenation (HDN). Ultimate goal is the analysis and understanding of the influence of the different metals on the sulfide structure and the HDN activity. Namely, insight into unsupported Ni-Mo-W sulfide catalysts is gained by describing the interactions among the metals and their impact on the catalytic active sites.

Chapter 2

Transition Metal Sulfides versus Hydrotreating - The Background

1. The Chemistry of Nickel, Molybdenum and Tungsten

1.1. The Transition Metals Ni, Mo and W

The elements in the 3rd to 11th group of the periodic system of the elements (PSE) are called transitions elements (Figure 2. 1).[59] They belong to the d-block elements and they are all metals. For these elements, the s-orbital electrons of the outer shells, and the d-orbital electrons take part in chemical bonding. Therefore, they exist in different oxidation states and exhibit different properties than those observed for the main-group metals The ground state of the electronic configuration of transition metals is defined by the successive filling of the d-orbitals, which are for the first row the 3d-orbitals and for the second and third row the 4d and 5d-orbitals, respectively.

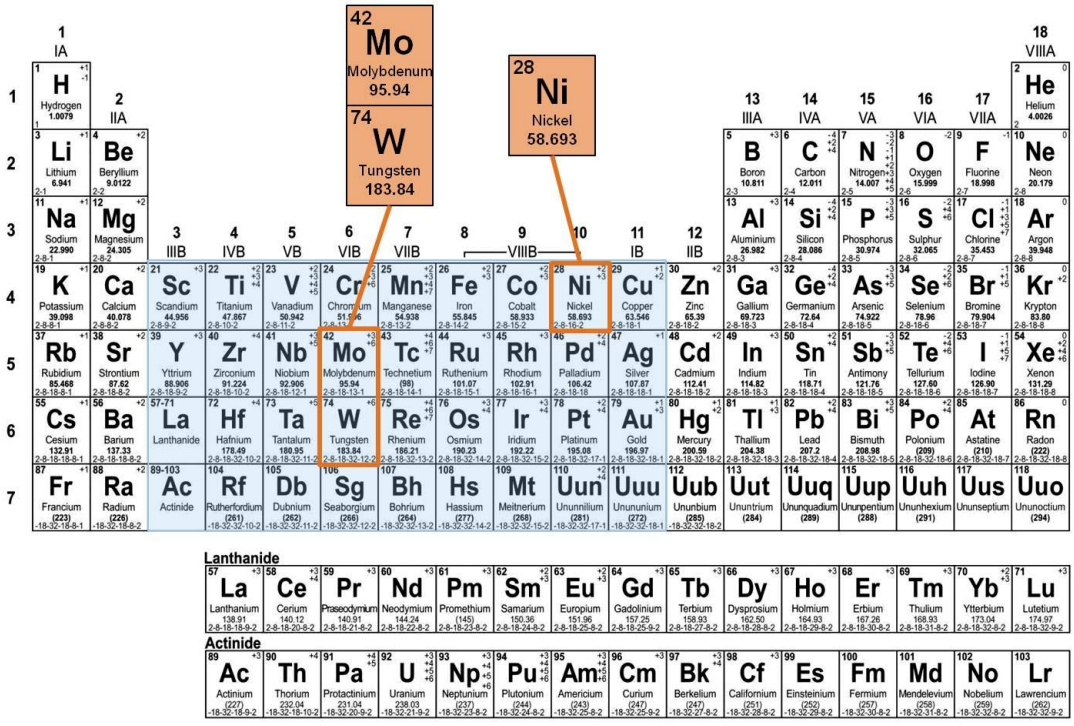

Figure 2. 1. Periodic system of elements. The transition metals are marked in blue, whereas the position of the elements of interest, Mo, W, and Ni are highlighted in orange and enlarged.

In the current work, the three transition metals of interest are nickel, molybdenum and tungsten. These metals belong to the rows 4, 5, and 6 of the d-block elements, respectively. Therefore, they are substantially different in their electronic configuration, which is shown in Table 2. 1. The 3d-orbitals of nickel are filled with eight electrons, which results in the preferred oxidation state +2. Nickel occurs frequently in nature, either as native metal, in iron ores or bound in sulfide or arsenic minerals, like millerite (NiS).[60] Molybdenum and tungsten

are in the 6th group of the PSE, thus, they exhibit six outer bonding electrons and the preferred oxidation states are +4, +5 and +6. The most stable one is the latter. They are not found as pure native metals, but commonly as oxides or, in the case of molybdenum, as sulfide minerals. The most important ores are molybdenite (MoS_2), wulfenite ($PbMoO_4$), wolframite ($(Mn,Fe^{II})WO_4$) and scheelite ($CaWO_4$).[60] However, molybdenum possesses a stable half-occupied $4d^5$-shell configuration, whereas tungsten exhibits a $5d^46s^2$ configuration. The reason is the relativistic contraction of the 6s-orbital and the expansion of the 5d-orbitals, which result in a decrease of the energy of the 6s-orbital and an increase of the 5d-orbital energy and thus, into a preferred electron occupation of the 6s-orbital. Furthermore, in the 6th row the 4f-orbitals are filled, which undergo a larger orbital expansion than the d-orbitals. Thus, the shielding of core protons by f-electrons is poor and a larger attraction between the s- and p-electrons and the atom core occurs, which increases further with increasing nuclear charge (atomic number N). As a consequence, the atomic and ionic radii of the 4d- and 5d-metals of the same group are almost the same, also known as lanthanide contraction. This effect can be seen in Table 2. 1, which shows almost the same radii for molybdenum and tungsten. Therefore, both elements show similar bond distances in compounds, are present in isomorphous compounds, and their compounds have similar chemical and physico-chemical behavior (energy of formation and solvation energies).[61] Moreover, the electronegativity (EN) of molybdenum and tungsten is similar, whereas nickel exhibits, as expected, a higher EN value (EN increases from bottom left to top right within the d-block elements). Nickel prefers the formation of bases, whereas molybdenum and tungsten tend to the formation of acids and they have a higher noble metal character.

Table 2. 1. General Properties of the Elements Ni, Mo, W.[60-61]

Element	N[a]	M, g/mol [b]	e^--configuration	Oxidation states	Radius, pm[c]	EN[d]
Nickel	28	58.69		+3		
			$[Ar]\ 3d^8\ 4s^0$	+2	55_{tet}, 69_{oct}	
			$[Ar]\ 3d^8\ 4s^2$	0	125_{CN12}	1.8
Molybdenum	42	95.94	$Kr]\ 4d^0\ 5s^0$	+6	59_{oct}	
				+5	61_{oct}	
			$[Kr]\ 4d^2\ 5s^0$	+4	65	
				+3	69	
			$[Kr]\ 4d^5\ 5s^1$	0	140_{CN12}	1.3
Tungsten	74	183.84	$[Xe]\ 4f^{14}\ 5d^0\ 6s^0$	+6	60_{oct}	
				+5		
			$[Xe]\ 4f^{14}\ 5d^2\ 6s^0$	+4	66_{tet}	
				+3	70	
			$[Xe]\ 4f^{14}\ 5d^4\ 6s^2$	0	141_{CN12}	1.4

[a] atomic number; [b] molar mass in gram per mol; [c] radii in 10^{-12} meter for the ions and the metal atoms with tet for tetrahedral, oct for octahedral and CN12 for metallic coordination number of 12; [d] electronegativity.

1.2. Selected Compounds of Ni, Mo and W

Nickel Compounds

The most relevant Ni compounds for the current work are nickel(II)-hydroxide $Ni(OH)_2$, nickel(II)-oxide NiO and the different nickel sulfides. Moreover, Ni(II) tends to form a high variety of complexes with different coordination symmetries, which are mainly octahedral and square planar, but also tetrahedral, trigonal bipyramidal and square pyramidal geometries are known.[62] For instance, with H_2O and NH_3 ligands Ni^{2+} forms octahedral complexes, i.e., $[Ni(H_2O]_6]^{2+}$, which is always present in aqueous solution or in hydrated solvable Ni salts. The Ni salts have characteristic colors in accordance to the three spin allowed electronic transitions in an octahedral ligand field, as presented in the term diagram in Figure 2. 2 (A), what allows their investigation by spectroscopy. In the case of large ligands with a high charge (Cl^-, O^{2-}, S^{2-}), a tetrahedral high-spin coordination with a small ligand field stabilization energy is favored, whereas by large ligand field stabilization energies square planar low-spin coordination symmetries are formed (Figure 2. 2).

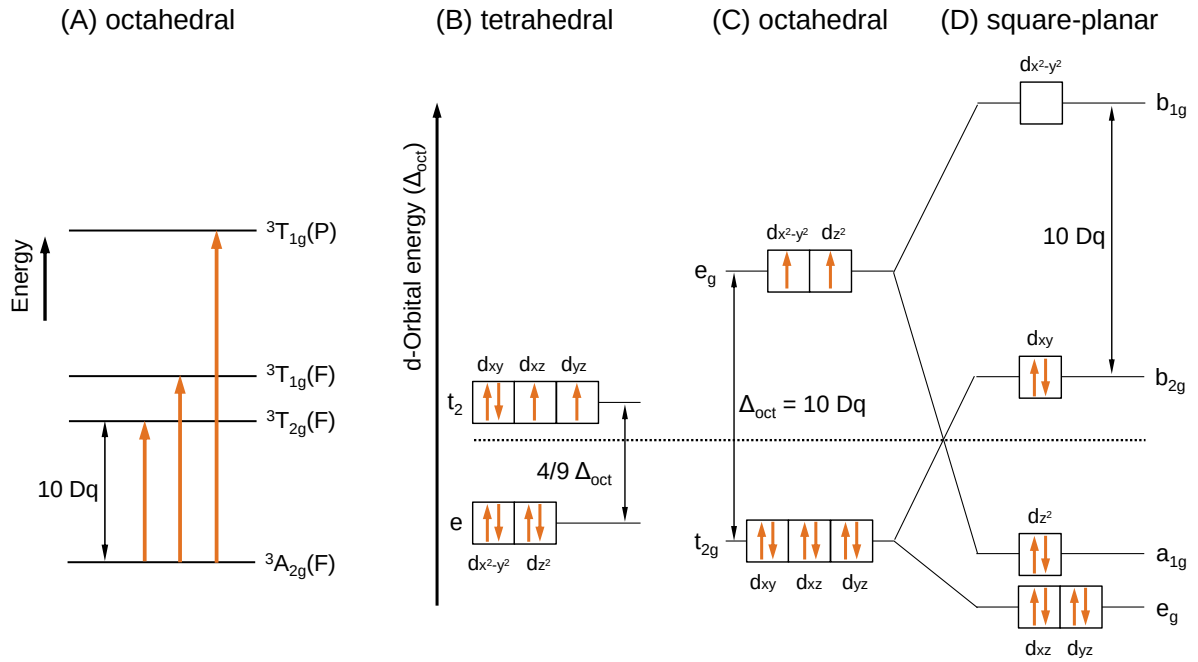

Figure 2. 2. Ligand field splitting of d^8 configuration in an octahedral (A, C), tetrahedral (B) and square-planar (D) ligand field. In (A) the splitting of the terms and the electronic transitions are schematically presented, whereas (B) to (D) show the splitting of the d-orbitals and their electron population.[60, 62]

The formed symmetries depend strongly on the ligand type, the concentration of the ligand, but also on the temperature and the counter ions.[62] Different coordination symmetries can be mutually converted by distortion, e.g., a strong tetrahedral distortion of an octahedron in z-

direction results in a square planar like coordination (Jahn-Teller-effect).[60] This flexibility in coordination symmetries of Ni^{2+} also accounts for its variety of nickel sulfides (vide infra).

In the oxygen compounds $Ni(OH)_2$ and NiO, Ni^{2+} is distorted octahedral coordinated as can be seen in Figure 2. 3. The crystal structure of $Ni(OH)_2$, more accurate β-$Ni(OH)_2$[63], is a layered structure with a hexagonal CdI_2-type lattice. It consists of stacked sandwiches composed by two OH^- anion layers and one Ni^{2+} layer in between. The OH^- anions are hexagonal close packed arranged and Ni^{2+} occupies the octahedral holes. Within the layers covalent Ni-O bonding with ionic character is present with a bond distance of 2.14 Å, whereas the layers are connected via weak van der Waals forces (Ni-Ni distance 3.12 Å within the layer and 4.60 Å across the layer). $Ni(OH)_2$ is easily formed in basic solutions of Ni(II) salts, but in presence of ammonia it dissolves and forms the blue $[Ni(NH_3)_6]^{2+}$ complex ion.[62] NiO is only soluble in acids and crystallizes in the NaCl-lattice type, which is a fcc (face-centered cubic) arrangement of O^{2-} ions and the octahedral holes are occupied by Ni^{2+} (Figure 2. 3). The Ni-O bonds are ionic with a bond distance of 2.09 Å (and 2.96 Å for Ni-Ni).

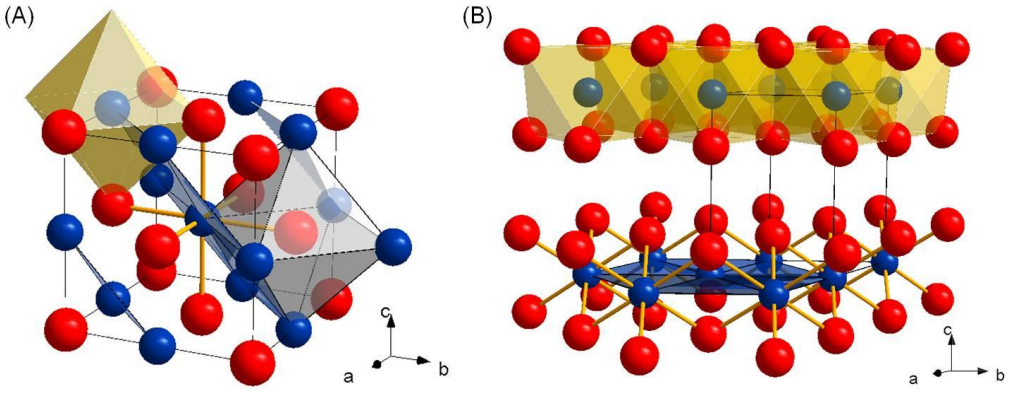

Figure 2. 3. Crystal structures of (A) NiO (amcsd #0017028)[64] in the cubic NaCl-structure type and (B) $Ni(OH)_2$ (amcsd #0011791)[64] in the layered CdI_2-structure type. Color code: Ni blue, O red; Ni-O polyhedra light orange, Ni-Ni coordination sphere blue, in (A) a $[ONi_6]$-octahedra is shown in grey.

The sulfur compounds of Ni are present in a high variety, as presented in the Ni-S phase diagram (Figure 2. 4).[65-67] An overview about the phases and their structural properties are given in Table 2. 2 and the structures of selected compounds are shown in Figure 2. 5. According to Figure 2. 4, the Ni sulfide phase with the highest proportion in the Ni-S system is the trigonal Ni_3S_2 phase (haezlewoodite). The structure can be described as an approximately body-centered cubic lattice of S^{2-}, in which Ni occupies the tetrahedral holes.[68] Thus, Ni is distorted tetrahedral coordinated by S^{2-} ions and also by Ni cations at a slightly longer distance (Table 2. 2). The coordination polyhedra are shown in Figure 2. 5(A). Another important phase is the godlevskite Ni_9S_8 with an orthorhombic crystal system and four formula units in one unit cell. Nickel is as well distorted tetrahedral coordinated by S^{2-},

but in the second coordination shell Ni is trigonal bipyramidal coordinated by Ni (Figure 2. 5(C)). Furthermore, the formal average oxidation state of Ni is with +1.8 higher than in Ni_3S_2.

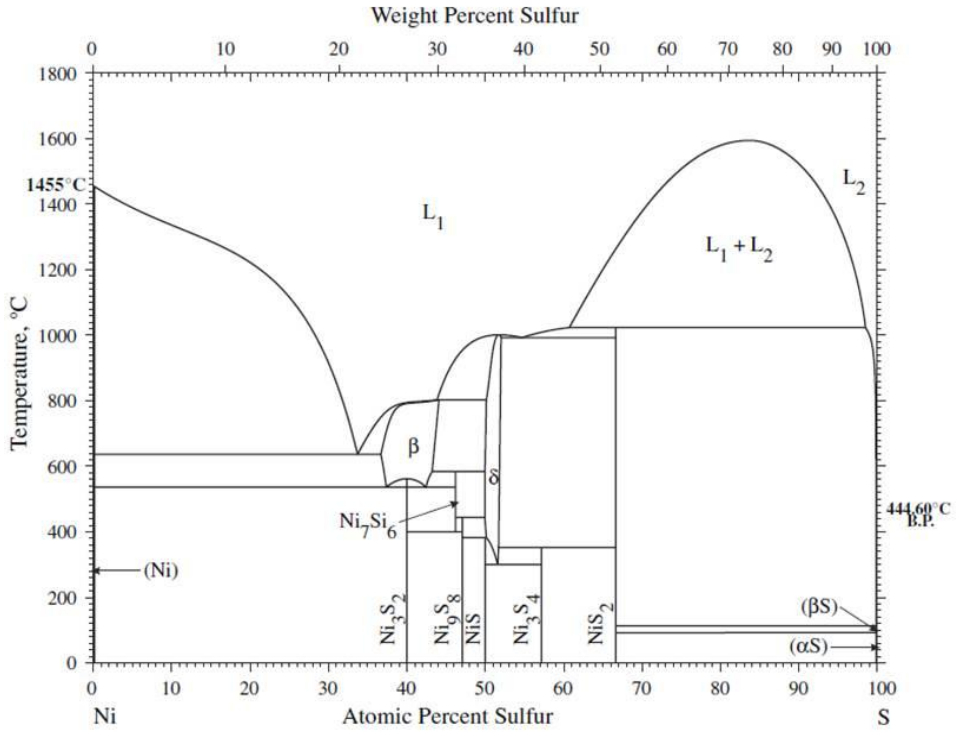

Figure 2. 4. Phase diagram for the system Ni-S. The picture is taken from Refs.[67] and [66].

The oxidation state of Ni in NiS is +2. NiS exhibits different polymorphs, the trigonal low temperature crystal structure, the millerite prototype, is shown in Figure 2. 5(D). This polymorph consists of three formula units per unit cell and square pyramidal coordinated Ni by S^{2-}. The arrangement of Ni is complex, therefore two different views are provided in Figure 2. 5(D). Overall, there are four equivalent Ni-Ni distances in a layered structure with two Ni neighbors in the same layer and the other both in the Ni layer above and below, respectively. An important high temperature modification of NiS is the hexagonal NiAs-type phase (space group P63/mmc), which has a layered structure and [NiO_6]-octahedra. The last structure shown in Figure 2. 5 is the cubic Ni_3S_4 (polydymite), in which Ni is present as Ni^{2+} and Ni^{3+}, thus, Ni has in average the highest oxidation state of the Ni sulfides considered here. Polydymite is formed at S concentrations above 35 wt.%, according to the phase diagram (Figure 2. 4). The unit cell consist of eight formula units and Ni^{2+} is tetrahedrally and Ni^{3+} octahedrally coordinated by S^{2-}. There are also different Ni-Ni coordination polyhedra, i.e., Ni^{3+} is trigonal-anti-prismatic coordinated and Ni^{2+} is surrounded by twelve other Ni atoms. NiS_2 possesses triclinic, distorted pyrite-type structure, and cubic, space group Pa-3, polymorphs with Ni^{2+} in an octahedral S coordination with a formal charge of -1 for S. In the orthorhombic α-Ni_7S_6 phase, with a small proportion in the phase diagram, a square-pyramidal coordination of Ni (like in the millerite-type NiS) is present.

Table 2. 2. Overview about Ni sulfides including their most important structural features.[a]

Sum formula	Average oxidation state	Space group	Coordination geometry[b]	1st coordination sphere[c]	2nd coordination sphere[c]
Ni_3S_2	+1.3	trigonal R 32	tetrahedral	2 Ni-S: 2.26 2 Ni-S: 2.27	4 Ni-Ni: 2.47
Ni_9S_8	+1.8	orthorhombic c 222	tetrahedral	2 Ni-S: 2.25 2 Ni-S: 2.28	3 Ni-Ni: 2.52 2 Ni-Ni: 2.89
NiS	+2.0	trigonal R 3m	square pyramidal	5 Ni-S: 2.31	4 Ni-Ni: 3.16
Ni_3S_4	Ni^{2+}(Td) Ni^{3+}(Oh)	cubic Fd-3m	tetrahedral octahedral	4 Ni-S: 2.15 6 Ni-S: 2.32	6 Ni-Ni: 3.36 12 Ni-Ni: 3.93
α-Ni_7S_6	+1.7	orthorhombic cmcm	square pyramidal	5 Ni-S: 2.32	4 Ni-Ni: 2.46
NiS_2	+2.0	triclinic P1	octahedral	3 Ni-S: 2.33 3 Ni-S: 2.43	4 Ni-S: 3.59 4 Ni-S: 3.73

[a]Based on cif structure files from the ICSD[69] and Pearson's Handbook of Crystallographic Data[65]; [b] coordination geometry of Ni in respect to first, closed neighbors; [c] the amount of neighbors, the type of neighbors and the distance in Å is given.

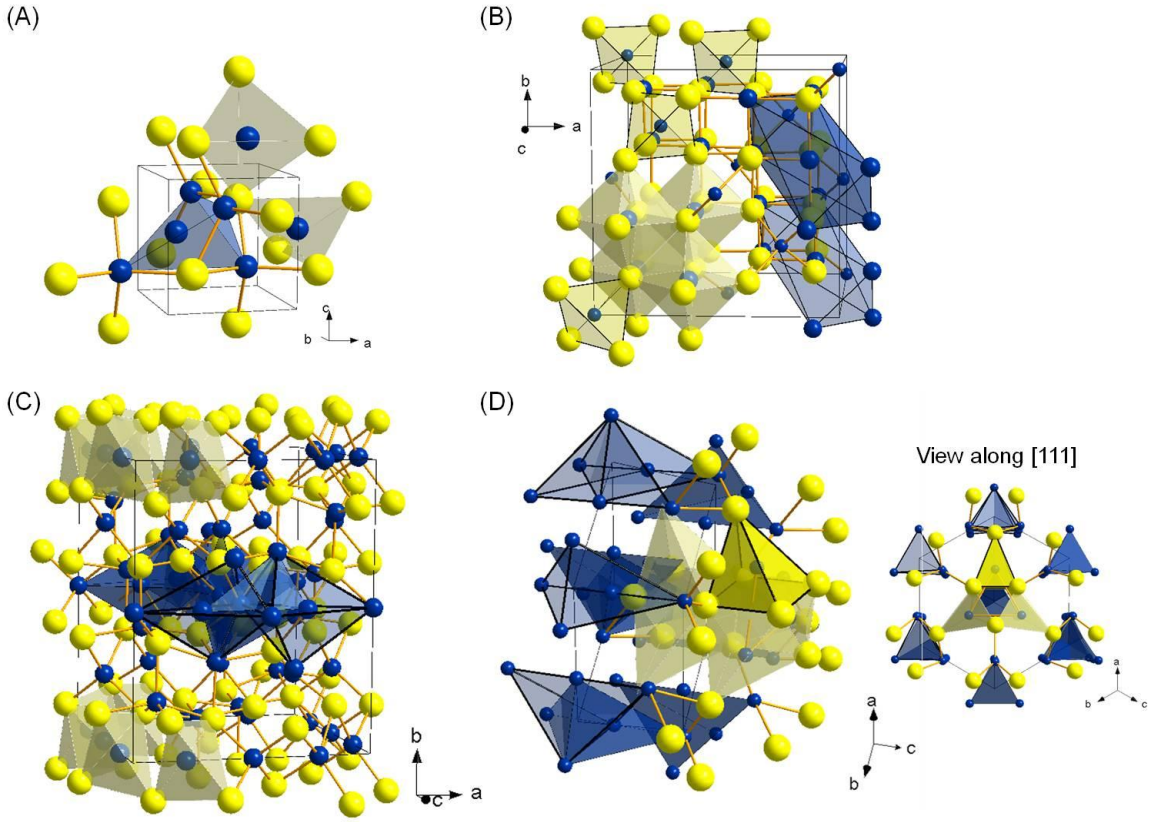

Figure 2. 5. Crystal structures of (A) Ni_3S_2 (ICSD #27521), (B) Ni_3S_4 (ICSD #57435), (C) Ni_9S_8 (ICSD #63080) and (D) NiS in millerite structure type (ICSD #29312).[69] The unit cell and the Ni-S and Ni-Ni coordination polyhedra are presented. Color code: Ni atoms and Ni-Ni polyhedra blue, S atoms and Ni-S polyhedra yellow.

Molybdenum and Tungsten Compounds

In the current work, only the oxygen and sulfur compounds of Mo and W are of interest. Due to the chemical similarity of Mo and W, the compounds of both metals are discussed together and their differences are eventually highlighted. In the following, if not explicitly said, both elements Mo and/or W are addressed together as "metals" or "metallates" and the symbol "M" is used instead of Mo and W.

There are different oxides with metallic oxidation states between +6 and +4 and oxo-anions like metallates, iso- and hetero-polymetallates anions with complex structures and usually M(VI) in octahedral coordination. Important structural features of selected oxygen compounds are summarized in Table 2. 3 and some structures are presented in Figure 2. 6 and Figure 2. 7. The common oxides are the $M(VI)O_3$ and $M(IV)O_2$, but there are also many oxides known with mixed metallic oxidation states (Mo_8O_{23}, Mo_4O_{11} or $W_{20}O_{58}$), which are prepared by heating of the trioxides. The dioxides MO_2 crystallize in a monoclinic distorted rutile-type structure and are metallic conductive compounds. Due to the lattice distortion, very short M-M distances are present which results in paired metal atoms with M-M bonds. The trioxides have different crystal structures all consisting of distorted $[MO_6]$-octahedra. However, the trioxides are different for Mo and W in terms of symmetry and therefore crystallographic structure and properties. The orthorhombic α-MoO_3[a] exhibits a unique layered structure of edge-connected heavily distorted $[MO_6]$-octahedra, which build chains in the z-direction and are connected via corners to the next layer in the x-direction (Figure 2. 6(A)). The strong distortion of octahedra allows also a description of the structure via $[MoO_4]$-tetrahedra, but both descriptions are idealized since 5 different Mo-O bond distances are identified.[70] MoO_3 is a white solid and has a melting point of 795 °C[62] and is known for its defect-structure with oxygen vacancies and partial reduced Mo, therefore, it is an n-type semiconductor with indirect band-gaps.[70] The compound γ-WO_3[a] has also conducting properties[71-72] is yellow and has a melting point of 1473 °C.[62] In Figure 2. 6, its three-dimensional structure of corner-connected distorted $[WO_6]$-octahedra is shown. The octahedra are much less distorted than in MoO_3 and the γ-WO_3 structure corresponds to a monoclinic distorted ReO_3-type.[73] There are synthetic mixed Mo-W-oxides known, which are present as solid solutions with structures similar to the ReO_3-type lattice. Low W concentrations and partial reduction could result in MoO_3-like structures with crystallographic share planes and phase separation.[71-72, 74-75] Both trioxides are not soluble in water or acids, but in bases they form metallates with MO_4^{2-} anions. This reaction is irreversible, the addition

[a] α-MoO_3 and γ-WO_3 are the stable crystal structures at ambient conditions. For WO_3, seven polymorphs are known, which have a ReO_3-type structure with different crystal systems and distortions of the $[WO_6]$-octahedra. β-MoO_3 crystallizes as well in a distorted ReO_3-type structure.

of acids to metallates initiates a condensation reaction and the formation of iso-polymetallates. A pH value smaller than 2 results in the formation of trioxide hydrates, also called molybdic or tungstic acid, which crystallize depending on the water content in different crystal systems.[60]

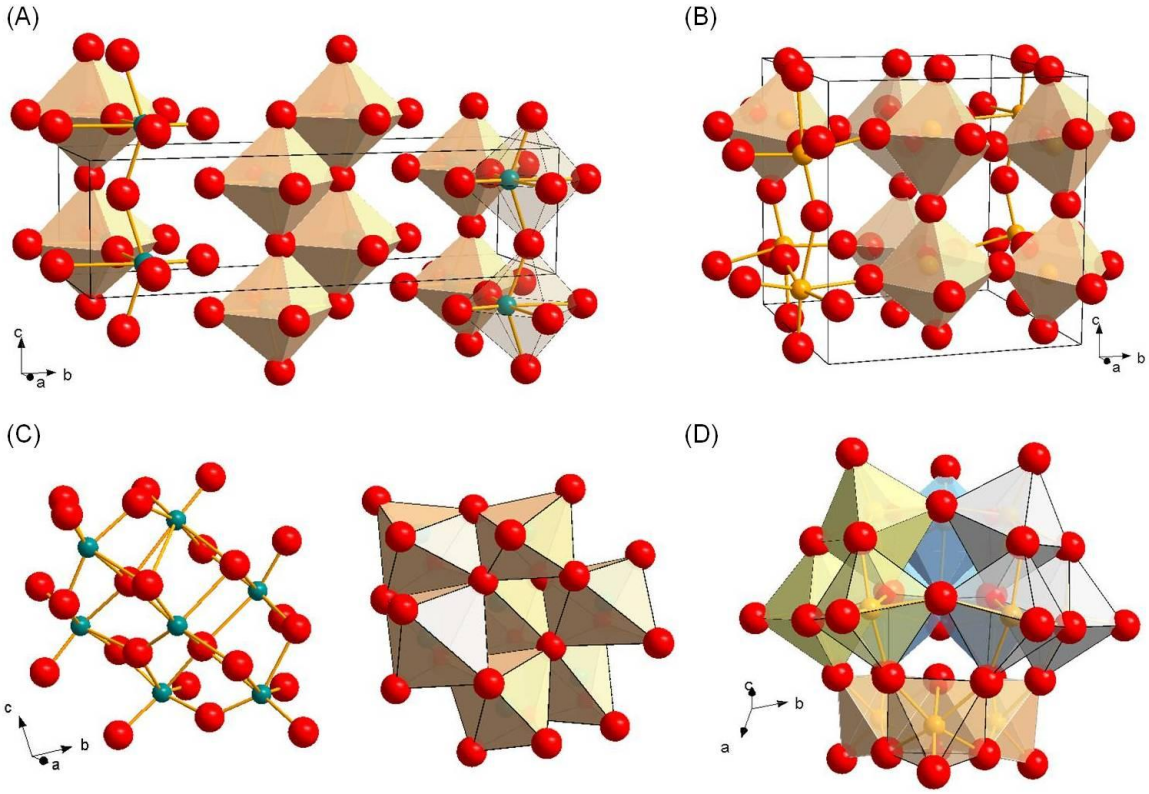

Figure 2. 6. Crystal structures of (A) α-MoO_3 (ICSD #35076)[69], (B) γ-WO_3 (COD #2106382)[76] (C) $[Mo_7O_{24}]^{6-}$ ion of $(NH_4)_6(Mo_7O_{24})$ (ICSD #27452)[69] and (D) the Keggin-ion $[H_2W_{12}O_{40})]^{8-}$ (COD #1010873)[77]. Color code: Mo light blue, W orange, O red; M-O polyhedra light orange; in (D) the 4 $[W_3O_{13}]$-units are colored differently.

Molybdates and tungstates typically consists of discrete, isolated $[MO_4]$-tetrahedra. In $CaMoO_4$ and $CaWO_4$, the M^{6+} ions are in an almost perfect tetrahedral coordination environment. Their structure-type is named after the scheelite mineral $CaWO_4$. The metallates K_2MoO_4, Na_2WO_4 and $CdMoO_4$ crystallize as well in the scheelite-type but appear already with slightly distorted isolated tetrahedra.[78-80] In contrast, $CdWO_4$ crystallizes in the wolframite-type structure consisting of distorted connected octahedra (Table 2. 3). Metallates with relatively large bivalent counter ions like the alkaline and earth alkaline metals as well as Pb crystallizes in the scheelite-type structure and smaller bivalent cations (Fe, Mn, Co, Ni) could crystallize in the wolframite-type structure. Cd^{2+} has an intermediate ionic radius, therefore different structures are observed.[80] A similar behavior is reported for Ni^{2+} metallates. $NiWO_4$ crystallizes in the wolframite-type structure, whereas for $NiMoO_4$ different polymorphs with 4-fold and 6-fold Mo^{6+} are known exhibiting differently connected polyhedra. In Figure 2. 7, the monoclinic α- , β- and ω-phase of $NiMoO_4$ are shown, the highest stability

is found for the β-form.[81] The β-modification crystallizes in the α-$MnMoO_4$-structure type with $[MoO_4]$-tetrahedra, which are only edge-connected to the strong distorted $[MnO_6]$-octahedra (or $[NiO_6]$-octahedra, respectively).[82] In the α-form, chains of edge sharing $[MoO_6]$- and $[NiO_6]$-octahedra are present and the ω-phase is isomorph to $NiWO_4$ exhibiting the wolframite-type structure. $NiWO_4$ consists of a distorted hexagonal close packed arrangement of oxygen atoms and distorted $[WO_6]$- and $[NiO_6]$-octahedra. As presented in Figure 2. 7(C), the octahedra with the same central atom are edge connected and the $[WO_6]$- and $[NiO_6]$-octahedra are corner connected.[83] In summary, different coordination geometries are possible for molybdates and tungstates and strong distortion of the polyhedra allows transformations among different polymorphs, which are usually induced by temperature or pressure changes. Moreover, the addition of Mo to tungstates or W to molybdates could also cause structural changes. For instance, for mixed $CdMo_xW_{1-x}O_4$ the scheelite-type and the wolframite-type structure are reported as a function of x. Both structures showed a limited solubility into each other, therefore the wolframite structure is predominant at Mo/W ratios below 0.5 and the scheelite structure above the Mo/W ratio of 0.5 accompanied with strong distortion of the polyhedra.[80]

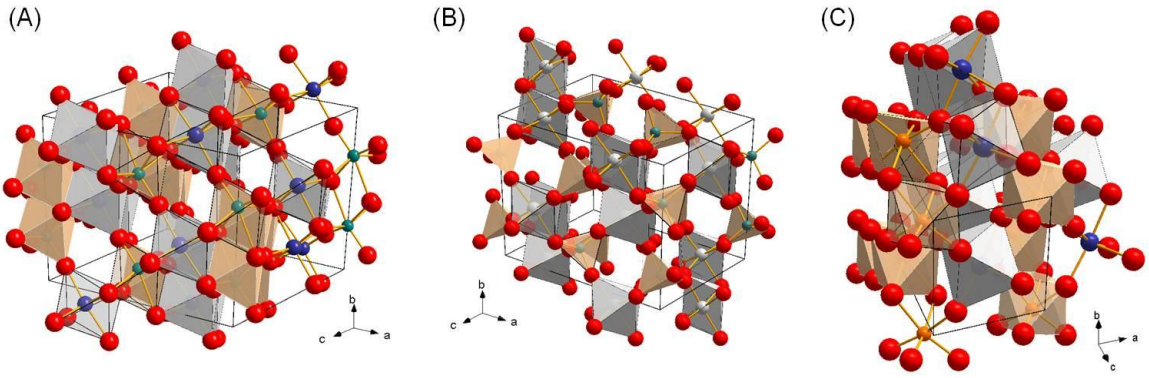

Figure 2. 7. Crystal structures of $NiMoO_4$ polymorphs. (A) α-$NiMoO_4$ (ICSD #0017028), (B) α-$MnMoO_4$ prototype of β-$NiMoO_4$ (ICSD #0011791) and (C) $NiWO_4$ isomorph to ω-$NiMoO_4$ (ICSD #0011791).[69] Coordination geometry and polyhedra connectivity are presented in an extended unit cell. Color code: Mo light blue, W orange, Mn grey, Ni blue, O red; Mo/W-O polyhedra light orange, Ni-O/Mn-O polyhedra grey.

The iso-polymetallates with the lowest molecular weight are dimolybdate $[Mo_2O_7]^{2-}$ and tetratungstate $[W_4O_{16}]^{8-}$, which form at pH-values around 6. The dimolybdate anion consist of corner connected distorted $[MoO_4]$-tetrahedra. A further pH-value decrease results in fast formation of heptamolybdate anion $[Mo_7O_{24}]^{6-}$ and subsequently to the octa- and oligomolybdate, which are all present in equilibrium. Ammonium heptamolybdate (paramolybdate) is shown in Figure 2. 6(C), which is a cluster of seven edge and corner connected distorted $[MoO_6]$-octahedra. The pH-controlled equilibrium reaction is slower for the tungstates, however, an heptatungstate is also observed as well as a deca- and dodecatungstate $[H_2W_{12}O_{40}]^{6-}$. The α-$[H_2W_{12}O_{40}]^{6-}$ anion, the metatungstate, is presented in

Figure 2. 6(D). It has a Keggin-ion type structure, i.e., it is composed by four agglomerates of three edge connected distorted [WO_6]-octahedra forming [W_3O_{13}]-units, which are all corner connected building a shell.[84] There are different dodecatungstates known, e.g. paratungstate $[H_2W_{12}O_{42}]^{6-}$.[85] Moreover, it is possible to incorporate other cations, like P or Si, in iso-polymetallates during precipitation, the resulting mixed compounds are called hetero-polymetallates.

Table 2. 3. Overview about selected Mo and W oxides including a few structural features.[a]

Sum formula	Ox. state[b]	Space group	Coordination geometry[c]	Polyhedra connection[c]	Remarks
MoO_2 WO_2	+4	monoclinic P 2_1/c	octahedral		distorted rutile-type d(M-M) = 2.5 Å
α-MoO_3	+6	orthorhombic P bnm	distorted octahedral	edge and corner	layer
γ-WO_3	+6	monoclinic P 2_1/n	distorted octahedral	corner	distorted ReO_3-type
$CdMoO_4$	+6	tetragonal I 4_1/a	tetrahedral	isolated	scheelite-type
$CdWO_4$	+6	monoclinic P 2/c	octahedral	edge and corner	wolframite-type
β-$NiMoO_4$	+6	monoclinic C 2/m	tetrahedral	isolated	α-$MnMoO_4$-type [NiO_6] highly distorted
α-$NiMoO_4$	+6	monoclinic C 2/m	octahedral	edge (chains)	α-$CoMoO_4$-type
$NiWO_4$	+6	monoclinic P 2/c	octahedral	edge and corner	wolframite-type
$(NH_4)_6(Mo_7O_{24})$	+6	monoclinic P 2_1/c	distorted octahedral	edge and corner	
$(NH_4)_6(H_2W_{12}O_{40})$	+6	cubic[84]	distorted octahedral	edge and corner	Keggin-ion type

[a]Based on cif structure files from the ICSD[69] and Ref.[60, 70, 77, 80-83, 86]; [b] Oxidation state of Mo or W; [c] Coordination geometry and connectivity of Mo-O or W-O polyhedra in respect to first, closed O neighbors, the connection to eventually other contained metal polyhedra (Mn-O, Ni-O) is explained in the text.

The addition of H_2S to acidic metallate MO_4^{2-} solutions results in hydrated MoS_3 and WS_3, which can react further to the thio-metallates MoS_4^{2-} and WS_4^{2-} under addition of alkaline sulfides, like $(NH_4)_2S$. However, the phase diagrams of the systems Mo-S and W-S show that in terms of stability and occurrence the metal(IV)-disulfides are the most relevant ones, although there are sulfur poor and sulfur rich phases (Figure 2. 8).[60, 87] The disulfides are formed by heating Mo and W oxides in a H_2S flow and both occur in nature as molybdenite (MoS_2) and tungstenite (WS_2). The color and appearance of the MS_2 compounds are similar to graphite, i.e., soft, easy to slip and cleave grayish black solids.

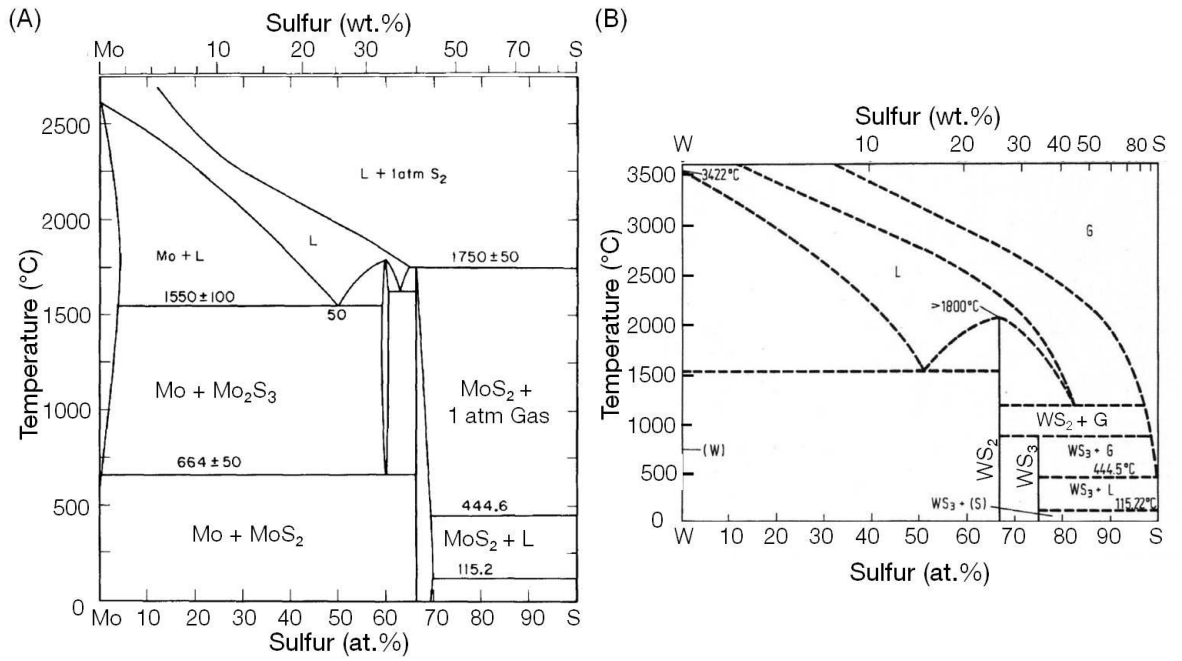

Figure 2. 8. Phase diagrams for the systems Mo-S (A) and W-S (B). The pictures are taken from Ref.[88] (Mo-S) and [89] (W-S).

MoS_2 and WS_2 are isomorph and have a layered structure, which is found in three different polytypes, in a hexagonal 2H, rhombic 3R and trigonal 1T system. This nomenclature is used to describe the different stacking sequences of the atom layers in a layered structure. The stacking sequences for the 1T, 3R and 2H systems and the corresponding space groups are shown in Figure 2. 9(A). In the trigonal 1T polytype the metal cations are octahedrally coordinated, whereas in the other both systems a trigonal-prismatic geometry is present. However, the hexagonal 2H polytype is the most common one, thus 2H-MoS_2 and 2H-WS_2 will be denoted as MoS_2 and WS_2 in the following. MoS_2 and WS_2 crystallize in a hexagonal crystal system with a dihexagonal-dipyramidal (hexagonal prismatic) crystal symmetry. The corresponding space group is the P 6_3/mmc with lattice parameters *a* of 3.16 Å and *c* of 12.29 Å. The hexagonal unit cell contains two formula units. The ions M^{4+} and S^{2-} are hexagonal packed in Mo and S sheets in the (001)-plane (ab-plane), whereas one M-sheet is sandwiched between two S-sheets along the z-axis (Figure 2. 9(B) and (C)). The metal cations occupy the half of the trigonal prismatic holes of the stacked S-sheets. Thus, S-M-S layers are created with empty trigonal-prismatic lattice sites between different layers, which results in a large inter-layer distance of around 6.2 Å and weak van der Waals forces between the layers. Within the S-M-S layers, i.e., between the 6-fold coordinated Mo and S covalent bonds are present with a bond distance of around 2.41 Å. Between the metal atoms a bond distance of around 3.16 Å is found with a coordination number of 6 (due to the hexagonal arrangement, Figure 2. 9(C)).

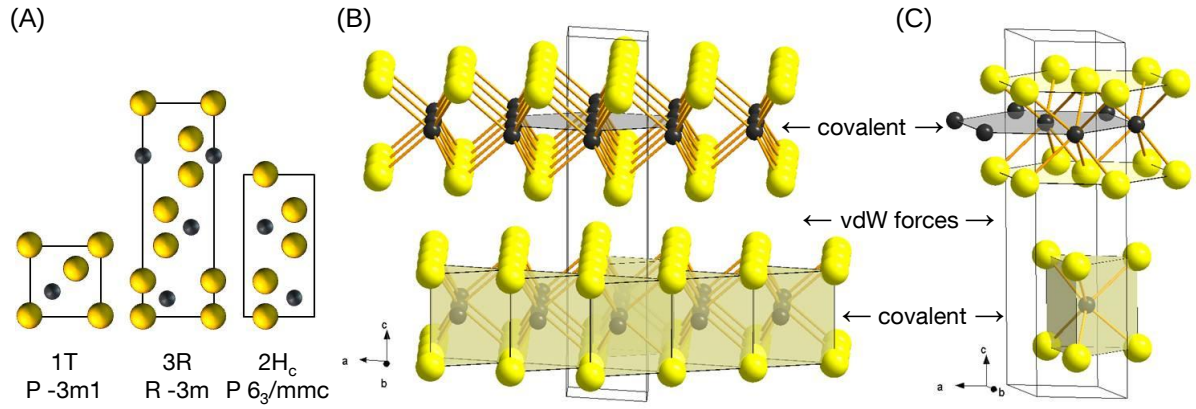

Figure 2. 9. The crystal structure of MS_2. In (A) the stacking of the atom layer in the different polytypes 1T, 3R and 2H are shown by a projection of the hexagonal (110) plane[90]; in (B) the 2H-MS_2 layers and in (C) the coordination geometry of the M^{4+} and S^{2-} are shown in the hexagonal unit cell (ICSD #644245)[69]. Additionally the bonding situations are indicated. Color code: M black, S yellow; M-S polyhedra yellow, M-M coordination sphere grey.

The multiple stacking of several S-M-S layers in the z-direction creates three-dimensional crystals. The amount of stacked S-M-S layers is called stacking degree, which can be visualized by electron microscopy or appears in form of an intense (002) reflections in X-ray diffraction (14.2° 2θ) and electron diffraction patterns (Figure 2. 10).[2, 31, 91-93] The characteristic bonding situation within MS_2 causes anisotropic behavior and anisotropic electronic and mechanical properties. For instance, the MoS_2 and WS_2 crystals grow faster along the a- and b-axis than in the z-direction[94], therefore the sulfides are often larger in terms of length than in height appearing as very long sulfide slabs with high stacking degrees (Figure 2. 10). MoS_2 and WS_2 are easy cleavable parallel to the ab-plane, which enables their use as lubricants.[14] Furthermore, the stacking degrees influence the electronic and band structure. The full description of the band structure of MS_2 is out of the scope of the current work. However, it is important to mention that MoS_2 and WS_2 are indirect d^2 semiconductor with a band gap of 1.0 to 1.5 eV.[19, 95] The band gab is caused by splitting of the d-orbitals in the trigonal prismatic ligand field of sulfur (d-orbital splitting was explained in Figure 2. 2). The $3p_x$ and $3p_y$ orbitals of sulfur form hybrid-orbitals with the d_{xy} and d_{x2-y2} orbitals of Mo and W, which creates the unfilled conduction bands. In contrast, the filled Mo/W-d_{z2} orbitals have a low energy state, therefore the mixing with the S-$3p_z$ orbitals is very weak and they are available to form the energetic valence band.[90, 95] With decreasing stacking degree of MoS_2 (and WS_2) a transition from a indirect to a direct optical band gap occurs with band gaps between 1.8 to 2.0 eV.[15, 18, 96]

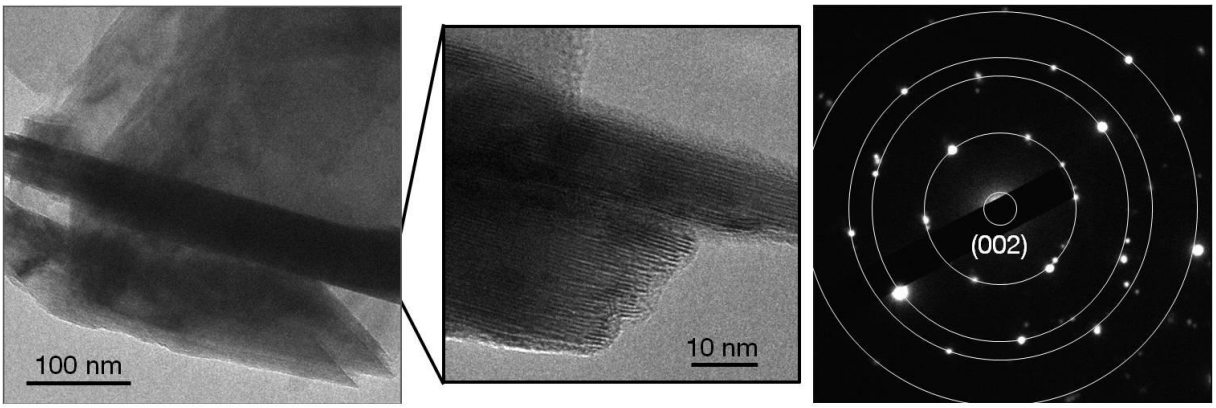

Figure 2. 10. Transmission electron microscopy study of commercial MoS_2 coupled with single area electron diffraction (SAED). Long MoS_2 crystals are presented (left), which are composed by several stacked sulfide slabs (middle). The corresponding SAED pattern shows intense reflection signals of highly crystalline MoS_2 (right). The inner ring is assigned to the (002)-reflection (lattice parameter of 6.2 Á, hidden by the probe), whereas all other rings/signals belong to smaller lattice plane distances.

The isomorphism of MoS_2 and WS_2 and the almost identical ionic radii of Mo^{4+} and W^{4+} should allow mixtures of both metals in one mixed sulfide compound. There are a few studies in literature analyzing mixed $Mo_{1-x}W_xS_2$ bulk and supported materials, single crystals or thin films. Bonneau et. al concentrated on the preparation of mixed $(Mo,W)S_2$ for the preparation of Mo-W-alloys. X-ray diffraction (XRD) and thermo gravimetric measurements brought them to the conclusion that $(Mo,W)S_2$ solid solutions were formed with varying Mo to W ratios.[17] XRD was also used by Srivastava et al. next to radial distribution functions and thermoelectric power, electrical conductivity, electron microscopy and UV-vis measurements for their $Mo_{1-x}W_xS_2$ ($0<x<1$) and $Mo_{0.5}W_{0.5}S_xSe_{2-x}$ ($0<x<2$) systems. They identified a 2H-MoS_2 structure and n- and p-type semiconducting behavior with similar band gaps for all their materials, whereas a high concentration of W and S resulted in strong structural defects and strains.[19, 97] Ho et al. analyzed the electronic structure and the temperature dependency of the band gap for $Mo_{1-x}W_xS_2$ single crystals and concluded a similar nature of the direct band gap in all investigated compositions. All these studies resulted in the conclusion that solid solutions were formed, where Mo and W were incorporated in the same disulfide system and separated MoS_2 and WS_2 phases were excluded. However, XRD is only applicable for perfect large sulfide crystals, only in this case shifts of reflection signals between mixed $Mo_{1-x}W_xS_2$ and separated MoS_2 and WS_2 phases would be visible and a differentiation would be possible. Electron microscopy, electric measurements and UV-vis spectroscopy as well as Raman spectroscopy[20] could give an indication whether Mo and W are interacting in the same sulfide phase or separated phases are present. However, the identification of an interlayer and/or intralayer mixed $Mo_{1-x}W_xS_2$ phase can be only done with element sensitive atomic resolved methods. In Figure 2. 11 (A) und (B), different interlayer $Mo_{1-x}W_xS_2$ phases are presented, in which the three-dimensional sulfide crystals are formed by stacked pure

[MoS_2]- and [WS_2]-layers with different stacking sequences. In an intralayer mixed $Mo_{1-x}W_xS_2$ phase, Mo and W are atomic mixed in one sulfide layer, which could occur as a random distribution of the metal ions, a well ordered mixture or as homogeneous solid solution (Figure 2. 11(C) und (D). Dumcenco et al. used high-resolution scanning transmission electron microscopy (HR-STEM) to visualize the distribution of Mo and W in single sulfide slabs with different Mo to W bulk ratios. They found random alloying of Mo and W,[22] similar to Figure 2. 11(D). Thomazeau et al. used extended X-ray absorption fine structure (EXAFS) to identify neighboring Mo and W in the same sulfide slab of bulk and γ-alumina supported mixed $Mo_{1-x}W_xS_2$ compounds. Their studies brought them to the conclusion, that $Mo_{1-x}W_xS_2$ lamellar solid solutions were formed dependent on the preparation procedure without giving further details on the type of mixing (inter- or intralayer, homogenous or randomly).[21, 50]

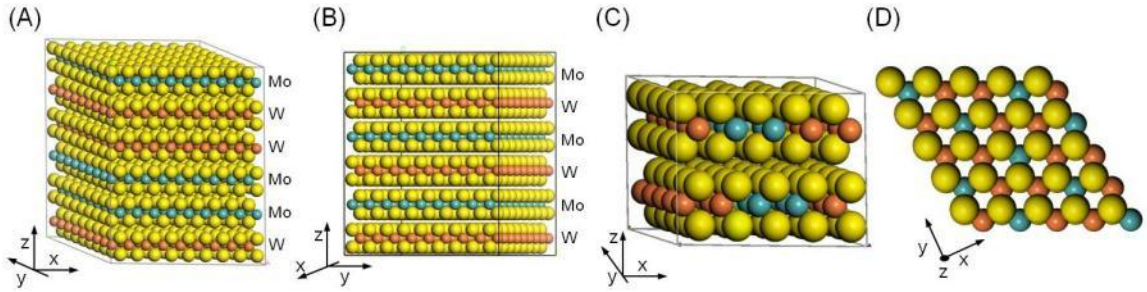

Figure 2. 11. Different possibilities of mixed $Mo_{1-x}W_xS_2$ phases. In (A) and (B) different stacking sequences of pure [MoS_2]- and [WS_2]-layers are shown, whereas in (C) a well ordered and in (D) a perfect homogeneous intralayer mixture of Mo and W in one sulfide slab are presented. Color code: Mo atoms light blue, W atoms orange and S atoms yellow circles.

2. Heterogeneous Catalysis in Hydrotreating

2.1. Hydrodenitrogenation

Heterocyclic nitrogen compounds with either pyrrolic or pyridinic structure and non-heterocyclic compounds, like aromatic and aliphatic amines, are typically contained in crude oil (Figure 1. 2).[52] A few important compounds are shown in Table 2. 4. The removal of nitrogen from these molecules is called hydrodenitrogenation (HDN) and is usually catalyzed by supported Ni promoted MoS_2. HDN studies on unsupported catalysts are comparable rare.[98-100] Aliphatic and saturated nitrogen compounds are much faster converted under hydrotreating conditions than heterocyclic, aromatic nitrogen compounds.[101] The Langmuir adsorption constants[102] given Table 2. 4 can be used as a measure for the reactivity since a strong adsorption on the catalyst surface, like for quinoline, results in a lower rate, slow desorption and blockage of active sites.

Table 2. 4: Selected nitrogen containing organic molecules as typical representatives of nitrogen compounds in crude oil and their calculated Langmuir adsorption constants K.

Name	Aniline (Phenylamine)	Pyridine	Quinoline	Indole (2,3-Benzopyrrole)	Carbazole (Dibenzopyrrole)
Chemical strcture	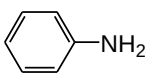		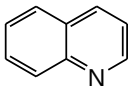	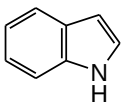	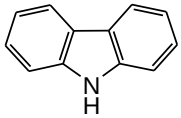
K, kPa^{-1}[102]	0.094	0.43	0.98	-	0.51

The reason for the low reactivity of aromatic compounds is the much lower bond energy of the C_{sp3}-N single bond (306 kJ/mol) than the one for the C_{sp2}-N double bond (616 kJ/mol).[52] Furthermore, the different molecules have different basicity, which determines the interaction strength and type with the catalyst surface. Basicity is explained by the electronic structure of these molecules. Nitrogen exhibits a free electron pair, which is either involved in the aromatic π-system, like in pyrollic structures, or not, like in pyridinic molecules or amines. Interaction of the lone pair with the π-system decreases the basicity of the nitrogen atom and increases the electron density of the aromatic ring. Therefore, pyrrolic compounds are considered as non-basic and they preferably interact with the catalyst surface via the electron rich aromatic ring. In contrast, amines and pyridinic compounds are strong bases, additionally the pyridinic π-system is relatively electron poor due to the electron-withdrawing properties of nitrogen. It is, therefore, assumed that amines and pyridinic compounds initially adsorb on the catalyst surface *via* the nitrogen atom.[103] However, the increasing adsorption

constants from aniline, over pyridine to quinoline suggest that nitrogen aromatics also interact via their aromatic π-system. The aromaticity of nitrogen compounds is in general higher than, e.g., that of sulfur compounds.[103] The low reactivity of aromatic nitrogen compounds is one of the reasons why the hydrogen consumption for hydrodenitrogenation (HDN) reactions is larger than for hydrodesulfurization. Another reason is the high bond energy of the C_{sp2}-N bond in the aromatic ring, which causes the need of the hydrogenation of the aromatic system prior to nitrogen removal. Even for anilines, hydrogenation is the first reaction step within their HDN process.[101] Hydrogenation steps of HDN reactions are reversible and exothermic, thus, the HDN rate and the selectivities could be affected by thermodynamic equilibria. With increasing temperature the equilibrium of hydrogenations is shifted backwards to the aromatic compound and the thermodynamics of the hydrogenation becomes rate controlling. Therefore, HDN is performed at high pressures to reach the kinetic controlled regime. Furthermore, hydrogenation of nitrogen free compounds does not take place as long as nitrogen containing molecules are present due to their higher adsorption constants.[101, 103]

All HDN reactions take place via two different reaction pathways, which are hydrogenation with a subsequent nitrogen removal step (HYDN) or via a direct denitrogenation (DDN). Thus, hydrogenation and hydrogenolysis reactions are involved in HDN reactions, which are irreversible C-N bond scissions. Additionally, ring-opening reactions occasionally occur. For a reliable kinetic and mechanistic study, proper model compounds have to be selected, which represent best the contained nitrogen compounds in crude oil. A quite often selected compound is quinoline due to its relatively large aromatic system and its carbocyclic and heterocyclic six-membered ring. This structure allows the study of all important reactions steps as presented in Figure 2. 12. Satterfield et al. proposed a reaction mechanism for quinoline[104], which was confirmed by several groups,[105-106] and lately by Gutiérrez et al.[3] There are two different pathways proposed, although, both start with a hydrogenation step. In the first route the carbocyclic ring is saturated to 5,6,7,8-tetrahydroquinoline (58THQ) and in the second route the saturation of the heterocyclic ring to 1,2,3,4-tetrahydro-quinoline (14THQ) occurs. In the subsequent step, 58THQ is hydrogenated to decahydroquinoline (DHQ), which is in equilibrium with 58THQ. At 370 °C and 5.0 MPa, DHQ is favored.[3] Afterwards, the ring opening of DHQ via C_{sp3}-N bond cleavage occurs to propylcyclohexylamine (PCHA). For the subsequent hydrogenolysis of PCHA, two different mechanisms are feasible, a Hofmann type β-H elimination or a S_{N2} type nucleophilic substitution of the NH_2-group by a SH-group (thiol). During Hofmann elimination, an acidic active site protonates the nitrogen and a base promotes the elimination of ammonia. The elimination mechanism is preferred at high temperatures and pressures, whereas the substitution mechanism happens at low pressures and high H_2S partial pressures. However,

the fact that the subsequent formation of propylcycohexene (PCHE) is fast as well as the close position of the NH_2-group to the carbocyclic ring, makes the elimination mechanism more likely.[6, 25] PCHE is composed by three isomers, which are 1-propylcyclohexene, 3-propylcyclohexene and propyliden-cyclohexane with 1-propylcyclohexene being the most stable one due to hyperconjugation (higher substituted double bond). The final step is the hydrogenation of PCHE to propylcyclohexane (PCH). In this first pathway, the ring opening of DHQ is the rate determining step.

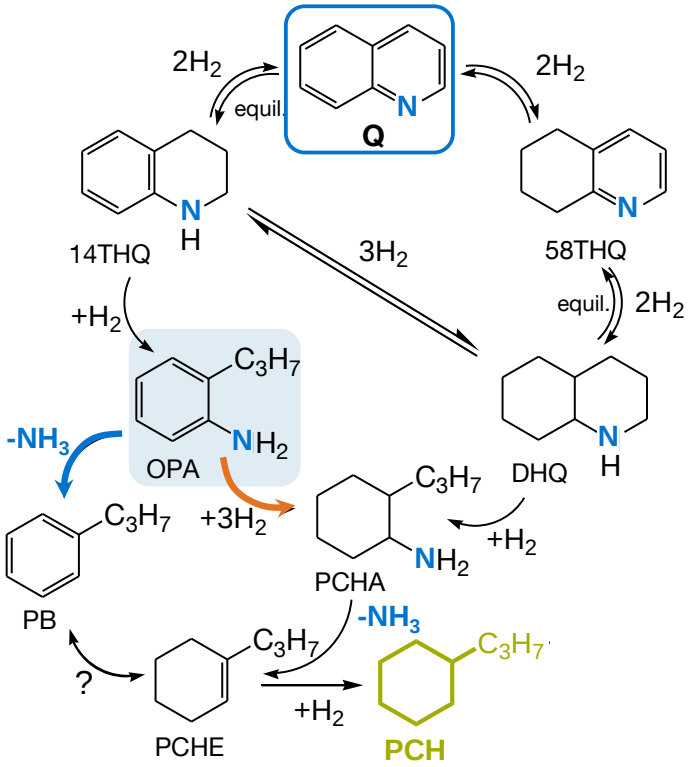

Figure 2. 12. Reaction network for hydrodenitrogenation (HDN) of quinoline (Q) showing the products 1,2,3,4-tetrahydroquinoline (14THQ), 5,6,7,8-tetrahydroquinoline (58THQ), decahydroquinoline (DHQ), o-propylaniline (OPA), propylcyclohexylamine (PCHA), propylbenzene (PB), propylcyclohexene (PCHE) and propylcyclohexane (PCH). The most important intermediate OPA and the favored end product PCH are highlighted. The blue arrow indicates the direct denitrogenation (DDN) and the orange arrow the hydrogenation (HYDN) pathway, respectively. The reaction between PB and PCHE, labeled with "?", is not observed as long as N compounds are present (based on Ref.[3]).

In the second HDN pathway, quinoline and 14THQ reach fast equilibrium composition, in which 14THQ is the predominant compound (at 370 °C and 5.0 MPa).[3] In following step, o-propylaniline (OPA) is formed after ring opening of 14THQ. OPA represents the most important intermediate in the quinoline mechanism and is therefore also often used as model compound. The subsequent conversion of OPA takes place via two different routes, which are the DDN route to propylbenzene (PB) and the HYDN route to propylcyclohexylamine (PCHA). The latter is the preferred route. In the second pathway the ring opening of 14THQ and the hydrogenation of OPA are the rate determining steps. Overall, the ring opening of

DHQ is faster than for 14THQ, which results in a slight preference for the quinoline conversion via 14-THQ to DHQ.[3]

For the kinetic modeling of HDN, it is in general assumed that all nitrogen compounds undergo a fast chemisorption following Langmuir Hinshelwood (LH) type mechanism and rate expressions (Equation I).[6, 107]

Equation I: Langmuir-Hinshelwood type kinetics for reactant R

$$-r_{overall} = k \cdot p_R^n \cdot p_{H2}^m = \frac{(k_1' + k_2') \cdot K_R \cdot p_R}{1 + K_R \cdot p_R + \sum K_{Products} \cdot p_{Products}} = k_1 \cdot p_R + k_2 \cdot p_R$$

with assumptions:
1. at $t \rightarrow 0$, partial pressure of products $p_{products} = 0$
2. reaction order of reactant R n = 1
3. reaction order of H_2 m = 0
4. $1 >> K_R \cdot p_R$ (adsorption constant · partial pressure of R)

and k: kinetic rate constant

In a simplified approach, all compounds in the network adsorb on the same active sites. The adsorption of hydrogen is neglected due to its constant pressure and a reaction order of one for the target nitrogen compound, herein after called reactant, is assumed. The coverage of the catalysts surface by the reactant and the initial concentration of the products are assumed negligible. Using these assumptions, Equation II can be used to express the reaction rate and after integration the conversion of the reactant allows the estimation of kinetic rate constants for space time dependent experiments.

Equation II: Reaction rate r and rate constant k of reactant R (incl. their transformation)

$$r_R = \frac{dp_R}{dt} \xrightarrow{Integration} \ln(c_{0,R} - c_{t,R}) = -k \cdot t_{space} \Leftrightarrow \ln(1 - X_R) = -k \cdot t_{space}$$

$$r_R \approx \frac{c_{t,R} - c_{0,R}}{t_{space}}$$

with: t: time; t_{space}: space time of flow reactor
c: concentration (c_0: start and c_t: final concentration)
X_R: conversion of reactant R

The temperature dependency of the calculated rate constants follows the Arrhenius approach, and therefore the overall apparent activation energies can be determined with Equation III. Alternatively, also the temperature dependency of reaction rates of the reactant, gained by the conversion at a constant space time (or yield of the products), can be used for a good approximation of apparent activation energies either for the whole HDN or for specific reaction steps.

Equation III: Arrhenius equation for the estimation of the apparent activation energy $E_{A,app}$

$$\ln k = \ln k_0 \cdot - \frac{E_{A,app}}{R \cdot T}$$

with: k_0: pre-exponential factor
R: molar gas constant (8.314 J · (mol · K)$^{-1}$)
T: temperature in K

However, the reaction order of quinoline is slightly below one[107] and also two active/adsorption site models in combination with LH kinetics resulted in improved kinetic fits. Additionally, the network for quinoline is complex and requires separate modeling for reaction intermediates, neglecting of products with low concentrations like PCHA or the combination of different compounds like the ones present in equilibrium (quinoline+14THQ or 58THQ+DHQ) to simplify the model.[3, 6]

Additionally to the compounds contained in the specific HDN network, there many different parameters, that have an influence on the HDN rate. For instance, hydrogen and H_2S partial pressure, but also other heteroatom containing molecules. Competitive adsorption could occur or different compounds in the feedstock could interact or even react with each other and change the reaction network. Sulfur compounds or H_2S are known to be beneficial for the overall activity since it enhances the C-N bond scission. On the other hand, sulfur compounds may poison the hydrogenation reaction and may block adsorption sites.[25, 101] H_2S plays further an important role in the active site creation (vide infra).

2.2. Hydrodesulfurization

Like in the case of nitrogen compounds, also the variety of sulfur containing organic molecules in crude oil is very large. Additionally, they are contained in every oil fraction, which explains the need of an hydrotreater for almost every fraction after distillation in a refinery (Figure 1. 1). The hydrodesulfurization (HDS) takes usually place on supported Co promoted MoS_2,[23, 52, 101, 108] whereas there is a tendency towards Ni promoted catalysts and also WS_2 based as well as unsupported materials are used to produce ultra-low sulfur diesel.[24, 43-44, 46, 48, 51, 109-110] For very challenging feeds hydrotreaters in a row are used, i.e., the sulfur content is stepwise reduced by using different hydrotreater sizes and catalyst loadings. The predominant classes of organosulfur compounds, sorted in respect to their chemical structure, are shown in Table 2. 5. There are molecules such as thiols, sulfides and disulfides and the aromatic organosulfur thiophenes, benzothiophenes and dibenzothiophenes. The latter aromatics are the main compounds in crude oil, whereas the concentration of aliphatic and aromatic thiols is low due to their high reactivity. As indicated by the relative rates in Table 2. 5, the HDS reactivity decreases in the following order: thiophene > benzothiophene > alkylbenzothiophene > dibenzothiophene >> 4,6-dialkyldibenzothiophene.[7, 101]

Table 2. 5: Selected sulfur containing organic molecules as typical representatives of sulfur compounds in crude oil and their hydrodesulfurization rates relative to thiophene[7].

Name	Thiophenol (Phenyl mercaptan)	Thiophene	Dibenzothiophene	4,6-Dimethyl-dibenzothiophene
Chemical strcture	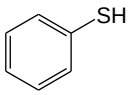		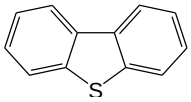	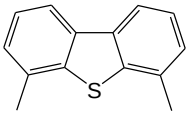
Relative rate	-	100	30	1

The process of sulfur removal exhibits hydrogenation and C-S bond scission steps, whereas the saturation of the aromatic systems is not required before C-S bond breaking (unlike in HDN). However, hydrogenation is thermodynamically favored and there are also different equilibrium stages involved in the conversion of sulfur compounds, but the applied HDS reaction conditions in industry and usually also in research laboratories avoid thermodynamic control.[52] Kinetics, i.e., the reaction rates of the reactant and the intermediates determine, therefore, the complexity of HDS reactions and networks, although H_2 pressure and temperatures could shift favored reaction pathways. The sulfur removal itself can occur via β-H Hofmann type elimination of H_2S using acid-base catalysis. Alternatively, hydrogenolysis could occur at the metal sulfide surface, in which the

organosulfur compound reacts with hydrogen releasing H_2S.[101] In general, there are some principal reaction steps, which take place during HDS of aromatic molecules. First, adsorption and coordination of the sulfur compound onto the active sites and the dissociative adsorption of hydrogen onto the sulfide surface. Secondly, hydrogenation of C=C double bonds and/or cleavage of two C-S bonds simultaneously or after each other and subsequent addition of hydrogen to the broken bonds. In the final step, the sulfur free hydrocarbon and H_2S desorb from the active sites.[7] Thus, HDS reactions are well described by Langmuir-Hinshelwood type kinetics.[109]

A specific model compound, considered in many kinetic studies is dibenzothiophene since it enables the investigation of all possible reaction steps proposed for sulfur compounds in real feedstocks without the additional complexity of sterical hindrance of sulfur like in 4,6-dimethyldibenzo-thiophene.[24, 108, 111-113] In Figure 2. 13, the HDS of dibenzothiophene (DBT) is presented. DBT is converted via two simultaneous routes. The first and predominant one is the direct desulfurization (DDS) to Biphenyl (BiPh) via hydrogenolysis. The second route starts with a partial hydrogenation of one benzoic ring to tetrahydrodibenzothiophene (H-DBT) that quickly undergoes different consecutive reaction steps. H-DBT is first hydrogenated to hexahydrodibenzothiophene, which is usually not observed in the reaction mixture and subsequent hydrogenolysis, probably via an arylthiol intermediate[101], takes place to phenylcyclohexane (PhCH). This reaction pathway is called hydrogenation route (HYDS). For the other products presented in Figure 2. 13, slightly different mechanisms are described in literature. The full saturated product bicyclohexane (BiCH) is occasionally observed. Gutiérrez et al. found that dodecahydrodibenzothiophene (DH-DBT) is formed by hydrogenation of H-DBT, which could react via hydrogenolysis to BiCH. They found no indications for the hydrogenation of BiPh over PhCH to BiPh. Their activity studies were performed on supported Ni-MoS_2 catalysts at 400°C and 7.3 MPa during the simultaneous HDN of o-propylaniline in a batch reactor. And also at lower temperatures and pressures (at 350°C and 5.0 MPa), PhCH formation by hydrogenolysis of H-DBT is reported by Kagami et al. for supported Co-MoS_2 and Ni-MoS_2 during the simultaneous HDS of 4,6-dimethyldibenzo-thiophene in a batch reactor.[113] However, hydrogenation of BiPh or PhCH is proposed and may occur at different reaction conditions.[7, 111] It is proposed that DDS occurs via σ-adsorption, i.e. adsorption perpendicular to the catalyst surface caused by interaction of the S atom from the organic molecule with Mo atoms on the catalyst surface, whereas the HYDS route is due to π-adsorption (parallel to the catalyst surface) via the aromatic system.[7, 101]

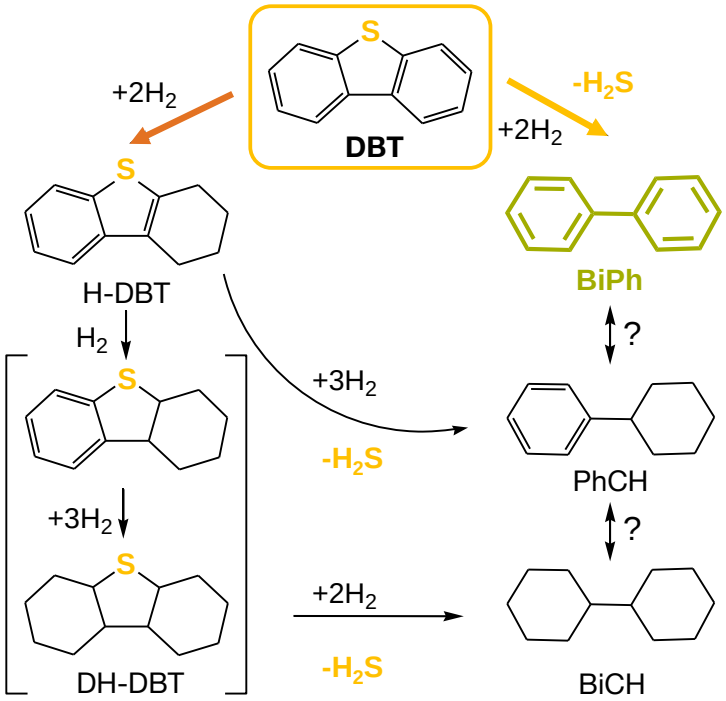

Figure 2. 13. Reaction network for hydrodesulfurization (HDS) of dibenzothiophene (DBT) showing the products biphenyl (BiPh), tetrahydrodibenzothiophene (H-DBT), phenylcyclohexane (PhCH), dodecahydrodibenzothiophene (DH-DBT) and bicyclohexane (BiCH). The favored end product BiPh is highlighted. The yellow arrow indicates the direct desulfurization (DDS) and the orange arrow the hydrogenation (HYDS) pathway, respectively. The reactions between BiPh, PhCH and BiCH are usually not observed but feasible therefore labeled with "?" (based on Ref. [109]).

The interaction between organosulfur compounds and other molecules in the feedstock, like N and O containing molecules, aromatics and H_2S, as well as the influence on the sulfur removal activity and selectivity by other compounds is widely studied in literature.[23, 26, 109, 114-116] For instance, it is found that the presence of H_2S suppresses the DDS route, whereas nitrogen containing compounds inhibit the whole HDS reaction due to competitive adsorption on the active sites. The extent of poisoning depends on the concentration and type of nitrogen compound, but already the presence of ammonia has an inhibiting effect. In complex hydrotreating mixtures, nitrogen containing molecules have always the highest influence on the conversion of all contained compounds, not only on the conversion of sulfur compounds, but also of oxygen containing molecules and heteroatom free aromatics. The reasons for the strong influence of nitrogen compounds are their comparable low reactivity and high adsorption strength.[101] The general reported trend for poisoning is: nitrogen compounds > organic sulfur compounds > polyaromatics, oxygen compounds, H_2S > monoaromatics.[7]

2.3. Hydrotreating Catalysts and Their Active Sites

Hydrotreating catalysts are supported or unsupported transition metal sulfides (TMS). The TMS relevant for hydrotreating are summarized in Table 2. 6, which shows the stable sulfide phases of the transition metals under reaction conditions (compare to Figure 2. 1). Among these TMS, the already discussed Ni, Mo and W sulfides, i.e., Ni_3S_2, MoS_2 and WS_2 are listed.

Table 2. 6. Hydrotreating active transition metals in their under reaction condition stable sulfide phase (compare to Figure 2. 1).[117]

TiS_2	V_2S_2	Cr_2S_2	MnS	FeS_x	Co_9S_8	**Ni_3S_2**
ZrS_2	NbS_2	**MoS_2**	TeS_2	RuS_2	Rh_2S_3	PdS
HfS_2	TaS_2	**WS_2**	ReS_2	OsS_x	IrS_x	PtS_2

Most of these materials have been tested in hydrotreating reactions, mainly in hydrodesulfurization (HDS). In Figure 2. 14(A), the HDS activity of different sulfides is presented in dependency of the metal-sulfur bond strength in form of a volcano-type plot. As can be seen, the noble metal sulfides turned out to be the most active materials, but also MoS_2 and WS_2 showed good performances.[8, 118] However, the steady development of hydrotreating catalysts and the search for highly active cheaper materials compared to the noble metals resulted in bimetallic NiMo, NiW, CoMo and CoMo sulfides. They show higher activity than the noble metal sulfides in combination with lower costs (Figure 2. 14(A) and (B)). Therefore, the investigation and understanding of these bimetallic sulfides is of economic and scientific interest already since the 1950's.[24, 26-27, 38, 104, 109, 119-130] The subsequent development of trimetallic sulfides with various compositions took 30 years and was first reported by Ho et al. in 1986.[2] However, just the successful introduction of unsupported NiMoW trimetallic sulfides, the so-called NEBULA catalysts family, in refineries 2001 and their outstanding hydrotreating performance was the reason for considering these formulations as a new hydrotreating catalyst generation.[2, 131] Recent studies indeed show that sulfided trimetallic formulations have promising high activities per volume, which is schematically presented in Figure 2. 14(B).[10, 44, 46, 51, 132]

Consequently, typical hydrotreating catalyst are based on MoS_2 or WS_2 and promoted with Ni or Co. Usually an oxidic carrier is used as support with metal loadings of Mo or W between 10 and 25 wt.%.[24-25, 33] The concentration of the promoter metals is lower with promoter to total metal ratios between 0.25 and 0.5, which is found as the optimum in terms of hydrotreating activity.[7, 101] The typical preparation method for supported metal catalysts is the incipient wetness impregnation by using concentrated aqueous metal salt solutions under

consideration of the pore volume and the point of zero charge of the support. Often the pH value needs to be adjusted and controlled and occasionally additives are used to control the later formed surface species or the dispersion. The final step is always a carefully controlled, stepwise performed calcination procedure. The used support materials are inert, mechanical stable materials with a high specific surface areas such as γ-Al_2O_3[25] but also SBA-15[24, 109] or carbon[133]. Among these materials, γ-Al_2O_3 or modified alumina is preferred due to its costs and handling. Alumina possesses a high concentration of surface hydroxyl groups, which could form bridging bonds to other molecules and phases, which enable the formation of different surface species with a high dispersion. For hydrotreating applications, the typically formed precursor species on alumina are heptamolybdate anions $Mo_7O_{24}^{6-}$, polytungstate species like WO_3 and oxidic species of Ni^{2+} (or Co^{2+}). They are bonded by metal-O-Al interactions to the alumina surface via the mentioned OH^- groups (with metal for Mo, W, Ni and Co).[78, 134]

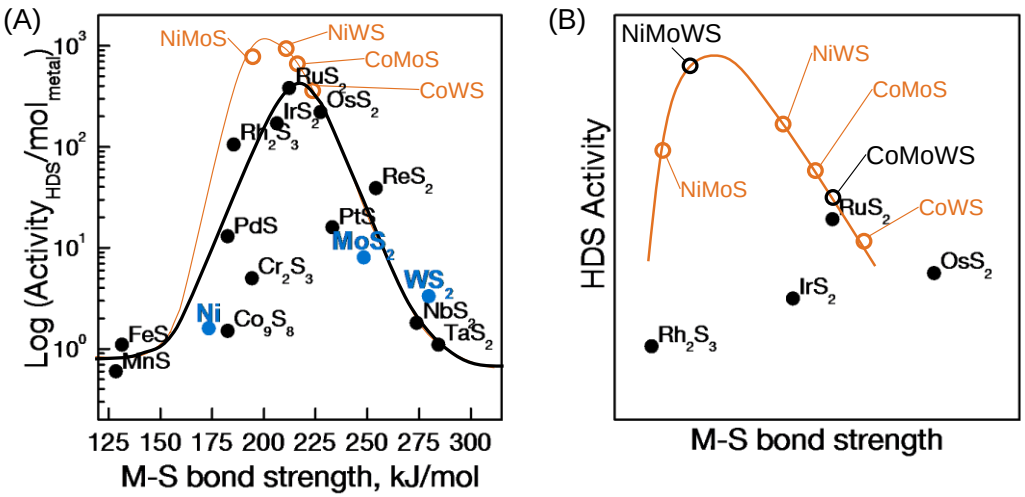

Figure 2. 14. Volcano plots of the transitions metal sulfides (TMS). In (A), the activity in HDS of TMS in dependency on the metal-sulfur (M-S) bond strength are presented, adapted from Ref.[8]. The here considered compounds are labeled in blue. Additionally, values of bimetallic materials are roughly plotted according to Ref.[132], which created a new volcano curve (orange). In (B), a schematic representation of the relative position of tri- and bimetallic TMS are shown (the monometallic TMS are kept for comparison to (A)), adapted from Ref. [132].

For unsupported hydrotreating catalysts different preparation procedures exist in literature.[44-45, 47, 49, 51, 135-138] The method most often used is co-precipitation in aqueous or organic solutions, applied at ambient conditions or under pressure. Additionally, chelating ligands, surfactants or oxidic binder are usually involved. The resulting products are either mixed oxides, metallates or thio-metallates, therefore the pH value is crucial for the control of the final formed phases (see Ch. 2.1.2). Subsequently, the products were dried or calcined or a controlled decomposition is performed. The unsupported bulk materials self-explanatory consist of much higher metal contents than the supported formulations and have usually Ni

and Co to total metal ratios of around 0.5. The use of the term "promoter" might be misleading for unsupported sulfides since Ni or Co are occasionally amount to 50 mol% of the whole catalyst.[44, 48, 51, 139]

The different metal oxide precursors, either supported or unsupported, were in-situ sulfided under controlled conditions independent on their industrial or research related hydrotreating application.[b] As a consequence, it is mandatory to investigate the oxidic precursor phase, from preparation until structure estimation, and the sulfidation process, i.e., estimation of the required temperature and pressure, as well as the resulting active sulfide phase. The crucial advantage of supports is the good dispersion of the active phase, which allows an optimized interaction with the organic molecules during the hydrotreating reactions. Furthermore, they can act as additional adsorption site for the reactants and they enable low loadings with active material, which reduces the costs of the catalysts. On the other hand, a strong interaction with reactants could initiate catalyst coking, i.e., catalyst deactivation or other undesired side reactions. The active phase can interact too strong with the support, thus, less adsorption and reaction sites are available for the reactants. During preparation, potentially active material can react with the support and form inactive species on the support surface, for example the formation of the Ni spinel $NiAl_2O_4$ is often discussed.[101] Additionally, the presence of a support and the active phase-support interaction complicate the investigation and characterization of the catalysts. Therefore, it is essential for hydrotreating applications to either optimize the support and the support-active phase interaction or to provide highly active unsupported sulfides with an excellent availability of the active sites. This points again to the importance of the analysis and understanding of the different material stages required for the design of new high active catalysts.

In the following, the structural features and active sites of NiMoS, NiWS and NiMoWS catalysts are described and discussed. Although there is still a lack of full understanding of these systems, a large body of knowledge has been accumulated in 100 years research.[8] It is assumed that most of the features and models are relevant for supported as well as unsupported systems, thus, a differentiation between both catalysts types will be only made if needed. The first striking characteristic of multimetallic sulfide catalysts is presented in Figure 2. 14. The addition of the promoter Ni to MoS_2 or WS_2 results in a very high activity. That means that there is a synergistic effect between Ni and the MS_2 phase (M stands for Mo or W). It is suggested that the promoted sulfides mimic the electronic structure of the noble-metal sulfide by forming a pseudo-binary systems with average electronic properties.[140] Moreover, higher hydrotreating activities are observed for shorter and well dispersed sulfide

[b] Also thio-metallate precursors usually require an additional in-situ sulfidation under pressure in the reactor since TMS tend to a fast surface reactions with air, like oxidation or water adsorption.

slabs, i.e. with a low amount of stacked sulfide slabs. These two major observations were tried to explain by different models for promoter-sulfide phase-interactions and by models for the general surface structure of TMS catalysts. These models combined with observations during hydrotreating reactions including activation procedure and reaction mechanism studies, enable the drawing of a general simplified picture of active sites present in TMS catalysts.

During sulfidation of the oxidic precursors segregation of Ni sulfide crystals and MS_2 layers is observed. Additionally, the presence of Ni introduces also defects and structural disorder in MS_2 (M stands for Mo and/or W). This observed disorder combined with the proposed synergistic effect resulted in three models to explain the interaction between Ni and MS_2. The first one is the "Pseudointercalation Model", in which Ni intercalates into the empty octahedral holes between the S-M-S layers of MS_2 (it is referred to the crystal structure of MS_2 shown in Figure 2. 9). And the promotion effect is explained by a charge transfer from Ni to M.[103] However, it was proven that intercalated phases are not stable under catalytic conditions and this model is, therefore, not applicable for hydrotreating catalysts.[8] The second model is the "Contact Synergy Model". The basic idea is that the different metal sulfide crystals are in a close contact and that the promotional effect occurs at the interface between them due to an electron transfer process.[103] The principle behind this idea appeared as not completely correct, however, Chianelli et al. improved and specified this model to the "Symmetrical Synergy Model".[140-141] They proposed a hypothetical phase diagram, in which two immiscible phases (Ni sulfide and MS_2) forming surface phases due to their interaction. That means, one bulk sulfide is surface-enriched with the other metal by contact. Recently, Ramos et al. could successfully show that such an interfacial surface phase exists by using molecular modeling and high-resolution transmission electron microscopy.[31] They found direct Co-Mo bonds with a distance of 2.76 Å and electron donation of Co to Mo over mutual S atoms in an unsupported Co/MoS_2 catalyst. The third model is the "Edge decoration model" or also called "CoMoS (NiMoS) decoration model" proposed by Topsøe et al.[120, 142-143] In this model the promoter is adsorbed on the edges of the MS_2 crystallites and occupies empty metal sites or replaces the metal in the hexagonally metal plane of MS_2 (compare with crystal structure of MS_2, Figure 2. 9). The decoration model is widely accepted for the interaction between the promoter and the metal disulfide phase and was proven by different groups and techniques, like Mößbauer spectroscopy, extended X-ray absorption structure (EXAFS), electron microscopy and by density functional theory (DFT).[16, 29-30, 33, 35, 37, 42, 144] In Figure 2. 15, the different metal sulfides species proposed for supported hydrotreating catalysts are presented. Overall, the promoter nickel is present in three different phases, adsorbed on the edges of MS_2 slabs, in segregated nickel sulfide crystals of different sizes and in-cooperated in alumina.[6-7] Except for the latter, it is

assumed that the same phases are as well present in unsupported catalysts. The crystalline domains are much larger in unsupported sulfides. Large Ni_xS_y crystals are observed, which are partly covered by long and highly stacked MS_2.[51, 145-146] In contrast, large crystals are not observed in supported sulfides. The MS_2 slabs are usually well dispersed on the support, short and with low stacking degrees and Ni_xS_y domains are only rarely identified.[25] As a consequence, the edge decoration model is preferable used to explain the high activity of supported catalysts (no large segregated phases), whereas the symmetrical synergy model is proposed for unsupported multimetallic formulations.[31] In general, it is however feasible that small Ni_xS_y domains are also in a close contact to MS_2 slabs in supported systems and in-cooperation of Ni can as well occur for long, highly stacked and unsupported MS_2 slabs, as tried to indicate in Figure 2. 15.

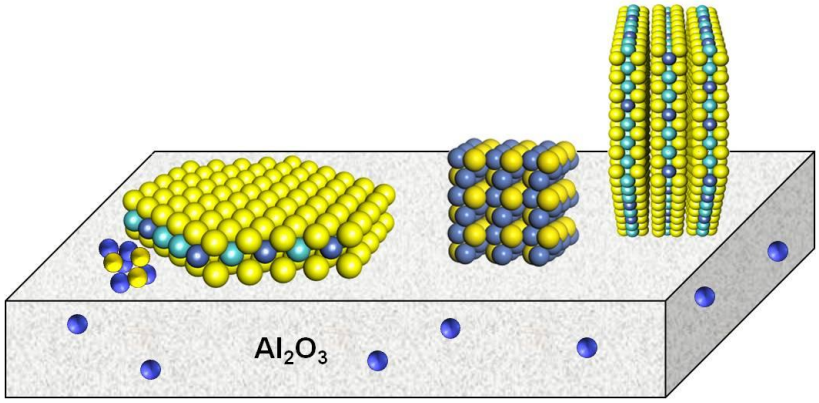

Figure 2. 15. The different sulfide species on a γ-Al_2O_3 support. There are single and stacked Ni promoted and unpromoted MoS_2 and WS_2 slabs parallel and perpendicular to the alumina surface next to different Ni sulfide crystals with different sizes. Eventually Ni^{2+} is incorporated in alumina. Color code: Mo/W light blue, Ni dark blue, S yellow.

For the edge decoration model, Louwers and Prins proposed a millerite-type structure for nickel at the edges of supported MoS_2 with a square pyramidal coordination by sulfur with a Ni-S bond distance of 2.22 Å (compare with crystal structures of Ni sulfides shown in Figure 2. 5) based on EXAFS measurements. In the second coordination shell of Ni, one or two molybdenum atoms are found with a Ni-Mo bond distance of 2.8 Å.[42] A square pyramidal or square planar Ni coordination was also earlier suggested by Niemann et al. and more recently by Kelly et al.[37, 147] However, DFT calculations and scanning tunneling microscopy (STM) have shown that the edge structure and chemistry is complex and very flexible, especially the sulfidation degree at the edges varies with H_2S and H_2 pressure (during hydrotreating).[29-30, 35, 129, 148] In Figure 2. 16, the different edges of MS_2 with different sulfidation degrees are shown as well as the possible coordination geometries of the metal. It is found that Mo/W are usually in a full trigonal prismatic coordination by sulfur at the metal edge (10-10 surface), i.e., 100 % sulfided under common hydrotreating conditions (structure in the top in Figure 2. 16). On the contrary, a sulfidation degree of only 50 % is preferred for

the sulfur edge (-1010 surface) of MS_2. Thus, a four-fold coordination of the metal is indicated forming a zigzag configuration with sulfur vacancies at the metal atom, as presented on the right side in Figure 2. 16. These vacancies are also called coordinatively unsaturated sides (CUS).

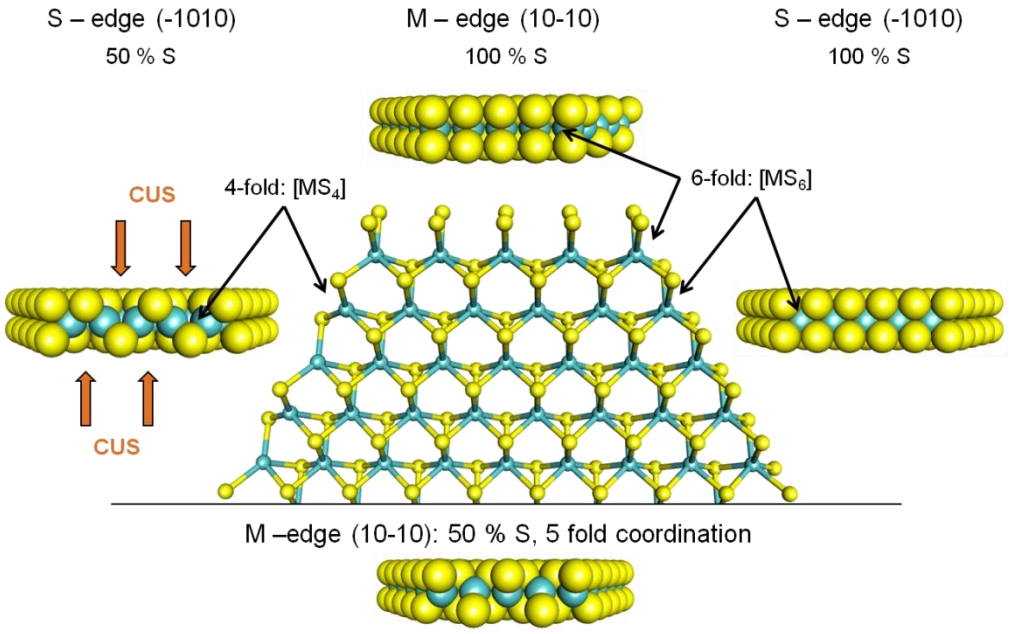

Figure 2. 16. Coordination geometry and sulfidation degree of Mo/W at different edge sites of MS_2 particle. In the center, the top view of a half MS_2 particle in hexagonal shape is presented using the ball-stick representation. This top view is surrounded by the corresponding side views of the edges. Additionally in the bottom, the side view of the metal edge with a sulfidation degree of 50 % is shown. The vacancies (CUS) are indicated with orange arrows for the S-edge (left). Color code: Mo/W light blue, S yellow. (The annotations of the surface plane correspond to the hexagonal unit cell.)

In Figure 2. 17, the edge structure of a MS_2 slab with in-cooperated Ni is shown. Raybaud et al. published DFT calculations, that showed a preferred location of Ni at the metal edge with a square planar sulfur coordination, i.e., with no sulfur atoms at the edge.[149] STM and DFT calculations brought Lauritsen et al. to the conclusions that the cluster size and shape influences the location and sulfidation degree of Ni. They found, Ni at both edges with a preferred sulfidation degree of 50 % and a co-existence of Mo and Ni at the metal edge.[30] Therefore, different sulfidation degrees, coordination geometries (structure in the bottom) and locations of Ni are presented in Figure 2. 17. That means, for Ni still a square pyramidal or planar sulfur coordination is feasible as predicted by EXAFS. Additionally, the in-cooperation of Ni results always in the formation of CUS.

In a subsequent DFT study, Moses et al. optimized sulfide edge structures at HDS typical H_2 and H_2S pressures and found the formation of SH^- groups, which are associated to the creation of CUS.[35] These functional groups, CUS and SH^- groups are considered as active sites in hydrotreating.

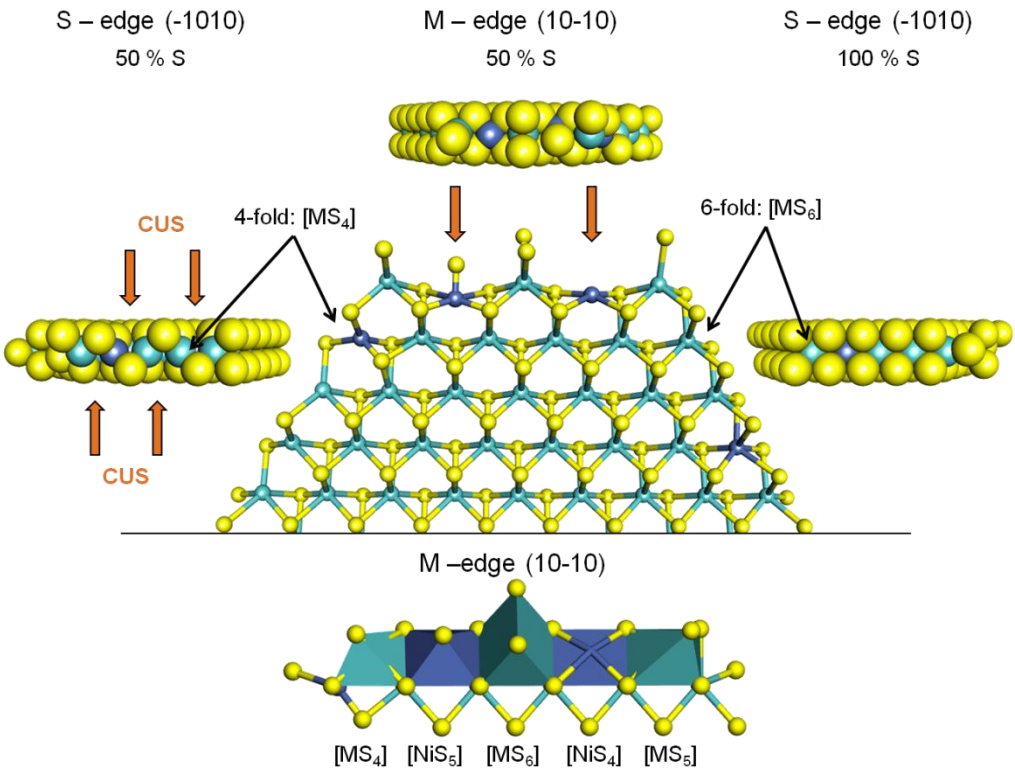

Figure 2. 17. Coordination geometry and sulfidation degree of Ni at different edge sites of MS_2 particle. In the center, the top view of a half MS_2 particle in hexagonal shape is presented using the ball-stick representation. The top view is surrounded by the corresponding side views of the edges. Additionally in the bottom, the coordination polyhedra of all 5 metals at the metal edge are shown. The vacancies (CUS) are indicated with orange arrows. Color code: Mo/W light blue, Ni dark blue, S yellow. (The annotations of the surface plane correspond to the hexagonal unit cell.)

In Figure 2. 18, possible locations of CUS and SH^- groups are shown as well as a reaction scheme proposed by Gutiérrez et al., which describes the formation of CUS and SH^- groups based on temperature programmed reactions.[3] CUS are created by reaction between hydrogen and edge sulfur atoms, which could proceed via SH^- groups (or directly to a formally reduced state of the metal atom). CUS have a Lewis acid character and could act therefore as adsorption site for sulfur or nitrogen containing molecules via the unpaired electrons of the heteroatom.[7] Therefore, these sites are assigned to the direct removal of heteroatoms, i.e., to the C-S and C-N bond scission. Hrabar et al. observed indeed a preferred direct nitrogen removal at vacancies associated to Mo atoms. Additionally, it is found that vacancies are especially sensitive to poisons like sulfur compounds (also H_2S) or other nitrogen compounds.[25] As shown in Figure 2. 18, H_2S adsorbs onto the vacancies of the sulfide surface and recreates SH^- groups.[150] SH^- groups are slightly Brønstedt acidic and have protonating properties, further they can act as adsorption sites.[3] However, CUS and SH^- groups in combination are crucial during hydrogen activation and therefore essential for hydrogenation as well as for C-S and C-N bond scissions.[35, 150] Furthermore it was proven, that their concentration increases with the addition of Ni to MoS_2,[150] which is also represented in Figure 2. 18 by CUS and SH^- groups close to the Ni atoms in the MS_2 particle.

The third presented type of active sites in Figure 2. 18 are the brim sites. Brim sites have a metallic-like character with a high electron density visible on STM images of unpromoted and promoted MoS_2 clusters.[151] They are located on the basal plane close to the edge and are considered as the active sites for hydrogenation.[7] In fact, they act as adsorption site due to interaction with the π-electron system of aromatic molecules, thus, the adsorption occurs parallel to the sulfide surface.[129] Once a molecule is adsorbed, SH^- groups located at the edge can provide the necessary hydrogen for the partial or full saturation of the molecule.

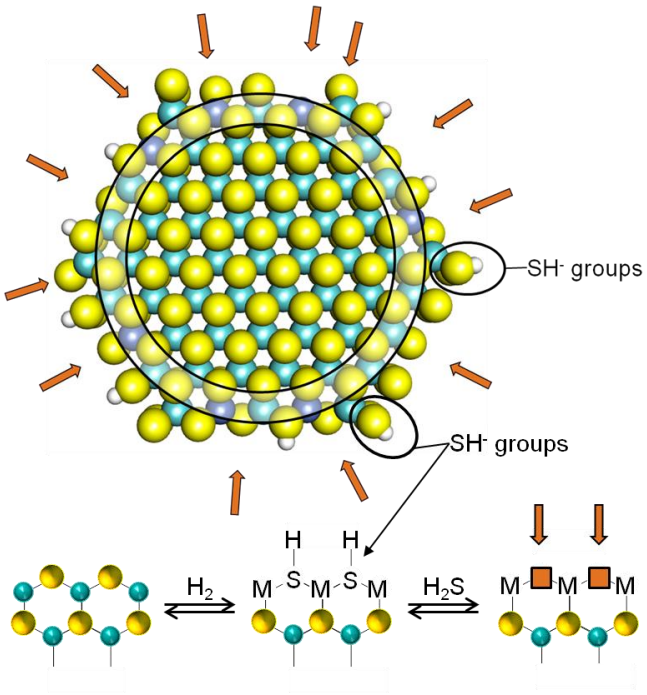

Figure 2. 18. Overview about the location of the proposed active sites (top) and a possible simplified mechanism for the creation of vacancies and SH- groups (bottom). The vacancies (CUS) are indicated with orange arrows and the brim sites region with the double ring close to the edge of the sulfide particle. Color code: Mo/W light blue, Ni dark blue, S yellow

Studies regarding the structure, active sites and structure-activity correlations for unsupported multimetallic sulfides are limited. The presence of various mono- and multimetallic phases with different crystallinity, morphologies and sizes hinders the accurate analysis of single active sites. However, since the same crystallographic species are formed and the same metals are contained like in the supported materials, the assumption of similar active sites is reliable. The previous description of active sites revealed that the majority of active sites is located at the edges of the MS_2 slabs. In bulk sulfides, the edge surface and also the available surface area for symmetrical synergy is small due to the large sulfide crystals. And also the contributions of basal planes of the MS_2 slabs (considered inactive) are occasional very large. However, multimetallic unsupported sulfides appear still with a high hydrotreating activity per volume. A full explanation of the creation and type of involved active sites is so far missing. Nevertheless, some clear general activity structure activity

correlations have been identified, which help gaining deeper understanding of bulk sulfides. For instance, the activity of unsupported catalysts increases with the surface area of the sulfides[31] and a close contact between the different phases (increased contact area) is also beneficial for the reaction.[51] Thus, the surface area and the interaction between the different metal phases is apparently important, which could account for the relevance of the symmetrical synergy model. Furthermore the morphology appeared as crucial for unsupported catalysts. Daage and Chianelli correlated the HDS selectivity with the sulfide morphology and proposed a model for the location of active sites in highly stacked unsupported sulfides.[152] The so-called "rim-edge" model is presented in Figure 2. 19.

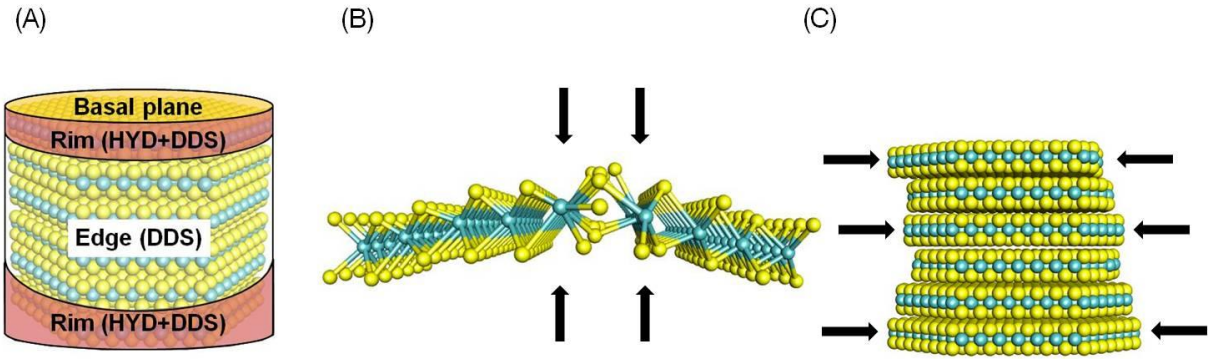

Figure 2. 19. Proposed active regions of unsupported MS_2. In (A) the "rim-edge" model[152] of stacked sulfide particles is shown with the rim-sites active for hydrogenation (HYD) and heteroatom removal (DDS), the edge-sites only active in heteroatom removal and the inactive basal plane; in (B) and (C) possible disorder of long, highly stacked MS_2 slabs is shown, which could provide accessibility of additional sites (black arrow) due to slab curvature (B) and mismatch in slab stacking (C). Color code: Mo/W light blue, S yellow.

In the "rim-edge" model, only the basal plane is considered as inactive. The rim sites, the edges of the top and bottom layer of a stacked sulfide particle, are active in heteroatom removal and hydrogenation, which agrees with the general idea about the location of active sites. However, the edge sites, the edges of the interior layers, are proposed to catalyze only the desulfurization. Therefore, highly stacked sulfides could show high selectivities towards the direct route of HDS and HDN. Another morphology related proposal was made by Iwata et al.[93, 153] They suggested that MS_2 curvature influences the ratio of basal plane to edge area and that strong bending creates new edge and hydrogenation active sites.[93, 153] In Figure 2. 19, well known defects for MS_2 crystals like bending and turbostratical disorder (mismatch of stacked MS_2 layers) [7, 154] are presented as well as possible available active sites are indicated. These structures show indeed that new edge-like sites are formed by distortion maybe initiated by fast MS_2 slab growth along the x- and y-axis or by interaction with and in-cooperation of other metals, e.g. Ni or W in MoS_2. However, it is uncertain if these new sites are also available for organic molecules during hydrotreating reactions, therefore, this proposal needs to be proven.

Chapter 3

γ-Al_2O_3-supported and unsupported (Ni)MoS_2 for hydrodenitrogenation of quinoline in the presence of dibenzothiophene

Jennifer Hein, Ana Hrabar, Andreas Jentys, Oliver Y. Gutiérrez, and Johannes A. Lercher

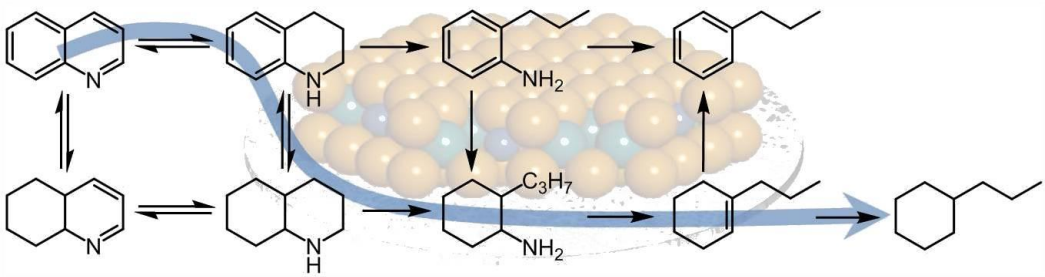

I want to break free (from your nitrogen): Ni and Al_2O_3 exert particular effects on the physicochemical and kinetic features of Mo oxide species and the corresponding MoS_2 phase. The support maximizes the concentration of active sites, whereas the promoter changes their intrinsic activity. In turn, the support also influences the promotion mechanism.[155]

Published in: ChemCatChem 2014, 6, 485 – 499.
DOI: 10.1002/cctc.201300856; ISSN: 1867-3899
Permission/License Number: 3681850593025

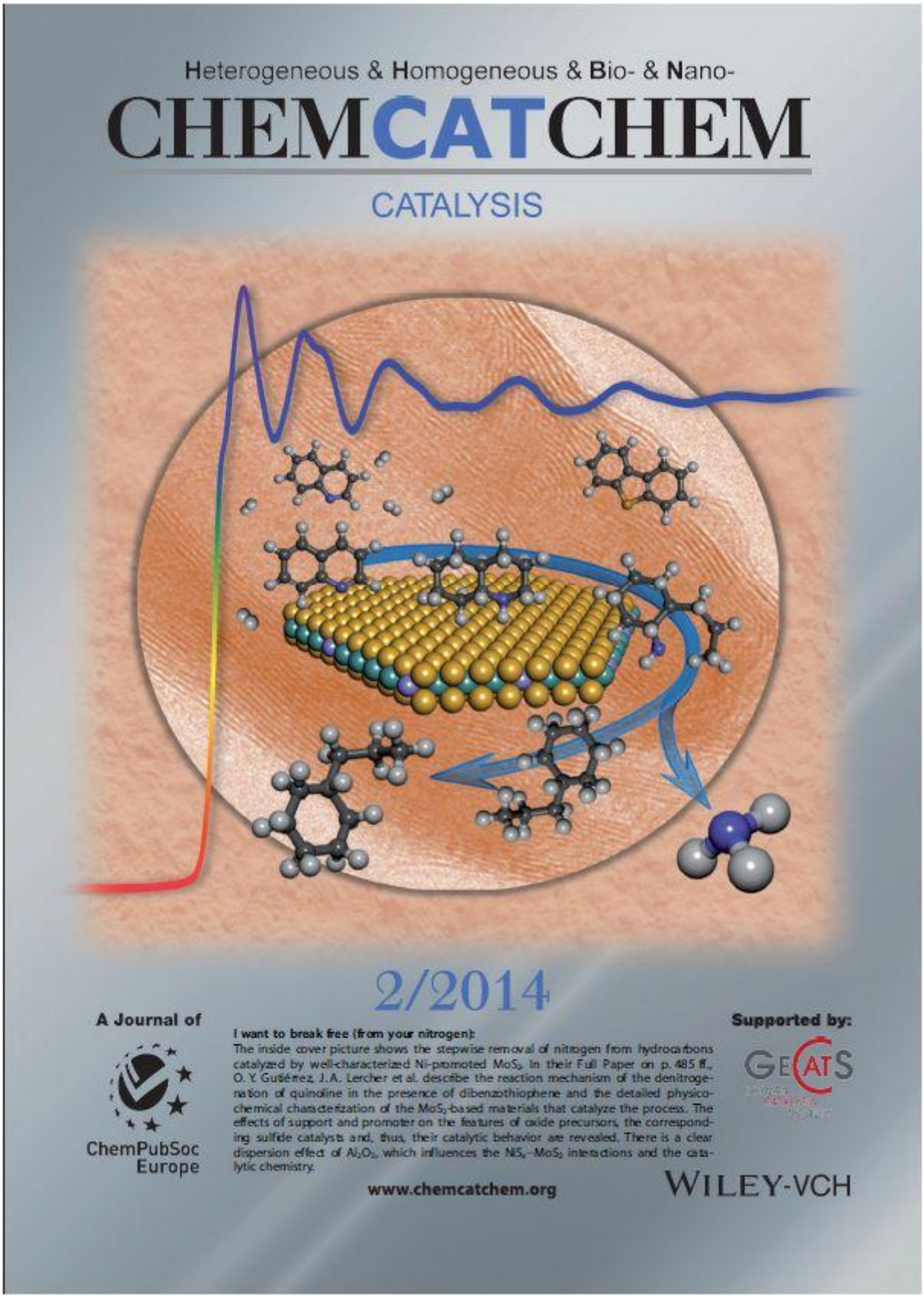
Heterogeneous & Homogeneous & Bio- & Nano-
CHEMCATCHEM
CATALYSIS
2/2014
A Journal of
ChemPubSoc Europe
I want to break free (from your nitrogen):
The inside cover picture shows the stepwise removal of nitrogen from hydrocarbons catalyzed by well-characterized Ni-promoted MoS_2. In their Full Paper on p. 485 ff., O. Y. Gutiérrez, J. A. Lercher et al. describe the reaction mechanism of the denitrogenation of quinoline in the presence of dibenzothiophene and the detailed physicochemical characterization of the MoS_2-based materials that catalyze the process. The effects of support and promoter on the features of oxide precursors, the corresponding sulfide catalysts and, thus, their catalytic behavior are revealed. There is a clear dispersion effect of Al_2O_3, which influences the NiS_x–MoS_2 interactions and the catalytic chemistry.
www.chemcatchem.org
Supported by:
GECATS
WILEY-VCH

1. Abstract

Supported MoS_2/γ-Al_2O_3 and Ni-MoS_2/γ-Al_2O_3 as well as unsupported Ni-MoS_2 were investigated in the hydrodenitrogenation (HDN) of quinoline in the presence of dibenzothiophene (DBT). The supported oxide catalyst precursors had a well-dispersed amorphous polymolybdate structure that led to a formation of high dispersed sulfide phase. In contrast, the unsupported NiMoS precursor consisted of a mixture of nickel molybdate and ammonium nickel molybdate phases forming stacked sulfide slabs after sulfidation. On all catalysts, the reaction pathway for the removal of N in quinoline HDN mainly followed the sequence quinoline → 1,2,3,4-tetrahydroquinoline → decahydroquinoline → propylcyclohexylamine → propylcyclohexene → propylcyclohexane. Hydrodesulfurization of DBT proceeded mainly via direct desulfurization towards biphenyl. For both processes the activity increased in the order MoS_2/γ-Al_2O_3 < Ni-MoS_2/unsupported < Ni-MoS_2/γ-Al_2O_3. The promotion of the MoS_2 phase with Ni enhances the activity of the unsupported catalyst to a greater extent than the supported one. However, the multiply stacked unsupported Ni-MoS_2 exhibited lower rates than Ni-MoS_2/γ-Al_2O_3 due to its lower dispersion.

2. Introduction

Hydrodefunctionalization and hydrogenation catalyzed by sulfide catalysts are key processes to obtain clean fuels. The increasing need for improving the efficiency of refining processes has stimulated a large number of fundamental studies on Ni- and/ or Co-promoted MoS_2.[29, 156] One of the main challenges in the understanding these materials is the large number of (structurally and chemically) different of adsorption sites, which all may be potentially active for H_2 activation, hydrogenation as well as C-S and C-N bond cleavage. Coordinatively unsaturated sites (CUS), i.e., exposed metal cations act as Lewis acids sites for the adsorption of electron pair donors such as S- and N-containing compounds. The SH^- groups at the termination of the sulfide slabs are Brønsted acidic, and provide hydrogenation for hydrogenolysis and hydrogenation. The existence of metal-like states on the basal planes close to the edge of the basal plane has also been proposed.[157] In addition to the nature of sites of MoS_2, also the type of support and the presences of promoters influence the properties of the catalyst. Both, promoter and support may affect the dispersion and structure of the MoS_2 phase as well as its intrinsic activity.

It has been demonstrated that the morphology of the MoS_2 play a main role in the activity and selectivity of the catalyst. For instance, the “rim-edge” model rationalizes that the

hydrodesulfurization (HDS) functionality of the MoS_2 slabs depends on shape and size of the MoS_2 particles.[152] While for the HDS of dibenzothiophene several structure-activity correlations have been proposed,[24, 158-159] only a few attempts to determine the influence of support, promoter and morphology of MoS_2 on the functionality of active sites in the hydrodenitrogenation (HDN) are reported.[160-163]

This study aims, therefore, to gain insight into the role of the promoter and the support on the activity of MoS_2 and to identify the sites active in HDN. Both goals are essential to gain a deeper understanding of the morphology-functionality relations for rationally designing improved HDN catalysts. The physicochemical properties and molecular structures of a series of supported $MoS_2/\gamma\text{-}Al_2O_3$ and Ni-$MoS_2/\gamma\text{-}Al_2O_3$ as well as an unsupported Ni-MoS_2 catalyst are described in detail. The performance of the catalysts is explored with respect to the HDN of quinoline (Q) in the presence of dibenzothiophene (DBT). The impact of support and promoting Ni as well as the functionality of the active sites is discussed using the detailed physicochemical and kinetic characterization of the sulfide catalysts.

3. Results

Characterization of oxide precursors and in-situ sulfidation studies

The supported oxide precursors are referred as $Mo/\gamma\text{-}Al_2O_3$ and $NiMo/\gamma\text{-}Al_2O_3$, whereas the precursor of the unsupported catalyst is denoted as NiMo/unsupported. The physicochemical properties of the oxide catalyst precursors are compiled in Table 1. The Mo concentration was 8.6 wt.% in both supported catalysts, which corresponds to 2.5 Mo atoms nm^{-2}. The Ni concentration in the NiMo supported catalyst was 3.6 wt.% Ni, i.e., a molar fraction of 0.4 for Ni. In the unsupported material, the Mo and Ni concentrations were 38 and 25 wt.%, respectively, i.e., a Ni molar fraction of 0.5.

Table 1. Physicochemical properties of the $Mo/\gamma\text{-}Al_2O_3$, $NiMo/\gamma\text{-}Al_2O_3$ and NiMo/unsupported oxide catalyst precursors.

Catalyst	Metal conc. [wt.%]		Ni molar fraction	Surface area [$m^2 \cdot g^{-1}$]	Pore volume [$cm^3 \cdot g^{-1}$]	Pore diameter [nm]
	Mo	Ni				
$\gamma\text{-}Al_2O_3$	-	-	-	237	0.75	8.8
$Mo/\gamma\text{-}Al_2O_3$	8.6	-	-	220	0.62	8.5
$NiMo/\gamma\text{-}Al_2O_3$	8.6	3.6	0.4	206	0.60	8.5
NiMo/ unsupported	38.2	25.1	0.5	26	-	-

We acknowledge that the properties of the oxide precursors and their sulfidation processes may be decisive for the properties of the corresponding sulfide catalysts. However, for the sake of brevity, we present the results of the characterization of the oxide precursors as well as the results of the in-situ sulfidation studies in the supporting information. In the following, we focus on the physicochemical and kinetic properties of sulfide catalysts.

Sulfide catalysts

The supported sulfide catalysts are denoted as $MoS_2/\gamma\text{-}Al_2O_3$ and $Ni\text{-}MoS_2/\gamma\text{-}Al_2O_3$. The unsupported sulfide catalysts is denoted as $Ni\text{-}MoS_2$/unsupported. The total NO uptake during adsorption at room temperature was 130, 160, and 66 µmol * g_{cat}^{-1} for $MoS_2/\gamma\text{-}Al_2O_3$, $Ni\text{-}MoS_2/\gamma\text{-}Al_2O_3$, and $Ni\text{-}MoS_2$/unsupported, respectively. Recently, it has been shown that NO may adsorb as mononitrosyl or dinitrosyl species on metal cations.[28] In order to quantitatively discuss the results, it is assumed that NO adsorbs as dinitrosyl species.[164] The concentration of the adsorption sites is thus 65 µmol * g_{cat}^{-1} for $MoS_2/\gamma\text{-}Al_2O_3$, 80 µmol * g_{cat}^{-1} for $Ni\text{-}MoS_2/\gamma\text{-}Al_2O_3$, and 33 µmol * g_{cat}^{-1} for $Ni\text{-}MoS_2$/unsupported. The lower concentration of accessible sites on the latter sample is attributed to a highly agglomerated sulfide phase. For the supported catalysts, the increase in concentration of coordinatively unsaturated sites (23 %) after Ni addition was by far lower than the concentration of Ni added (68 %). We conclude, thus, that NO does not adsorb selectively on Ni and that Ni cations are randomly distributed on the MoS_2 phase.

The XRD patterns of sulfided catalysts and reference sulfide materials are given in Figure 1. Supported $MoS_2/\gamma\text{-}Al_2O_3$ and $Ni\text{-}MoS_2/\gamma\text{-}Al_2O_3$ exhibited two diffraction signals at around 33 and 58° 2θ attributed to the (100) plane with inter-planar distance of 2.7 Å and to the (110) plane with inter-planar distance of 1.6 Å of MoS_2, respectively. The signal at 14° 2θ, characteristic for the (002) plane with interplanar distance of 6.1 Å,[165] was not observed, probably due to the low degree of stacking in the MoS_2 particles. The XRD pattern of the $Ni\text{-}MoS_2$/unsupported catalyst exhibited well-defined reflections at 14, 33, 40, 50, and 59° 2θ corresponding to MoS_2 and 27, 31, 33, 51, and 56° 2θ corresponding to Ni_9S_8 (traces of the Ni_3S_2 and Ni_3S_4 phases are also identified). The relatively high intensity of the reflection at 14° 2θ indicates a significantly higher stacking degree in $Ni\text{-}MoS_2$/unsupported than in $MoS_2/\gamma\text{-}Al_2O_3$ and $Ni\text{-}MoS_2/\gamma\text{-}Al_2O_3$ catalysts. The FWHM at 14° 2θ was 2.1°, which is related to a average crystal size of around 40 Å (using the Scherrer equation), and corresponds to a stacking degree (number of MoS_2 slabs in a average MoS_2 particle) of 7.

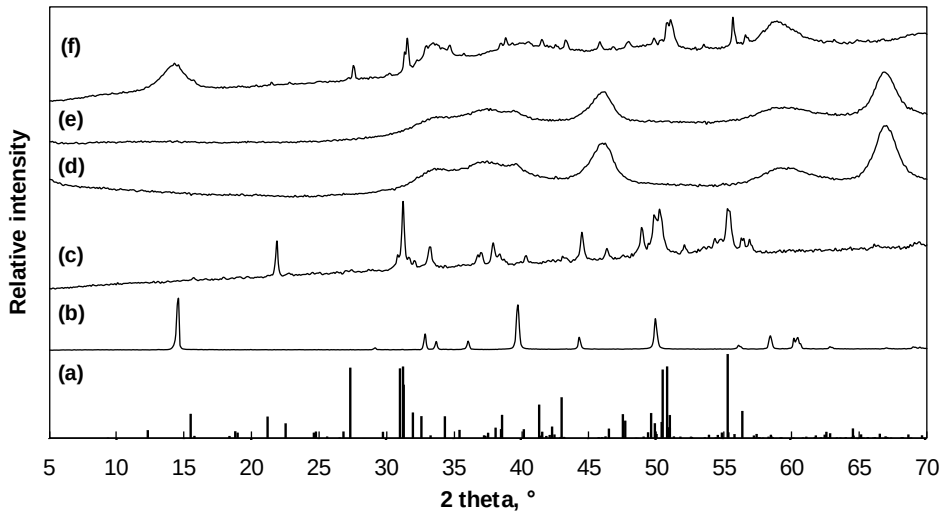

Figure 1. Stick pattern of (a) Ni_9S_8 (ICSD #63080) and X-ray diffraction patterns of: (b) MoS_2, (c) Ni_3S_2, (d) $MoS_2/\gamma\text{-}Al_2O_3$, (e) Ni-$MoS_2/\gamma\text{-}Al_2O_3$, and (f) Ni-$MoS_2$/unsupported.

Selected TEM micrographs of the supported sulfided catalysts were shown in Ref. [25]. The distribution of the number of layers that form the MoS_2 clusters and their length calculated from the micrographs are shown in Figure 2. Typical fringes that correspond to the MoS_2 phase were observed with the average length of 7.2 and 5.4 nm for $MoS_2/\gamma\text{-}Al_2O_3$ and Ni-$MoS_2/\gamma\text{-}Al_2O_3$, respectively. The average stacking degree was 1.6 for $MoS_2/\gamma\text{-}Al_2O_3$ and 1.9 for Ni-$MoS_2/\gamma\text{-}Al_2O_3$. The stacking degree of only very few MoS_2 particles exceeded three sulfide layers confirming a good dispersion of the sulfided slabs on $\gamma\text{-}Al_2O_3$ as suggested by the absence of the reflection at 14° 2θ in XRD.

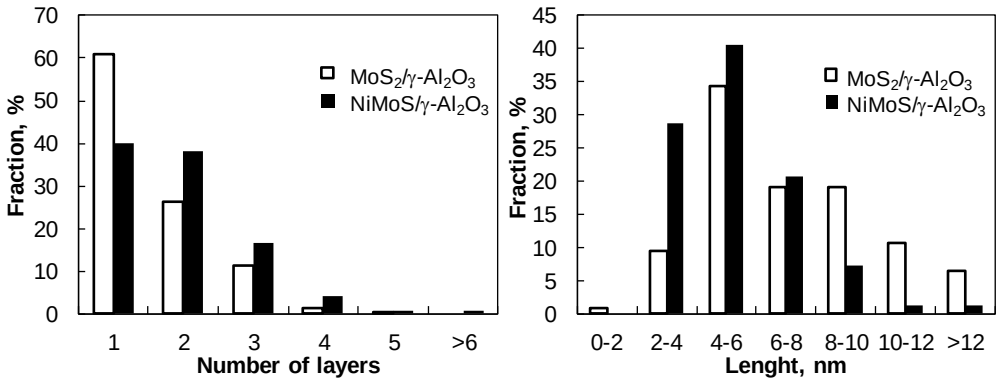

Figure 2. A) Number of layers and B) length of the MoS_2 particles in $MoS_2/\gamma\text{-}Al_2O_3$ and Ni-$MoS_2/\gamma\text{-}Al_2O_3$ calculated from representative TEM micrographs (shown in Ref. [25]).

The TEM micrographs of the unsupported sulfide catalyst showed the existence of highly stacked and bent MoS_2 particles (Figure 3 A). The characteristic curvature is a consequence of a rapid growth along the basal plane and a very slow growth along the c-axis.[94] The interplanar distance between the two molybdenum layers in (002) direction was about 6 Å, with an average stacking degree between 4 and 7. However, it is difficult to define the limits

of the MoS_2 clusters in the unsupported catalyst. Therefore, it is not attempted to determine length and stacking distributions. Diffraction patterns of selected areas were obtained for the unsupported sulfide catalyst, a representative example is shown in Figure 3 B.

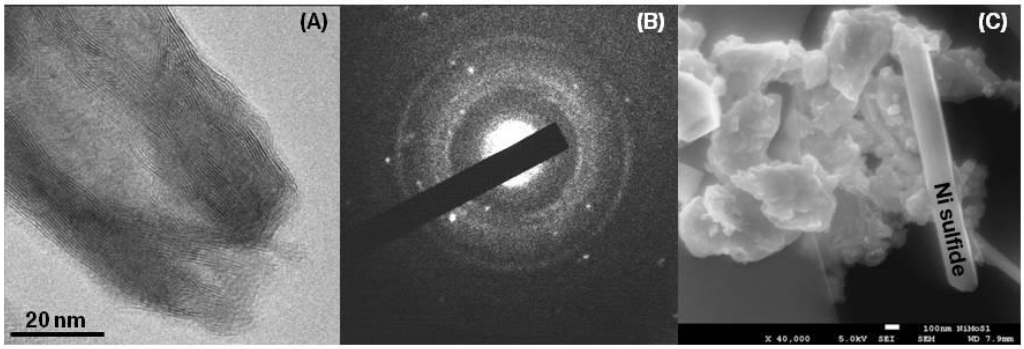

Figure 3. A) TEM image, B) selected-area diffractogram, and C) HR-SEM image of Ni-MoS_2/unsupported. The rings in (B) and stacked particles in (C) are identified as the MoS_2 phase, whereas the dots in (B) and the needles in (C) belong to Ni_9S_8 and Ni_3S_4. Scale bars = A) 20 nm, C) 100 nm.

The continuous rings observed in the XRD patterns result from MoS_2, present as small particles. Additional, high crystalline phases were found (single dots in the pattern) and identified as Ni_9S_8 and Ni_3S_4. These findings are in good agreement with the XRD characterization. The HR SEM micrographs coupled with EDX clearly showed that large Ni_xS_y crystals are present, which are partially covered by the MoS_2 structures. That means, the MoS_2 particles engulf the Ni sulfide crystals and they could, therefore, not be observed with the TEM micrographs.

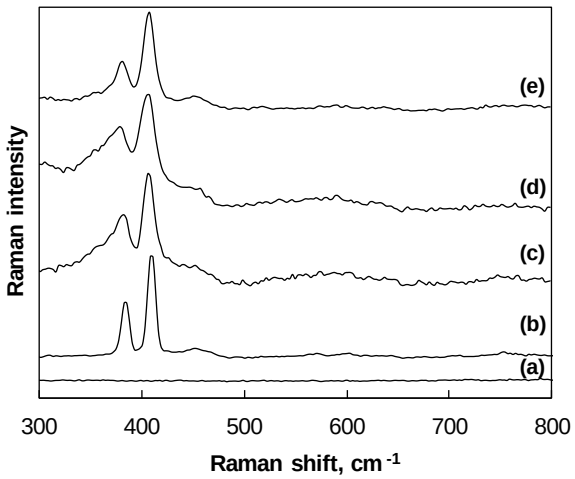

Figure 4. Raman spectra of the reference materials a) Ni_3S_2 and b) MoS_2 and of the sulfided catalysts c) MoS_2/γ-Al_2O_3, d) Ni-MoS_2/γ-Al_2O_3, and e) Ni-MoS_2/unsupported.

Representative Raman spectra of MoS_2/γ-Al_2O_3, Ni-MoS_2/γ-Al_2O_3, and Ni-MoS_2/unsupported catalysts are compiled in Figure 4. Bands related to the MoS_2 phase (Figure 4 b) were found in all three samples, i.e., 287, 383, and 409 cm^{-1}, corresponding to the S-Mo-S

vibration along the basal plane, the Mo-S vibration along the basal plane, and the S-Mo-S vibration along the c-axis, respectively.[166-167] The presence of Ni sulfides in the Ni-containing catalysts could not be confirmed by this technique probably because of their low Raman activity (the reference Ni_3S_2 material did not exhibit any band).

The X-ray absorption near edge structure (XANES) and the Fourier transformed extended X-ray absorption fine structure (FT-EXAFS) at the Mo K-edge of the reference materials, sulfided supported, and unsupported catalysts are shown in Figure 5. The absorption edge energy and the local environment around Mo of the sulfided catalysts and the MoS_2 reference material were almost identical. In accordance to the well-known layered sandwich structure of 2H-MoS_2, the first contribution at around 1.9 Å (not phase corrected) can be referred to Mo-S and the second one at 2.8 Å (not phase corrected) to Mo-Mo distances.[168] Interestingly, the Mo-S contribution was more intense for the both Ni containing catalysts, whereas the Mo-Mo signal intensity was the highest for the bulk MoS_2 reference sample.

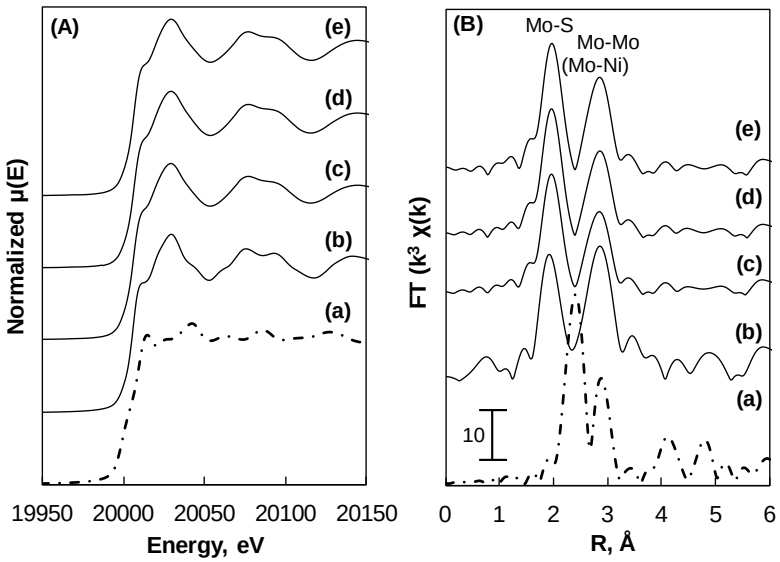

Figure 5. A) Mo K-edge XANES and B) FT of k^3 weighted EXAFS of references and sulfide catalysts: a) Mo foil, b) MoS_2, c) Mo/γ-Al_2O_3, d) Ni-MoS_2/γ-Al_2O_3, and e) Ni-MoS_2/unsupported.

The XANES and the FT-EXAFS data at the Ni K-edge of the reference materials, sulfided supported and unsupported catalysts are presented in Figure 6. At around 8332 eV, a small pre-edge was found in the XANES, typical for tetrahedrally or pentagonally coordinated Ni species (Figure 6 B). The absorption edge energy of Ni-MoS_2/γ-Al_2O_3 was 8339 eV, whereas an edge energy of 8338 eV was observed for the Ni-MoS_2/unsupported and the Ni_3S_2 reference material. The features in the FT-EXAFS at the Ni K-edge were similar to the ones found in the bulk Ni_3S_2 reference material that has a trigonal space group (R32), in which Ni is tetrahedrally coordinated by four S atoms with an interatomic distance of around 2.3 Å. The second coordination shell, defined by four Ni atoms, is located at approximately 2.5 Å.[69]

This closely spaced environment is reflected in the intense and broad backscatter signal in the FT-EXAFS of the Ni_3S_2 reference material. The observed contributions of the catalysts showed, however, much lower intensities and were shifted to shorter distances compared to that of Ni_3S_2. Moreover, the more distant Ni-Ni contribution of Ni_3S_2 at approximately 3.7 Å (not phase corrected) was almost absent in the catalysts.

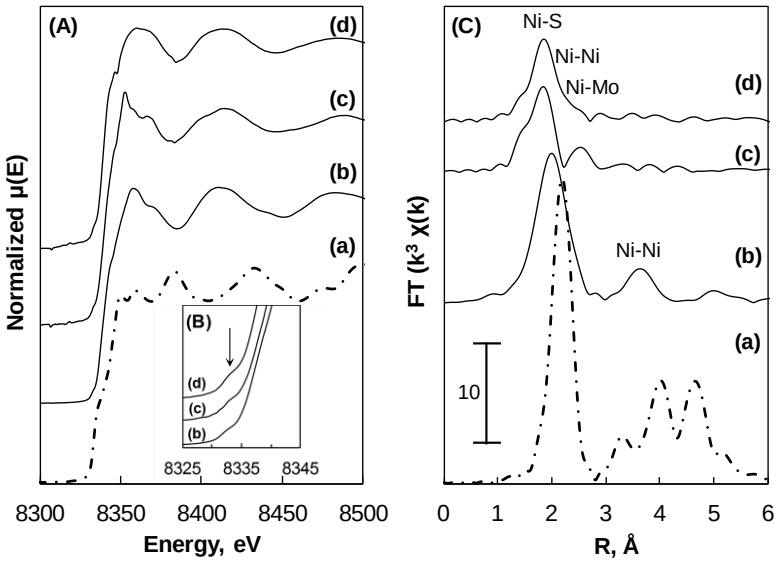

Figure 6. A) Ni K-edge XANES, B) pre-edge region, and C) FT of k^3 weighted EXAFS of references and sulfide catalysts: a) Ni foil, b) Ni_3S_2, c) Ni-MoS_2/γ-Al_2O_3, and d) Ni-MoS_2/unsupported.

Linear combination fitting (LCF) as well as the use of difference spectra were applied to explore the data using the XANES of the reference bulk materials MoS_2 and Ni_3S_2 and the oxidic precursors (the most important results and figures for this analysis are provided in the Supporting information in Table S4 and Figure S10). Analysis of the difference spectra shows that the XANES of the catalysts cannot be reproduced by using only sulfide references. Therefore, the XANES of the oxidic precursor were used in addition to the references for the LCF. The XANES of MoS_2/γ-Al_2O_3 at the Mo K-edge can be described with a contribution of 93 % from the MoS_2 reference and a contribution of 7 % of the Mo/γ-Al_2O_3 catalyst precursor XANES. The XANES of Ni-MoS_2/γ-Al_2O_3 is reproduced with 94 % of the XANES of MoS_2 and 6 % contribution of the oxidic precursor at the Mo K-edge and 85 % contribution of Ni_3S_2 and 15 % contribution of the oxide precursor at the Ni-edge. The LCF of the XANES of Ni-MoS_2/unsupported needs 98 % MoS_2 at the Mo K-edge and 95 % Ni_3S_2 at the Ni K-edge to reproduce the experimental XANES, the difference corresponds to the oxidic precursor.

Table 2. Best fit results for k^3-weighted EXAFS data of the sulfided catalysts at Mo K-edge in k space. N: coordination number, r: distance, E_0: inner potential, σ^2: Debye-Waller factor (absolute error).

Catalyst	Shell	r, Å	N	σ^2, Å^2	E_0, eV
$MoS_2/\gamma\text{-}Al_2O_3$ (R = 0.0017)	Mo-S	2.41 (0.01)	5.7 (0.3)	0.0028 (0.0003)	6.12 (1.25)
	Mo-Mo	3.17 (0.01)	4.3 (0.3)	0.0028 (0.0003)	3.62 (1.25)
$Ni\text{-}MoS_2/\gamma\text{-}Al_2O_3$ (R = 0.0012)	Mo-S	2.41 (0.01)	6.6 (0.2)	0.0031 (0.0001)	1.57 (0.28)
	Mo-Ni	2.79 (0.03)	0.2 (0.1)	0.0024 (0.0022)	1.57 (0.28)
	Mo-Mo	3.17 (0.01)	4.1 (0.2)	0.0023 (0.0002)	1.57 (0.28)
$Ni\text{-}MoS_2$/unsupported (R = 0.0014)	Mo-S	2.40 (0.01)	6.4 (0.2)	0.0028 (0.0001)	0.66 (0.28)
	Mo-Ni	2.66 (0.02)	0.3 (0.1)	0.0020 (0.0018)	0.66 (0.28)
	Mo-Mo	3.17 (0.01)	4.4 (0.2)	0.0019 (0.0001)	0.66 (0.28)
MoS_2 (R = 0.0093)	Mo-S	2.40 (0.02)	5.8 (0.6)	0.0019 (0.0007)	-0.50 (4.47)
	Mo-Mo	3.16 (0.02)	6.0 (0.6)	0.0014 (0.0005)	-0.50 (4.47)

The approach of combining the XANES of sulfide references and oxidic precursors allowed a precise modeling of the XANES measured for the sulfided catalysts. However, the difference spectra analysis between the experimental XANES and the model spectra generated by LCF indicates that other phases (most likely crystallographic structures with neighboring Mo and Ni) also contribute to the XANES of the catalysts, especially at the Ni K-edge. As a consequence, Mo-Ni and Ni-Mo scattering contributions were added for the multi edge fitting procedure of the EXAFS to obtain structural parameters of the catalysts. The structure of the reference Ni_3S_2 is described by two Ni-S and two Ni-Ni contributions, while for the $Ni\text{-}MoS_2/\gamma\text{-}Al_2O_3$ catalyst these paths were not distinguishable and only a single path was used to fit the Ni-S and Ni-Ni contributions. Additionally, to describe the EXAFS at the Ni K-edge a Ni-O path at 2.0 Å and a Ni-Ni path at 3.0 Å is necessary to describe the Ni-O interaction. In the case of $Ni\text{-}MoS_2$/unsupported this oxidic Ni-Ni contribution did not improve the fit. For both Ni-containing catalysts, the overall multi edge fit is improved by approximately 20 % when adding the Mo-Ni (Ni-Mo) contributions. The best fit for the Mo-S, Mo-Ni and Mo-Mo contributions is presented in Table 2 and for the Ni-S, Ni-Ni and Ni-Mo contributions in Table 3 (the corresponding fitted EXAFS are provided in Figures S11 and S12).

Table 3. Best fit results for k^3 weighted EXAFS data of the sulfided catalysts at Ni K-edge in k space. N: coordination number, r: distance, E_0: inner potential, σ^2: Debye-Waller factor (absolute error).

Catalyst	Shell	r, Å	N	σ^2, Å^2	E_0, eV
Ni-MoS_2/γ-Al_2O_3 (R = 0.0012)	Ni-O	1.94 (0.01)	0.9 (0.2)	0.0000 (0.0001)	1.77 (0.92)
	Ni-S	2.24 (0.01)	2.4 (0.2)	0.0027 (0.0005)	1.77 (0.92)
	Ni-Ni	2.59 (0.03)	1.0 (0.4)	0.0099 (0.0035)	1.77 (0.92)
	Ni-Mo	2.79 (0.03)	0.2 (0.1)	0.0024 (0.0022)	1.77 (0.92)
	Ni-Ni	3.02 (0.04)	0.5 (0.2)	0.0049 (0.0042)	1.77 (0.92)
Ni-MoS_2/unsupported (R = 0.0014)	Ni-O	1.94 (0.06)	0.3 (0.1)	0.0015 (0.0007)	2.82 (1.24)
	Ni-S	2.20 (0.01)	1.2 (0.2)	0.0000 (0.0001)	2.82 (1.24)
	Ni-S	2.31 (0.02)	1.5 (0.2)	0.0011 (0.0009)	2.82 (1.24)
	Ni-Ni	2.59 (0.02)	1.5 (0.4)	0.0064 (0.0018)	2.82 (1.24)
	Ni-Mo	2.66 (0.02)	0.3 (0.1)	0.0020 (0.0018)	2.82 (1.24)
Ni_3S_2 [a]	Ni-S	2.23	2.0	-	-
	Ni-S	2.27	2.0	-	-
	Ni-Ni	2.47	2.0	-	-
	Ni-Ni	2.49	2.0	-	-

[a] The structural parameters of Ni_3S_2 correspond to the crystallographic data in ICSD #27521.[69]

An almost complete first coordination shell with a coordination number N_{Mo-S} = 5.7 (at 2.41 Å) and lower N_{Mo-Mo} = 4.3 (at 3.17 Å) were found in the MoS_2/γ-Al_2O_3 catalyst compared to the bulk MoS_2 with N_{Mo-S} = 5.8 (at 2.40 Å) and N_{Mo-Mo} = 6 (at 3.16 Å). In the Ni promoted catalysts the coordination numbers were N_{Mo-S} = 6.6 and N_{Mo-Mo} = 4.1 for Ni-MoS_2/γ-Al_2O_3 and N_{Mo-S} = 6.4 and N_{Mo-Mo} = 4.4 for Ni-MoS_2/unsupported. Moreover, a new Mo-Ni contribution was found with the coordination number of N_{Mo-Ni} = 0.2 (at 2.79 Å) in the supported catalyst and of N_{Mo-Ni} = 0.3 (at 2.66 Å) in Ni-MoS_2/unsupported. The Mo-Mo contribution overlaps with the Mo-Ni, therefore, the latter is not directly observable in the FT-EXAFS data (Figure 5). The first coordination shell of nickel in Ni-MoS_2/γ-Al_2O_3 consists of an oxygen atom with N_{Ni-O} = 0.9 (at 1.94 Å) and in Ni-MoS_2/unsupported with N_{Ni-O} = 0.3 (at 1.94 Å). Considering that Ni oxide species are octahedrally coordinated (N_{Ni-O} = 6), those coordination numbers can be related to concentrations of Ni oxide species of 15 % in

Ni-MoS_2/γ-Al_2O_3 and of 5 % in Ni-MoS_2/unsupported, which is in line with the LCF analysis described above. The high concentration of Ni oxide species in Ni-MoS_2/γ-Al_2O_3 can be attributed to $NiAl_2O_4$ spinel due to the presence of Ni atoms at 3.02 Å with N_{Ni-Ni} = 0.5. The second coordination shell in Ni-MoS_2/γ-Al_2O_3 consist of S atoms with a distance of 2.24 Å, which is in between the values of the two Ni-S coordination shells in the reference Ni_3S_2 (2.23 and 2.27 Å). Note that due to the smaller particle size of the catalysts these two shells could not be separated. The third coordination shell consists of Ni atoms and shifts to higher distances and lower total coordination numbers (Ni-Ni and Ni-S) for Ni-MoS_2/γ-Al_2O_3 compared to Ni_3S_2. In Ni-MoS_2/unsupported two sulfur coordination shells were observed. The first at 2.20 Å with N_{Ni-S} = 1.2 was shifted to a shorter distance and the second at 2.31 Å with N_{Ni-S} = 1.5 to a longer distance compared to the Ni_3S_2 reference. The Ni-Ni backscattering was found at the same distance as in Ni-MoS_2/γ-Al_2O_3 with a higher coordination number of 1.5. Similarly to Ni-MoS_2/γ-Al_2O_3, the coordination number of the Ni-S contribution in Ni-MoS_2/unsupported was lower than in Ni_3S_2. Moreover, in both Ni containing catalysts an additional Ni-Mo contribution was found with the coordination number of N_{Ni-Mo} = 0.2 at 2.79 Å and of N_{Ni-Mo} = 0.3 at 2.66 Å in the supported and unsupported catalysts, respectively.

The HDN of quinoline as a space time dependent experiment

The HDN reaction network of quinoline (Q) is presented in Scheme 1. The reaction proceeds via hydrogenation of the pyridinic ring to form 1,2,3,4-tetrahydroquinoline (14THQ) or hydrogenation of the aromatic ring to 5,6,7,8-tetrahydroquinoline (58THQ). Further hydrogenation of 14THQ or 58THQ forms decahydroquinoline (DHQ). The reaction can then continue via two routes, i.e., the ring opening of 14THQ to o-propylaniline (OPA) and of DHQ to propylcyclohexylamine (PCHA). OPA is converted to propylbenzene (PB) via direct denitrogenation, whereas nitrogen is removed from PCHA to form propylcyclohexene (PCHE). According to the detailed analysis in Ref. [3] the hydrogenation of the phenyl ring in OPA is the rate determining step in the sequence; Q → 14THQ (via hydrogenation) → OPA (via ring opening) → PCHA (via denitrogenation). In the sequence: DHQ → PCHA (via ring opening) → PCHE (via denitrogenation) → propylcyclohexane (PCH) (via hydrogenation), the C(sp^3)-N bond cleavage in the primary amine (PCHA) is fast and the rate of the C(sp^3)-N bond cleavage in DHQ is the rate limiting step.

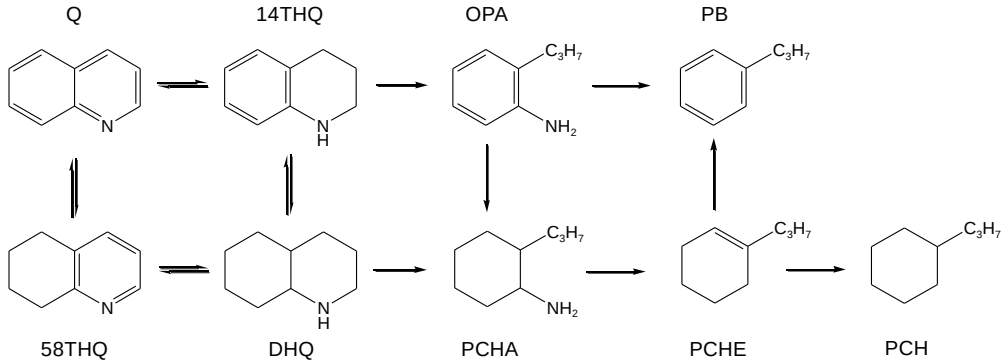

Scheme 1. HDN reaction network of Q. Abbreviations: 14THQ, 1,2,3,4-tetrahydroquinoline; 58THQ, 5,6,7,8-tetrahydroquinoline; DHQ, decahydroquinoline; OPA, o-propylaniline; PCHA, propylcyclohexylamine; PB, propylbenzene; PCHE, propylcyclohexene; PCH, propylcyclohexane.

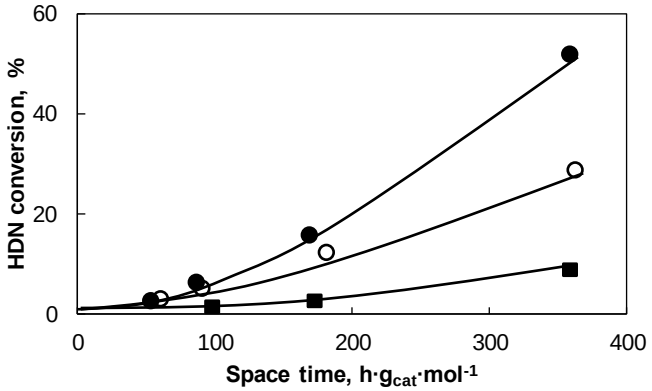

Figure 7. Quinoline HDN conversion as a function of the space time at 370 °C on MoS_2/γ-Al_2O_3 (■), Ni-MoS_2/γ-Al_2O_3 (●), and Ni-MoS_2/unsupported (○).

Q HDN conversion showed a non-linear dependency as function of the space time at 370 °C (Figure 7). At first the rate of N removal is negligible, but as soon as a significant concentration of DHQ is reached the rate increased (Figures 8-10). The HDN activity increased in the order: MoS_2/γ-Al_2O_3 < Ni-MoS_2/unsupported < Ni-MoS_2/γ-Al_2O_3. The initially low rate is a direct consequence of the inhibition by 14THQ that is stronger adsorbed on the catalyst surface than Q.[169]

The effect of the space time on the product distribution is shown in Figures 8-10. At first Q was quickly converted to 14THQ reaching the equilibrium (Figure S13). Furthermore, over the whole space time studied, DHQ and 58THQ were in thermodynamic equilibrium (Figure S13). Therefore (Q + 14THQ), and (DHQ + 58THQ) were lumped together for further analysis. The observed primary products, exhibiting linearly increasing yields at low space time values were (58THQ + DHQ) and OPA. Further conversion led via the secondary products, PCHA and PCHE to the final products: PB and PCH. Three isomers of PCHE were detected and lumped together for further analysis: 1-propylcyclohexene (with the highest yield according to its highest stability), 3-propylcyclohexene, and propylidene cyclohexane.

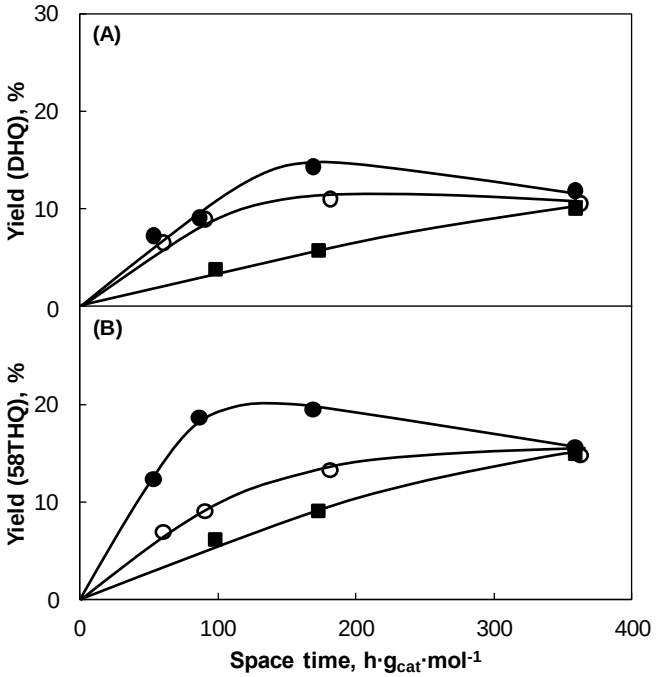

Figure 8. Yield of A) DHQ and B) 58THQ as a function of the space time at 370 °C on $MoS_2/\gamma\text{-}Al_2O_3$ (■), Ni-$MoS_2/\gamma\text{-}Al_2O_3$ (●), and Ni-MoS_2/unsupported (○).

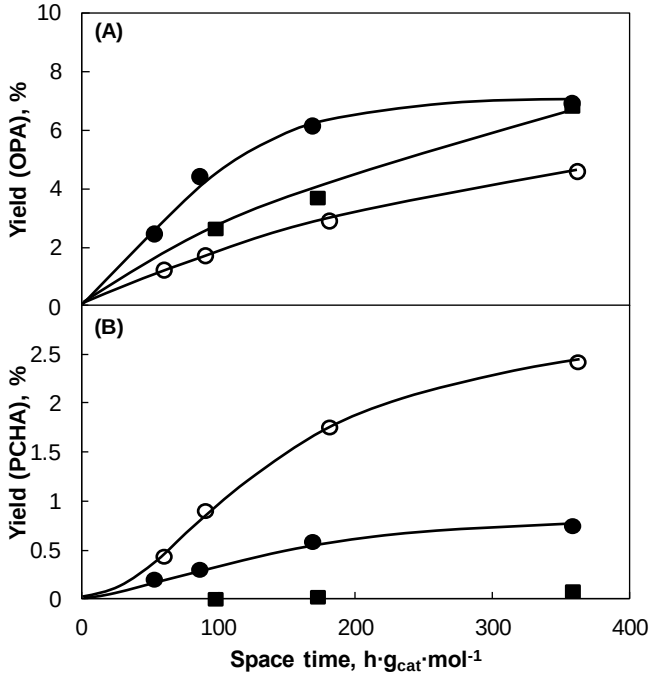

Figure 9. Yield of A) OPA, and B) PCHA as a function of the space time at 370 °C on $MoS_2/\gamma\text{-}Al_2O_3$ (■), Ni-$MoS_2/\gamma\text{-}Al_2O_3$ (●), and Ni-MoS_2/unsupported (○).

The rate of DHQ formation, via hydrogenation of the benzoic ring in 14THQ and the rate of 58THQ formation, via hydrogenation of the benzoic ring in quinoline, was the highest on Ni-$MoS_2/\gamma\text{-}Al_2O_3$ and the lowest on $MoS_2/\gamma\text{-}Al_2O_3$ (Figure 8). The rate of 14THQ ring opening to form OPA increased in the following order: Ni-MoS_2/unsupported < $MoS_2/\gamma\text{-}Al_2O_3$ < Ni-$MoS_2/\gamma\text{-}Al_2O_3$. This ring opening of 14THQ, via C(sp^3)-N bond cleavage to form OPA, has

a lower reaction rate compared to the parallel hydrogenation of the benzoic ring to form DHQ, (Figures 8A and 9A).

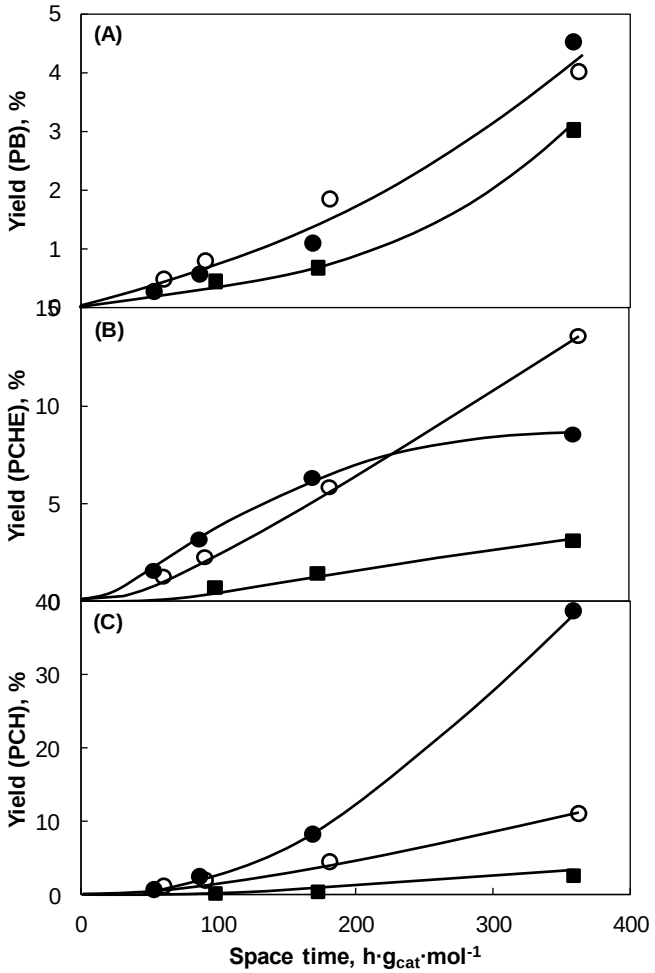

Figure 10. Yield of A) PB, B) PCHE, and C) PCH as a function of the space time at 370 °C on MoS_2/γ-Al_2O_3 (■), Ni-MoS_2/γ-Al_2O_3 (●), and Ni-MoS_2/unsupported (○).

Further hydrogenation of OPA to PCHA is negligible as long as Q, 14THQ, 58THQ and DHQ are present, because of their strong adsorption on the catalyst surface.[170-171] The other ring opening intermediate, PCHA (from DHQ), was either not detected or the yield was < 1 % on Ni-MoS_2/γ-Al_2O_3 and < 2.5 % on Ni-MoS_2/unsupported catalyst. The rate of nitrogen removal from PCHA to PCHE, which is hydrogenated to PCH increased in the following order: MoS_2/γ-Al_2O_3 < Ni-MoS_2/unsupported < Ni-MoS_2/γ-Al_2O_3.

In parallel to the HDN of Q, the conversion of DBT was also followed (Figure 11). The Ni promoted catalysts exhibited higher HDS conversion rates, for instance, at the space time of 100 h·g$_{cat}$·mol^{-1}, the DBT conversion was 12 % on MoS_2/γ-Al_2O_3, 45 % on Ni-MoS_2/unsupported, and 90 % on Ni-MoS_2/γ-Al_2O_3. The product distribution (Figure 11B and C), indicated that the main route for DBT conversion was direct desulfurization, with biphenyl (BPh) as the only product. Low yields of phenylcyclohexane (PhCH) were detected

over the whole space time: < 2 % on $MoS_2/\gamma\text{-}Al_2O_3$, < 8 % on $Ni\text{-}MoS_2/\gamma\text{-}Al_2O_3$ (and none with $Ni\text{-}MoS_2$/unsupported).

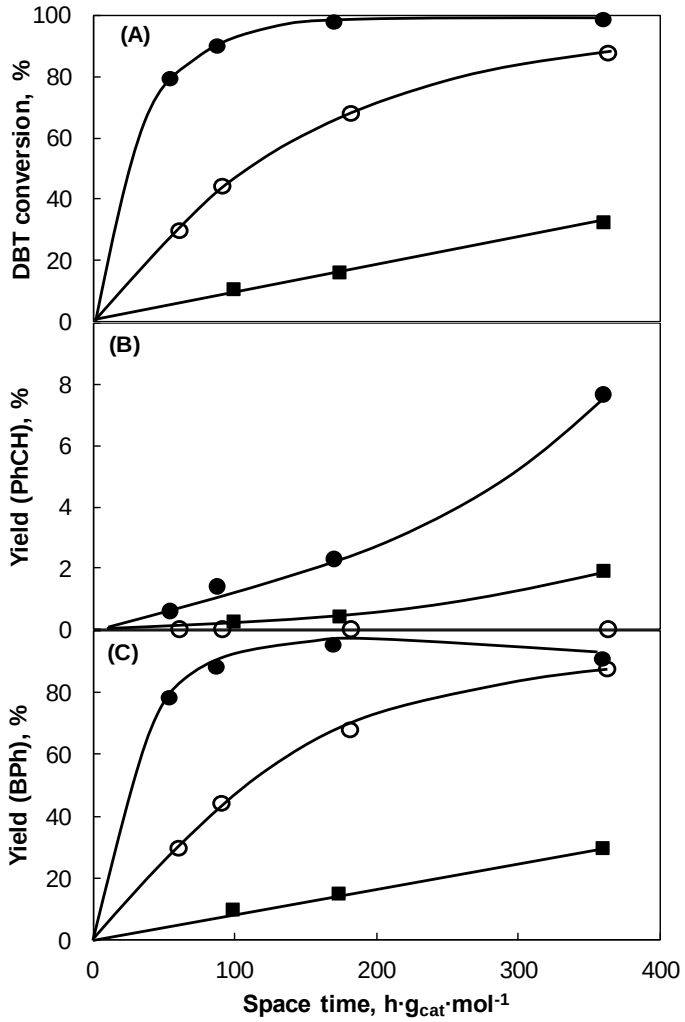

Figure 11. A) DBT conversion and yields of B) PhCH and C) BPh as a function of space time in the parallel reaction with the HDN of Q at 370 °C performed on $MoS_2/\gamma\text{-}Al_2O_3$ (■), $Ni\text{-}MoS_2/\gamma\text{-}Al_2O_3$ (●), and $Ni\text{-}MoS_2$/unsupported (○).

The temperature dependence of HDN of quinoline

The rate of nitrogen removal strongly depends on the reaction temperature and exhibits a S-shaped increase (Figure 12). At 290 °C only hydrogenation to 14THQ and DHQ occurs, while at 330 °C the first ring opening and nitrogen-free products are observed (Figures 13-15). Further temperature increase to 370 °C accelerates the rate of nitrogen removal. However, above 370 °C the HDN rate increases only slightly. This modest increase in N removal originates from the Q-14THQ thermodynamic equilibrium, which shifts towards Q at increasing temperatures.[172]

The product distribution shifted with increasing reaction temperature from hydrogenated products through ring opening products towards nitrogen-free products. The yield of 58THQ (product of the benzoic ring hydrogenation) exhibited only on the Ni-MoS_2/γ-Al_2O_3 catalyst a maximum at 380 °C (20 %), while the Ni-MoS_2/unsupported and MoS_2/γ-Al_2O_3 catalysts showed an increase of the 58THQ yield with increasing temperature reaching 30 % at 400 °C (Figure 13B).

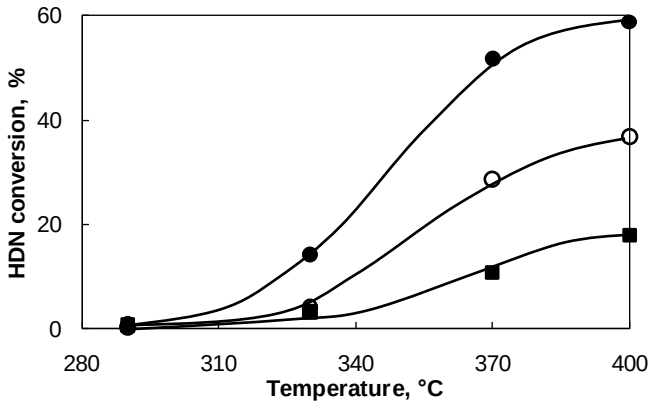

Figure 12. Q HDN conversion as a function of the temperature at the space time of 350 h g_{cat} mol^{-1} on MoS_2/γ-Al_2O_3 (■), Ni-MoS_2/γ-Al_2O_3 (●), and Ni-MoS_2/unsupported (○).

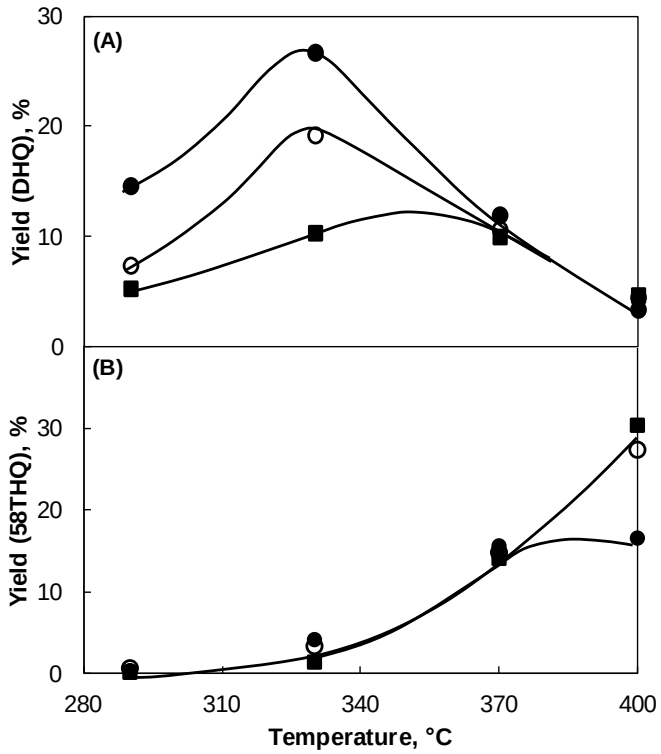

Figure 13. Yield of A) DHQ and B) 58THQ as a function of the temperature at the space time of 350 h g_{cat} mol^{-1} on MoS_2/γ-Al_2O_3 (■), Ni-MoS_2/γ-Al_2O_3 (●), and Ni-MoS_2/unsupported (○).

DHQ showed maximum yield at around 330 °C on Ni-MoS_2/γ-Al_2O_3 (27 %) and Ni-MoS_2/unsupported (20 %), while on MoS_2/γ-Al_2O_3 the maximum appeared at around

350 °C (12 %; Figure 13A). While the OPA yield increased with increasing temperature, the PCHA yield exhibited maximum at around 330 °C (1.5 %) on Ni-MoS_2/γ-Al_2O_3 and at around 350 °C (3.5 %) on Ni-MoS_2/unsupported (Figure 14A and B).

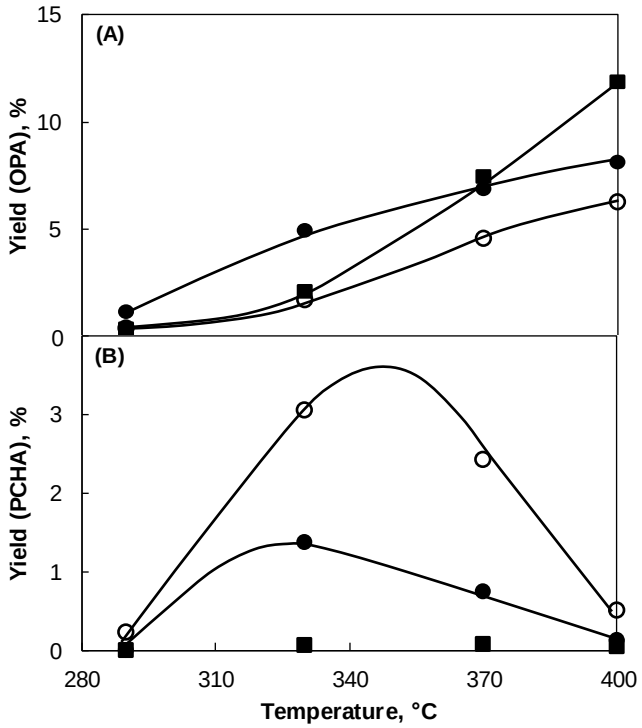

Figure 14. Yield of A) OPA, and B) PCHA as a function of the temperature at the space time of 350 h g_{cat} mol^{-1} on MoS_2/γ-Al_2O_3 (■), Ni-MoS_2/γ-Al_2O_3 (●), and Ni-MoS_2/unsupported (○).

The conversion to N-free products began at 330 °C. The PB yield increased with temperature reaching 3.3, 8.5, and 12.5 % at 400 °C on MoS_2/γ-Al_2O_3, Ni-MoS_2/unsupported, and Ni-MoS_2/γ-Al_2O_3, respectively (Figure 15A). PCHE exhibited a maximum yield at 370 °C on Ni-MoS_2/γ-Al_2O_3 (8.5 %), while a S-shaped dependency was observed on MoS_2/γ-Al_2O_3 and Ni-MoS_2/unsupported, reaching 7 % and 17 % respectively, at 400 °C (Figure 15B). The PCH yield increased with increasing temperature on the studied catalysts, reaching the maximum of 8.1, 10, and 41.6 % on MoS_2/γ-Al_2O_3, Ni-MoS_2/unsupported and Ni-MoS_2/γ-Al_2O_3, respectively (Figure 15C).

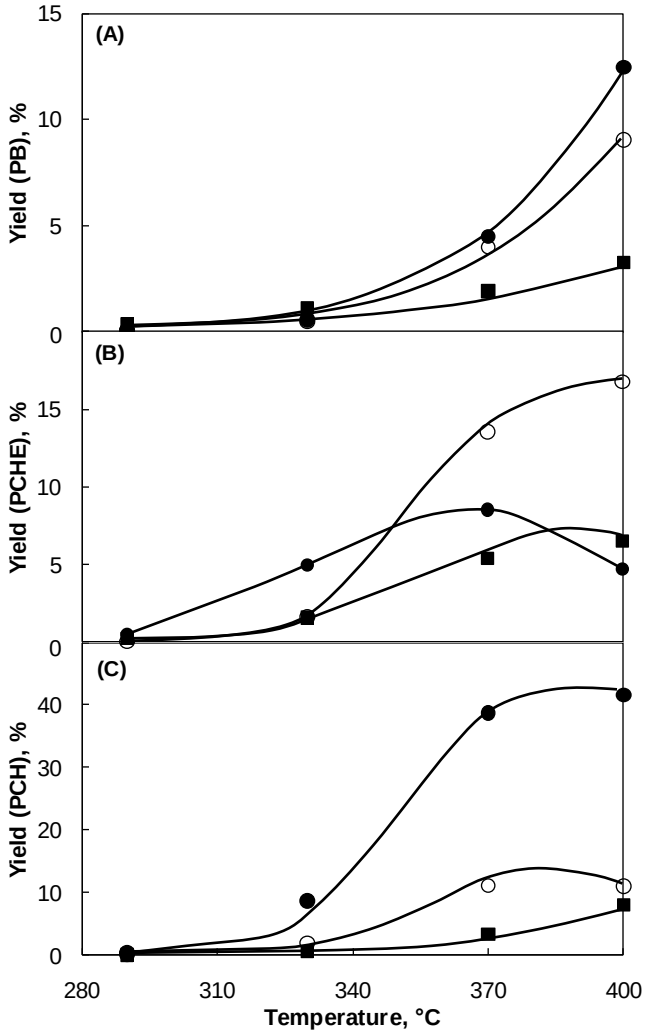

Figure 15. Yield of A) PB, B) PCHE, and C) PCH as a function of the temperature at the space time of 350 h g_{cat} mol^{-1} on $MoS_2/\gamma\text{-}Al_2O_3$ (■), Ni-$MoS_2/\gamma\text{-}Al_2O_3$ (●), and Ni-MoS_2/unsupported (○).

The conversion of DBT was also followed (Figure 16). The DBT conversion increased from 5 (at 290 °C) to 43 % (at 400 °C) on $MoS_2/\gamma\text{-}Al_2O_3$, and from 32 (at 290 °C) to 90 % (at 400 °C) on Ni-MoS_2/unsupported. On Ni-$MoS_2/\gamma\text{-}Al_2O_3$ the DBT conversion reached 100 % already at 330 °C. The product distribution (Figure 16B and C), indicated that the yield of hydrogenated product, PhCH, increased with increasing the reaction temperature reaching 4 % on $MoS_2/\gamma\text{-}Al_2O_3$, 7 % on Ni-$MoS_2$/unsupported, and 12 % on Ni-$MoS_2/\gamma\text{-}Al_2O_3$. BPh was the main product in all cases. On $MoS_2/\gamma\text{-}Al_2O_3$ the BPh yield increased continuously up to 40 % at 400 °C. On Ni-MoS_2/unsupported the yield reached 80 % at 370 °C and remained constant, whereas on Ni-$MoS_2/\gamma\text{-}Al_2O_3$ the BPh yield increased to ~100 % at 320 °C and decreases at higher temperatures.

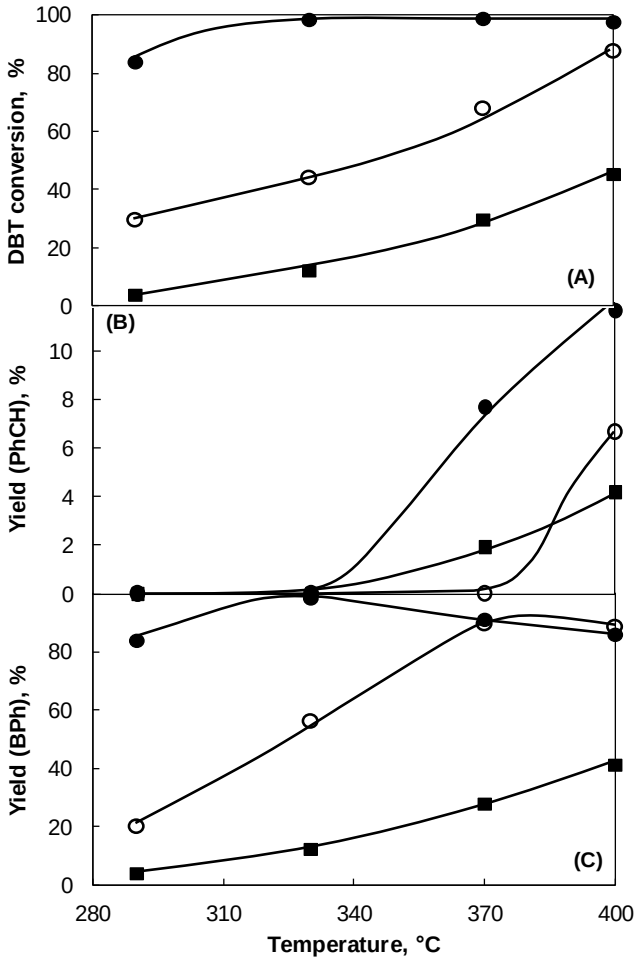

Figure 16. A) DBT conversion, B) yield of PhCH (B), and C) yield of BPh (C) as a function of temperature in the parallel reaction with the HDN of Q at the space time of 350 h g_{cat} mol^{-1} on $MoS_2/\gamma\text{-}Al_2O_3$ (■), Ni-$MoS_2/\gamma\text{-}Al_2O_3$ (●), and Ni-MoS_2/unsupported (○).

4. Discussion

Catalyst characterization - oxide precursors and its sulfidation

The Mo concentration of 2.5 Mo atoms·nm^{-2} in the supported materials is far below the monolayer concentration of $\gamma\text{-}Al_2O_3$ (4.6-5 atoms·nm^{-2}).[173] Accordingly, XRD patterns do not exhibit reflections of a crystalline Mo-containing phase (Figure S1 d and e), and the Raman spectra indicate the existence of well-dispersed polymolybdate species[174-178] (Figure S3 A,e-A,f). The presence of the characteristic pre-edge peak in the Mo K-edge XANES (at 20005 eV), indicates that in those species Mo is present in a distorted octahedral coordination geometry (Figure S4 A).[177, 179]

After Ni promotion the Raman band corresponding to the terminal Mo=O symmetric stretching vibration is shifted downwards from 961 cm^{-1} in Mo/$\gamma\text{-}Al_2O_3$ to 947 cm^{-1} in

NiMo/γ-Al_2O_3. The shoulder at 860 cm^{-1} assigned to the asymmetric stretching vibration of Mo-O-Mo bridging bond becomes more intense suggesting that Ni increases the aggregation of the Mo species, i.e., Ni leads to higher oligomerization degree of oxide Mo species.[180-181] This is confirmed by the analysis of the UV-vis spectra, which shows that the number of nearest Mo neighbors increased with the addition of Ni. The creation of these new Mo-O-Mo bonds may occur from terminal Mo=O groups or by breaking Al-O-Mo bonds with the support.

The NiMo/unsupported oxide catalyst precursor presents a mixture of nickel molybdate ($NiMoO_4$), and ammonium nickel molybdate ($(NH_4)HNi_2(OH)_2(MoO_4)_2$; see XRD patterns in Figure S1 f and Raman spectrum in Figure S3 A,f). The Ni to Mo metal ratio of 1.07 (Table 1) matches well with the stoichiometry of the identified compounds. The average number of nearest Mo neighbors determined by UV-vis and X-ray absorption spectroscopy confirms the presence of molybdates. The XANES at the Mo K-edge showed pre-edge features characteristic for tetrahedral molybdenum species (Figure S4 A, g) and the UV-vis spectra (Figure S3 B, f) exhibited two features assigned to octahedrally coordinated Ni^{2+} (ammonium nickel molybdate) and tetrahedrally coordinated Ni^{2+} (nickel molybdate). The ammonium nickel molybdate species in NiMo/unsupported can be, therefore, described as a layered structure of distorted nickel octahedra and molybdenum tetrahedra forming layers in the c-direction.[182]

The temperature-programmed sulfidation of both supported Mo/γ-Al_2O_3 and NiMo/γ-Al_2O_3 oxide precursors showed a profile with three sections.[25] In the low temperature region oxygen is substituted by sulfur, as seen by H_2S consumption in the TPS and the decrease of the shortest Mo-O bond coupled with the formation of new Mo-S contribution shown in the FT-EXAFS (Figure S9). The terminal Mo=O bonds are the most reactive in polymolybdate-like structure and, therefore, among the first ones to form oxy-sulfide species.[183] In the second section, molybdenum is reduced from Mo^{6+} to Mo^{4+}, indicated by the H_2S release in TPS profiles and the disappearance of the pre-edge feature in XANES. The reduction temperature is shifted from 225 °C (Mo/γ-Al_2O_3) to 205 °C (NiMo/γ-Al_2O_3) due to the presence of Ni,[25] which induces weaker interaction of the oxide precursor with the support. The last region is characterized by further H_2S consumption and formation of new Mo-Mo contributions at larger distance than in the precursors, indicating the further conversion to the final MoS_2/γ-Al_2O_3 and Ni-MoS_2/γ-Al_2O_3. The TPS profile of NiMo/unsupported exhibited a continuous H_2S consumption over the whole temperature range. H_2S release was not observed, however, the reduction to Mo^{4+} in $(NH_4)HNi_2(OH)_2(MoO_4)_2$ and $NiMoO_4$ occurs between 270 °C and 305 °C as deduced by XANES data (Figures S8 and S9).

Catalyst characterization: active phases present in the sulfide catalysts

MoS_2 is present in S-Mo-S sandwiched structures (MoS_2 slabs), in which S atoms coordinate Mo to form trigonal prisms. The stacking of these structures, stabilized by van der Walls interactions, leads to laminar assemblies. The support stabilizes MoS_2 with a relatively small number of layers (low stacking degree). In contrasts to the MoS_2 phase, the morphology of the supported, Ni- or Co-promoted MoS_2 phase has been controversial. Several models of active phases have been proposed to explain the synergy between (W)Mo and (Ni)Co (see, e.g., ref. [184]). At present, variants of the "Co-Mo-S" model, proposed originally by Topsøe et al.,[185] are widely accepted. This model suggests that Mo cations are substituted by Ni or Co at the edge position of the MoS_2 slabs. Strong evidence has been reported for this model including EXAFS data,[142, 186] DFT calculations,[148] and STM.[32, 187]

The characterization results of the studied alumina-supported catalysts show that the MoS_2 slabs are well dispersed on alumina (XRD and TEM, Figures 1-3) and that the bulk and surface structure of MoS_2/γ-Al_2O_3 and Ni-MoS_2/γ-Al_2O_3 corresponds to well-defined MoS_2. Indications of minority oxide species during the LCF analysis of the XANES points to a very low concentration of Mo oxide species, as Mo-O contributions were not needed to fit the EXAFS of the sulfide catalysts (Table 2). The only oxide species identified in the sulfided catalysts is a minority concentration of spinel $NiAl_2O_4$, whereas most of the Ni is present in sulfide phases. The presence of a Ni-Ni distance of 2.59 Å in the EXAFS, however, points to the formation of segregated Ni sulfides (Table 3). These Ni sulfides have to be very dispersed as they show only a low coordination number for the Ni-Ni contributions compared to Ni_3S_2, and none of these phases were identified in XRD and TEM. The Mo-Ni contribution indicates the formation of a Ni-Mo-S phase, which dominates the performance (vide infra). The Mo-Ni coordination number of 0.2 is smaller than that generally reported for Ni-Mo-S,[41, 168] however, the Ni-S, and Ni-Mo distances match very well with the millerite-type structure proposed for that phase.[42] The difference in Mo-S coordination numbers for promoted and unpromoted catalyst (6.6 and 5.7, respectively) is also in line with the features expected for the NiMoS and MoS_2 phases. The higher coordination in the former indicates a higher degree of sulfidation for the Ni-Mo-S phase, resulting from the weakened Mo-support interaction.[188] The characterization of the alumina-supported oxide precursors by Raman (Figure S3 B) and TPS [25] also confirms the weaker interaction of the Ni promoted sulfides with the support. The very different catalytic performance also gives a clear evidence for the existence of different phases in MoS_2/γ-Al_2O_3 and Ni-MoS_2/γ-Al_2O_3 catalysts (vide supra).

The phases present in Ni-MoS_2/unsupported must be discussed separately because the morphology of the unsupported species differs from the alumina-supported sulfides. The

unsupported oxide precursor is a mixture of two well-defined crystalline species [identified by Raman spectroscopy, XRD, and TEM coupled with selected-area electron diffraction-(SAD)], whereas highly dispersed polymolybdates were present on the supported counterparts. Thus, the sulfidation of the unsupported oxide precursor follows different kinetics during TPS compared to the supported materials. Obviously, the same reactions must occur for all three catalysts, i.e., O-S exchange and reduction of Mo^{6+}. For the unsupported catalyst, however, the segregation of Ni species to form Ni_3S_2 and the diffusion of the sulfidation and reduction agents to the core of the relatively large oxide crystals produces a continuous H_2S consumption, which does not allow differentiation between the stages of sulfidation. Nevertheless, the catalytic activity can be related only to sulfide phases, because after sulfidation only a fraction of oxide species remains in the catalyst (LCF analysis). It has been shown by Mößbauer spectroscopy that in unsupported catalysts, the existence of “Co-Mo-S”-like phases occur at similar molar ratio than on supported catalysts.[120, 189]

The activity of the unsupported catalysts has been less stringently associated to the formation of the Co(Ni)MoS phase[190] than for supported catalysts, probably because the promoted structure may be different in non-supported sulfides than in supported ones. For instance, it has been proposed that a synergy between MoS_2 and Co sulfides replace the decoration of MoS_2 by Co in bulk multimetallic sulfides.[31, 191] We found by EXAFS fitting of Ni-MoS_2/unsupported two distances for Ni-S contributions (2.20 and 2.31 Å) and a distance of 2.66 Å for Ni-Mo, that is, smaller than the millerite-type structure claimed for Ni-MoS_2/γ-Al_2O_3. In a recent paper, Chianelli et al,[31] modeled the MoS_2-Co_9S_8 interface with Co in a cubic structure that follows the structure observed by EXAFS (i.e., two Co-S distances and Co-Mo distance shorter than that expected in a millerite structure[192]), therefore, we speculate that in the unsupported catalyst the MoS_2 phase is also promoted by Ni_xS_y clusters in addition to the edge decoration with Ni atoms. The presence of Ni_xS_y was also shown by XRD (Figure 1) and HR-SEM (Figure 3) and the Ni-Ni path at 2.59 Å found by EXAFS analysis. Moreover, the coordination number of the Ni-Ni contribution (N_{Ni-Ni}) can be used as an indicator for the proportion of Ni present in Ni_xS_y clusters. Given that a higher value for N_{Ni-Ni} is observed for Ni-MoS_2/unsupported than for Ni-MoS_2/γ-Al_2O_3, the amount of Ni_3S_2 is higher in Ni-MoS_2/unsupported.

It is plausible to assume that Ni_xS_y forms when Ni^{2+} has reached a certain concentration at the edges of MoS_2 particles. Note that the Mo/Ni ratio is close to 1 in the catalyst, i.e., the concentration of Ni is much higher than that required for the formation of the NiMoS phase.[159] Although it is difficult to determine the exact concentration and nature of the Ni_xS_y species present from the experimental results of this study, it is evident that the

Ni-MoS_2/unsupported catalyst is a physical mixture of at least three sulfide phases, with Ni-promoted MoS_2 structures dominating the catalytic behavior.

Unfortunately, it is currently not possible to strictly differentiate between the contributions of Ni_xS_y particles (probably also present in a wide range of sizes) and Ni-atoms incorporated at the edges of the MoS_2 slabs. Regardless of the specific nature of the impact of Ni, the Ni-Mo interaction is clearly observed in the catalytic behavior. The unsupported catalyst is the second most active for HDN although the concentration of CUS determined for this catalyst is only the half of that determined for MoS_2/γ-Al_2O_3 (resulting from NO uptake). Hence, the intrinsic activity of the unsupported catalyst is more similar to that of Ni-MoS_2/γ-Al_2O_3 than to that of MoS_2/γ-Al_2O_3. From the EXAFS analysis Mo-Ni coordination numbers of 0.2 and 0.3 were obtained for Ni-MoS_2/γ-Al_2O_3 and Ni-MoS_2/unsupported, clearly indicating Mo-Ni interactions.

The HDN of quinoline

The first steps of the HDN reaction network can be simplified to the scheme shown in Table 4 because Q and 14THQ as well as 58THQ and DHQ rapidly equilibrated under the reaction conditions used (Figure S13). The overall (Q+14THQ) conversions, i.e., (k_1+k_2), was satisfactorily fitted to a first order kinetics with a correlation coefficient (R^2) above 0.99. The k_1/k_2 ratio was assumed to equal the initial OPA·(58THQ+DHQ)$^{-1}$ selectivity. Therefore, the absolute values of k_1 and k_2 were deduced from the overall conversion and the initial selectivity. The values of k_3 and k_2' were adjusted from the experimental concentration profiles of the products. The values of the subsequent steps of the HDN network are not quantitatively discussed, because the strong adsorption of bicyclic compounds of Q may lead to inaccurate reaction rate constants. For a more detailed description see ref. [3].

On all catalysts, the hydrogenation of (Q+14THQ) is faster than the dehydrogenation of (58THQ+DHQ). The k_2/k_2' ratios are in good agreement with the equilibrium constants among the bicyclic compounds.[3] On the other hand, the ring opening in DHQ is much faster than that of 14THQ likely due to the lower intrinsic reactivity of the latter. Indeed, the ring opening of 14THQ may be a rate limiting step in the whole HDN process, together with the hydrogenation of OPA.[3] The activity of the catalysts (k_1+k_2) followed the same trend than that observed for HDN conversion (Figure 7), i.e., MoS_2/γ-Al_2O_3 < Ni-MoS_2/unsupported < Ni-MoS_2/γ-Al_2O_3. Interestingly, the (de)hydrogenation activity (k_2 and k_2') follows the same trends, whereas the rates of the ring opening steps increased in the order

Ni-MoS_2/unsupported ≤ MoS_2/γ-Al_2O_3 < Ni-MoS_2/γ-Al_2O_3 for 14THQ (k_1) and MoS_2/γ-Al_2O_3 < Ni-MoS_2/γ-Al_2O_3 ≤ Ni-MoS_2/unsupported for DHQ (k_3).

Table 4. Pseudo-first order rate constants for the main reaction steps of a simplified reaction network for the hydrodenitrogenation of Q.

Catalyst	k_i (mol·h^{-1}·g_{cat}^{-1})·10^{-5}			
	k_1	k_2	k_2'	k_3
MoS_2/γ-Al_2O_3	0.32	1.06	0.22	1.03
Ni-MoS_2/γ-Al_2O_3	0.64	4.96	0.94	3.30
Ni-MoS_2/unsupported	0.28	3.13	0.63	3.80

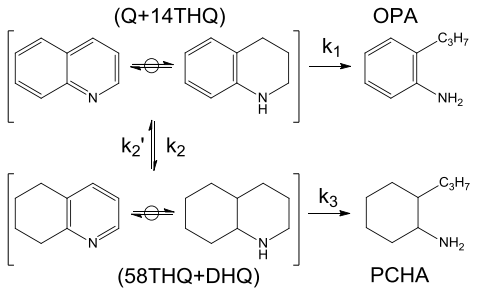

On the nature of the active sites

The specific geometric arrangement of the active sites in the MoS_2 and Ni-promoted phases remains inconclusive to date. The general agreement is that the edges of the MoS_2 slabs, decorated or not with Ni, are catalytically active. The adsorption of reactants occurs, via electron donation from heteroatoms or aromatic rings, on coordinatively unsaturated sites (CUS), i.e., Mo or Ni atoms with Lewis acid character. Detailed descriptions of these interactions are to be found in numerous reviews on the subject (for instance refs. [27, 156, 193-195]). The basic sulfur anions are also claimed to play a fundamental role in the activity of the sulfide phase, (probably also in combination with CUS) for H_2 activation.[3] After the dissociative adsorption of H_2 (or H_2S) on these sites $(S\text{-}S)^{2-}$ dimers or S^{2-}-CUS pairs, SH^- groups are created at the edges. These groups provide the hydrogen required for hydrogenation and hydrogenolysis. Furthermore, the SH^- groups have been identified to have an acidic character in C(sp_2)-N bond scission mechanisms.[68, 196] The basal planes of the MoS_2 slabs are considered in general inactive. Based on scanning tunneling microscopy studies, Lauritsen et al. [185] proposed, however, additional active sites located on the basal planes adjacent to the edges of MoS_2. These so-called “brim” sites, exhibit a metal character (ability to donate and accept electrons) are claimed to adsorb reactants and catalyze some hydrogenation step in the HDS of thiophene.

At this point we relate the activity results with the above-described potential sites in the catalysts. It has been shown that the promoted Ni-MoS_2/γ-Al_2O_3 catalyst is superior for nitrogen removal compared to its “parent” MoS_2/γ-Al_2O_3 catalyst in the whole temperature range (Figure 12). This observation is well in line with the assumption that upon addition of Ni, Mo cations are substituted at the edge positions of the MoS_2 slabs creating new and more active catalytic sites for HDN.[29] However, it is important to note that Ni does not promote the

removal of nitrogen from all N-containing compounds. Direct denitrogenation of OPA decreases with the incorporation of Ni to the MoS_2 slabs.[25, 160] Thus, the active site for the DDN of OPA is related only with Mo-associated CUS. At the same time, the hydrogenation of the OPA phenyl ring is dramatically enhanced by Ni probably due to the promotion of brim sites.[25] Accordingly, the promoted Ni-MoS_2/γ-Al_2O_3 catalyst exhibits a higher hydrogenation rate than MoS_2/γ-Al_2O_3 (k_2 increases by factor five, Table 4).

If the reaction steps of Q HDN could be related with specific locations in the MoS_2 particles one would expect that the absence of support and high stacking degree of the sulfides in Ni-MoS_2/unsupported lead to completely different catalytic performance compared to Ni-MoS_2/γ-Al_2O_3. However, the performance of Ni-MoS_2/unsupported is similar to that of Ni-MoS_2/γ-Al_2O_3. For instance, in the (de)hydrogenation steps the presence of Ni is more important than the presence of the support (k_2 and k_2' of Ni-containing catalysts are much higher than those of MoS_2/γ-Al_2O_3). The Ni-MoS/unsupported catalyst exhibits lower hydrogenation rate than the supported Ni-MoS_2/γ-Al_2O_3 counterpart, i.e., k_2 is 1.6 times faster on the latter. This difference is ascribed to the higher dispersion of the supported Ni-MoS_2/γ-Al_2O_3.

Evidence to assign catalytic activity for hydrogenation to the brim sites has not been obtained. If these sites catalyze hydrogenation, higher stacking degree should have resulted in lower hydrogenation rates, because the brim sites are found only on the basal planes of the stacked layers. This would be true, however, only at constant length of the sulfide slabs, whereas the strong variation of physical shape of the sulfide particles did not allow a detailed analysis of the impact of sites on basal planes.

The DHQ ring opening occurs via Hofmann-type elimination to form PCHA and subsequently PCHE.[3] The Hofmann-type elimination requires an acid site, for the quaternization of the nitrogen atom, and a basic site for the removal of a β-H atom. This dual site consists of SH^- groups with acidic character and basic S^{2-} ions.[3, 68] The trend in k_1 (ring opening of 14THQ) is correlated with the dispersion of the sulfide phase, therefore suggesting that Ni does not play an important role in the ring opening of 14THQ. Less straightforward to understand is the trend with respect to ring opening of DHQ (k_3) which is clearly enhanced by the presence of Ni, but apparently lowered by the support. Considering that the activity of Ni sulfides for C-N bond cleavage is lower than that of MoS_2,[197] it is not possible to argue that the higher value for k_3 on Ni-MoS_2/unsupported is due to the segregated Ni sulfide phase. Therefore, we tentatively attribute the higher value of k_3 on Ni-MoS_2/unsupported than on Ni-MoS_2/γ-Al_2O_3 to steric hindrance in the sulfide-support interface aggravated by the relatively more bulky structure of DHQ than 14THQ.

The HDS of DBT suggests that the functionality of the active sites for HDS does not depend on their position in the MoS_2 slabs, because the selectivity does not depend on the morphology or presence of support (Figure 16) in the conditions used in this study. The main pathway is the direct desulfurization occurring via sulfur σ-bonding on sulfur vacancies (CUS). Therefore, the concentration of such coordinatively unsaturated sites should correlate the rate of the HDS reaction. For the catalysts studied, the concentration of accessible cations at the perimeter of the sulfide slabs increases as follows: Ni-MoS_2/unsupported < MoS_2/γ-Al_2O_3 < Ni-MoS_2/γ-Al_2O_3 (determined by NO adsorption). Despite the higher CUS concentration on MoS_2/γ-Al_2O_3, Ni-MoS_2/unsupported exhibits higher HDS rate. This contrast suggests that the intrinsic rate of HDS increases due to the incorporation of nickel to the NiMoS phase. For the Ni-containing catalysts, the HDS activity is indeed determined by the dispersion of the Ni-Mo-S phase, higher in Ni-MoS_2/γ-Al_2O_3 than in Ni-MoS_2/unsupported.

5. Conclusions

A series of oxide (Ni)Mo catalysts precursors were synthesized and characterized. The supported Mo/γ-Al_2O_3 oxide material exhibited a well-dispersed amorphous polymolybdate structure. The addition of Ni causes weaker interaction of Mo species with the support and, therefore, higher oligomerization degree. In contrast, the NiMo/unsupported material exhibited a mixture of nickel molybdate ($NiMoO_4$), and ammonium nickel molybdate ($(NH_4)HNi_2(OH)_2(MoO_4)_2$).

The sulfided, MoS_2/γ-Al_2O_3, Ni-MoS_2/γ-Al_2O_3, and Ni-MoS_2/unsupported active catalysts were characterized and tested in the hydrodenitrogenation (HDN) of quinoline in the presence of dibenzothiophene. The MoS_2 phase on the support had high dispersion with the average stacking degrees of 1.6 and 1.9, for MoS_2/γ-Al_2O_3 and Ni-MoS_2/γ-Al_2O_3, respectively and particle lengths of 7.2 (MoS_2/γ-Al_2O_3) and 5.4 nm (Ni-MoS_2/γ-Al_2O_3). Ni-MoS_2/unsupported exhibited the largest stacking degree (approximately 7) and slab lengths (15-20 nm). The presence of Ni increased the concentration of coordinatively unsaturated sites (CUS) in the supported catalyst (65 μmol·g^{-1} in MoS_2/γ-Al_2O_3 and 80 μmol·g^{-1} in Ni-MoS_2/γ-Al_2O_3), whereas lower CUS concentration on Ni-MoS_2/unsupported catalyst (33 μmol·g^{-1}) was a consequence of higher agglomeration degree.

The main route for the N removal in the quinoline HDN is: quinoline → 14THQ (equilibrated step) → DHQ (via hydrogenation) → PCHA (ring opening via C(sp^3)-N bond cleavage) → PCHE (Hofmann-type elimination via C(sp^3)-N bond cleavage) → PCH (via hydrogenation). The ring opening of DHQ is rate determining in this sequence. The rates of

nitrogen removal appreciably increase only when a significant amount of 14THQ has been converted to DHQ. The hydrodesulfurization and hydrodenitrogenation activities follow the trend: $MoS_2/\gamma\text{-}Al_2O_3$ < Ni-MoS_2/unsupported < Ni-$MoS_2/\gamma\text{-}Al_2O_3$. Ni-$MoS_2/\gamma\text{-}Al_2O_3$ exhibited higher rates than $MoS_2/\gamma\text{-}Al_2O_3$ due to the promotion of Ni. The Ni-MoS_2/unsupported catalyst exhibited lower rates than Ni-$MoS_2/\gamma\text{-}Al_2O_3$, likely due to the low dispersion of the former. Ni-MoS_2/unsupported is more active than $MoS_2/\gamma\text{-}Al_2O_3$ despite of the higher CUS concentration of the latter. Therefore, Ni-MoS_2/unsupported exhibited higher intrinsic rates due to the promotion mechanisms of Ni species. In turn, whereas we attribute the promoter effect to the formation of the Ni-Mo-S phase (Ni atoms decorating MoS_2) on the support, we propose that in the unsupported catalyst, particles of Ni_xS_y also form at the MoS_2 edges exerting a promoter effect (although weaker than the single Ni atom decoration effect). The ring opening steps are the only ones that seem to be more influenced by the morphology of the sulfide phase than by the presence of promoter.

6. Experimental Section

Catalyst preparation

Supported Mo and NiMo catalysts. The oxide precursors were prepared by a two-step incipient wetness impregnation of $\gamma\text{-}Al_2O_3$ (237 $m^2 \cdot g^{-1}$). Prior to impregnation, the support was dried at 120 °C in static air and treated at 560 °C for 2 hours under synthetic air flow. In the first step the carrier was impregnated with an aqueous solution of ammonium heptamolybdate, $(NH_4)_6Mo_7O_{24} \cdot 4H_2O$ (99.98%, Aldrich). After impregnation, the catalyst was dried at 120 °C overnight in static air atmosphere and then treated at 500 °C for 4 hours (heating rate of 1 °C·min^{-1}) under synthetic air flow. One part of the prepared sample was preserved as oxidic Mo catalyst precursor and the other was used as a support for the impregnation with an aqueous solution of nickel nitrate, $Ni(NO_3)_2 \cdot 6H_2O$ (≥98.5%, Aldrich). After impregnation, the NiMo precursor was thermally treated as in the case of the Mo precursor. The molybdenum concentration in the Mo and NiMo oxide precursors was 8.6 wt.% (2.5 atom·nm^{-2}), whereas the Ni concentration in the NiMo precursor was 3.6 wt.%.

The *sulfide catalysts* were obtained by sulfidation of the oxide precursors under 10 % H_2S in H_2 flow at 400 °C and 1.8 MPa for 8 hours. After cooling to room temperature in the sulfiding agent, the catalysts were flushed with hydrogen and stored in nitrogen atmosphere. Hereafter, the oxidic precursors are referred as $Mo/\gamma\text{-}Al_2O_3$ and $NiMo/\gamma\text{-}Al_2O_3$, whereas the corresponding supported sulfide catalysts are denoted as $MoS_2/\gamma\text{-}Al_2O_3$ and Ni-$MoS_2/\gamma\text{-}Al_2O_3$.

Unsupported NiMo catalyst. The oxide precursor of the unsupported catalyst was prepared by co-precipitation.[135] Ammonium heptamolybdate $(NH_4)_6Mo_7O_{24}\cdot 4H_2O$ (Aldrich) was dissolved in bidistilled water at room temperature in a three neck flask with a reflux condenser. Aqueous ammonia (28-30%) was added under continuous stirring until the pH of the solution changed from 5.5 to 9.5. In parallel, an aqueous solution of nickel nitrate $Ni(NO_3)_2\cdot 6H_2O$ (Aldrich) (pH = 6) was heated to 60 °C and then added dropwise to the ammonium heptamolybdate solution (kept at 90 °C). A light green precipitate formed at pH = 7 was further stirred and then filtered. The filter cake was dispersed into maleic acid solution (0.05 mol·l^{-1}, pH = 1.5) to form a slurry (pH = 6). After filtration, the collected precipitate was vacuum dried overnight at room temperature and further dried at 120 °C for 12 hours (heating rate of 1 °C·min^{-1}) in flowing synthetic air. The sulfidation of the unsupported catalyst precursor was performed in 10 % H_2S in H_2 flow at 400 °C and 1.8 MPa for 12 hours. After cooling to room temperature in the sulfiding agent, the catalyst was flushed with hydrogen and stored in nitrogen atmosphere. The oxidic precursor is denoted as NiMo/unsupported and the sulfide catalysts as Ni-MoS_2/unsupported.

Catalyst characterization

Texture and elemental analysis. The BET surface areas and pore size distributions were determined from the analysis of the N_2 adsorption-desorption isotherms at -196 °C of the oxidic precursors. A PMI Automated BET Sorptomatic 1900 Series instrument (Thermo Finnigan) was used to carry out the experiments. Prior to the adsorption, the supported samples were evacuated at 250 °C for 2 hours and the unsupported catalyst precursor was evacuated at 120 °C for 4 hours. Elemental analysis was carried out at the Microanalytical Laboratory of the TU München.

NO adsorption. NO adsorption was performed as a pulse experiment at room temperature to probe the concentration of adsorption sites and average edge dispersion in the studied metal sulfide catalysts. A detailed description of the experiment can be found elsewhere.[25]

X-ray diffraction (XRD). The crystal structure of the samples was determined by powder X-ray diffraction. The crystallographic phases were identified by using the inorganic crystal structure database (ICSD).[69] The XRD patterns were collected with a Philips X'Pert System (Cu-Kα radiation, 0.1542 nm), using a nickel K_β-filter and a solid state detector (X'Celerator). The operating conditions were 45 kV and 40 mA. The prepared catalysts were measured with step size of 0.017° and scan time of 115 s per step. Selected reference materials were measured 5 min with step size of 0.017° and scan time of 10 s per step.

The Scherrer equation was used to determine the stacking degree of the sulfide slabs in the unsupported catalyst in the knowledge that the diffraction at 2θ = 14° corresponds to the (002) plane with interplanar distance of 6.1 Å (distance between the molybdenum layers in MoS_2):

$$L = \frac{K \cdot \lambda}{\Delta(2\theta) \cdot \cos\theta}$$

were *L* is the mean size of ordered (crystalline) domain, *K* is the Scherrer shape factor (0.9), *λ* is the used X-ray wavelength, *θ* is the measured Bragg angle, and *Δ(2θ)* is the line broadening in radians. To calculate the line broadening the following equation was used:

$$\Delta(2\theta) = FWHM - 0.1$$

where FWHM is the full width at the half maximum in radians, and 0.1 is the instrument typical parameter.

Electron microscopy. Measurements were performed in transmission mode coupled with selective area electron diffraction (TEM-SAD) and in scanning mode at high resolution coupled with energy dispersive X-ray spectroscopy (HR-SEM-EDX). Samples of the catalysts were ground and ultrasonically dispersed in ethanol. Dispersion drops were applied on a copper-carbon grid. TEM and SAD measurements were carried out in a transmission electron microscope device JEOL JEM-2011 with an accelerating voltage of 120 keV. For the HR-SEM and EDX mapping measurements, a high resolution FE-SEM, JSM 7500 F (JEOL) with EDX (Oxford) was used. The micrographs were taken with a secondary electron imaging (SEI) detector and an accelerating voltage of 5 keV.

Raman spectroscopy. Raman spectra were obtained with a 514 nm Ar laser on a Renishaw Raman Spectrometer (Type 1000) equipped with CCD detector and a Leica microscope DM LM. Prior to the measurements, the calibration was done with a Si(111) crystal. The wavenumber accuracy was within 1 cm^{-1}. Oxidic catalyst precursors and reference materials were analyzed under ambient conditions in the form of self-supported wafers. In situ measurements were performed by placing the sample into a quartz capillary connected to a flow system and attached to a heating wire. The sulfidation was performed in 10% H_2S in H_2 at 400 °C for 1 hour and spectra were taken every 100 °C. Afterwards the sample was cooled to room temperature and the flow was switched to N_2 to record further spectra. Finally, the sample was heated to 400 °C again in flowing synthetic air for acquisition of the final spectra.

Diffuse reflectance UV-vis spectroscopy (DR UV-vis). The diffuse reflectance technique was applied to collect ultraviolet-visible-near infrared spectra using an Avantes AvaSpec-2048

fiber optic spectrometer equipped with a CCD detector array. The combined deuterium and halogen light source, Ava Light-DH-S-BAL, was used in combination with a fiber optic cable FCR-7UV400-2-SR-HT. Spectra of oxide catalyst precursors and reference materials were recorded under ambient conditions. The samples were placed as powder in a Teflon sample holder which provided 1 mm sample thickness.

X-ray absorption spectroscopy (XAS). The structural properties of the oxide catalyst precursors, the sulfided catalysts as well as during the catalyst sulfidation were studied in-situ by X-ray absorption spectroscopy at the X1 beamline at *Hasylab, DESY,* Hamburg, Germany. The data set was completed with experiments performed on the *BM 26A DUBBLE*, (dutch-belgian) beamline at the *ESRF,* Grenoble, France*.* Spectra were recorded in transmission mode at the Mo K-edge (20 000 eV) using Si (311) crystals and at the Ni K-edge (8333 eV) using Si (111) crystals in the monochromator, respectively. The contributions of the higher harmonics were minimized by detuning the second crystal of the monochromator to 60% of the maximum intensity. Energy calibration was performed with a molybdenum and nickel metal foil, respectively, measured simultaneously with the samples. The samples were prepared as self-supporting wafers and placed into a stainless steel in situ flow cell. The measured reference compounds were mixed with cellulose to achieve a total absorption of μx = 1.5. The spectra of oxide precursors, sulfided catalysts and those of reference compounds used for EXAFS analysis were collected in He flow and at liquid N_2 temperature (LNT) to minimize thermal vibrations. At least two spectra of each sample were averaged to enhance the signal to noise ratio. After the EXAFS measurements of the oxidic catalyst precursors, quick XAFS scans with a resolution of 180 seconds were continuously taken during the catalyst sulfidation in a flow of 10% H_2S in H_2 with a heating rate of 5 °C·min^{-1} up to 400 °C followed by an isothermal period of 1 hour.

Quick XAFS data were processed with XANES dactyloscope software (version 2012/4).[198] The scattering contributions in the pre- and post-edge of the background were removed from the X-ray absorption using a third-order polynomial function and afterwards all spectra were normalized to the average post-edge height of one. The XANES and EXAFS data were analyzed with IFEFFIT using the Horae-package (ATHENA and ARTEMIS, version 1.2.11). [199-200] After the removal of the background absorption and normalization, the oscillations were weighted with k^3 and Fourier-transformed within the limit of 3.5-14 $Å^{-1}$ for the oxide precursor and of k = 3 - 12.0 $Å^{-1}$ for the sulfided catalyst. The local environments of the Mo and Ni atoms in the sulfided catalysts were determined in k-space from the EXAFS data. Single and multiple scattering contributions for Mo-S, Mo-Mo, Ni-S and Ni-Ni (phase shifts and backscattering amplitudes) were calculated with FEFF [201] by using the geometries of the crystallographic information files (cif) of the ICSD.[69] The amplitude reduction factor S_0^2

was determined from reference compounds and found to be 1.16 for Mo and 1.00 for Ni. For Ni-MoS_2/γ-Al_2O_3 and Ni-MoS_2/unsupported, the EXAFS at the Mo K-edge and at the Ni K-edge were simultaneously fitted to identify Mo-Ni and Ni-Mo contributions, respectively. The Debye-Waller factor σ^2 and the distance R between Mo-Ni and Ni-Mo were constrained to be equal and the coordination numbers N for Mo-Ni and Ni-Mo were constrained by the molar ratio of Ni and Mo in the catalysts ($N_{Mo\text{-}Ni} = n(Ni)/n(Mo) \cdot N_{Ni\text{-}Mo}$).

Temperature-programmed sulfidation (TPS). Temperature-programmed sulfidation (TPS) was carried out to study the influence of nickel on the sulfidation mechanism. The oxide precursor (0.1 g) was placed in a flow reactor equipped with a ceramic oven. The activation was performed in 10% H_2S in H_2 with a heating rate of 5 °C·min^{-1}. At 400 °C the temperature was held isothermally for 1 hour. Evolved gasses were detected by a quadrupole mass spectrometer (Balzers QME 200).

Catalytic performance

The HDN of quinoline (Q) was studied in the presence of dibenzothiophene (DBT) in a continuous flow trickle bed reactor system at constant feed composition and pressure of 5.0 MPa. The reactor was loaded with 0.05 g of oxide catalyst precursor for each run. Gas and liquid feeds were introduced into the reactor via high pressure mass flow meters (Bronkhorst) and a HPLC pump (Shimadzu LC-20AD), respectively. After separation of the liquid and gas effluent phase, the liquid was collected via 16 port sampling valve every 1.5 h. The liquid samples were analyzed by off line gas chromatography using a HP 6890 GC equipped with a flame ionization detector (FID) and 60 m DB-17 capillary column.

Prior to the kinetic experiments, the catalysts were activated in situ in 10% H_2S in H_2 flow at 400 °C and 1.8 MPa for 12 hours. HDN was investigated as space time dependent experiments at 370 °C. The space time was defined as $m_{cat} \cdot F_N^{-1}$, where m_{cat} is the amount of the oxide catalyst precursor and F_N is the molar flow of Q [h $g_{catalyst}$ mol_Q^{-1}]. Additionally, HDN was carried out as temperature dependent experiments (290-400 °C) at a constant space time of 350 h·$g_{cat} \cdot mol^{-1}$. Steady state was reached after 16 h time on stream. All reactions were performed in excess of hydrogen, with a constant ratio of hydrogen to hydrocarbon of 330 $Ndm^3 \cdot dm^{-3}$. The initial concentration of Q (Aldrich, 98%) was set to 1000 ppm wt N (equivalent to 14.6 kPa of Q) in a mixture of 5% hexadecane (Merck, 99%) in tetradecane (Alfa Aesar, 99+%) as a solvent. DBT (Aldrich, 99%) was added at the concentration of 500 ppm wt S (equivalent to 3.2 KPa of DBT). The conversion towards nitrogen free products was referred as the HDN conversion. For a more detailed description see Ref. [3].

Chapter 4

Physicochemical characterization of unsupported Ni-Mo-W oxides

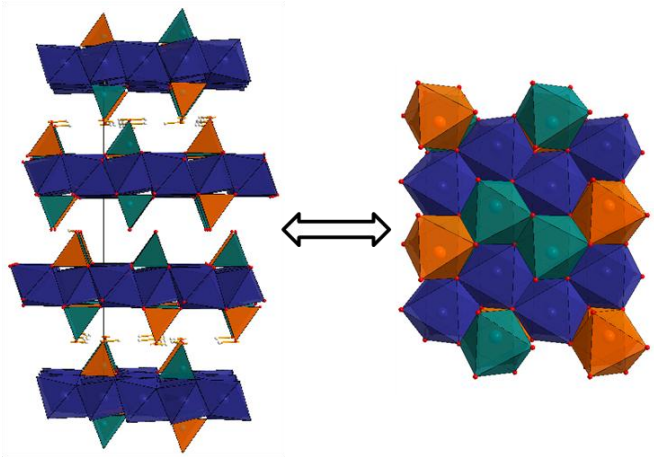

This chapter deals with the preparation and characterization of four unsupported mixed metallic oxides. Two bimetallic, $NiMo_{Ox}$ and NiW_{Ox}, and two trimetallic oxides, $NiWMo1_{Ox}$ and $NiMoW2_{Ox}$, are investigated by using N_2-physisorption, X-ray diffraction, scanning electron microscopy and Raman, UV-vis and X-ray absorption spectroscopy. Furthermore, various Ni, Mo and W containing oxide reference materials with known structures are characterized for comparison with the investigated oxides. The target of this study is the determination of the coordination geometry of Ni, Mo and W in the four oxide materials as well as of possible intermetallic interactions, which will be used to identify the contained crystallographic phases. The described unsupported multimetallic oxides will be applied in the following chapters as oxide precursors for catalyst sulfides.

1. Preparation and Characterization Techniques

Synthesis of the Mixed Oxides

The oxides were synthesized by a pH controlled co-precipitation method in aqueous solution using ammonium heptamolybdate $(NH_4)_6Mo_7O_{24} \cdot 4H_2O$ (AHM; Sigma-Aldrich), ammonium metatungstate $(NH_4)_6(W_{12}O_{40})H_2 \cdot x\,H_2O$ (AMT; Fluka), nickel nitrate $Ni(NO_3)_2 \cdot 6H_2O$ (Sigma-Aldrich), aqueous ammonia (28-30 % NH_3 in H_2O; Sigma-Aldrich) and maleic acid $(CH)_2$-$(COOH)_2$ (Sigma-Aldrich).[135] The obtained precipitates were vacuum dried overnight at room temperature and subsequently dried at 120 °C for 12 hours in flowing synthetic air.

The NiMo bimetallic oxide. In a three neck flask with a reflux condenser, aqueous ammonia was added to a colorless AHM solution (0.032 mol/l) until its pH value changed from 5.5 to 9.0. Afterwards the solution was heated to 90 °C under continuous stirring. Subsequently, during stirring a warm aqueous solution of nickel nitrate (0.250 mol/l; pH = 6.0) was dropwise added to the warm AHM solution and the pH value was further controlled by aqueous ammonia. The formed yellow-greenish precipitate (pH = 7.5) was stirred at 90 °C for 30 min, collected by filtration and then dispersed into maleic acid solution (0.050 mol/l, pH = 1.5). The resulting slurry (pH = 6.5) was heated to 70 °C and filtrated. Subsequently, the drying procedure was performed. The oxide is denoted as $NiMo_{OX}$.

The NiW bimetallic oxide. In a three neck flask with a reflux condenser, an AMT solution was prepared (0.023 mol/l), aqueous ammonia was added until a pH value of 9.0 and afterwards the mixtures was heated to 90 °C under continuous stirring. Subsequently, a warm aqueous solution of nickel nitrate (0.250 mol/l; pH = 6.0) was dropwise added to the AMT solution. The formed green precipitate (pH = 7.0) was further stirred at 90 °C, collected by filtration and then dispersed into maleic acid solution (0.050 mol/l, pH = 1.5). The resulting slurry (pH = 7.0) was heated to 70 °C and filtrated. After drying, the oxide is denoted as NiW_{Ox}.

The NiWMo1 trimetallic oxide. In a three neck flask with a reflux condenser, AHM and AMT were dissolved in bi-distilled water at room temperature (0.018 mol/l AHM and 0.010 mol/l AMT). Afterwards, aqueous ammonia was added to the colorless mixed metal solution until a pH value of 9.5 was reached and the mixture and was heated to 90 °C under continuous stirring. Subsequently, a warm aqueous solution of nickel nitrate (0.250 mol/l; pH = 6.0) was slowly added to the mixed metal solution. The formed light yellow-greenish precipitate (pH = 7.0) was stirred at 90 °C for 30 min, collected by filtration and then

dispersed into maleic acid solution (0.050 mol/l, pH = 1.5). The resulting slurry (pH = 6.0) was heated to 70 °C and filtrated and dried. The oxide is denoted as $NiWMo1_{OX}$.

The NiMoW2 trimetallic oxide. In a three neck flask with a reflux condenser, 0.018 mol/l AHM and 0.005 mol/l AMT are dissolved in water, aqueous ammonia was added until a pH value of 9.0 and the mixture was heated to 90 °C under continuous stirring prior to the addition of the warm nickel solution. The subsequent procedure is equal to the synthesis of the NiWMo1 oxide. The resulting oxide is denoted as $NiMoW2_{Ox}$.

Experimental Details of the Material Characterization

Elemental analysis. Elemental analysis was carried out at the Microanalytical Laboratory of the TU München. The content of the metals Mo, Ni and W were photometrically determined after different alkaline and acid pulping procedures. The elements C, H, N and S were analyzed by the vario EL CHN analyzer (ELEMENTAR), which is based on the combustion of the samples at temperatures of about 800 °C. The oxygen concentration was indirect estimated, as difference value after the measurement of all other possibly contained elements.

Nitrogen-Physisorption. The N_2 adsorption-desorption isotherms and the subsequent BET surface areas were determined with an automated PMI Sorptomatic 1990 Series instrument (Thermo Finnigan). Prior to the adsorption, the oxides were evacuated at 120 °C for 4 hours. After pre-treating the system was cooled down to -196 °C and liquid nitrogen was added to the sample until the adsorption equilibrium, i.e., until the saturation pressure of nitrogen p_0 was reached. The adsorption analysis was performed in the range of p/p_0 = 0-1.0. Additionally, the nitrogen desorption was recorded for the determination of the pore size distributions. For the final calculations, the weight after evacuation was used.

Powder X-Ray Diffraction (XRD). The crystal structures of the powdered samples were determined by X-ray diffraction using the X'Pert Pro PW 3040/60 (PANalytical). The Bragg-Brentano diffractometer was equipped with a copper X-ray tube (Cu-$K_{\alpha 1}$ radiation 0.154 nm), nickel K_β-filter and a solid state detector (X'Celerator). The measurements were carried out with a $10 \cdot 10^{-9}$ m slit mask in a range from $2\theta = 5°$ to $2\theta = 70°$ at 45 kV and 40 mA. All samples were prepared on a Si(111) sample holder and placed on a spinner configuration. The oxides were measured for 1 h with a step size of 0.017 ° and scan time of 115 s per step, whereas selected reference materials were measured for 5 min with a step size of 0.017 ° and 10 s per step. The crystallographic phases were identified by using the Inorganic Crystal Structure Database (ICSD).[69]

UV-vis Spectroscopy (DR UV-vis). The diffuse reflectance technique was applied to collect ultraviolet-visible-near infrared spectra using an Avantes AvaSpec-2048 fiber optic spectrometer equipped with a CCD detector array. The combined deuterium and halogen light source, Ava Light-DH-S-BAL, was used in combination with the optical fiber probe FCR-7UV400-2-SR-HT. Spectra of oxides and reference materials were recorded under ambient conditions. The sample powders were placed in a Teflon sample holder providing 1 mm sample thickness. The UV-vis spectra were acquired as absorbance A, function of the wavelength and calculated at pixel n by AvaSoft-Basic 7 with the following equation:

$$A_n = -\log\left(\frac{\text{sample}_n - \text{dark reference}_n}{\text{whitereference}_n - \text{dark reference}_n}\right)$$

where the white reference is obtained by the empty Teflon sample holder and the dark reference by closed beam shutter.

After normalization of the spectra in energy space, they were de-convoluted using a Levenberg-Marquardt algorithm implemented in the Fityk 9.7 software. The absorption bands were fitted by Gauss functions and an error function was used to describe the absorption edge.[70] During the fitting procedure the FWHM of the Gauss functions were kept constants and reasonable limits for the peak positions were set. Each spectrum was de-convoluted with a minimum amount of parameter. Moreover, the data were plotted as $(A \cdot h\nu)^2$ versus $h\nu$ (with h Planck constant and ν frequency) in order to estimate the band gap (from the intersection between the base line and least square linear fit through the low energy edge).[202]

Raman Spectroscopy. Raman spectra were recorded with a Renishaw Raman Microscope (Type 1000, dispersive spectrometer) equipped with CCD detector and a Leica microscope DM LM. The used excitation wavelength of 514 nm was provided by a multi-line argon-ion gas laser (Stellar-Pro Select 150 of MODU-Laser) operating at 20 mW power. Prior to the measurements, the calibration was done with a Si(111) crystal. The wavenumber accuracy was within 1 cm^{-1}. All samples, investigated oxides and reference materials, were analyzed under ambient conditions in the form of self-supported wafers in a range of 100 to 4000 cm^{-1} using a laser slit of 5 µm and an exposure time of maximum 100 s. To ensure representative spectra of every sample, different positions on the wafers were focused and Raman scattering was recorded.

Electron microscopy. The morphology and particle size of the different samples were visualized by different electron microscopic methods. The oxides were analyzed in the scanning mode (SEM) with the REM 5900 LV microscope (JEOL). After evacuation the samples were placed on a graphite foil and subsequently sputtered with gold. SEM micrographs were taken with an accelerating voltage of 25 kV with a maximum magnification

of $4.0 \cdot 10^4$ using secondary and backscatter electrons as well as energy-dispersive X-ray spectroscopy (EDX) mapping.

X-ray absorption spectroscopy (XAS). The structural properties of the oxides were studied by X-ray absorption spectroscopy at the X1 beamline at Hasylab, DESY, Hamburg, Germany. Spectra were recorded in transmission mode at the Mo K-edge (20000 eV), W L_{III}-edge (10207 eV) using Si (311) crystals and at the Ni K-edge (8333 eV) using Si (111) crystals in the monochromator, respectively. The contributions of the higher harmonics were minimized by detuning the second crystal of the monochromator to 60% of the maximum intensity. Energy calibration was performed with a molybdenum, tungsten and nickel metal foil, respectively, measured simultaneously with the samples. The samples were prepared as self-supporting wafers and placed into a stainless steel in situ flow cell. The measured oxides and reference compounds were diluted with cellulose to achieve a total absorption of $\mu x = 1.5$. The spectra used for EXAFS analysis were collected in He flow at liquid N_2 temperature (LNT) to minimize thermal vibrations. At least two spectra of each sample were averaged to enhance the signal to noise ratio.

All spectra were analyzed with the Demeter- package (ATHENA and ARTEMIS, version 0.9.20) using FEFF6 and IFEFFIT.[199-200, 203] The scattering contributions in the pre- and post-edge of the background were removed from the X-ray absorption using the auto-background function and afterwards all spectra were normalized to the average post-edge height of one. Subsequently, the oscillations were weighted with k^3 and Fourier-transformed within the limit of $k = 2.5 - 14.0$ Å^{-1}.

2. Results and Discussion

Characterization of the unsupported multimetallic oxides

Two bimetallic ($NiMo_{Ox}$, NiW_{Ox}) and two trimetallic oxides ($NiWMo1_{Ox}$, $NiMoW2_{Ox}$) were obtained with the elemental compositions and surface areas shown in Table 1. The final metal molar ratios in the oxides, especially the Mo to W ratio, could be fairly controlled with the used co-precipitation method.

Table 1. Elemental composition and specific surface area of the oxides

Catalyst	Composition [mmol/g] [a]							Metal molar ratio	Specific surface area [m^2/g^{-1}]
	Ni	Mo	W	C	H	N	O	Ni : Mo : W	
$NiMo_{Ox}$	4.4	3.6	-	0.2	16.7	3.0	21.1	1.2 : 1.0 : 0.0	30
$NiMoW2_{Ox}$	4.4	1.6	1.4	0.4	10.8	0.3	19.3	3.1 : 1.1 : 1.0	55
$NiWMo1_{Ox}$	3.6	1.0	2.1	0.5	12.9	0.9	17.6	3.6 : 1.0 : 2.0	29
NiW_{Ox}	2.2	-	3.0	0.2	9.5	0.6	19.4	1.0 : 0.0 : 1.4	39

[a] The content of oxygen was determined as difference after the measurement of the weight percent of Ni, Mo, W, C, H and N.

The C-H-N analysis combined with the indirect estimation of oxygen indicates the highest molar fraction in all oxide samples for oxygen followed by hydrogen, which point to the presence of oxides, hydroxides, hydroxo or aqua complexes in all samples. Low concentrations of N and C suggest that ammonium ions and traces of maleic acid are still present in the oxides. The highest N content appeared in $NiMo_{Ox}$ and the lowest in $NiMoW2_{Ox}$, whereas the highest C concentrations were found in the trimetallic materials.

Figure 1 shows the N_2 isotherms of the four oxides. All of them are type II isotherms (IUPAC) with small hysteresis (especially for NiW_{Ox}). Such isotherms are representative of solids with low porosity caused by few mesopores and macropores, likely those formed by the voids between particles of the material.[204] The specific surface areas determined by the BET method of all four materials are in the same range (Table 1). The trimetallic $NiMoW2_{Ox}$ oxide appears with the highest surface area of 55 m^2/g, whereas the second trimetallic material $NiWMo1_{Ox}$ possesses the lowest surface area with 29 m^2/g among the four oxides.

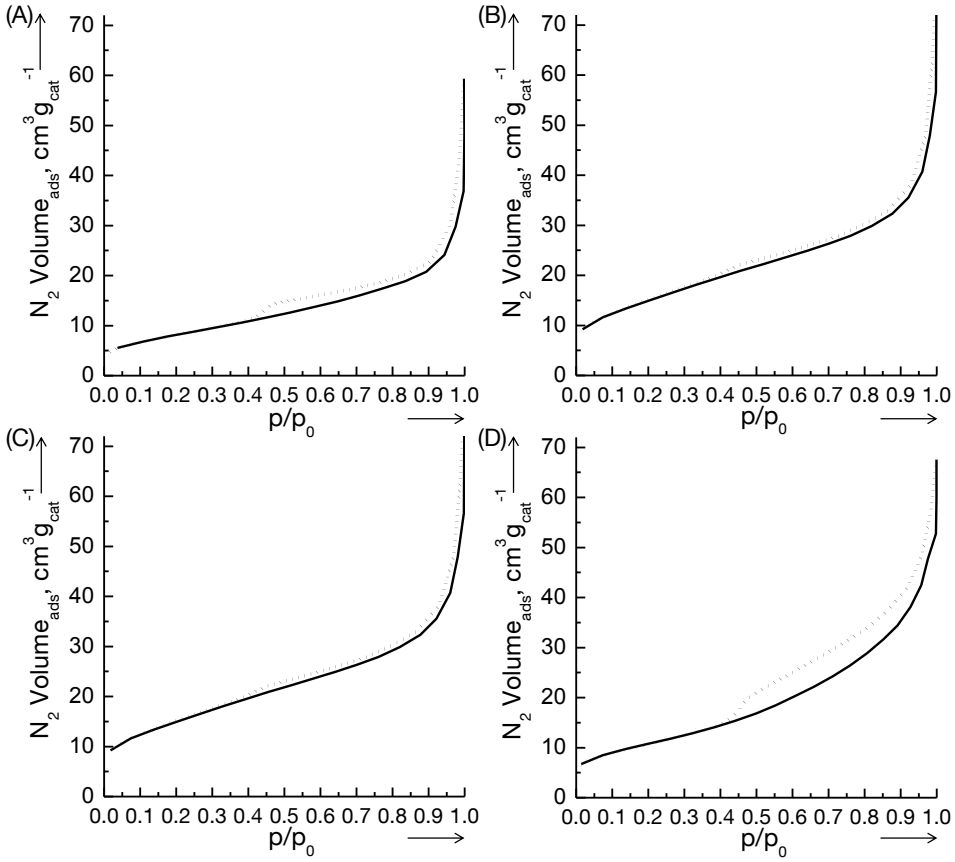

Figure 1. N_2 physisorption isotherms of the unsupported oxide samples $NiMo_{Ox}$ (A), $NiMoW2_{Ox}$ (B), $NiWMo1_{Ox}$ (C) and NiW_{Ox} (D). Adsorption (solid line) and desorption (dotted line) isotherms are presented.

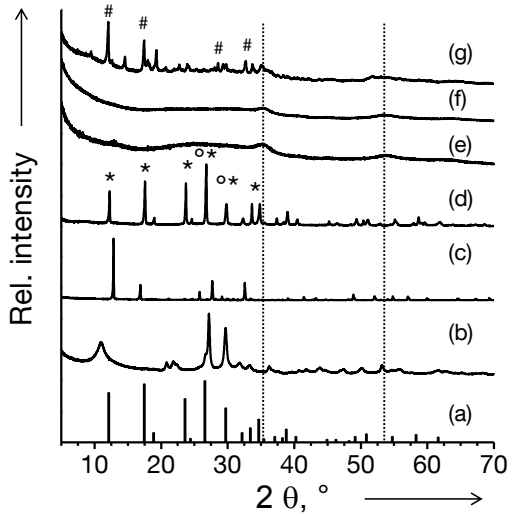

Figure 2. XRD pattern (Cu-K_α) of reference materials (a) $(NH_4)HNi_2(OH)_2(MoO_4)_2$ (ICSD #165342 [69]; indicated by *), (b) $NiMoO_4$ (indicated by °) and (c) $NiWO_4$ (indicated by #), and of the unsupported oxides $NiMo_{Ox}$ (d), $NiMoW2_{Ox}$ (e), $NiWMo1_{Ox}$ (f) and NiW_{Ox} (g). The positions of the two broad reflections of the trimetallic oxides are indicated.

The XRD patterns of the oxide samples and reference materials are shown in Figure 2 and 3. The two bimetallic materials exhibit intense reflections of crystalline phases. Direct comparisons with the patterns of the references allow straightforward identification of the crystal phases in these materials. $NiMo_{Ox}$ is composed by $(NH_4)HNi_2(OH)_2(MoO_4)_2$ (ICSD #165342 [69]) with a layered structure[182] and traces of $NiMoO_4$. The commercial $NiMoO_4$ is a mixture of the α- and β-phase (HT), with a higher concentration of the latter according to its XRD pattern.[205] In NiW_{Ox}, $NiWO_4$ is the main phase, whereas the less intense reflections could be originated by traces of $Ni(OH)_2$ (ICSD #024015)[69] and nickel hydroxide hydrate[63] (19.3, 33.7, 35.1 °2θ) or WO_3 (22.8, 23.9, 28.6 and 33.7 °2 θ). A few reflections remain unidentified (like that at 14.6 °2 θ and a broad one at 52.1 °2 θ) and amorphous phases are present as indicated by the background. In strong contrast to the bimetallic oxide, the trimetallic materials were completely amorphous. Thus, the addition of the third metal to the bimetallic oxide results in a loss of crystallinity. The XRD patterns of both trimetallic materials exhibit only broad features at 35.1 and 53.6 °2θ. The broad reflection at 35.1, also found in NiW_{Ox}, is assigned to $Ni(OH)_2 \cdot H_2O$. Figure 3 shows that the signal at 53.6 °2θ could be neither explained by a number of different references nor by the used metal salts during synthesis. In general, the observed broad reflections and the X-ray amorphous patterns could be the result of small entities of different crystalline phases like $NiWO_4$, $Ni(OH)_2$ and $(NH_4)HNi_2(OH)_2(MoO_4)_2$, whose reflections overlap.

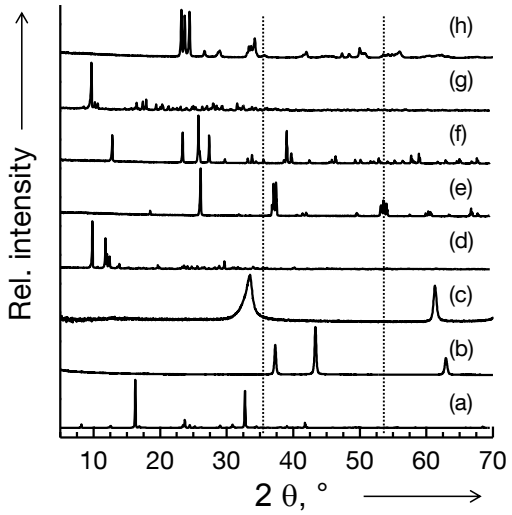

Figure 3. XRD pattern (Cu-K_α) of reference materials (a) $Ni(NO_3)_2 \cdot 6H_2O$, (b) NiO, (c) $Ni(OH)_2$, (d) $(NH_4)_6Mo_7O_{24} \cdot 4H_2O$, (e) MoO_2, (f) MoO_3, (g) $(NH_4)_6(W_{12}O_{40})H_2$ and (h) WO_3. The positions of the two broad reflections of the trimetallic oxide samples are indicated.

The different morphologies found for the oxides are presented in Figure 4. For the bimetallic samples, agglomerated irregular particles with a broad particle size distribution were observed by SEM. $NiMo_{Ox}$ contained particles with diameters of 140 to 1400 mm and for NiW_{Ox} particle diameters up to 3000 mm were found. The trimetallic materials appeared

with uniform, hexagonal- to circular-shaped stacked plates with a narrow particle size distribution. The particle diameters of the particles in $NiWMo1_{Ox}$ were between 140 to 360 mm, and for $NiMoW2_{Ox}$, the particle size range was 200-330 nm. A similar morphology was reported for a $Mo_xW_{1-x}O_3$ solid solution, but with a broader particle size distribution.[72] NiW_{Ox} was composed by the largest particles, followed by $NiMo_{Ox}$, and finally $NiWMo1_{Ox}$, and $NiMoW2_{Ox}$ with similar particle sizes. Additionally, EDX mapping and backscatter electron images indicated homogeneous metal distribution in all four oxides, monometalic Ni, Mo or W phases were not found.

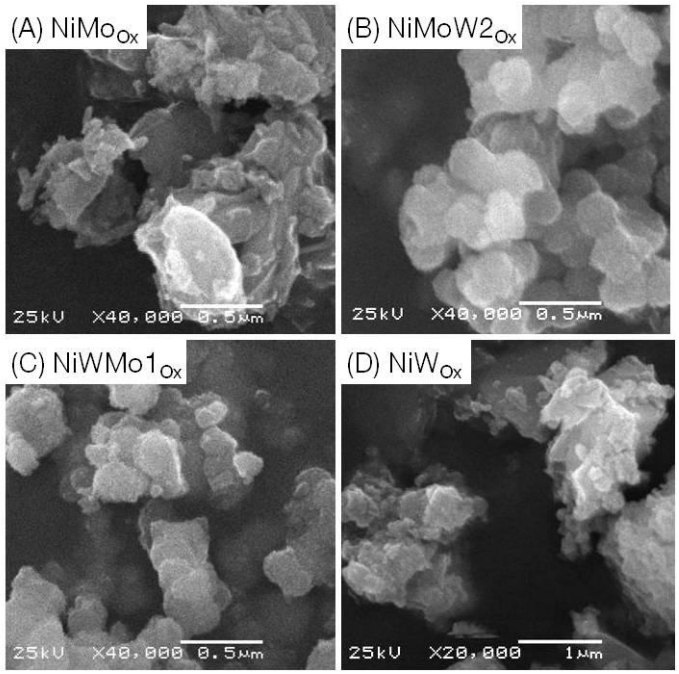

Figure 4. Representative scanning electron micrographs of the unsupported oxides $NiMo_{Ox}$ (A), $NiMoW2_{Ox}$ (B), $NiWMo1_{Ox}$ (C) and NiW_{Ox} (D). The images were taken at 25 kV and $4{\cdot}10^4$ magnification, only for (D) $2{\cdot}10^4$ magnification was used.

Raman spectra of the four oxides as well as of different reference materials are presented in Figures 5 and 6. In Figure 5 and 6(A) the Raman shift region of metal-oxygen lattice vibrations are shown, whereas Figure 6(B) shows the region of non-metal vibrations. The measured reference spectra were in very good agreement with literature, therefore they were used to assign the observed scattering bands in the oxide samples. [78-79, 86, 134, 173, 206-208] As presented in Table 2, there are four main different metal-oxygen (M-O) vibration modes (with M for Mo, W or Ni); stretching vibrations of terminal M-O, and bridging M-O-M bonds, and the corresponding deformation modes, where the terminal ones could be either M-O single bonds or M=O double bonds.

A sharp Mo-O deformation band at 320 cm^{-1} and a shoulder at 370 cm^{-1} were found for $NiMo_{Ox}$, and the corresponding stretching bands were at 767, 831, 875 and 908 cm^{-1} (Figure 5). Stretching modes of bridging Mo-O-Mo bonds were not observed. Additionally, a weak

and broad band was present at 462 cm^{-1}, which could be caused by Ni-O bonds.[207, 209] The majority of the vibration bands were well distinguishable from each other, which pointed to a well crystallized oxide phase as indicated by XRD. The band positions in the spectra of $NiMo_{Ox}$ and intensity ratios were similar to the ones for K_2MoO_4. However, they were shifted by around 20 cm^{-1} to higher wavenumbers and were broader compared to the spectra of K_2MoO_4. Additionally, the stretching vibrations at lower wavenumbers were similar in $NiMoO_4$ and $NiMo_{Ox}$ (Table 2 and Figure 6(A)).

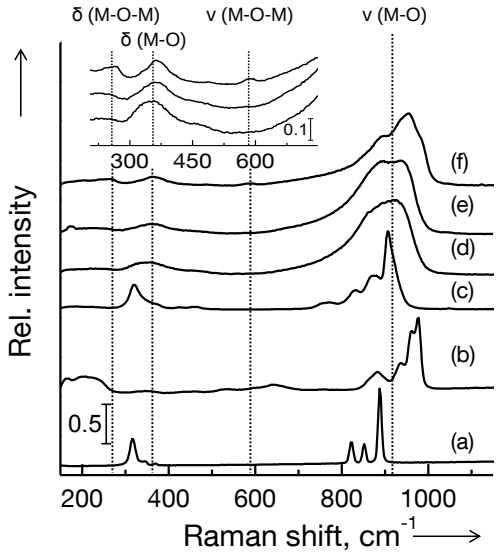

Figure 5. Raman spectra (λ_{ex} = 514 nm) of reference materials K_2MoO_4 (a), $(NH_4)_6(W_{12}O_{40})H \cdot xH_2O$ (b), and of the unsupported oxides $NiMo_{Ox}$ (c), $NiMoW2_{Ox}$ (d), $NiWMo1_{Ox}$ (e) and NiW_{Ox} (f) (the inset shows (d), (e) and (f) enlarged). The band positions of metal (M) – oxygen (O) vibrations are indicated by the dotted vertical lines and assigned to the corresponding deformation (δ) and stretching (ν) modes.

In K_2MoO_4, Mo is tetrahedrally coordinated and in β-$NiMoO_4$ a distorted tetrahedral Mo-coordination is present.[81] Therefore, the bands in $NiMo_{Ox}$ were assigned to distorted $[MoO_4]$-tetrahedra, which were isolated due to the absence of Mo-O-Mo bridging bond vibrations.[86] Furthermore, similar band positions like in $NiMo_{Ox}$ were also observed for ammonium nickel molybdate $(NH_4)HNi_2(OH)_2(MoO_4)_2$ (321 and 904 cm^{-1})[182], which was identified by XRD (Figure 2). This ammonium nickel molybdate is composed by isolated $[MoO_4]$-tetrahedra and $[NiO_6]$-octahedra like β-$NiMoO_4$.[205] The Raman band broadening was similar in the spectra of $NiMoO_4$ and $NiMo_{Ox}$ (Figure 6(A)). Spectroscopic bands of lattice vibrations are broad (compared to liquids or gases) because of their indiscrete vibrational energy levels caused by the overlap of discrete energy levels of single molecules within the solid to an electronic band. Distortion of the lattice, disorder or mixture of differently coordinated species broadens vibrational bands even more (due to broadening of the electronic band).[78, 177] A strong disorder for $NiMo_{Ox}$ is excluded based on the high crystallinity and the well-defined long range order evident by XRD results. Therefore, it is

proposed, that the broader bands in the spectra of $NiMo_{Ox}$ (and $NiMoO_4$) are the result of distortion of the excited Mo-O bonds due to an interaction between the Ni and Mo-polyhedron. Moreover, it is assumed that the Ni species in $NiMo_{Ox}$ is associated to OH-groups, since the spectra of $NiMoO_4$ with pure $[NiO_6]$-octahedra does not contain bands between 400 and 500 cm^{-1} in contrast to $Ni(OH)_2$ (Figure 6(A)).

Table 2. The measured Raman scattering bands of references and the oxide samples and their assignments [a] (λ_{ex} = 514 nm).

Material	δ (M-O-M)	δ (M-O)	ν (M-O-M)	ν (M-O)
$NiMo_{Ox}$		320, 370		767, 831, 875, 908 (462)
$NiMoW2_{Ox}$		352		(879), 923 (471)
$NiWMo1_{Ox}$		363		894, 936
NiW_{Ox}	264	363	(584)	894, 952
K_2MoO_4		318, 346, (370)		822, 852, 888
AMT	221	346	642, (529)	882, 935, 961, 976
$NiMoO_4$		357		(782), 834, 860, 949
AHM	221 (246)	364 (334)	861 (546, 629)	883, 909, 934

[a] The bands are assigned to the possible deformation (δ) and stretching (ν) modes of metal (M) - oxygen (O) bonds, where M stays for Mo and/or W (or Ni) according to Refs. [78-79, 86, 134, 173, 206-208]. It is not differentiated between symmetric and asymmetric lattice vibrations. Weak or unresolved bands are given in parentheses. The abbreviations AMT stands for $(NH_4)_6(W_{12}O_{40})H_2 \cdot xH_2O$ and AHM for $(NH_4)_6Mo_7O_{24} \cdot 4H_2O$.

The other bimetallic oxide, NiW_{Ox}, has broader bands than $NiMo_{Ox}$ at higher wavenumbers. The W-O bond is stronger than Mo-O (7.0 eV and 5.8 eV, respectively),[210] which is the reason for the higher wavenumbers of W-related bands since the vibrational energy, i.e., Raman shift, is direct proportional to the bond strength (and inversely proportional to the reduced mass). The line width of the bands reflects the disorder and the presence of different W species indicated by XRD and SEM. Interactions with a Ni-containing species feasible like in the case of $NiMo_{Ox}$. The most intense bands are observed at 894 cm^{-1} and 952 cm^{-1}. Additionally, weak deformation modes at 363 cm^{-1} and 264 cm^{-1} are found next to a very weak stretching mode of bridging bonds at around 584 cm^{-1}. These band positions indicate polytungstates and distorted $[WO_6]$-octahedra as in $(NH_4)_6(W_{12}O_{40})H_2 \cdot xH_2O$ (AMT). Raman shifts at 893 cm^{-1} and 950 cm^{-1} are also reported for the octahedral coordinated W^{6+} in $NiWO_4$ and hydrated WO_3, respectively.[86, 211]

The Raman spectra of the trimetallic oxides are similar to each other and exhibit very broad vibration bands with positions in between the ones of the bimetallic materials. The estimated wavenumbers of the bands of $NiMoW2_{Ox}$ are 352 cm^{-1}, 923 cm^{-1} and a shoulder at around 879 cm^{-1}. All bands are assigned to the vibration modes of terminal M-O bonds (with M either Mo or W; Table 2). A very weak and broad stretching band is identified at around 471 cm^{-1}, which is assigned to Ni-O bonds.[207, 209] The bands of $NiWMo1_{Ox}$ are shifted to higher wavenumbers compared to $NiMoW2_{Ox}$, i.e., 363 cm^{-1}, 894 cm^{-1}, and 936 cm^{-1}, the latter two having the same intensity. Moreover, the first stretching vibration of M-O of $NiWMo1_{Ox}$ has the same Raman shift than that of NiW_{Ox} (894 cm^{-1}) and also $NiMoW2_{Ox}$ and $NiMo_{Ox}$ exhibit comparable values for this mode (875 and 879 cm^{-1}). These observations point to the presence of Mo-O and W-O species similar to the ones in the bimetallic materials. The overlapping of this variety of Mo and W vibration modes and to the low crystallinity concluded from XRD cause the line broadening. In NiW_{Ox}, a distorted octahedral coordination for W, whereas in $NiMo_{Ox}$ a distorted tetrahedral coordination for Mo are observed, which raises the question as whether both species are separate or form solid solutions in the trimetallic oxides. The observed wavenumbers of the bands in the Raman spectra, in between the values for the bimetallic materials, as well as the strong overlapping of the bands, suggest an intense interaction between Mo and W. Similar trends were observed for a mixed $CdMo_xW_{1-x}O_4$ compound with varying x, where scheelite-type $CdMoO_4$ ($[MoO_4]$-tetrahedra) was mixed with wolframite-type $CdWO_4$ ($[WO_6]$-octahedra).[80] Bond length and bond angle change while Raman bands shift and split for their mixed compounds led to the conclusion of a solid solution. Thus, we propose that in the investigated trimetallic oxides highly distorted $[MoO_4]$-tetrahedra next to $[WO_6]$-octahedra are present in the same structure. Moreover, the coordination polyhedra in $NiWMo1_{Ox}$ seem to have a higher octahedral character (Raman spectrum similar to NiW_{Ox}). The connectivity of the polyhedra cannot satisfactorily be addressed due to the broad bands, although M-O-M bridging bands are absent (see inset in Figure 5).

The high wavenumber region of the oxides and references is investigated to identify possible non-metal vibrations in the samples (Figure 6(B)). Between 3100 cm^{-1} and 3600 cm^{-1} a broad OH-band in all four oxides is observed, which is typically assigned to surface adsorbed hydroxyl-groups.[207, 212] In $NiMo_{Ox}$, and $NiMoW2_{Ox}$, a shoulder at around 3590 cm^{-1} is identified as an associated hydroxyl-group (compare to the spectra of $Ni(OH)_2$).[207] The sharp band at around 3230 cm^{-1} is assigned to asymmetric N-H stretching vibrations of an ammonium ion,[182] whereas the band at around 3580 cm^{-1} could be a O-H or a N-H vibration.[212] The stretching mode of the ammonium ion is most pronounced in $NiMo_{Ox}$ and decreases with increasing W content, whereas in NiW_{Ox} this band is not identified. The weak doublet at around 2650 cm^{-1} in $NiMo_{Ox}$ and $NiMoW2_{Ox}$ could indicate an O-H vibration of a

carboxylic acid. Moreover, bands between 1350 cm^{-1} and 1750 cm^{-1} are observed, typical for deformation modes of N-H[182] and O-H but also for stretching vibrations of C=O, which could indicate traces of maleic acid.[213]

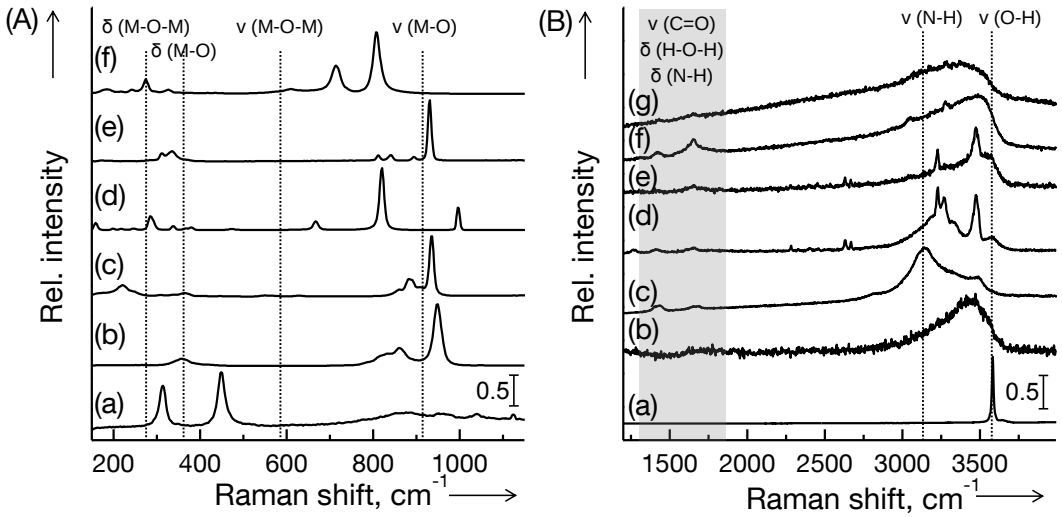

Figure 6. Raman spectra (λ_{ex} = 514 nm) of two different vibration regions. In (A) additional reference materials are presented and typical band positions of possible metal (M) – oxygen (O) vibrations are indicated: $NiOH_2$ (a), $NiMoO_4$ (b), $(NH_4)_6(Mo_7O_{24}) \cdot 4H_2O$ (c), MoO_3 (d), Na_2WO_4 (e) and WO_3 (f). In (B) the higher wavenumber region of $NiOH_2$ (a), $NiMoO_4$ (b), $(NH_4)_6(Mo_7O_{24}) \cdot 4H_2O$ (c), and of the unsupported oxides $NiMo_{Ox}$ (d), $NiMoW2_{Ox}$ (e), $NiWMo1_{Ox}$ (f) and NiW_{Ox} (g) is presented and non-metal vibrations are indicated. The bands are assigned to possible deformation (δ) and stretching (ν) modes.

The diffuse reflectance (DR) UV-vis absorption spectra of the four oxide samples as well as of $NiMoO_4$ and $Ni(OH)_2$ are presented in energy space in Figure 7. The spectra of the oxides are similar to the spectra of the reference compounds.

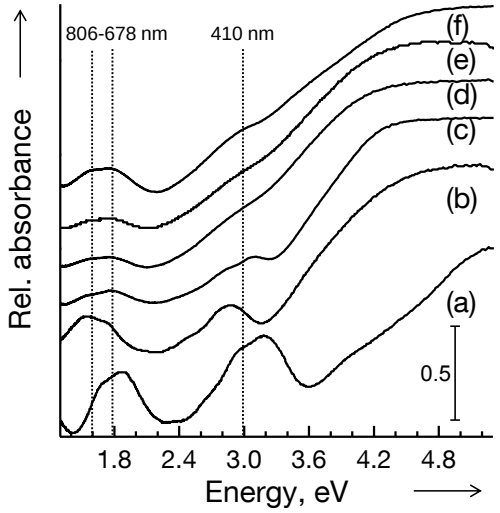

Figure 7. Diffuse reflectance UV-vis spectra of reference materials $NiOH_2$ (a), $NiMoO_4$ (b), and of the unsupported oxide samples $NiMo_{Ox}$ (c), $NiMoW2_{Ox}$ (d), $NiWMo1_{Ox}$ (e) and NiW_{Ox} (f). The absorption bands of the oxides in the vis-region are indicated by the dotted lines.

The bands are analyzed by deconvolution.[70] The results are summarized in Table 3 and the fitted spectra are presented in Figure 8. The spectra of $NiMoO_4$ and $Ni(OH)_2$ are fitted for comparison (Figure 9). Absorption edge energies of the oxide samples and reference compounds estimated by a least square fit approach (Figure 10[202]) are as well contained in Table 3.

Table 3. Diffuse reflectance UV-Vis spectroscopy results of the oxide samples and of reference materials.

Material	Absorption bands by deconvolution [eV] [a]	Edge energy [eV] [b]
$NiMo_{Ox}$	1.54, 1.80, 3.05, 3.08	3.53
$NiMoW2_{Ox}$	1.60, 1.81, 3.11	3.26
$NiWMo1_{Ox}$	1.61, 1.83, 2.87	3.31
NiW_{Ox}	1.60, 1.83, 2.96	3.43
$NiMoO_4$	1.52, 1.77, 2.55, 2.74, 2.90, 3.59 (5.01)	3.50
$Ni(OH)_2$	1.65, 1.87, 2.46, 2.66, 2.91, 3.21 (4.30)	4.24
WO_3	not determined	2.77 (5.3)
MoO_3	not determined	2.94 (4.8)
AMT	not determined	3.29 (4.1)
AHM	not determined	3.39 (3.1)
K_2MoO_4	not determined	4.36 (0.0)
Na_2WO_4	not determined	4.98 (0.0)

[a] Deconvolution was performed with a Levenberg-Marquardt fit procedure using Gauss functions for the absorption bands and an error function for the absorption edge.[70] [b] Edge energy is determined by a least square fit (Figure 10) and is used to calculate the number of nearest neighbors for Mo with $N_{Mo} = 16 - 3.8 \cdot E_g$ or for W with $N_W = 11.89\text{-}2.37 * E_g$, given in parentheses.[79, 202] The abbreviations AMT stands for $(NH_4)_6(W_{12}O_{40})H_2 \cdot xH_2O$ and AHM for $(NH_4)_6(Mo_7O_{24}) \cdot 4H_2O$.

In the DR-UV-vis spectra of $NiMo_{Ox}$, four absorption bands are identified in the visible region with peak maxima at 1.54, 1.80, 3.05 and 3.08 eV (806, 689, 407 and 403 nm, respectively). The absorption edge in the UV region is at 3.53 eV (352 nm). The band at 3.08 eV is very weak, but was needed to fit the asymmetric broad band. During the deconvolution of the spectra of the other three oxides only three bands were needed to describe the experimental spectra. The first absorption band is constant at 1.6 eV (773 nm) for all W containing oxides. The second band shifts to slightly higher energies with increasing W content, i.e., from $NiMo_{Ox}$ (1.80 eV; 689 nm) over $NiMoW2_{Ox}$, and $NiWMo1_{Ox}$ to NiW_{Ox} (1.83 eV; 678 nm). The energy of the third absorption band increases in the following order: $NiMoW2_{Ox}$ (3.11 eV; 399 nm) > $NiMo_{Ox}$ > NiW_{Ox} > $NiWMo1_{Ox}$ (2.87 eV; 432 nm). And for the absorption edge

energy another trend is observed, which is: $NiMo_{Ox}$ > NiW_{Ox} > $NiWMo1_{Ox}$ > $NiMoW2_{Ox}$. The spectra and absorption band positions observed for $NiMo_{Ox}$ and $NiMoO_4$ are similar, whereas the bands of the other oxide samples are in between the ones of the both Ni containing references (except for the high energy band).

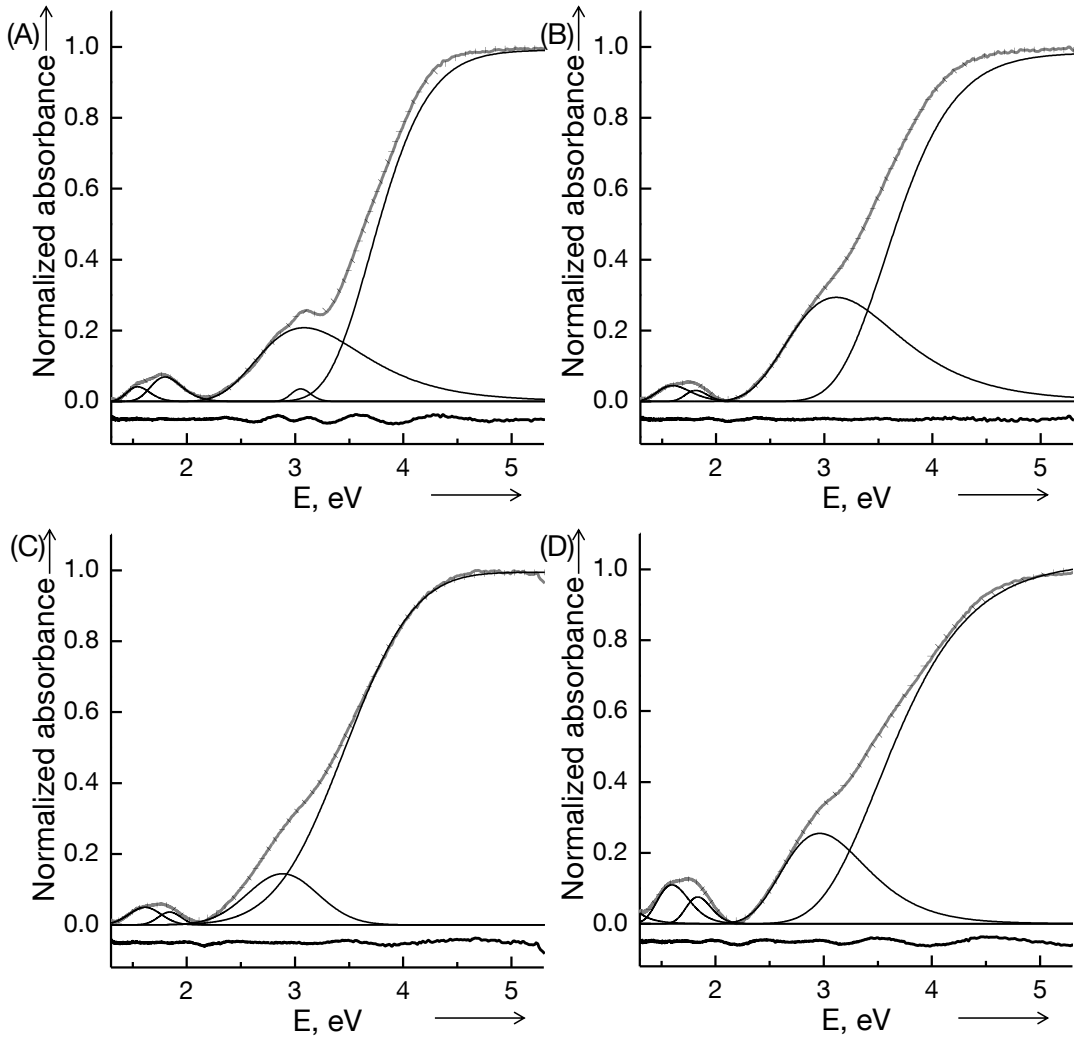

Figure 8. Diffuse reflectance UV-Vis spectra (solid grey line) and modeled spectra by deconvolution (dotted line) of the oxide samples $NiMo_{Ox}$ (A), $NiMoW2_{Ox}$ (B), $NiWMo1_{Ox}$ (C) and NiW_{Ox} (D). Additionally, the used functions (Gauss and error function) and in the bottom the residuals are presented.

For a d^0 electronic configuration like in the case of Mo^{6+} and W^{6+}, only ligand-metal charge transfer (LMCT) electronic transitions from O^{2-} to the Me^{6+} are expected. Typically, the band maxima of these LMCT transitions are between 3.1 and 6.2 eV, although W^{6+} compounds appear at slightly lower energies than Mo^{6+} compounds.[79, 214] Thus, the observed absorption bands between 1.5 and 3.1 eV are likely caused by d-d transitions within the contained Ni species. Indeed, for Ni^{2+} in an octahedral ligand field, present in $Ni(OH)_2$, NiO, $NiMoO_4$ and $NiWO_4$, absorption bands at around 1.7, 2.9 and 3.2 eV (730, 430 and 390 nm, respectively)

are assigned to electronic transitions from the ground state $^3A_{2g}$ to the $^3T_{1g}(P)$ and $^3T_{1g}(F)$ states. Tetrahedrally coordinated Ni^{2+} exhibits additional bands between 1.9 and 2.1 eV (600 nm to 650 nm) caused by $^3T_1(F)$ to $^3T_1(P)$ transitions.[215-217] Therefore, an octahedral coordination for Ni^{2+} is concluded for the oxides like in the references $Ni(OH)_2$ and $NiMoO_4$. Moreover, the comparison of the fitted bands of $Ni(OH)_2$ and $NiMoO_4$ revealed that the whole spectra of $NiMoO_4$ is shifted to lower energies. This energy shift can be explained by polarization of O^{2-} by the presence of Mo^{6+} and hence a modification of the ligand field and a distortion of the $[NiO_6]$-octahedra. Especially the band at 1.52 eV of $NiMoO_4$ is the result of these interactions. For $NiWO_4$, a band shift from 3.2 eV to 2.8 eV, compared to NiO, is reported as indicator for the presence of W^{6+}.[215-216] Thus, the band positions of all oxides indicate that the contained $[NiO_6]$-octahedra interact with Mo^{6+}, W^{6+} or both. The slightly higher energies for the oxide samples than for $NiMoO_4$ or $NiWO_4$ (1.6 and 2.9 eV instead of 1.5 and 2.8 eV, respectively) are attributed to small differences in the Ni^{2+} symmetry (distortion of the octahedron), Ni-O bond length or by the presence of hydroxide ions next to different Mo^{6+} and W^{6+} clusters.

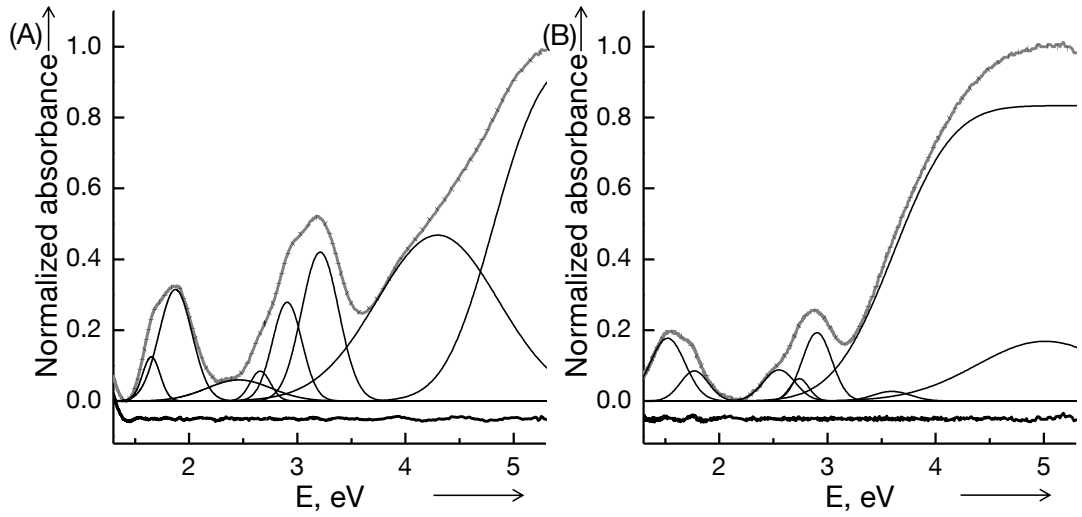

Figure 9. Diffuse reflectance UV-Vis spectra (solid grey line) and modeled spectra by deconvolution (dotted line) of the reference materials $NiOH_2$ (A) and $NiMoO_4$ (B). Additionally, the used functions (Gauss and error function) and in the bottom the residual are presented.

The analysis indicates that an intense interaction between all contained metal oxide species is present and that the involved coordination polyhedra are distorted in the oxides, which is reflected by the broad absorption bands. Especially, the high energy absorption bands are most probably caused by superposition of various electronic transitions of different metals. This is evident for $NiMoW2_{Ox}$ with a broad band at 3.1 eV (400 nm), which is typical for charge transfer transitions of all contained metals. Moreover, for a $Mo_xW_{1-x}O_3$ solid solution, a very broad absorption band with a peak maximum between the ones for the pure oxide compounds was reported and has been paralleled with a change of the electrical properties

and defect-site creation (symmetry distortion and restructuring).[218] On the other hand, band broadening accompanied by a red shift is reported for increasing cluster sizes, which is especially pronounced at the absorption edge and well studied for Mo and W oxides with different condensation degrees. It is known, that the spectrum is dominated by the lowest edge energy, i.e., by the largest oxide cluster independent on the possible presence of different cluster.[79, 177, 202, 214, 219] In turn, the edge energy can be used to calculate the size of the largest contained Mo or W cluster. For both metals comparable mathematical correlations have been proposed, which confirms that the edge energies of metal oxide clusters are primarily determined by the number of bridging M-O-M bonds (degree of condensation) and less by the excited metal itself.[79] The presence of other metals, however, creating bridging bonds like Ni or Mo and W in one cluster, may influence the edge energy position and therefore the estimated cluster size. The developed correlations by Weber for Mo^{6+}-clusters[202] and by Ross-Medgaarden and Wachs for W^{6+}-clusters[79] were used to make an estimate about the number of next nearest Mo and/or W neighbors (amount of bridging bonds), respectively, for the oxide samples. Additionally, the number of M-O-M bonds was as well calculated for reference materials containing only one transition metal (Table 3, values in parentheses).

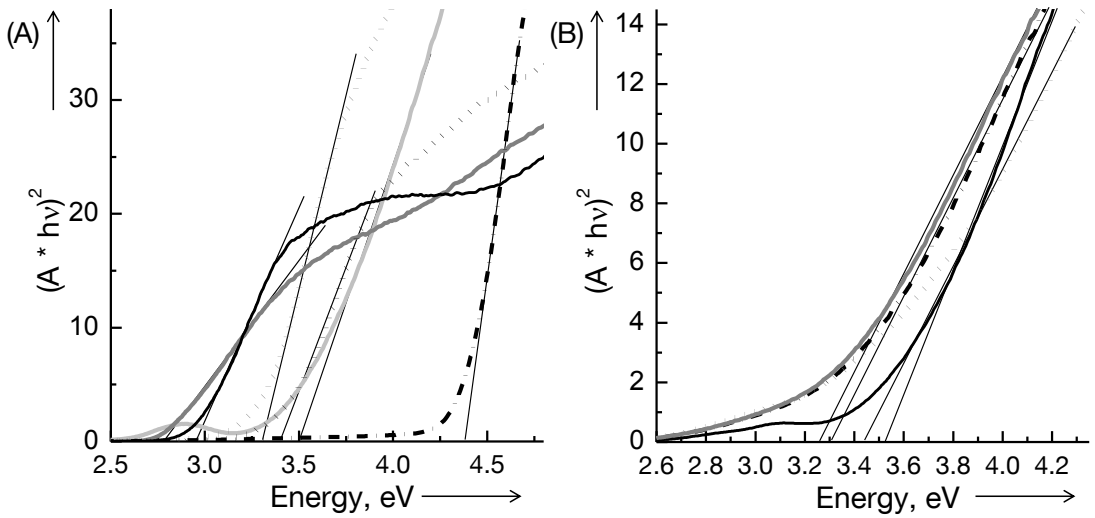

Figure 10. Determination of the absorption edge energy. In (A) the transformed diffuse reflectance UV-Vis spectra of the reference materials WO_3 (—), MoO_3 (—), $(NH_4)_6(W_{12}O_{40})H \cdot xH_2O$ (••••), $(NH_4)_6(Mo_7O_{24}) \cdot 4H_2O$ (••••), $NiMoO_4$ (—), and K_2MoO_4 (–•–•) and in (B) of the unsupported oxide samples $NiMo_{Ox}$ (—), $NiMoW2_{Ox}$ (—), $NiWMo1_{Ox}$ (–•–•) and NiW_{Ox} (••••) are shown. The absorption edges are obtained by the intercept point of least square fits with the energy axis indicated by the straight lines.

The estimated number of nearest Mo neighbors for $NiMoO_4$ and $NiMo_{Ox}$ are 2.7 and 2.6, which is typical for Mo dimers or polymeric chains. However, β-$NiMoO_4$, the predominant phase in the commercial $NiMoO_4$, crystallizes in the α-$MnMoO_4$ structure-type, which consists of "isolated" [MoO_4]-tetrahedra connected via three edges to [NiO_6]-octahedra.[82]

The same polyhedra connectivity is reported for $(NH_4)HNi_2(OH)_2(MoO_4)_2$, although bridging hydroxyl groups are involved.[182] It is therefore concluded that the edge energy reflects not only the size and polyhedra connectivity of mono-metallic cluster, but is also influenced by the connectivity of Mo^{6+} and W^{6+} polyhedra to the $[NiO_6]$-octahedra. For NiW_{Ox}, 3.8 nearest W neighbors are estimated by the edge energy (3.4 eV), which is typical for edge and corner connected $[WO_6]$-octahedra present in AMT (3.3 eV). Under considerations of the findings for $NiMoO_4$, it is assumed that interactions between Ni^{2+} and W^{6+} species in NiW_{Ox} increase the observed number of nearest W^{6+} neighbors. Therefore, a $NiWO_4$-like structure is proposed for NiW_{Ox} with edge sharing WO_6-chains and bridging bonds between $[NiO_6]$- and $[WO_6]$-octahedra[80, 83] resulting in smaller W^{6+}-clusters than those present in AMT (Keggin-structure type)[84]. For the trimetallic oxides, two values for the next nearest metal neighbors, for Mo and W, are calculated. The Mo-clusters have 3.4 ($NiWMo1_{Ox}$) and 3.6 ($NiMoW2_{Ox}$) nearest neighbors, i.e., much larger than the ones estimated for $NiMo_{Ox}$ and $NiMoO_4$. The numbers for W-O-W bridging bonds are with 4.0 for $NiWMo1_{Ox}$ and 4.2 for $NiMoW2_{Ox}$ slightly larger than for NiW_{Ox}. Despite the inter-metallic interactions and possible connectivity between the different metal oxide polyhedra, the large estimated numbers of nearest neighbor suggest the presence of polymeric species while isolated Mo^{6+} or W^{6+} oxide polyhedra are excluded.

The X-ray absorption near edge structure (XANES) and the Fourier-transformed extended X-ray absorption fine structure (FT-EXAFS) of the four oxide samples and of different reference materials are shown at the Ni K-edge (Figure 11), Mo K-edge (Figure 14) and at the W L_{III}-edge (Figure 16).

At the Ni K-edge, the XANES of the oxides are similar to $NiMoO_4$ as well as to $NiWO_4$ or NiO (Figure 11(A)). The absorption edges are determined between 8347.0 eV for $NiMoW2_{Ox}$ (and $NiMoO_4$) and 8347.5 eV for $NiMo_{Ox}$, which points to a slightly lower Ni oxidation state for $NiMoW2_{Ox}$ than for $NiMo_{Ox}$.[220] The most intense white line is observed for $NiMoW2_{Ox}$, followed by $NiMo_{Ox}$, NiW_{Ox} and $NiWMo1_{Ox}$, which has the same low intensity than the reference $NiMoO_4$. Thus, the XANES at the Ni K-edge of all four oxide samples is typical for Ni in the oxidation state +2, as well as for an oxygen environment.

The LCF analysis revealed that the XANES of all oxides are best reproduced by the XANES of NiO and $NiMO_4$ (with M for Mo or W; Figure 12 and Table 4). The LCF of the XANES of $NiMoW2_{Ox}$ resulted even in 100 % NiO. For the other oxides a lower NiO fraction was determined with 45 % NiO for $NiMo_{Ox}$, 39 % NiO for NiW_{Ox} and 22 % NiO for $NiWMo1_{Ox}$. The contribution of $NiMO_4$ decreased from 78 % in $NiWMo1_{Ox}$ over NiW_{Ox} (61 %) and $NiMo_{Ox}$ (20 %) to $NiMoW2_{Ox}$ (0 %). The XANES of $NiMo_{Ox}$ required additionally 35 % $Ni(OH)_2$ during the LCF. The quality of the fit (R value in Table 4) and the difference spectra between the

experimental and fitted XANES, presented in the bottom of each diagram in Figure 12, illustrate that the reference spectra alone are not sufficient to reproduce the XANES of the oxide samples, especially in the case of $NiMoW2_{Ox}$ and NiW_{Ox}. This suggests the presence of phases other than the used references.

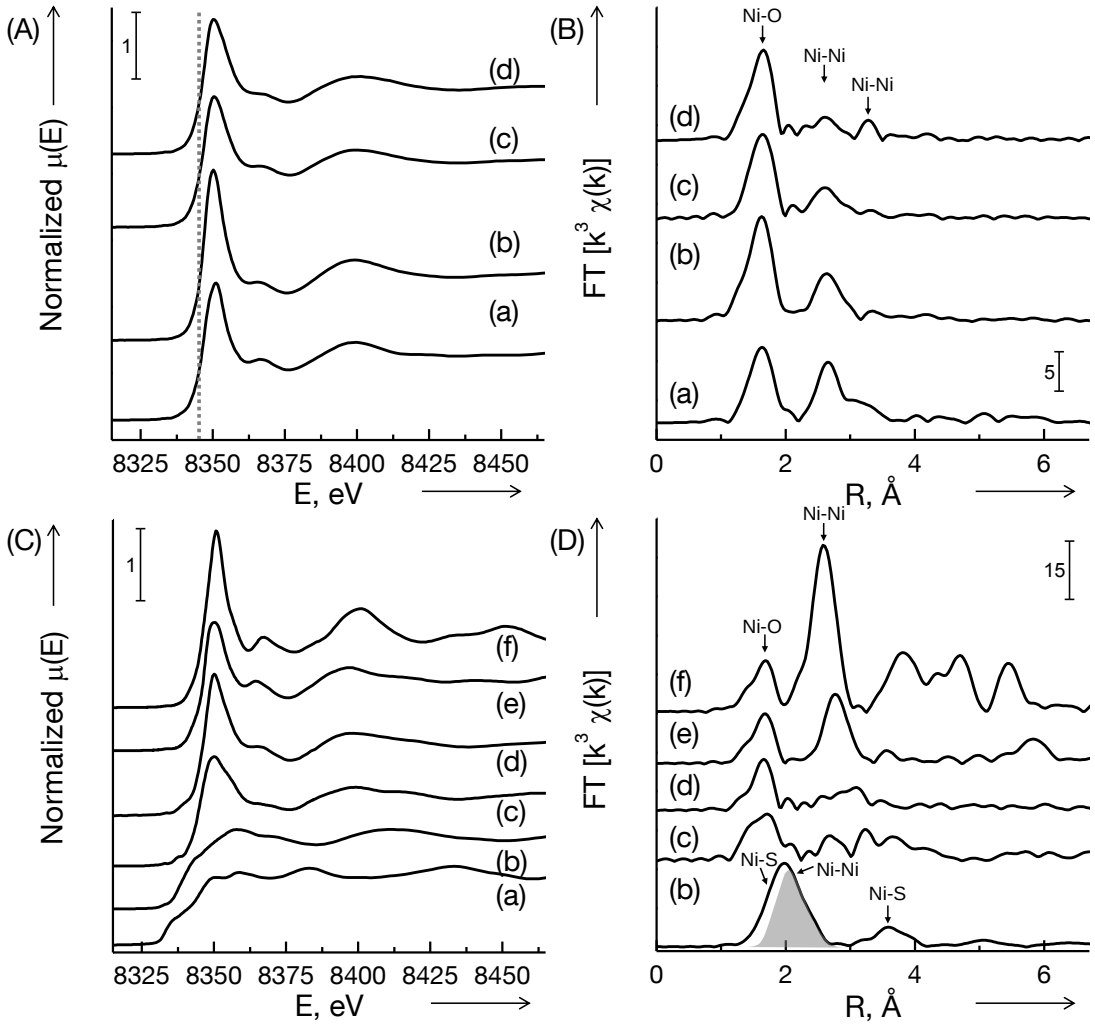

Figure 11. XANES at the Ni K-edge (A, C) and the corresponding Fourier transforms of k^3 weighted EXAFS (B, D) of oxide samples (A, B) and reference materials (C, D). In (A) and (B) are presented: $NiMo_{Ox}$ (a), $NiMoW2_{Ox}$ (b), $NiWMo1_{Ox}$ (c) and NiW_{Ox} (d). And (C) and (D) contain: Ni foil (a), Ni_3S_2 (b), $NiWO_4$ (c), $NiMoO_4$ (d), $NiOH_2$ (e) and NiO (f). In (D) the Ni foil is not presented. The absorption edge and most important contributions are indicated.

The Ni K-edge probes directly the unoccupied density of states of the 4p-orbital via the 1s-4p electric dipole transition, therefore the intensity of the white line is proportional to the ionic character (vacant 4p-orbitals) of the absorber atom.[221-222] This trend can be seen in Figure 11(A), where the white line intensity increased from covalent Ni-S in Ni_3S_2[38] over $NiMoO_4$ to NiO. The reference NiO crystallizes in the cubic NaCl-type structure and has ionic Ni-O bonds. The Ni-O bonds in the layered structure of $Ni(OH)_2$ (CdI_2-type) are covalent with ionic character, whereas the Ni-O bonds in the $[NiO_6]$-octahedra of $NiMoO_4$ (and $NiWO_4$) are

even more covalent[81] compared to NiO. Therefore, it is concluded that the ionic character of Ni is the highest in $NiMoW2_{Ox}$ and the highest density of states of the Ni 4p-orbitals is found for $NiWMo1_{Ox}$.

Table 4. LCF results of the modeled XANES for the oxidic samples.

Catalyst	Absorber metal	Weight of used XANES, %			R factor [a]	Integrated area of the residual [b]
		$NiMO_4$	metal oxide	left		
$NiMo_{Ox}$	Ni	20.2	45.0 (NiO)	34.8 (NiOH2)	0.0005	0.583
	Mo	84.8	no (MoO3)	15.2 (AHM)	0.0088	0.156
$NiMoW2_{Ox}$	Ni	0	100 (NiO)	no	0.0131	0.222
	Mo	71.3	22.9 (MoO3)	5.8 (AHM)	0.0006	0.080
	W	0	100 (WO3)	no	0.0731	8.308
$NiWMo1_{OX}$	Ni	77.8	21.7 (NiO)	0.4 (NiOH2)	0.0006	0.157
	Mo	62.7	36.9 (MoO3)	0.4 (AHM)	0.0005	0.322
	W	1.5	98.5 (WO3)	no	0.0034	0.368
NiW_{Ox}	Ni	60.6	39.4 (NiO)	no	0.0042	0.661
	W	25.7	74.3 (WO3)	no	0.0025	0.114

[a] The godness of the LCF. [b] The left area between the measured and modeled XANES (residual). M in $NiMO_4$ stands either for Mo or W and AHM for $(NH_4)_6(Mo_7O_{24}) \cdot 4H_2O$.

The pre-edge feature observed for $NiMoO_4$ at 8333.7 eV is less pronounced in the oxide samples and is almost absent in $NiMoW2_{Ox}$ (Figure 13). The presence of a pre-edge peak at K-edge XANES is mainly caused by an electric dipole transition from an s-orbital to the p component of a d-p hybrid orbital.[220, 223] Such hybridization is not (or only to small extent) possible for metal atoms in a perfect octahedral environment. In Figure 11(A), no pre-edge is observed for NiO and $NiOH_2$, where Ni^{2+} is octahedral coordinated by oxygen, whereas a distorted octahedral environment of Ni^{2+} like in $NiWO_4$ and $NiMoO_4$ caused a weak pre-edge feature. The reported pre-edge peaks for Ni^{2+} in literature are usually weak even in a perfect tetrahedral coordination due to its high $3d^8$ configuration.[224] However, tetrahedral coordinated Ni^{2+} induces a much more intense pre-edge than six-fold coordinated compounds[223] as can be seen in comparison to the sulfides species in Figure 13. Therefore, it is concluded that Ni^{2+} is distorted octahedral coordinated by oxygen in all four precursors in

agreement with Raman and DR-UV-vis spectroscopy. The [NiO_6]-octahedron in $NiMoW2_{Ox}$ seems less distorted (lower pre-edge intensity).

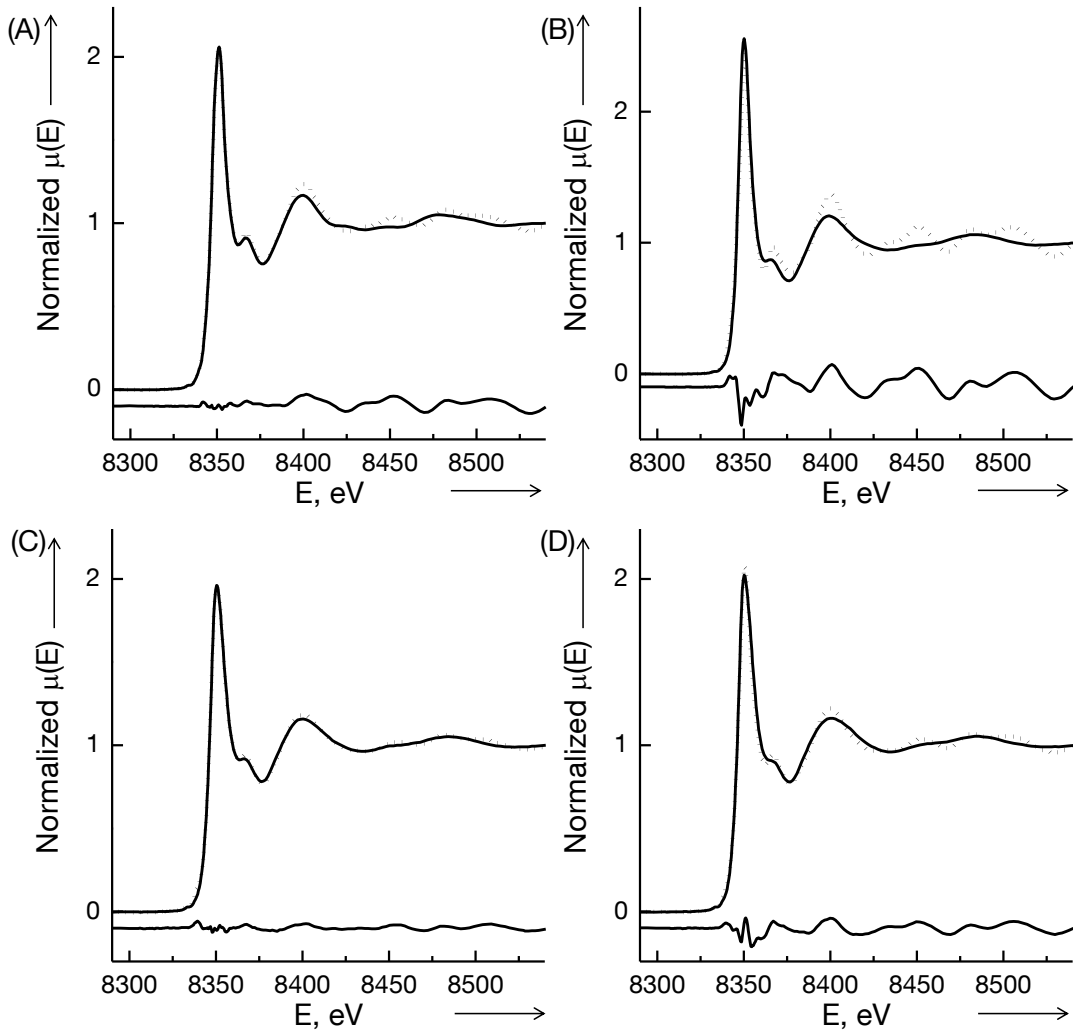

Figure 12. XANES (solid line) and modeled XANES by LCF (dotted line) at the Ni K-edge of the oxide samples $NiMo_{Ox}$ (A), $NiMoW2_{Ox}$ (B), $NiWMo1_{Ox}$ (C) and NiW_{Ox} (D). Additionally, the residual is presented in the bottom.

The Fourier transforms (FT) of the k^3 weighted EXAFS at the Ni K-edge show a strong first contribution at around 1.6 Å (not phase corrected), which is assigned to Ni-O according to the reference $NiMoO_4$ (Figure 11(B)).[33] This first feature is the sharpest and the most intense one for $NiMoW2_{Ox}$, which confirms a less distorted environment for Ni^{2+} compared to the other oxides and $NiMoO_4$. The second contribution at around 2.6 Å (not phase corrected) caused by Ni-Ni (or Ni-Mo) backscatter appears at shorter distances for all samples than for $NiMoO_4$ and also with a different intensity and shape. In comparison with the FT of the other measured Ni reference compounds (Figure 11(D)), the position of this Ni-Ni contribution in the oxide samples is similar to that in Ni-Ni in NiO, $Ni(OH)_2$ or $NiWO_4$. Moreover, in the bimetallic oxides, contributions at higher distances are visible. Specially, the FT of NiW_{Ox} is similar to $NiWO_4$ over the whole R space. The higher contributions indicate the presence of a

distinct periodic structure for Ni in NiW_{Ox} as well as in $NiMo_{Ox}$. Thus, the qualitative findings of the FT-EXAFS are in agreement with the ones from the XANES analysis and Raman spectroscopy. That is, a NiO or $Ni(OH)_2$-like Ni environment in $NiMo_{Ox}$ and $NiMoW2_{Ox}$, a $NiWO_4$ structure in NiW_{Ox} and a mixture of $NiWO_4$ and $NiMoO_4$ - like structures in $NiWMo1_{Ox}$.

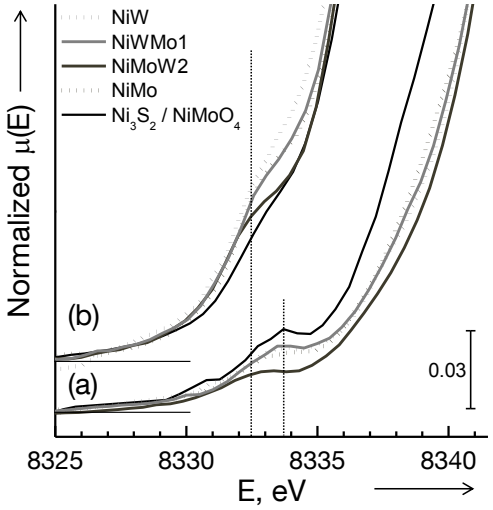

Figure 13. The pre-edge region of the XANES at the Ni K-edge of (a) oxides presented in Figure 11 and for comparison (b) of sulfides is shown. The pre-edge position of the references Ni_3S_2 and $NiMoO_4$ (—) is indicated by the dotted vertical lines. The following lines are used for the samples: $NiMo_{Ox}$ (▪▪▪), $NiMoW2_{Ox}$ (▬), $NiWMo1_{Ox}$ (▪▪), and NiW_{Ox} (▪▪▪).

At the Mo K-edge, the XANES of $NiMo_{Ox}$, $NiMoW2_{Ox}$ and $NiWMo1_{Ox}$ are similar to each other (Figure 14(A)). Taking into account all Mo references, the shape and peak positions of the $NiMoO_4$ XANES fits the best to the oxide samples (Figure 14(C)). Accordingly, the best LCF results are obtained with a high percentage of $NiMoO_4$ (Table 4, Figure 15). The XANES of $NiMo_{Ox}$ is a mixture of 85 % $NiMoO_4$ and 15 % $(NH_4)_6(Mo_7O_{24})\cdot 4H_2O$ (AHM). In the XANES of $NiMoW2_{Ox}$, $NiMoO_4$ is included with 71 % and in $NiWMo1_{Ox}$ with 63 %. Additionally, the XANES of MoO_3 and AHM are needed (with low percentages) to fit the XANES of both trimetallic oxides.

The absorption edge position of $NiMoO_4$ is 20017.7 eV, which is slightly higher than the ones determined for the oxide samples. The following trend is found for decreasing absorption edge energy: $NiMoW2_{Ox}$ (20017.2 eV) ~ $NiWMo1_{Ox}$ (20017.1 eV) > $NiMo_{Ox}$ (20016.7 eV). Moreover the highest and sharpest white line is observed for $NiMo_{Ox}$ and the least intense one for $NiWMo1_{Ox}$. The absorption edge position and the edge jump of a K-edge indicate the oxidation state as well as the population of the p-orbital of the absorber atom.[220] Therefore, we conclude that Mo has the oxidation state +6 in all oxide samples (like in $NiMoO_4$), although in $NiMo_{Ox}$ the oxidation state of Mo seems to be lower. Moreover, the 5p-orbitals of Mo^{6+} are less occupied in $NiMo_{Ox}$ compared to the trimetallic materials. A remarkable feature

of the Mo K-edge XANES is the intense pre-edge peak at 20003.9 eV for $NiMo_{Ox}$, 20004.3 eV for $NiWMo1_{Ox}$, and 20004.8 eV for $NiMoW2_{Ox}$ ($NiMoO_4$: 20004.5 eV). Its intensity is comparable for all oxides and less intense than for $NiMoO_4$ but much higher than for AHM or MoO_3. As the intensity of the pre-edge feature depends on the symmetry and coordination number of the absorber atom,[179, 223] it is concluded that in all oxide samples Mo^{6+} is distorted tetrahedral coordinated like in the most stable β-$NiMoO_4$[81-82] phase (and not distorted octahedral as in MoO_3 or AHM).

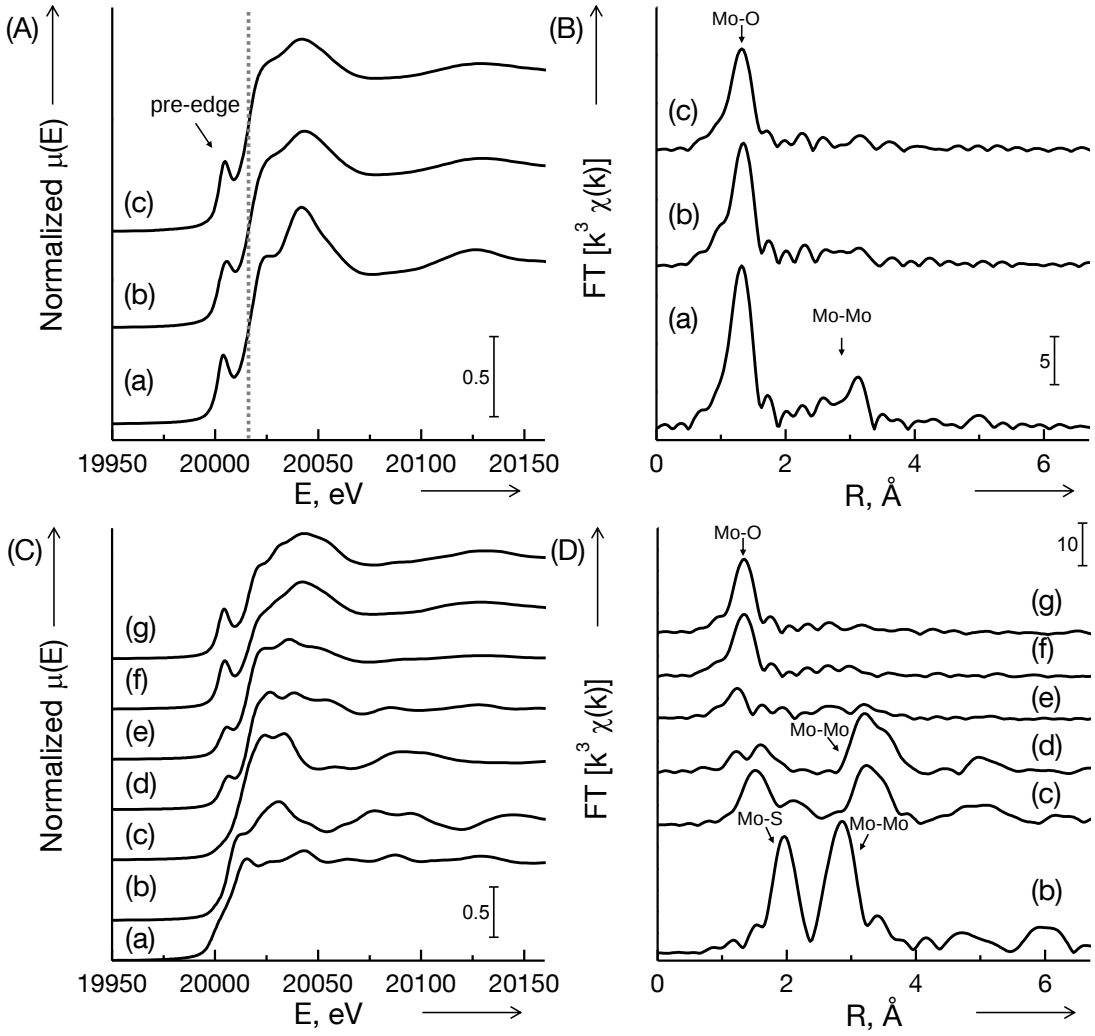

Figure 14. XANES at Mo K-edge (A, C) and the corresponding Fourier transforms of k^3 weighted EXAFS (B, D) of oxide samples (A, B) and reference materials (C, D). In A and B are presented: $NiMo_{Ox}$ (a), $NiMoW2_{Ox}$ (b), $NiWMo1_{Ox}$ (c). And C and D contain: Mo foil (a), MoS_2 (b), MoO_2 (c), MoO_3(d), $(NH_4)_6(Mo_7O_{24}) \cdot 4H_2O$ (e), $NiMoO_4$ (f) and K_2MoO_4 (g). In D the Mo foil is not presented. The absorption edge and most important contributions are indicated.

FT of the k^3 weighted EXAFS of the oxide samples are presented in Figure 14(B). All oxides show one strong contribution at around 1.3 Å (not phase corrected), which is assigned to Mo-O as for the reference $NiMoO_4$.[225-226] The FT of $NiMo_{Ox}$ shows a weak contribution at 3.2 Å (not phase corrected), where a Mo-Mo backscattering pair is present in AHM or MoO_3

(Figure 14(D)), i.e., typical for polymolybdates.[40] The shortest Mo-Mo bond distances in MoO_3 and AHM are between 3.2 and 3.5 Å, whereas Mo-Ni and Mo-Mo bond distances of 3.6 and 3.9 Å, respectively, are present in the layered $(NH_4)HNi_2(OH)_2(MoO_4)_2$ structure.[182] Thus, the contribution observed in $NiMo_{Ox}$ could originate from different backscatters in different structures and does not prove the presence of polymolybdates. In the trimetallic oxides higher contributions are almost absent.

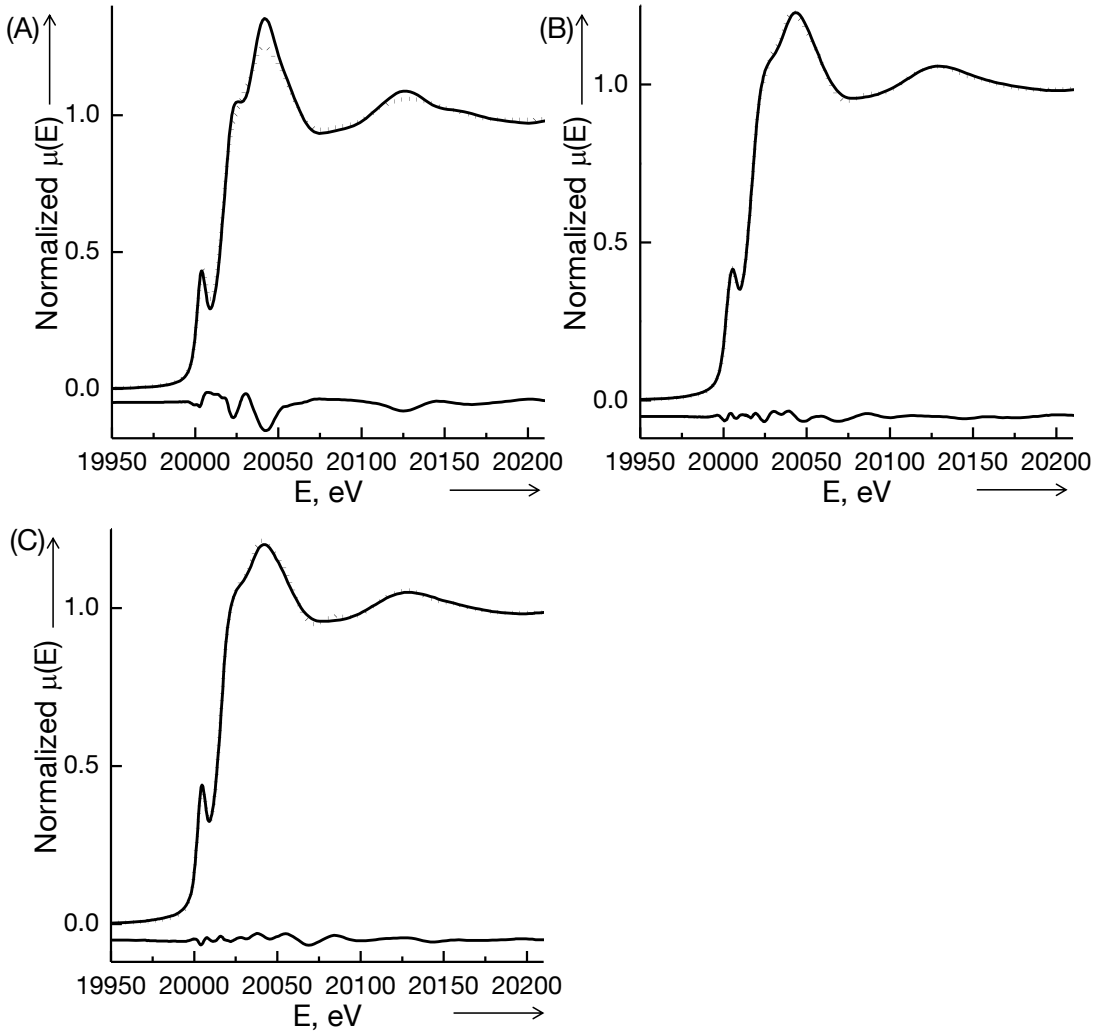

Figure 15. XANES (solid line) and modeled XANES by LCF (dotted line) at the Mo K-edge of the oxide samples $NiMo_{Ox}$ (A), $NiMoW2_{Ox}$ (B) and $NiWMo1_{Ox}$ (C). Additionally, the residual is presented in the bottom.

In conclusion, Mo^{6+} is present in distorted $[MoO_4]$-tetrahedra (like in β-$NiMoO_4$) in all oxides, although there are also a few characteristics of AHM and MoO_3. Thus, the tetrahedral Mo^{6+} coordination symmetry suggested by Raman spectroscopy is confirmed by XAS. The trimetallic oxides show similar Mo K-edge XANES except for small differences in intensities and energy position. For instance, $NiMoW2_{Ox}$ appears with a less intense pre-edge peak at a slightly higher energy and the Mo-O contribution is higher in the FT compared to $NiWMo1_{Ox}$.

These differences could be caused by strong distortion of the [MoO_4]-tetrahedra,[224, 226] i.e. the fraction of octahedral Mo^{6+} sites is higher in $NiMoW2_{Ox}$. But also the higher Mo content in $NiMoW2_{Ox}$ could have an influence on its XAS features.

At the W L_{III}-edge, a very sharp onset at the adsorption edge due to the $2p_{3/2}$ - $5d_{3/2}$ electric dipole transition is observed for NiW_{Ox}, $NiMoW2_{Ox}$, $NiWMo1_{Ox}$ and for the reference WO_3 (Figure 16(A) and (C)). The absorption edge is determined with 10211.7 eV for WO_3, 10212.0 eV for NiW_{Ox}, 10212.5 eV for $NiWMo1_{Ox}$, and 10212.6 eV for $NiMoW2_{Ox}$.

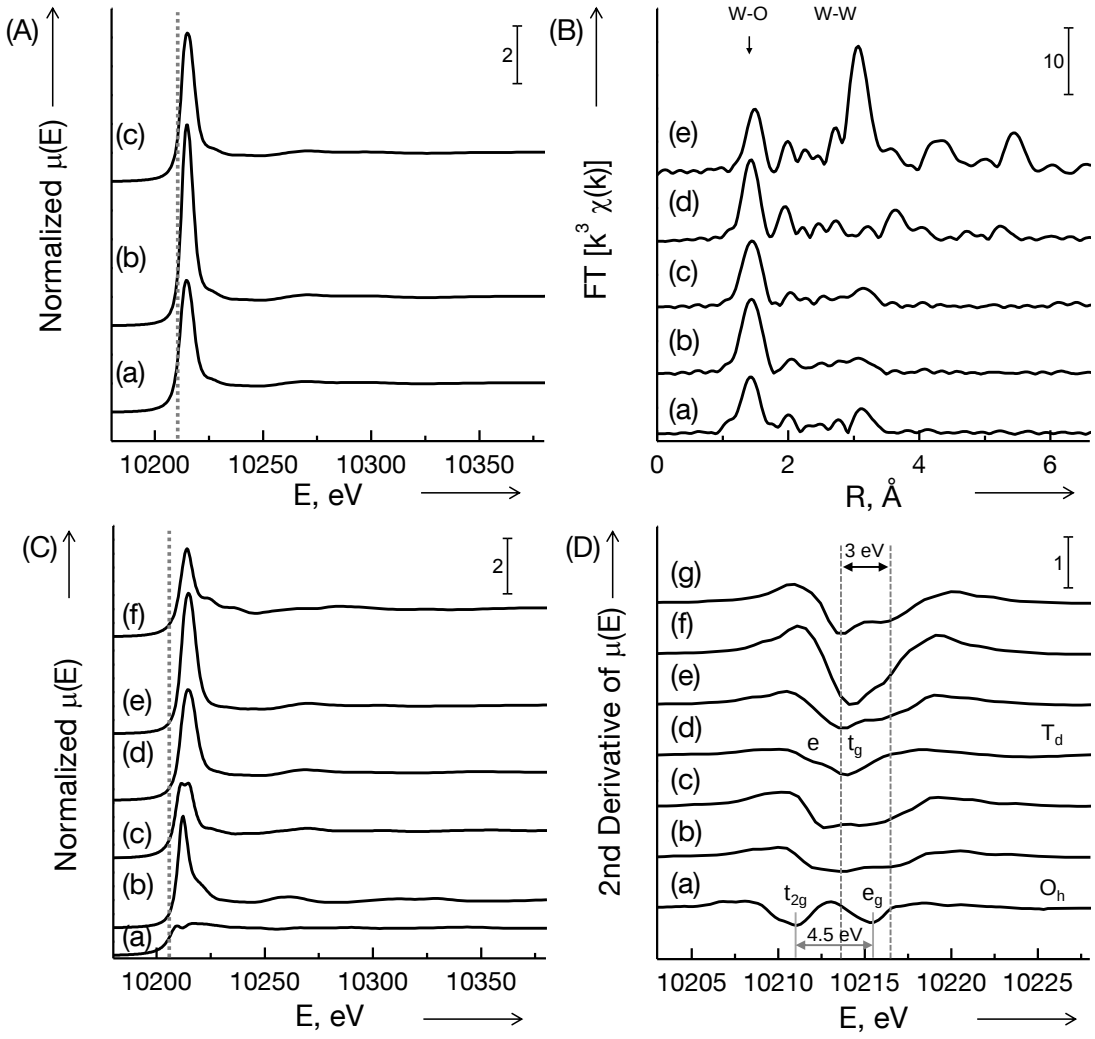

Figure 16. XANES at the W L_{III}-edge (A, C) and the corresponding Fourier transforms of k^3 weighted EXAFS (B) of oxide samples (A, B) and reference materials (C, B). In (A) and (B) are presented: NiW_{Ox} (a), $NiMoW2_{Ox}$ (b), $NiWMo1_{Ox}$ (c) and additionally in (B) WO_3 (d) and $NiWO_4$ (e). And (C) contains: W-foil (a), WS_2 (b), $NiWO_4$ (c), $(NH_4)_6(W_{12}O_{40})H \cdot xH_2O$ (d), WO_3 (e), and Na_2WO_4 (f). The absorption edge and most important contributions are indicated. In (D) the second derivative of the W L_{III}-edge absorption is presented showing $NiWO_4$ (a), $(NH_4)_6(W_{12}O_{40})H \cdot xH_2O$ (b), WO_3 (c), and Na_2WO_4 (d) and the oxide samples NiW_{Ox} (e), $NiMoW2_{Ox}$ (f) and $NiWMo1_{Ox}$ (g) (the dotted lines mark the gap between the two found peaks in the oxides indicating d-orbital splitting).

The best LCF of the oxide samples were gained with a very high percentage of WO_3 (Table 4, Figure 17). Only for NiW_{Ox}, the XANES is best reproduced by the addition of 26 %

of $NiWO_4$ to the XANES of WO_3. The LCF of $NiMoW2_{Ox}$ revealed 100 % WO_3, but the quality of the fit was poor and better fitting could not be gained by using the XANES of the available references. All measured W-references are shown in Figure 17(A), which also show the similarity of the XANES of the oxide samples to WO_3.

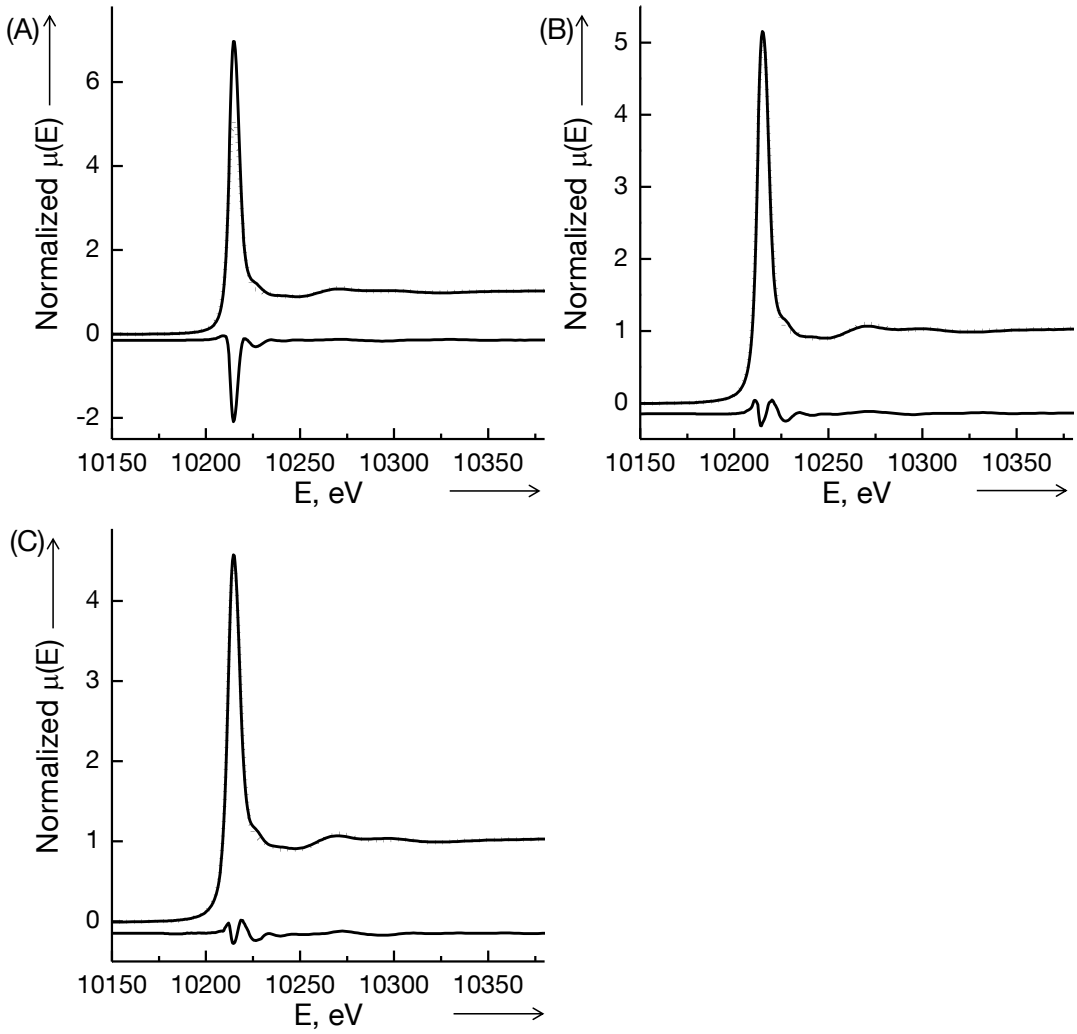

Figure 17. XANES (solid line) and modeled XANES by LCF (dotted line) at the W L_{III}-edge of the oxide samples $NiMoW2_{Ox}$ (A), $NiWMo1_{Ox}$ (B) and NiW_{Ox} (C). Additionally, the residual is presented in the bottom.

In conclusion, W has the oxidation state +6 in all oxide samples and is present in an environment similar to WO_3. The highest white line is observed for $NiMoW2_{Ox}$ followed by $NiWMo1_{Ox}$ (same as WO_3) and NiW_{Ox}. According to the implications of the W L_{III} absorption edge and white line intensity,[227-229] $NiMoW2_{Ox}$ has the highest oxidation state and the lowest population of the 5d-orbitals, whereas NiW_{Ox} has the highest density of states. Additionally, the absorption intensity and shape of a p-d electric dipole transition are also influenced by the symmetry (structure) of the absorber atom since the d-orbitals are involved in the bonds.[230] Indeed, comparison of the reference materials shows that the shape and intensity of the white line differs strongly among the measured compounds (Figure 16(C)). For

instance, WO_3 has a very intense white line, whereas it is comparable weak for Na_2WO_4 and additionally a white line splitting is observed for $NiWO_4$.

The area beneath the white line signal, reflects the mixing ratio of O 2p and W 6p-orbitals into the W 5d-orbitals. In tetrahedral structures, like in Na_2WO_4, the p-character of the p-d hybrid orbitals is high, but the electric transition from W 2p-orbitals for the WL_{III}-edge to the 6p-orbitals is dipole forbidden.[231] Therefore, the L_{III}-edge absorption intensity of tetrahedral complexes is weaker than for octahedral ones holding little p-d hybridization, as observed for the white line of Na_2WO_4 (T_D) compared to WO_3 (O_h). Moreover, the white line of L_{III}-edges is composed by two different peaks, which are caused by the 2p electric dipole transitions to the split d-orbitals (e- and t-orbitals) created by the ligand field of the different coordination geometries. Splitting of these two dipole transitions and, therefore, in the white line is visible in dependence on the strength and type of ligand field.[228, 230, 232] At the W L_{III}-edge, the split is often not sufficiently resolved, therefore the second derivative of the XANES spectra is used to clarify the splitting[231, 233] as presented for the oxide samples and selected references in Figure 16(D). In $NiWO_4$, a gap of 4.5 eV between both observed signals in the second derivative is observed, which reflects the energy split between the t_{2g} and e_g-orbitals in an octahedral ligand field.[230] Indeed, $[WO_6]$-octahedra with a minor distortion are present in $NiWO_4$.[83] The observed energy split for WO_3, where W^{6+} is distorted octahedral coordinated is 3.5 eV smaller. For tetrahedrally coordinated W^{6+} in Na_2WO_4 only one broad signal (t_g-orbitals) is observed next to a weak shoulder at the low energy site (e-orbitals).

For NiW_{Ox} and $NiWMo1_{Ox}$, an energy split of 3.0 eV in the second derivative is observed. The shape of the second derivative of $NiMoW2_{Ox}$ exhibits a broad intense signal with a shoulder at higher energy and a gap of 2.7 eV. Therefore, W^{6+} is distorted-octahedrally coordinated in all three oxides, which is in agreement with their high white line intensities. In $NiMoW2_{Ox}$, the $[WO_6]$-octahedron distortion is the strongest and the W^{6+} coordination might have as well tetrahedral character in respect to the d-orbital splitting. The observed high white line intensity of $NiMoW2_{Ox}$ is apparently contradictory to this conclusion (stronger tetrahedral distortion should be reflected in a lower intensity). However, the L_{III} XANES is influenced not only by the absorber symmetry and first shell coordination number, but also other elements in the framework (in the second shell)[234] or organic ligands[233] could modify the electronic structure and geometry. Thus, the high white line intensity of $NiMoW2_{Ox}$ is attributed to the presence of Mo^{6+}, Ni^{2+} and/or $(CH)_2(COO^-)_2$ ligands in the neighborhood of W^{6+} in $NiMoW2_{Ox}$.

The FT of the k^3 weighted EXAFS at the W L_{III}-edge of the oxide samples and WO_3 and $NiWO_4$ is presented in Figure 16(B). The FT show one strong contribution at short distance assigned to W-O[33] (around 1.4 Å, not phase corrected) and only weak contributions at higher distances. The W-O contribution intensity decreases in the following order:

$NiMoW2_{Ox}$ > $NiWMo1_{Ox}$ > NiW_{Ox}. However, the highest FT intensities over the whole R-space are found for the references. The positions of the higher W-W or W-O contributions in the oxide samples match well with the ones of $NiWO_4$ and WO_3, pointing to a periodic W structure in the oxides. Especially at around 3.1 Å (not phase corrected), a relative intense W-W contribution[33] is visible for NiW_{Ox}, which is still present in $NiWMo1_{Ox}$ with low intensity and almost absent in $NiMoW2_{Ox}$. This observation could be explained by the lower bulk W concentration in $NiMoW2_{Ox}$ than in $NiWMo1_{Ox}$.

Overall in the FT at the W L_{III}-edge and Mo K-edge, the M-M contributions (M stands for Mo or W) are much weaker for the trimetallic oxides than for the bimetallic ones. Metal bulk concentrations alone cannot explain the absence of higher contributions at both edges. According to the XANES analysis, similar crystallographic structures are evident in all oxide samples, which suggest similar long range order (similar second shell neighbor atoms). Low coordination numbers, i.e. weak FT signals are usually correlated to small particles, which could be also excluded for the oxides in respect to the particles sizes found via SEM. A similar phenomenon observed for trimetallic sulfide material was interpreted as Mo and W being neighboring atoms in the same crystal structure, which causes destructive interference in the overall EXAFS due to the phase shift of π between Mo and W absorber-backscatter pairs.[235] Following this idea, the EXAFS at the Mo K-edge and W L_{III}-edge of the trimetallic oxides are compared to the bimetallic oxides and references (Figure 18). The EXAFS features of the wave functions of Mo or W present in the bimetallic oxides between 9 and 16 $Å^{-1}$ disappear with increasing concentration of W or Mo, respectively, in the trimetallic oxides. In literature, a similar W-EXAFS trend is reported for mono-metallic W^{6+}-oxide species as a consequence of a symmetry change from an octahedral to tetrahedral W^{6+} environment.[231] However, the identified strong distorted symmetries, the unusual XANES behavior, and the bad XANES LCF results combined with the changes in the EXAFS at both edges, indicate that Mo and W are present next to each other in distorted [MO_6]-octahedra in the same metallate structure, especially pronounced in $NiMoW2_{Ox}$. The edge or corner connections of polyhedra with different center atoms create stress in the metallate structure, which results in polyhedra distortion.

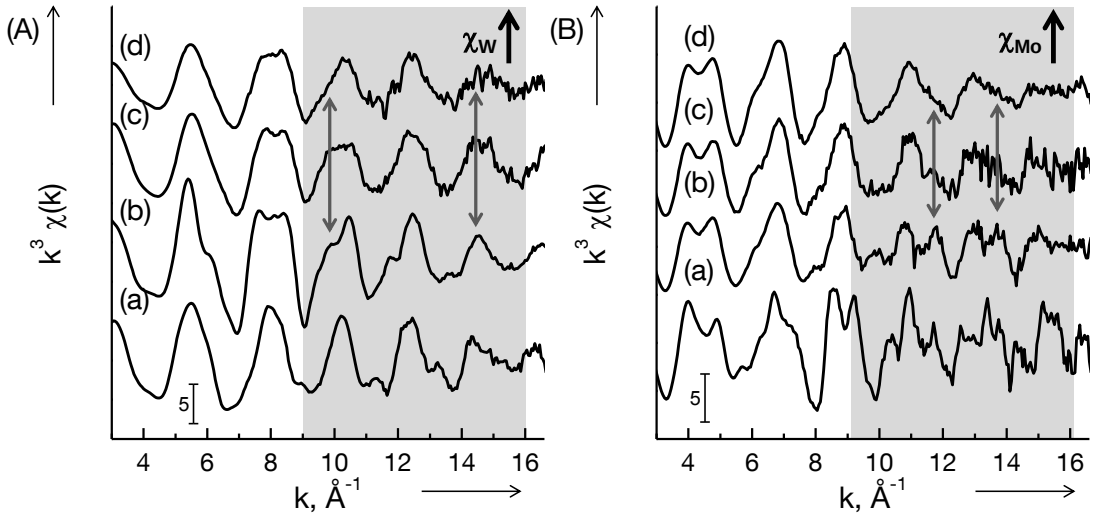

Figure 18. k^3 weighted EXAFS at the Mo K-edge (A) of the references $NiMoO_4$ (a) and of the oxide samples $NiMo_{Ox}$ (b), $NiMoW2_{Ox}$ (c) and $NiWMo1_{Ox}$ (d) (the W concentration increases from bottom to top). And at the W L_{III}-edge (B) of the references WO_3 (a) and of the oxide samples NiW_{Ox} (b), $NiWMo1_{Ox}$ (c) and $NiMoW2_{Ox}$ (d) (the Mo concentration increases from bottom to top). The changes of the EXAFS functions are indicated with the grey arrows and the box.

Summarizing, the XAS data and analysis showed that $NiMo_{Ox}$ consists of Ni^{2+} and ionic Ni-O bonds arranged in distorted $[NiO_6]$-octahedra. The resulting structure is comparable to $Ni(OH)_2$. Mo has the oxidation state +6, or slightly lower, and is distorted tetrahedral coordinated by oxygen. The population of the Mo 5p and Ni 2p-orbitals indicates that interactions with ions (OH^-, NH_4^+) or organic $(CH)_2(COO^-)_2$ ligands are possible. Moreover, a weak Mo-Mo(Ni) contribution is identified, which makes a $(NH_4)HNi_2(OH)_2(MoO_4)_2$-like structure likely. In NiW_{Ox}, Ni^{2+} and W^{6+} are distorted octahedrally coordinated. The XANES LCF and the FT-EXAFS showed a very good agreement with $NiWO_4$ at both absorption edges. However, a more ionic character of the Ni-O bonds as well as a lower population of the W 5d-orbitals, and a lower d-orbital splitting in NiW_{Ox} than in $NiWO_4$, point to a modification of the $NiWO_4$ structure. Thus, strong $[WO_6]$-octahedron distortion and interaction with Ni^{2+} (and maybe W^{6+}) with OH^- is concluded.

In the trimetallic oxides, Ni^{2+} and W^{6+} are distorted octahedrally coordinated and Mo^{6+} is present in distorted $[MoO_4]$-tetrahedra. However, the symmetry and electronic structure of Ni, Mo and W present small differences in both materials. In $NiMoW2_{Ox}$, the ionic character of the Ni-O bonds is much higher and the $[NiO_6]$-octahedra are less distorted than in $NiWMo1_{Ox}$. The XANES and FT-EXAFS analysis resulted in a NiO or $Ni(OH)_2$-like structure present in $NiMoW2_{Ox}$. In $NiWMo1_{Ox}$, a mixture of $NiMoO_4$ and $NiWO_4$ is concluded. The fraction of octahedral coordinated Mo^{6+} and tetrahedral coordinated W^{6+} are higher in $NiMoW2_{Ox}$ (the $[MoO_4]$-tetrahedra and $[WO_6]$-octahedron are stronger distorted) compared to $NiWMo1_{Ox}$. Moreover, the presence of Mo and W polyhedra in the same metallate structure is concluded

and more pronounced in $NiMoW2_{Ox}$. Therefore, it is concluded that strong distortion of the M polyhedron (M for Mo or W) is mandatory to form mixed metallate structures. Finally, $NiMoW2_{Ox}$ consists of $[NiO_6]$- and strongly distorted $[MO_6]$-octahedra, which apparently interact with the different contained ions (OH^-, NH_4^+) or the organic $(CH)_2(COO^-)_2$ ligands. The structural features of $NiWMo1_{Ox}$ appear as mixture of the $NiMo_{Ox}$ and NiW_{Ox} structure. However, the density of states is higher for the Ni 2p-orbitals and lower for W 5d-orbitals compared to both bimetallic oxides, therefore a lower interaction between OH^- groups and Ni and a weak interaction of W with the organic $(CH)_2(COO^-)_2$ ligands is likely for $NiWMo1_{Ox}$.

On the structure of the oxide samples

The bimetallic $NiMo_{Ox}$ oxide exhibits the structure of the layered ammonium nickel molybdate $(NH_4)HNi_2(OH)_2(MoO_4)_2$, which is presented in Figure 19. This structure consists of four Ni-Mo-oxide-layers in one unit cell stacked in c-direction. The layers are separated by ammonium ions and hydroxyl groups, which are bonded to terminal oxygen atoms of the metal polyhedra. Every layer is composed by chains of edge connected $[NiO_6]$-octahedra sandwiched between isolated $[MoO_4]$-tetrahedra. Every $[MoO_4]$-tetrahedron is connected via three corners to three different $[NiO_6]$-octahedra. Two of the $[NiO_6]$-octahedra belong to the same chain. The fourth $[MoO_4]$-tetrahedra corner is exposed into the interspace.[182, 236] The distance between two neighboring $[MoO_4]$-tetrahedra is 6.0 Å, whereas it is only 3.9 Å between two Mo atoms across the layer (the tetrahedra on top and on the bottom of the layer). The Mo-O and Ni-O bond distances are similar to the ones in the β-$NiMoO_4$ structure.[236] Interestingly, this structure allows Ni/Mo ratios between 0.75 and 1.5 and exhibits therefore well ordered octahedral holes (Ni^{2+} vacancies).[205] The structural refinement revealed the presence of additional framework hydrogen, which is proposed to be associated to bridging hydroxyl bonds and explains the additional H in the chemical formula.

The presence of this ammonium nickel molybdate structure in $NiMo_{Ox}$ was evident by XRD and confirmed by the presence of distorted octahedral Ni^{2+} and tetrahedral Mo^{6+} coordinations. Furthermore, the presence of isolated $[MoO_4]$-tetrahedra in a close interaction with Ni species next to hydroxyl- and ammonium groups was concluded by Raman, UV-vis and X-ray absorption spectroscopy. The highest measured Mo-O stretching vibration was at 908 cm^{-1}, which correlates with a Mo-O bond distance of 1.73 Å and a bond order of 1.66 using the mathematical models of Hardcastle and Wachs.[206] This value is in a very good agreement with the Mo-O bond distance in $(NH_4)HNi_2(OH)_2(MoO_4)_2$ and the bond order reflects the distorted tetrahedra and the exposed Mo-O bond in the interlayer space. Additionally, Raman spectroscopy and XAS pointed to Ni species associated to hydroxyl-groups, which finally allowed the exclusion of β-$NiMoO_4$.

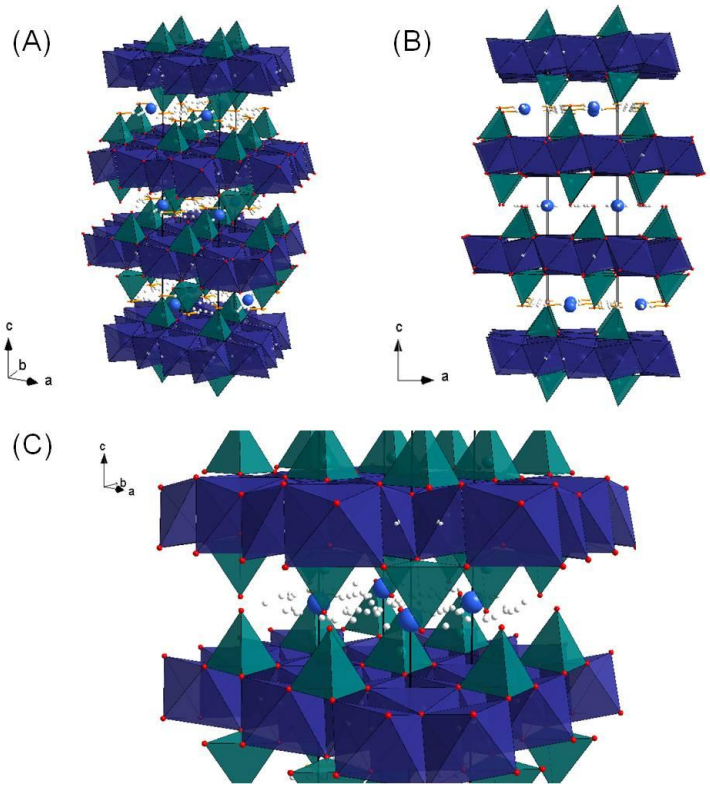

Figure 19. Proposed structure for the bimetallic $NiMo_{Ox}$ oxide, which is the layered ammonium nickel molybdate $(NH_4)HNi_2(OH)_2(MoO_4)_2$ (ICSD #165342).[182] The extended trigonal unit cell of the structure is shown in the polyhedral representation in different viewing directions (A) and (B) and in (C) two layers are enlarged presented with blue octahedra for Ni, green tetrahedra for Mo and circles for N (light blue), O (red) and H (white).

For the bimetallic NiW_{Ox} oxide a structure similar to the one of $NiWO_4$ is proposed (Figure 20). This wolframite structure has a monoclinic lattice system including a distorted close packing of O atoms and a 25 % occupation of the octahedral holes by Ni and W. Ni^{2+} and W^{6+} are distorted octahedrally coordinated by oxygen at which all metal atoms are regularly displaced parallel to the b-axis within their oxygen octahedra. The octahedra with the same central atom are edge-connected and the different octahedra by corners. Due to this arrangement, a layered-like structure of alternating $[NiO_6]$- and $[WO_6]$-chains perpendicular to the a-axis is created.[83] This structure is very common for ortho-tungstates and is also found as a high temperature structure-type of $NiMoO_4$.[81, 86]

During the XRD analysis, $NiWO_4$ was identified as crystalline phase and also the spectroscopy results pointed to its presence. Distorted octahedral coordination of Ni^{2+} and W^{6+} was evident with all methods and also polymeric $[WO_6]$-octahedra and an intense interaction between Ni^{2+} and W^{6+} were concluded. Additional signals and the amorphous background in the XRD pattern, large particle size distribution of irregular formed particles (SEM), and broad spectroscopic bands indicate the presence of other phases in addition of the crystalline $NiWO_4$.

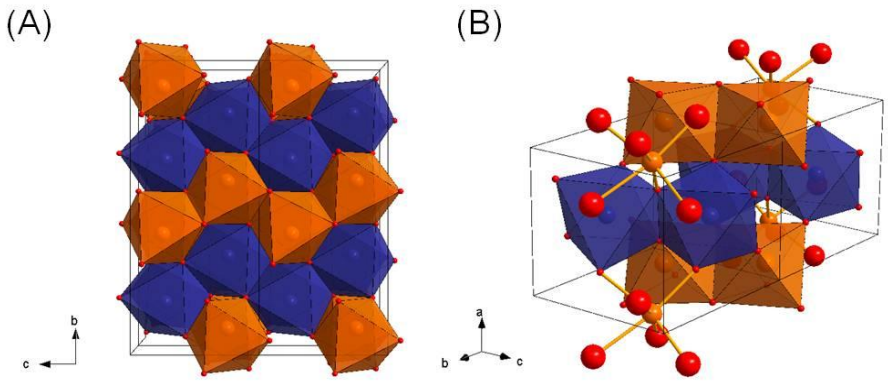

Figure 20. Proposed main phase of the bimetallic NiW_{Ox} oxide, which is the monoclinic $NiWO_4$ (ICSD #15852) presented in a polyhedral representation.[83] In (A) eight unit cells in a-direction, each containing two formula units, is shown and in (B) the polyhedra connectivity is presented by two unit cells with blue octahedra for Ni, orange octahedra for W and red circles for O.

Using the reported equation for W oxides by Hardcastle, the shortest W-O bond distance is calculated with 1.74 Å and a corresponding bond order of 1.8 is estimated from the high frequency Raman band (952 cm^{-1}). These values are typical for terminal W=O bonds in polymeric species, for instance hydrated WO_3.[237] The values obtained from the second Raman band at 894 cm^{-1} are in agreement with the $NiWO_4$ structure (d(W-O) = 1.8-2.1 Å compared to 1.77 Å and a bond order of 1.6 from Raman). The presence of a WO_3 phase was also suggested by XRD characterization next to a $Ni(OH)_2$-like phase, which were both confirmed by XAS. Raman spectra indicated the presence of surface hydroxyl groups and water, whereas no ammonium ions or carboxylic acid were evident. Finally, XANES showed a high ionicity for Ni^{2+} and a high density of states for W^{6+} which might be caused by interaction of Ni^{2+} with hydroxyl groups and W^{6+} with water. In conclusion, the main phase of NiW_{Ox} is indeed $NiWO_4$ but W^{6+} is stronger distorted than predicted by the wolframite structure, maybe due to the interaction with water and hydroxyl groups. Additionally, the presence of pure metal phases like $Ni(OH)_2$ and WO_3 in low concentrations is likely. A layered structure and interactions with ammonium ions are excluded.

The local environments of Mo, W and Ni in the trimetallic oxides comprises distorted [NiO_6]- and [WO_6]-octahedra and distorted [MoO_4]-tetrahedra (as for all oxide samples). The Raman and UV-Vis spectra of the trimetallic materials appeared as a mixture of the spectra of the bimetallic materials exhibiting band maxima in between the values of the bimetallic oxides. Using the Raman M-O stretching modes (the lower one for Mo and the highest for W)[80], the Mo-O bond distances are calculated[206] with 1.75 Å (bond order: 1.57) for $NiMoW2_{Ox}$ (879 cm^{-1}) and with 1.74 Å (bond order: 1.61) for $NiWMo1_{Ox}$ (894 cm^{-1}). The W-O bond distances are estimated[237] with 1.75 Å (bond order: 1.65; 923 cm^{-1}) for $NiMoW2_{Ox}$ and 1.74 Å (bond order: 1.69; 936 cm^{-1}) for $NiWMo1_{Ox}$. Thus, the M-O bond distances and bond orders are almost the same than in $NiMo_{Ox}$ and NiW_{Ox}.

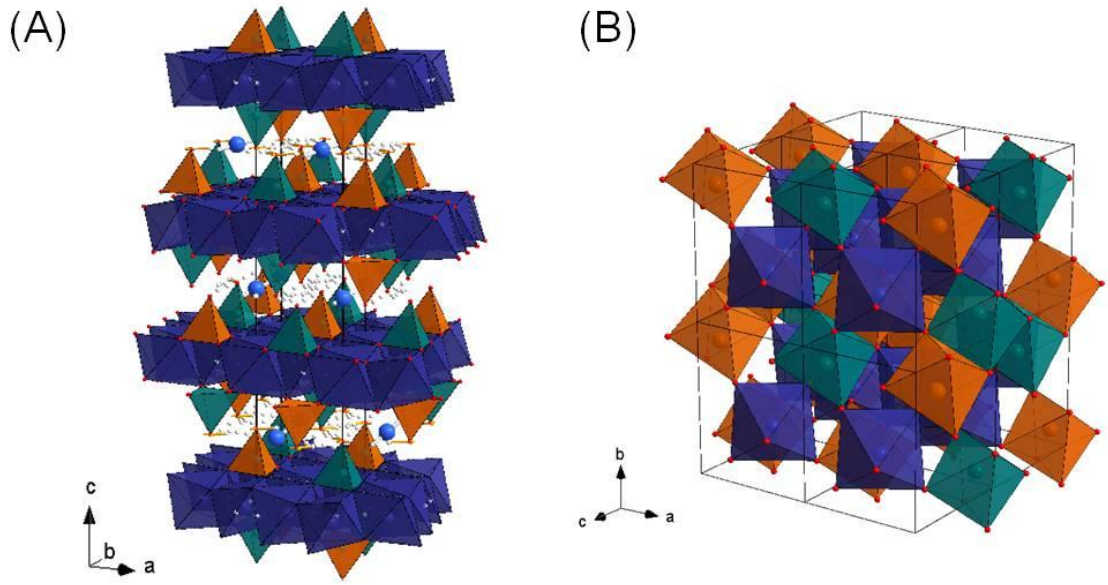

Figure 21. Possible structures for trimetallic Ni-Mo-W oxides based on (A) the trigonal $(NH_4)HNi_2(OH)_2(MoO_4)_2$ (ICSD #165342)[182] and (B) the monoclinic $NiWO_4$ (ICSD #15852)[83]. Both structures are presented in the polyhedral representation, whereas in (A) the extended unit cell and in (B) eight unit cells are shown with blue octahedra for Ni, green polyhedra for Mo, orange polyhedra for W and circles for N (light blue), O (red) and H (white).

The more distant coordination shells of the metals are comparable for all oxides in respect to their FT-EXAFS and number of next nearest metal neighbors (cluster size) determined by the UV-vis edge energy. Additionally, interactions among the three metals were concluded by combining all spectroscopic results and under consideration of literature describing the easy mixing of Mo and W in one oxide phase.[75, 80, 235] In conclusion, the structures of the trimetallic oxide samples are based on the structures found for $NiMo_{Ox}$ and NiW_{Ox}, where Mo or W are partially replaced by the other metal as presented in Figure 21. These proposed trimetallic oxide structures would need to undergo a restructuring and polyhedra distortion to compensate the different coordination geometries of Mo and W (which is not presented in Figure 21). The question arises as to whether one of these structure types is preferred or mixed structures are present.

The oxide $NiWMo1_{Ox}$ does not exhibits Ni-O Raman bands assignable to $Ni(OH)_2$ and only weak bands of associated hydroxyl groups. Furthermore, low relative intensities of the Ni^{2+} associated UV-vis bands are observed and Ni^{2+} has a high covalent character in XANES. Therefore, the fraction of Ni^{2+} associated to hydroxyl groups like in the layered compounds $Ni(OH)_2$ or $(NH_4)HNi_2(OH)_2(MoO_4)_2$ is remarkable low. The $[MoO_4]$-tetrahedra are distorted like in $NiMo_{Ox}$, whereas the $[WO_6]$-octahedra show a similar distortion than in NiW_{Ox}. The XANES analysis revealed coordination symmetries of Mo and W similar to $NiMoO_4$ (Mo-T_d), $NiWO_4$ (W-O_h), and also MoO_3 (Mo-O_h) and WO_3 (W-O_h). The presence of these polymeric Mo and W oxide species is confirmed by UV-vis spectroscopy. In general, the Raman and

UV-vis spectra of $NiWMo1_{Ox}$ are more comparable to NiW_{Ox} (W-O_h) than to $NiMo_{Ox}$ (Mo-T_d) and also their W-XANES is similar (especially their densities of W 5d-states). In a solid state study, the transformation of a wolframite-type $CdW_{1-x}Mo_xO_4$ (O_h) structure to a scheelite-type $CdW_{1-x}Mo_xO_4$ (T_d) structure was analyzed in dependence of x. It was found that the octahedral W coordination in the wolframite structure is stable when Mo replaces W in octahedral sites up to a 1:1 ratio.[80] Thus, a mixed metallate with a higher W concentration compared to Mo, like in $NiWMo1_{Ox}$ with W to Mo of 2:1 would prefer the octahedral metallate coordination of the wolframite structure. Accordingly, we conclude that in $NiWMo1_{Ox}$, the trimetallic phase crystallizes preferential in the wolframite structure (Figure 22(B)). The replacement of W by Mo introduces a tetrahedral distortion of the [WO_6]-octahedra, which might hinder the growth of large crystalline domains, but allows a distorted octahedral coordination for W and a distorted tetrahedral one for Mo. Hence, the structure presented in Figure 22(B) differs slightly from the real structure, where the polyhedra interact with ammonium ions and carboxylic acid. The presence of other phases, also mono- and bimetallic oxides, cannot be excluded. Specially, the formation of bimetallic $NiWO_4$ and $NiMoO_4$ could occur, but only in low concentrations based on the observed regular formed particles with a small particle size and a homogenous composition.

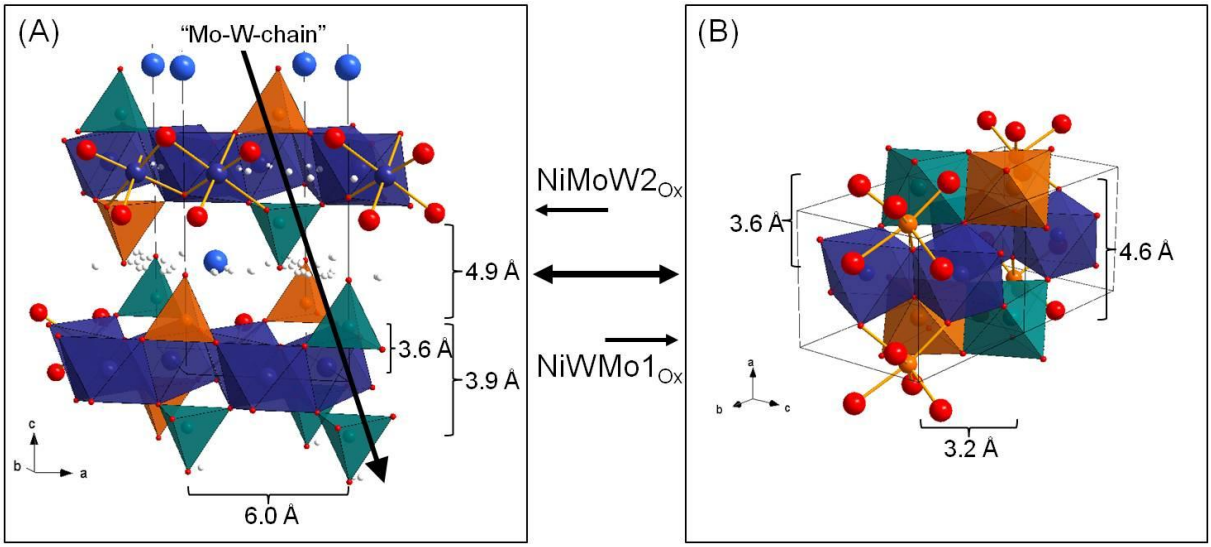

Figure 22. The idealized proposed coordination symmetries and polyhedra connectivity for the trimetallic $NiWMo1_{Ox}$ and $NiMoW2_{Ox}$ oxides, whereat the real bonding situation is most probably somewhere in between structure (A) and (B). In (A) the half trigonal unit cell (c/2) of a layered structure based on $(NH_4)HNi_2(OH)_2(MoO_4)_2$ (ICSD #165342)[182] and in (B) two monoclinic unit cells (extended in b-direction) of a closed packed structure based on $NiWO_4$ (ICSD #15852)[83] are presented with blue octahedra for Ni, green polyhedra for Mo, orange polyhedra for W and circles for N (light blue), O (red) and H (white).

The trimetallic oxide $NiMoW2_{Ox}$ had a W to Mo ratio of 0.9:1.0, which makes the wolframite structure less likely than in $NiWMo1_{Ox}$. High ionic character for Ni^{2+}, associated hydroxyl groups, and Ni-O vibration bands were identified. Additionally, the incorporation of

ammonium ions and carboxylic acid was evident by Raman spectroscopy. The positions of the Raman vibrations, the Ni XANES and Ni FT-EXAFS of $NiMoW2_{Ox}$ as well as the UV-vis absorption bands and the Mo XANES were comparable to the spectra of $NiMo_{Ox}$ to a certain extent. Thus, the presence of a layered ammonium nickel metallate structure is very likely (Figure 22(A)). In literature, there are different preparation procedures for trimetallic Ni-Mo-W oxides, but their structures are just rarely determined.[47, 49, 51, 98, 238-239] For few materials, XRD patterns, similar to those of our materials, are reported with proposed layered structures.[51] Recently, Amaya et al. reported a layered ammonium nickel molybdate structure for a trimetallic oxide prepared by a hydrothermal method, which resulted in a semi-crystalline material and allowed phase identification via XRD.[47] Accordingly, the formation of a layered structure seems feasible for $NiMoW2_{Ox}$. The strong distortion of $[MoO_4]$-tetrahedra and $[WO_6]$-octahedra, the poor XANES LCF results, the very low density of W 5d states, the broad spectroscopic bands, and the Mo and W EAXFS point to an intense interaction of the three metals in the same structure. Especially, the Mo-W interaction is more pronounced in $NiMoW2_{Ox}$ compared to $NiWMo1_{Ox}$. The results suggest further that the coordination polyhedra of Mo and W have the same distorted symmetry and that they are connected (as concluded from the absorption edge energy and the cluster size). Polymerization of mixed metallic oxo-metallate species in solution is known to occur at pH values higher than 6, which was the case during the oxide synthesis.[75] The layered structure presented in Figure 22(A) exhibits well-ordered vacancies within the Ni layers and the isolated $[MO_4]$-tetrahedra connected to the same vacancy have the shortest M-M distance within the whole structure. This open structure is, therefore able to compensate polyhedra distortion and central atom displacement and allows condensation of Mo and W polyhedra. Accordingly, short Mo-W-chains of tetrahedral distorted octahedra could grow across the Ni layer (through the vacancies) and modify the structure towards a wolframite-like structure. The exact position and alignment of the mixed Mo-W clusters remains, however, undefined.

3. Conclusions

Four unsupported mixed metallic oxides were prepared with a pH controlled co-precipitation method and in detail characterized. These are two bimetallic, $NiMo_{Ox}$ and NiW_{Ox}, and two trimetallic oxides, $NiWMo1_{Ox}$ and $NiMoW2_{Ox}$. The combination of different analytical methods, such as XRD, Raman, UV-vis and X-ray absorption spectroscopy, as well as the systematic comparison of the investigated oxides with each other and with reference materials allowed the identification of the coordination geometries of Ni, Mo and W and the contained phases. The Ni to total metal ratio in the samples is between 0.4 and 0.6 and the Mo to W ratios are 1:2 and 1:1 in $NiWMo1_{Ox}$ and $NiMoW2_{Ox}$, respectively. The

bimetallic materials are crystalline and appear with irregular formed particles with different shapes and sizes, whereas the trimetallic oxides are X-ray amorphous composed by small, stacked spherical particles with a narrow particle size distribution. For all four oxides a strong interaction between the different metal oxide species is found and different distorted coordination geometries for Ni, Mo and W are identified. Nickel is present as Ni^{2+} in distorted oxygen octahedra in all samples. The bimetallic $NiMo_{Ox}$ oxide is mainly composed by a layered ammonium nickel molybdate $(NH_4)Ni_2(OH,H_2O)(MoO_4)_2$ with $[MoO_4]$-tetrahedra, whereas the predominant phase in NiW_{Ox} is the monoclinic closed packed $NiWO_4$ with $[WO_6]$-octahedra. The Mo and W environments in the trimetallic oxides is similar to those found in the bimetallic materials. However, the formed crystallographic structures is dependent on the Mo to W ratio, moreover Mo-W mixed phases are found. The Mo-W interaction is especially pronounced in $NiMoW2_{Ox}$, for which a layered ammonium nickel metallate structure similar to $(NH_4)Ni_2(OH,H_2O)(Mo_{0.5}W_{0.5}O_4)_2$ with highly distorted metal $[MO_4]$-tetrahedra is concluded. The multimetallic structure contained in $NiWMo1_{Ox}$ is better described with a distorted wolframite-type structure in the form of $NiMo_{0.33}W_{0.67}O_4$, which contains edge and corner connected distorted metal polyhedra.

Chapter 5

Distribution of metal cations in Ni-Mo-W sulfide catalysts

Jennifer Hein, Oliver Y. Gutiérrez, Eva Schachtl, Pinhong Xu, Nigel D. Browning, Andreas Jentys, Johannes A. Lercher

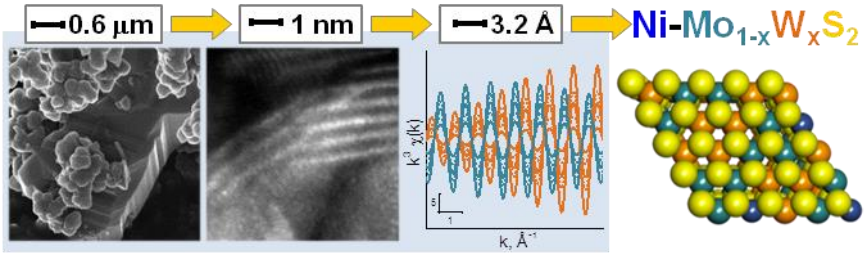

Stronger together than apart: structural features of multimetallic sulfides are described via advanced characterization. Intralayer mixed $Mo_{1-x}W_xS_2$ crystals have better interaction with the promoter Ni than bimetallic catalysts. Thus, the NiMoW formulation, with high proportion of Ni-$Mo_{1-x}W_xS_2$, is the most active for hydrotreating.

Accepted by ChemCatChem 2015; will be published in the special issue on "Advanced Microscopy and Spectroscopy for Catalysis"
DOI: 10.1002 cctc.201500788

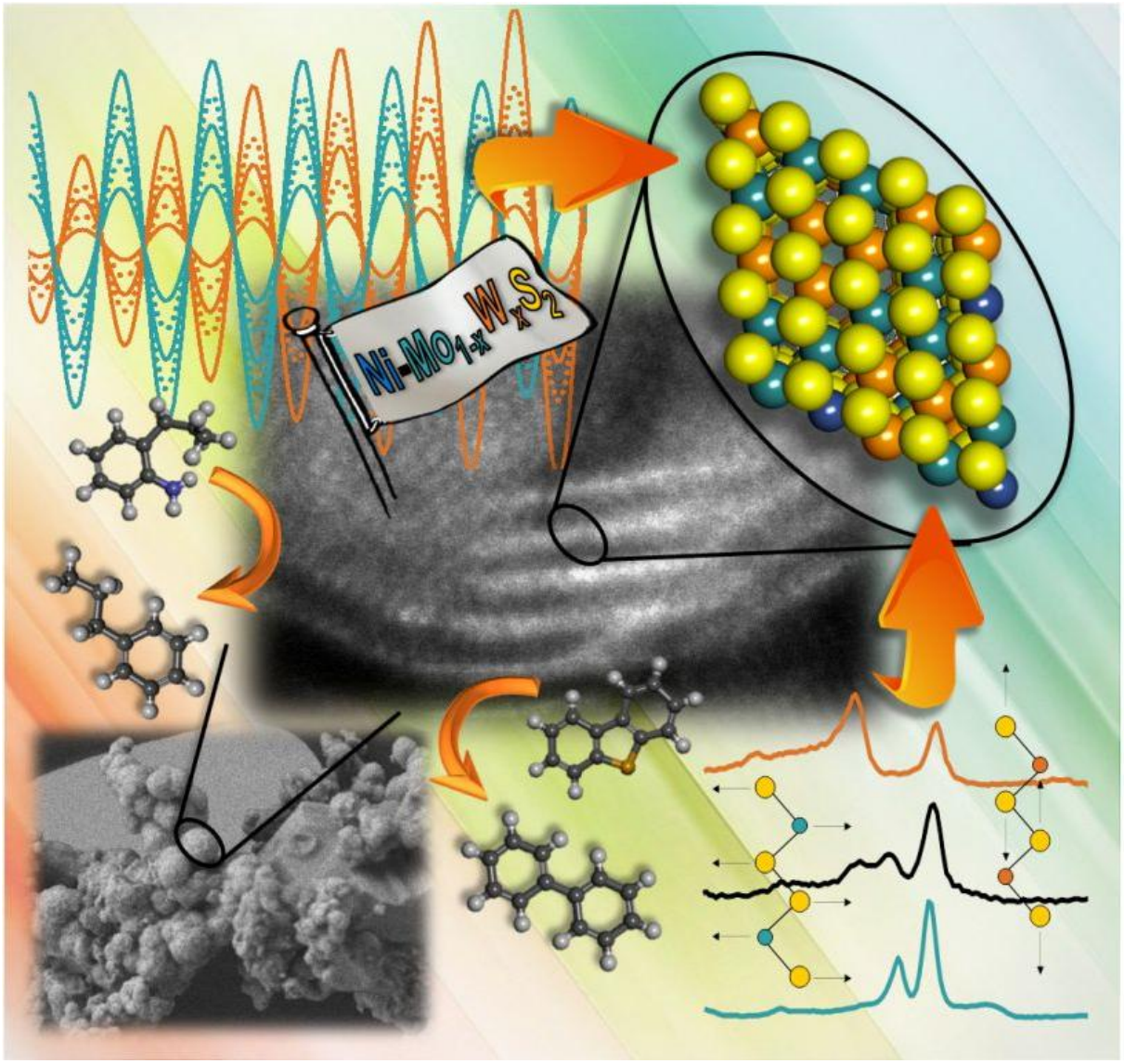
Ni-Mo1-xWxS2

1. Abstract

The distribution of metal cations in and the morphology of unsupported NiMoS, NiWS, and NiMoWS sulfide catalysts were explored qualitatively and quantitatively. In the bi- and trimetallic catalysts, $Mo(W)S_2$ nanoparticles are deposited on Ni sulfide particles of varying stoichiometry and sizes (crystalline Ni_9S_8, and Ni_3S_4 were identified). These nanoparticles are stacks of $Mo(W)S_2$ slabs with varying size, degrees of bending and mismatch between the slabs. High resolution electron microscopy and X-ray absorption spectroscopy based on particle modeling revealed a statistically distribution of Mo and W within individual layers in NiMoWS, forming intralayer mixed $Mo_{1-x}W_xS_2$. Ni is associated with MoS_2, WS_2, and $Mo_{1-x}W_xS_2$ creating Ni-promoted phases. The incorporation of Ni at the edges of the slabs was the highest for NiMoWS. This high concentration of Ni in NiMoWS as well as its long bent $Mo_{1-x}W_xS_2$ slabs were paralleled by the highest activity for nitrogen and sulfur removal from model hydrocarbons such as o-propylaniline and dibenzothiophene.

2. Introduction

MoS_2 and WS_2 are isostructural and isomorphic semiconductors with a layered structure. The ability of MoS_2 and WS_2 to activate H_2 and to catalyze hydrogenation and hydrogenolysis of C-N and C-S bonds makes them interesting catalysts. Thus, MoS_2 and WS_2 (bulk and supported) have been widely applied as catalysts in hydrotreating of oil fractions,[3, 6-8] biomass-derived feedstocks,[9] as well as in photo- and electrochemistry.[11-13] The wide applicability triggered activities to synthesize well-defined morphologies and in turn tailored band structures.[5, 240] There has been also impressive progress in atom-level characterization of MoS_2 and WS_2.[16, 22] Most of these studies, however, focused on model catalysts, prepared under conditions facilitating the analysis (e.g., in situ monolayer growth). Wet chemistry prepared sulfide materials similar to those used industrially are significantly more complex and hardly accessible for these advanced characterizations. This holds also true for the promotion of the MoS_2 and WS_2 by Ni^{2+} or Co^{2+} cations, which were mainly explored via averaging techniques such as XAS.[37, 42, 155]

While bimetallic catalysts are already challenging, trimetallic Ni-Mo-W sulfide materials make the task even more complex.[2, 44] Studies on the consequences of combining Mo and W in a single sulfide were in consequence only performed in the absence of Ni or Co.[19-20, 22]

The target of the current work is, therefore, to investigate the structure, morphology, and the distribution of catalyst constituents in three wet-chemically prepared sulfides qualitatively

and quantitatively. We address not only the distribution of W and Mo, but also the location and nature of the incorporated Ni. A comprehensive EXAFS study of all three metal edges in combination with HAADF-STEM was used and combined with TEM, XRD, and Raman spectroscopy. Systematic comparison of theoretical EXAFS of model clusters was used to analyze in detail the influence of the backscatter Mo, W and Ni at different distances. The impact of the physicochemical properties on catalytic activity was explored for nitrogen and sulfur removal from o-propylaniline and dibenzothiophene, respectively.

3. Experimental Part

Catalyst preparation. Two bimetallic, NiMoS and NiWS, and one trimetallic NiMoWS materials were prepared by a pH controlled co-precipitation in aqueous solution in accordance to Ref.[135]. The precursors were subsequently sulfided in 10 vol.-% H_2S in H_2 flow at 400 °C and 1.8 MPa for 12 hours. Ammonium heptamolybdate (AHM), ammonium metatungstate (AMT), Ni nitrate, aqueous ammonia and maleic acid were used as reactants during the synthesis.

Powder X-Ray Diffraction (XRD). The crystal structure of the samples was determined by X-ray diffraction using an X'Pert Pro PW 3040/60 (PANalytical) diffractometer equipped with a copper X-Ray tube, a Ni K_β-filter to obtain monochromatic Cu-$K_{\alpha1}$ radiation (0.154 nm) and a solid state detector (X'Celerator). The measurements were carried out with a 10 x 10^{-9} m slit mask in a range from $2\theta = 5°$ to $2\theta = 70°$ at the operating conditions of 45 kV and 40 mA. The sulfided catalysts were measured for 1 h with step size of 0.017 ° and scan time of 115 s per step and for selected reference materials 5 min scans with a step size of 0.017 ° and 10 s per step were used. The crystallographic phases were identified by using the Inorganic Crystal Structure Database (ICSD).[69] The Scherrer equation, was used to determine the stacking degree of sulfide slabs in the catalysts, knowing that the diffraction at around 14° 2θ corresponds to the (002) plane with interplanar distance of 6.1 Å (distance between the metal cation layers in MoS_2 or WS_2). The measured full width at the half maximum (FWHM) was corrected by the diffractometer typical line broadening of 0.1 estimated by instrument calibration.

Raman Spectroscopy. Raman spectra were recorded with a Renishaw Raman system (Type 1000, dispersive spectrometer) equipped with CCD detector and a Leica microscope DM LM. The excitation wavelength of 514 nm was generated by a multi-line argon-ion gas laser (Stellar-Pro Select 150 of MODU-Laser) operating at 20 mW power. The wavenumber accuracy was within 1 cm^{-1}. Sulfide catalysts and reference materials were analyzed under ambient conditions in the form of self-supported wafers.

Electron microscopy. The morphology and particle size of the different samples were analyzed by electron microscopic methods. Standard measurements of the sulfide catalysts were performed in transmission mode coupled with selective area electron diffraction (TEM-SAED) with a JEM-2011 (JEOL) with an accelerating voltage of 120 keV. The average length of the sulfide slabs in the catalysts was estimated by the length measurements of around 500 different bundles of metal sulfide slabs from different sample spots. Moreover, high resolution scanning electron microscopy coupled with energy dispersive X-ray spectroscopy (HR-SEM-EDX) was carried out with a high resolution FE-SEM, JSM 7500 F (JEOL) with EDX detector (Oxford). The HR-SEM micrographs were taken with the lower secondary electron imaging detector (LEI) and an accelerating voltage of 2 keV. Additionally, high-angle annular dark-field imaging with a scanning transmission electron microscope (HAADF-STEM) was performed using an aberration-corrected FEI Titan 80/300S. The device was operating at 80 keV and the HAADF collection inner angle was 75 mrad.

X-ray absorption spectroscopy (XAS). The structural properties of the sulfided catalysts were studied by X-ray absorption spectroscopy at the X1 beamline at Hasylab, DESY, Hamburg, Germany. The data set was completed with experiments performed on the BM 26A - DUBBLE, (Dutch-Belgian) beamline a*t* the ESRF, Grenoble, France. Spectra were recorded in transmission mode at the Mo K-edge (20 000 eV), W L_{III}-edge (10207 eV) and at the Ni K-edge (8333 eV). Prior to EXAFS measurements, the sulfide catalysts were re-sulfided in the stainless steel in situ flow XAS cell.

Prior to the analysis of the experimental XAS data, a systematic EXAFS modeling was performed using mixed $Mo_xW_yS_2$ clusters created with Accelrys Material Studio 7.0 on the basis of the crystallographic structure of pure MoS_2 and WS_2. These mixed disulfide phases were used to calculate the Mo-W and W-Mo phase shifts and backscattering amplitudes at different distances using FEFF9 and VIPER.[198, 241] All XAS spectra were analyzed with the Demeter-package (ATHENA and ARTEMIS, version 0.9.20) using FEFF6 and IFEFFIT.[199, 203] After background removal and normalization to the average post-edge height to one, the oscillations were weighted with k^3 and Fourier-transformed within the limit of k = 2.5 -14.0 $Å^{-1}$. The local environments of the Mo, W and Ni atoms in the sulfided catalysts were determined in k-space from the EXAFS. Single and multiple scattering phase shifts and backscattering amplitudes were calculated with FEFF[203] based on crystallographic information files (cif files) of the ICSD[69] and on the structure of model mixed $Mo_xW_yS_2$ clusters. The EXAFS at the Mo K-edge, W L_{III}-edge and at the Ni K-edge were simultaneously fitted. During fitting the Debye-Waller factor σ^2 and the distance r between two types of the metals were constrained to be equal (i.e. $r_{A-B} = r_{B-A}$) and the coordination numbers N_{A-B} and N_{-B-A} were constrained by the molar ratio of A and B in the catalysts ($N_{A-B}/N_{B-A} = n(B)/n(A)$). The R factor and the absolute

errors of all parameter, which are the estimated standard deviation and the statistical uncertainties of the starting parameter determined by IFEFFIT[199], were used to evaluate a certain fit result.

Catalytic activity studies. Kinetic studies were carried out in a continuous flow trickle bed reactor system equipped with high pressure mass flow meters and a HPLC pump. The stainless steel, glass-coated tubular reactor was loaded with 0.025 g of catalyst, diluted in 1 g SiC. The liquid samples were analyzed by an off line gas chromatography (HP 6890 GC) equipped with a flame ionization detector and 60 m DB-17 capillary column. The hydrotreating reactions were performed as temperature dependent experiments at constant space-time of 49 $h \cdot g_{cat}/mol_{OPA}$ and total pressure of 5.0 MPa. Prior to the activity test reactions, the precursors were activated in situ in 10 vol.-% H_2S in H_2 flow at 400 °C and 1.8 MPa for 12 hours. The reactions were carried out in excess of H_2 and with a mixture of hydrocarbons keeping the flow ratio of H_2 to liquid constant at 330 Ndm^3/dm^3. The initial reactant concentration was set to 1000 ppm N as o-propylaniline (OPA) in a mixture of 1000 ppm S as dimethyldisulfide (DMDS), 4.94 wt% hexadecane and 93.95 wt% tetradecane as solvent. Together with the OPA hydrodenitrogenation (HDN) activity, also the hydrodesulfurization (HDS) activity was studied by co-feeding 500 ppm S as dibenzothiophene (DBT) to the liquid feed. At the beginning of the experiment, a feed with OPA and DMDS was introduced at 370 °C. These starting conditions were kept for 48 hours, although steady state conditions were usually reached after 24 hours time on stream. Afterwards, the temperature was decreased to 360 and 350 °C and the liquid feed was changed to an OPA-DBT mixture to perform HDN and HDS simultaneously. After 30 hours at 370 °C, the activity of the parallel HDN and HDS was also tested at 360 and 350 °C. At the end of the run, the initial reaction conditions (370 °C and pure OPA feed) were applied again. For all experiments, the same results were found after the initial stabilizing time of 48 hours and at the end of the run.

4. Results and Discussion

Composition and crystallinity

The composition of NiMoS, NiWS and the trimetallic NiMoWS sulfide are summarized in Table 1. All materials had similar Ni molar fractions and the molar ratio of Mo to W in the trimetallic catalyst was 1.3. The XRD patterns showed $Mo(W)S_2$ and Ni sulfide phases as well as an X-ray amorphous material in all catalyst (Figure 1). The reference materials, MoS_2, WS_2, and Ni_3S_2 are shown for comparison. The reflections of all references are in agreement

with the data published in the ICSD database (MoS_2: #644245; WS_2: #202366; Ni_3S_2: #27521).[69] Sharp signals in the patterns of the sulfide catalysts correspond to different Ni sulfides. In NiMoS and NiMoWS, orthorhombic Ni_9S_8 (ICSD #63080) was the dominant phase (as indicated by the intense reflection at 27.4° 2θ) with traces of trigonal Ni_3S_2 (21.9° 2θ). The reflection at 26.6° 2θ in NiWS is assigned to the cubic phase of Ni_3S_4 (ICSD #57435). Additionally, Ni_9S_8 was found in low amounts in NiWS.

Table 1. Composition and of the unsupported sulfided catalysts.

Catalyst	Composition [mmol/g]			X_{Ni} [mol/mol]	Av. stacking degree of MoS_2 and WS_2 [a]
	Ni	Mo	W		
NiMoS	4.6	3.7		0.55	5.7
NiMoWS	4.0	1.8	1.4	0.56	5.1
NiWS	2.5		2.8	0.47	4.4

[a] Average number of slabs forming a MoS_2 particle as determined by applying the Scherrer-equation on the (002) reflection at 14.1° 2θ which, is associated to the interplanar distance of 6.1 Å.

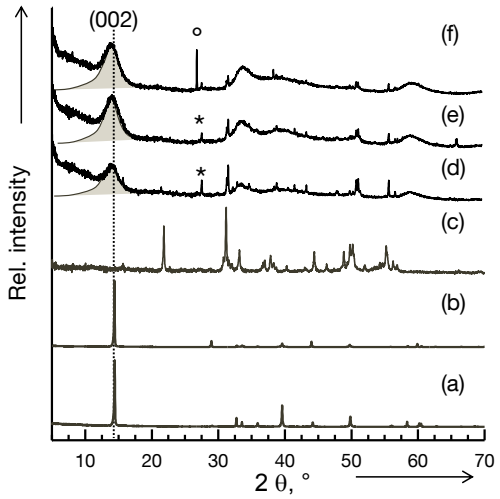

Figure 1. XRD pattern of the reference bulk materials MoS_2 (a), WS_2 (b) and Ni_3S_2 (c), and of the unsupported sulfide catalysts NiMoS (d), NiMoWS (e) and NiWS (f). The profiles fitted under the (002) reflection at around 14.2 °2θ (grey filled) were used to determine the stacking degree of the MoS_2 and WS_2 slabs. The most important reflection of Ni_9S_8 (*) and Ni_3S_4 (°) are indicated.

Broad reflections at 14.2, 33, 40 and 60° 2θ are assigned to hexagonal phases of MoS_2 and WS_2. The (002) reflection around 14.2° 2θ of the catalysts appeared at smaller angles compared to the references. In NiWS this reflection was observed at 14.0° 2θ, for NiMoWS at 14.1° 2θ, and for NiMoS at 14.2° 2θ. This indicates that the lattice parameters *d* (i.e., the distance between the metal sulfide layers) for the catalysts are between 6.32 and 6.23 Å, whereas the distance between the stacked layers in the bulk reference materials is 6.15 Å in WS_2 (14.4° 2θ) and 6.1 Å in MoS_2 (14.5° 2θ). This difference reflects disorder of the metal

sulfide layers, e.g., bending, which occurs when the slabs grow significantly longer in the x and y direction than in the z direction.[2] Additionally, line broadening and the amorphous background, especially at low diffraction angles, are an indication for turbostratic disorder and uncorrelated single sulfide layers.[154, 242]

Raman spectroscopic characterization

Raman spectra of catalysts and reference materials are shown in Figure 2. The assignment of the bands is described in the supporting information. Direct evidence for Ni sulfides was not obtained through Raman spectroscopy.

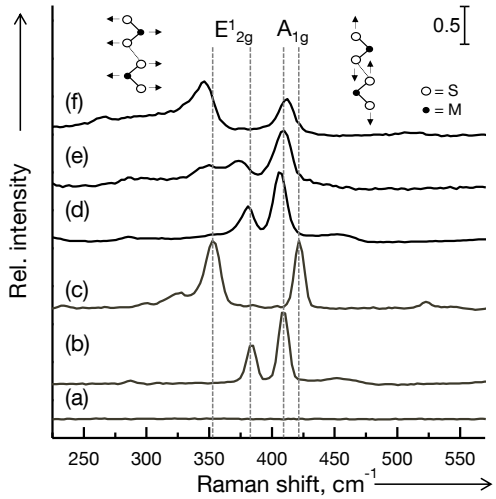

Figure 2. Raman spectra (λ_{ex} = 514 nm) of the reference Ni_3S_2 (a; no Raman bands), MoS_2 (b) and WS_2 (c), and of the unsupported sulfided catalysts NiMoS (d), NiMoWS (e) and NiWS (f). The shift of the most intense Raman bands of the references are indicated by the dotted vertical lines and the corresponding atomic displacement of the E^1_{2g} (left) and A_{1g} (right) mode is illustrated.

In the sulfide catalysts NiMoS and NiWS, only the sulfide A_{1g} and E^1_{2g} modes were observed (Figure 2 (d) and (f)). The corresponding bands were shifted to lower wavenumbers and were broader than the bands of the reference materials. For instance, the A_{1g} mode appeared at 405 cm^{-1} for NiMoS, and at 413 cm^{-1} for NiWS (in the reference materials this band appeared at 409 cm^{-1} for MoS_2 and 421 cm^{-1} for WS_2). The downward shift was attributed to weaker metal sulfur bonds caused by the low stacking degree in the catalysts and the concomitant weak van der Waals forces, which allow atom displacement.[243] The asymmetry of the bands of A_{1g} and E^1_{2g} modes was concluded to be caused by highly bent slabs, which influenced the symmetry selection rules leading to a second-order Raman signal, which overlapped with A_{1g} and E^1_{2g} bands.[91] The spectrum of NiMoWS (Figure 2 (e)) appears to be a combination of the spectra of the bimetallic catalysts. The band at 410 cm^{-1} is assigned to the A_{1g} mode of Mo-W composite species.[51] The bands at 374 cm^{-1} and 349 cm^{-1} are assigned to E^1_{2g} modes of Mo-S and W-S, respectively, in agreement with

observations when W systematically replaced Mo in Mo(W)S_2 crystals.[20] The shift of both E^1_{2g} modes, compared to the references MoS_2 and WS_2, is attributed to a structural disorder of the sulfide slabs.

Electron microscopic characterization

Figure 3(C) shows a representative HR-SEM image of NiMoWS. The microstructure of the catalysts consists of large Ni_xS_y crystals (only Ni and S in a ratio of 1:1 are observed by EDX mapping) covered by spherical particles identified as MoS_2 or WS_2 by EDX mapping. Interestingly, Ni and S were identified across the whole sample, whereas Mo and W were detected only in the round pellets. The characterization by scanning He ion microscopy (SHIM) of all catalysts confirms the observations made by HR-SEM (supporting information).

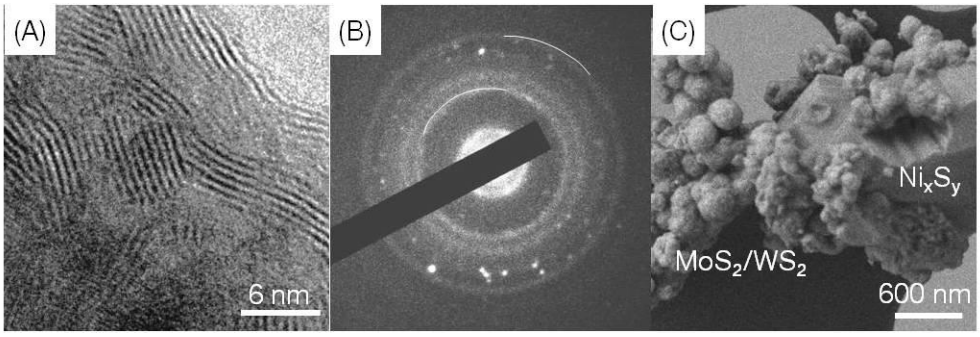

Figure 3. Representative electron microscopy images study of sulfide NiMoWS; TEM image (A), selective area electron diffractogram (B) and HR-SEM image (C). The rings in (B) and stacked pellets in (C) are identified as MoS_2 and WS_2 phases whereas the dots in (B) and the large particles in (C) belong to different Ni sulfides.

Micrographs obtained by TEM (Figure 3A for NiMoWS and S1) show that the sulfide agglomerates contained crystalline domains of different size and morphologies. The averaged stacking degree of around five for NiMoWS in the small crystals is in good agreement with the values obtained from XRD (Table 1). Furthermore, the structural disorder, i.e., bending (the MoS_2 slabs are not straight along the x and y axis) and random orientation of the crystal domains observed in the micrographs is consistent with the increased lattice parameters in z direction derived from XRD and the shifts and asymmetry of the Raman signals of the A_{1g} and E^1_{2g} modes. The longest slabs were found for NiMoWS with an average length of 20 nm, whereas slabs of 15 nm and 10 nm were present in NiWS and NiMoS, respectively. The presence of Ni_xS_y species associated to WS_2 and MoS_2 was confirmed by electron diffraction (SAED) of selected area. For instance, Figure 3 (B) shows the SAED of NiMoWS, where the dots corresponded to single Ni_9S_8 crystals (interplanar distances of 2.8, 2.6, 2.3, 1.8 and 1.7 Å according to ICSD #63080[69]). The presence of MoS_2/WS_2 phases was indicated by the broad rings in agreement with the broad reflections in the XRD patterns.

Hence, all catalysts are concluded to contain mixtures of sulfide phases. MoS_2 or WS_2 slabs form stacks with a relatively high degree of disorder, i.e., bending and misalignment among them. In turn, these microcrystalline domains agglomerate with random orientations forming spherical particles. Nickel sulfides exist in a variety of phases and particle sizes ranging from very large (few microns), which act as support for $Mo(W)S_2$ agglomerates and may produce diffraction patterns (Figure 3(B)), to small particles, which seem to be occluded inside the $Mo(W)S_2$ agglomerates.

Aberration corrected HAADF-STEM with atomic resolution was used to analyze the sulfide slabs with their basal (001) plane parallel and perpendicular to the electron beam (Figure 4). Figure 5(A) shows a representative HAADF-STEM image of the top view of the basal plane of NiMoWS. The fact that particles do not exhibit sharp edge structures is attributed to the non-aligned terminations of the stacked sulfide slabs.[244] The distance between the bright spots assigned to Mo or W atoms is around 0.6 nm, which matches the distance of the second metal-metal coordination sphere of the hexagonal lattice of metal disulfides (5.48 Å). Additionally, the ADF profile shows weak signals in a distance of 0.2 nm from W and Mo, which are assigned to S atoms.[22, 244] The appearance of relatively bright and dark spots with different contrast (within 3 Å) next to each other in Mo or W positions hints to the presence of projections of metal atoms with very different averaged molar mass in the same sulfide slab. We propose that this corresponds to the preferred presence of Mo and W forming bimetallic sulfide slabs, as also indicated by Raman spectroscopy. Such differences in Z-contrast were also used to deduce the formation of mixed $Mo_{1-x}W_xS_2$ layers by ADF studies of model $Mo_{1-x}W_xS_2$ particles combined with atomically resolved electron energy loss spectroscopy (EELS).[22]

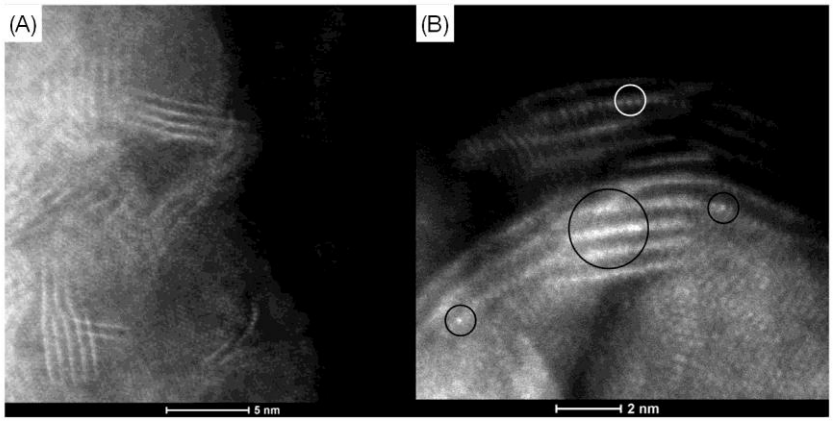

Figure 4. Aberration-corrected HAADF-STEM image of the sulfided NiMoWS catalyst; (A) overview image at 300 keV, (B) side view in [001] direction at 80 keV. The brighter atoms indicate the heaviest element in NiMoWS, i.e. W atoms (marked by the circles).

In contrast to microscopy studies of monolayers or cleaved single crystals reported,[5, 16, 244] strong Z-contrast of atoms and perfectly resolved ADF images are not expected for the multi-

layer bent structures studied. On the other hand, Ni atoms, if incorporated to the $Mo(W)S_2$ structure should be located at the edges of the slabs, according to the Co(Ni)-Mo-S model. However, identification of a third element by differences in Z-contrast was not possible due to the less defined edges of the slabs and the qualitatively nature of the HAADF-STEM image analysis. In order to unequivocally stablish the formation of mixed Mo-W sulfides within one layer level and to elucidate the interaction of $Mo(W)S_2$ with Ni, detailed analysis of the X-ray absorption spectra is required.

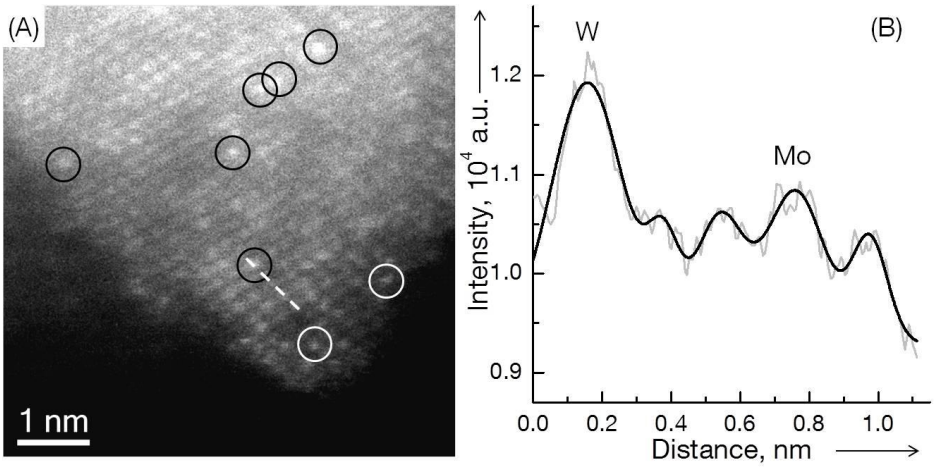

Figure 5. Representative aberration-corrected HAADF STEM image at 80 kV of the sulfided NiMoWS catalyst; (A) top view, MS_2 [001] direction along the electron beam, (B) distribution of the ADF counts along the indicated white line in (A). The circles indicate the heavier and therefore brighter W atoms.

X-ray absorption spectroscopy

The formation of intralayer $Mo_{1-x}W_xS_2$ slabs in NiMoWS has to be reflected by Mo-W and W-Mo contributions at 3.16 Å, while the scattering between Ni and the other metals should be observed in higher coordination spheres. The X-ray absorption near edge structure (XANES) at the Ni and Mo K-edge as well as at the W L_{III}-edge are summarized in the supporting information (Figure S3). The corresponding Fourier transforms (FT) of the k^3 weighted extended X-ray absorption fine structure (EXAFS) are presented in Figure 6. Detailed descriptions of the XANES and of the corresponding linear combination fittings are presented in the supporting information.

The first contributions in the Fourier transforms of the EXAFS at the Ni K-edge of the catalysts (Figure 6(A)), at around 2 Å (not phase-shift corrected) is assigned to Ni-S[155] contributions, which shifted to lower distances compared to Ni_3S_2. A second pronounced contribution at around 3.5 Å (not phase-shift corrected) was assigned to Ni-Ni contributions in Ni_3S_2 (ICSD #27521[69]). In the catalysts, this contribution is very weak.

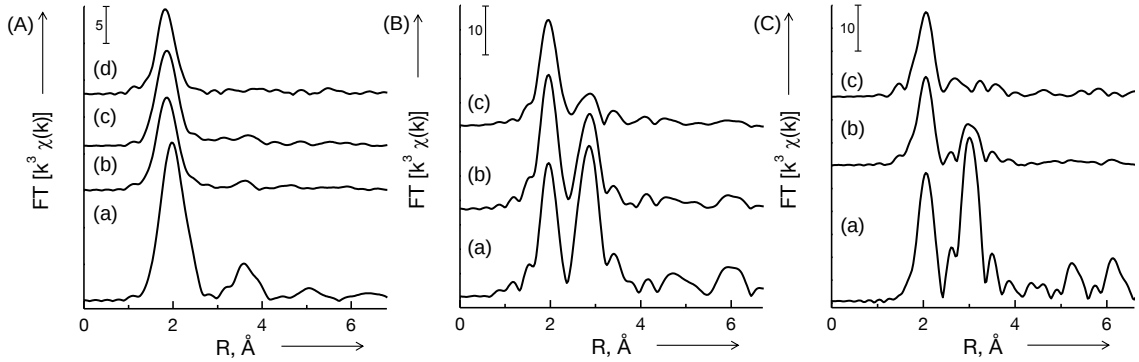

Figure 6. Fourier transforms of k^3 weighted EXAFS at the Ni K-edge (A), Mo K-edge (B) and W L_{III}-edge (C) of the references Ni_3S_2 (A,a), MoS_2 (B,a) and WS_2 (C,a) as well as of the catalysts NiMoS (A,b and B,b), NiMoWS (c) and NiWS (A,d and C,b).

The FT of the EXAFS at the Mo K-edge and at the W L_{III}-edge are shown in Figure 6(B) and Figure 6(C), respectively. The contributions of Mo-S[155] and W-S[33] were observed around 2 Å (not phase-shift corrected). The same distances (and similar intensities at the Mo K-edge) were found for the references and the catalysts. The second shell contributions at around 3 Å (not phase-shift corrected) at both edges were assigned to metal backscatter within the Mo(W)S_2 structure.[33, 155] At both edges (Mo K, and W L_{III}), the metal-metal contributions were weaker in the catalysts than in the references. In NiMoWS the intensities of the second shell contributions were even lower than the EXAFS of the bimetallic one. The weak metal-metal contributions at around 3 Å in NiMoWS are explained by the rather poor alignment of the atoms in the short and bent MoS_2 or WS_2 slabs.[33, 245] However, this apparently contradicts the conclusions from XRD, Raman spectroscopy and electron microscopy that the slabs in NiMoWS are ordered and are the largest among the studied materials. The reason for the weak metal-metal contributions in the FT is attributed to the specifics of the k^3 weighted EXAFS of the catalysts at the Mo K-edge and W L_{III}-edge and the corresponding bulk reference materials in Figure 7 (the k^3 weighted EXAFS functions of the samples at the Ni K-edge are presented in Figure S7 of the supporting information). Note that the amplitudes of the oscillations were weaker for the catalysts and the fine structure was less pronounced. Moreover, at the Mo K-edge and the W L_{III}-edge, the EXAFS of the trimetallic NiMoWS catalyst was different from the reference and the bimetallic catalysts between 9 and 16 $Å^{-1}$.

These differences in the EXAFS could be caused by neighboring atoms with opposite backscattering phases like Mo and W,[21, 50] resulting in destructive interference. This is in line with the intralayer $Mo_{1-x}W_xS_2$ mixed sulfides suggested by HAADF-STEM[31,32]. To assign the amplitudes and phase shifts of the M-M absorber-backscatter pairs, a series of mixed $Mo_{1-x}W_xS_2$ model clusters were generated based on the structure of MS_2 and the corresponding EXAFS were calculated. Special emphasis was given to the different

backscattering of Mo and W atoms at the Mo K and at the W L_{III}-edges, respectively. Intralayer and interlayer mixtures were included as model clusters as well as different intermetallic arrangements and coordination numbers.

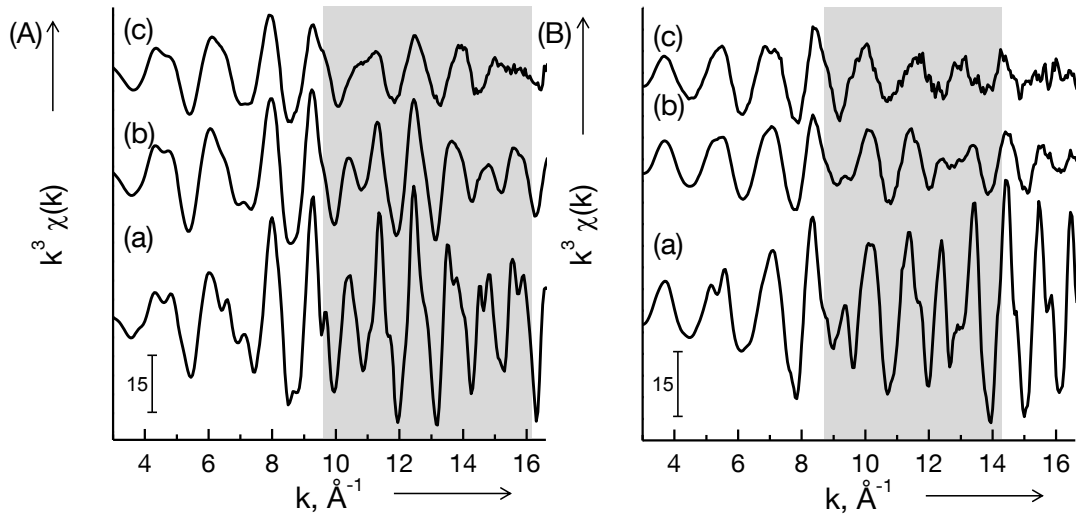

Figure 7. EXAFS at the Mo K-edge (A) and at the W L_{III}-edge (B) of MoS_2 (A, a), WS_2 (B, a) and of the catalysts NiMoS (A, b), NiWS (B, b) and NiMoWS (c). In the grey highlighted region, the EXAFS differ strongly from each other.

EXAFS of interlayer and intralayer mixed $Mo_{1-x}W_xS_2$ model particles

Thus, a MoS_2 particle (16x16 Å) was created by using 5 hexagonal unit cells in a- and b-direction, which corresponds to two stacked sulfide layers containing 5 Mo atoms in a and b-direction (presented in the supporting information as Particle 1). The EXAFS function and its Fourier transformation are presented in Figure S8. The oscillations of the Mo-S scattering dominate in the lower k region up to 8 Å^{-1}, whereas the metallic backscatter (i.e., the element with the higher molecule weigh) determines the backscattering in the higher k region. As predicted by the EXAFS function,[220] the most intense oscillations were found for the two next neighbors at $r_{Mo\text{-}S}$ = 2.41 Å and $r_{Mo\text{-}Mo}$ = 3.16 Å. However, the backscattering of the more distant neighbors is needed to describe the structure as visualized by Figure S8(C) and (D). Note that the approach using the crystallographic structure describes perfectly ordered, and large particles (where most of the atoms have full coordination) leading to the highest possible intensity of the oscillations. The coordination number of the next neighbors and at a distance of 6.42 Å, i.e., $N_{Mo\text{-}S}$ and $N_{Mo\text{-}Mo}$ is therefore 6 for the model Particle 6.

In distorted particles, the structural disorder leads to a decrease in the intensity of the oscillations at higher k values, which are typically accounted for in the analysis of the EXAFS by including higher Debye-Waller terms. However, the metal-metal coordination number is reduced for MoS_2 particles with high distortion and disorder, especially at the particle

edges.[245] Bending or distortion, as observed for the investigated sulfides, causes also differences in the bond distances of the metal-metal neighbors for a few atoms such as in edge distorted particles. Therefore, bending could reduce the coordination number at the specific distance. This is the focus of an ongoing theoretical EXAFS investigation. For the present case, it suffices to understand the intermetallic interactions using the small 5x5 particles with two layers and the central metal atoms as absorber.

Let us analyze next the incorporation of W into the MoS_2 lattice. For the first possibility of model clusters, interlayer mixed $Mo_{1-x}W_xS_2$ particles, Mo and W disulfide layers were stacked in different sequences to reach a stacking degree of 6 (as found by TEM and XRD for NiMoWS). The chosen stacking sequences were *abbaab* and *ababab*, where a stands for the [MoS_2] layer and b for the [WS_2] layer. The Mo-W coordination number at 6.42 Å was varied from 0 for a monometallic disulfide slab over 3 for the *abbaab* stacking sequence to the maximum number possible of 6 in the *ababab* sequence. Additionally, clusters of different sizes and shapes were created.

Selected clusters are presented in the supporting information as particle 2, and the corresponding EXAFS and FT at the Mo K-edge are shown in Figure 8. In comparison to the pure MoS_2 cluster, the Mo EXAFS has new weak features at 12.5 and 15 $Å^{-1}$, especially for $N_{Mo-W} = 6$ (Figure 8(A,c)). However, the presence of W in the next sulfide layers is just slightly noticeable in the Mo EXAFS and FT. Increasing size or a hexagonal shape for the sulfide layer does not change the EXAFS oscillations. These observations demonstrate that the distance to the next layer at 6.42 Å is too far away to influence the EXAFS of the absorber Mo atom significantly.

On the other hand, the particle size or shape does not influence the calculated phase shifts and amplitudes for the central Mo atom, while the coordination number averaged over the whole particle is influenced by size and particle shape (vide infra). The squared MoS_2 particle with 5x5 Mo atoms (Particle 1) has average $N_{Mo-S} = 5.2$ and $N_{Mo-Mo} = 4.5$. These values increase with particle size and change with the shape. For the 9x9 *abbaab* $MoWS_2$ particle (Particle 2(b)) the coordination numbers were $N_{Mo-S} = N_{W-S} = 5.6$ and $N_{Mo-Mo} = N_{W-W} = 5.1$, whereas for the hexagonal ababab $MoWS_2$ particle with a diagonal of 27 Mo atoms (a good representation of the investigated catalysts) $N_{Mo-S} = N_{W-S} = 5.9$ and $N_{Mo-Mo} = N_{W-W} = 5.7$ were calculated (Particle 2(c)).

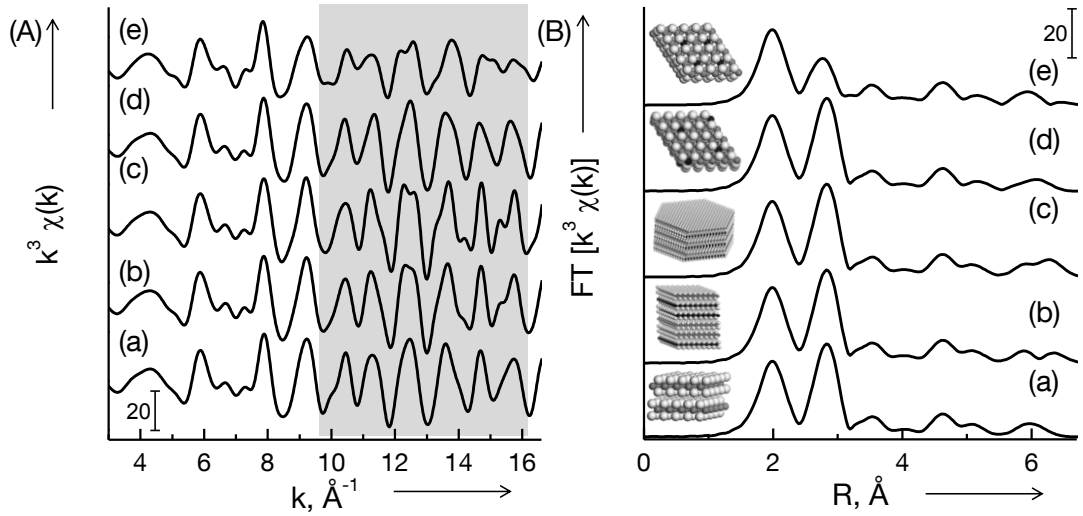

Figure 8. EXAFS at the Mo K-edge and the corresponding Fourier transforms of MoS_2 (a), $MoWS_2$ with Mo-W = 3 at 6.42 Å, stacking sequence abbaab (b), $MoWS_2$ with Mo-W = 6 at 6.42 Å, stacking sequence abababab (c), $MoWS_2$ with Mo-W = 2 at 5.48 Å (d), $MoWS_2$ with Mo-W = 2 at 3.16 Å (e). The used particles are also shown in supporting information (Color code: grey = Mo, black = W, light grey = S).

To determine the influence of Mo-W interactions on the EXAFS of model clusters with Mo and W in the same slabs, W atoms were incorporated at within a layer of MoS_2 (Particle 2(d) and (e) in the supporting information). These clusters contain 4 W atoms and 21 Mo atoms per sulfide layer and mixed metallic coordination numbers of 2. In particle 2(d), two Mo atoms were replaced by W at 6.33 Å and 5.48 Å with regard to the central Mo atom. In Particle 2(e), a coordination number of N_{Mo-W} = 2 was calculated at distances of r_{Mo-W} = 5.48 Å and 3.16 Å. The EXAFS and the corresponding FT calculated for these particles are shown in Figure 8. The EXAFS of the Particle 2(d) with long Mo-W distances were very similar to those of pure MoS_2, i.e., the coordination number of N_{Mo-W} = 2 is too low and the distance between Mo and W atoms is too large to influence the overall EXAFS. Interestingly, the presence of W at r_{Mo-W} = 3.16 Å in Particle 2(e) has a large influence on the EXAFS despite the low coordination number of N_{Mo-W} = 2. The EXAFS oscillations change between k = 10 - 16 Å^{-1} and the second contribution in the FT at around 3 Å is strongly reduced compared to pure MoS_2, similar to the EXAFS observed for the unsupported NiMoWS sulfide catalyst.

The analysis of the EXAFS of model clusters demonstrates that the formation of structures containing MoS_2 next to WS_2 phases cannot be ruled out by XAS. On the other hand, the theoretical EXAFS shows that the presence of the intralayer mixed $Mo_{1-x}W_xS_2$ EXAFS of NiMoWS is clearly established.

After concluding that Mo and W form intralayer $MoWS_2$ mixtures in NiMoWS, several intralayer $Mo_{1-x}W_xS_2$ clusters consisting of two layers with 5x5 atoms and varying N_{Mo-W} at

r_{Mo-W} = 3.16 Å were created and the corresponding EXAFS were calculated (two Particles 2(d) and 2(e) were already discussed). Other cluster in this series with Mo and W as central atom are presented as Particle 3 and Particle 4 in the supporting information. Clusters with N_{Mo-W} of 0, 1, 2, 3, 4 and 6 were generated by this approach. As the first metal-sulfur contribution at 2.4 Å was not influenced by the replacement of Mo by W (see Figure 8) only metal-metal scattering paths of the model clusters are discussed in the following.

The EXAFS of an absorber-backscatter pair is the result of the interference between the outgoing spherical wave of the photoelectron generated by the absorption process and the spherical wave backscattered from the neighboring atoms. The phase differences of both waves depend on the type of the atoms involved and distance between them. As an example, the phase functions (shown in the supporting information) were calculated at k = 11.34 A^{-1} as ϕ_{Mo-Mo} = 1.42*π, ϕ_{Mo-W} = 2.41*π at the Mo K-edge, and ϕ_{W-W} = 4.38*π, and ϕ_{W-Mo} = 3.39*π at the W L_{III} edge by using tabled phase shifts.[227] These values indicate that the phase functions of these particular absorber-backscatter pairs are shifted by π at both metal edges. Subsequently, the EXAFS of the metal-metal scattering paths were calculated with different coordination numbers (Figure 9).

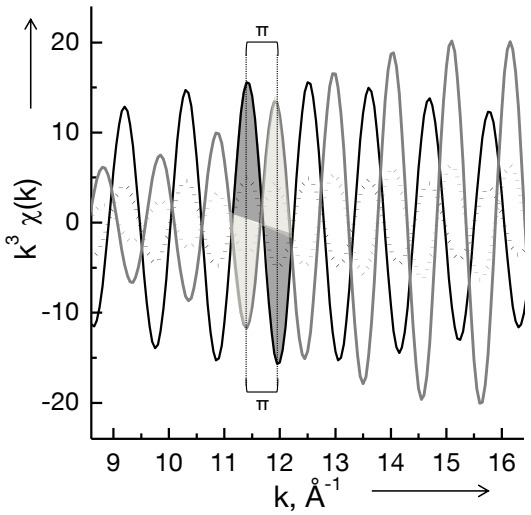

Figure 9. Calculated k^3 weighted Mo-Mo paths (black lines) and Mo-W paths (grey lines) at 3.16 Å at the Mo K-edge visualize the π shift between both scattering paths (solid lines corresponds to N(M-M) = 6 and dotted lines to N(M-M) = 2).

The π shift between the both scattering paths was observed in a wide range between 9 and 14 $Å^{-1}$ and was consistent for different coordination numbers and distances. The presence of both scattering paths in one sample leads to a destructive interference. Therefore, the EXAFS of an Mo:W = 1:1 solid solution in a $Mo_{1-x}W_xS_2$ system with a homogeneous dispersion of Mo and W is only determined by the metal-sulfur atom-backscatter pairs in the k range from 9 to 14 $Å^{-1}$. Figure S9 shows all involved single scattering paths and the

resulting overall EXAFS and FT of the 5x5 mixed sulfide cluster with $N_{Mo-W} = 3$ at $r_{Mo-W} = 3.16$ Å (Particle 3 (f)) at the Mo K-edge. The metal-sulfur paths are dominant, although complete extinction of the metal-metal contributions does not occur. All EXAFS and the corresponding FT for the clusters created (Particles 3 and 4) are presented in Figure S10 for the Mo K-edge and in Figure S11 for the W L_{III}-edge. The EXAFS oscillations and their FT at both edges strongly changed in the region k = 9 - 16 Å for clusters with varying intermetallic coordination number at r = 3.16 Å. The second metal-metal contribution steadily decreases with increasing mixed metallic coordination number starting from a value for N_{Mo-W} and N_{W-Mo} of 2. Furthermore, a splitting of the signal was observed and the lowest intensity was obtained for $N_{Mo-W} = 3$ and $N_{W-Mo} = 2$.

The experimental data of NiMoWS catalyst and the EXAFS of model clusters are compared at the Mo K-edge and the W L_{III}-edge in Figures 10 and 11. For the experimental data, the intensity was lower and less features are visible in the EXAFS as well as in FT compared to the model clusters. This indicates that the NiMoWS catalyst does not have a long-range crystalline structure and consists of different phases. Figures 10 and 11 also allow a qualitative comparison of the EXAFS of NiMoWS with those of the model clusters, the patterns of NiMoWS (shown in the lines labeled with (d)) fit well between the model patterns with N = 2 and N = 3. Therefore, mixed metallic coordination numbers between 2 and 3 exist in NiMoWS. Thus, for the final EXAFS fitting (multi-edge fitting), the theoretical FEFF-paths of the clusters with N (Mo-W) and N (W-Mo) of 3 and 2, respectively, were used.

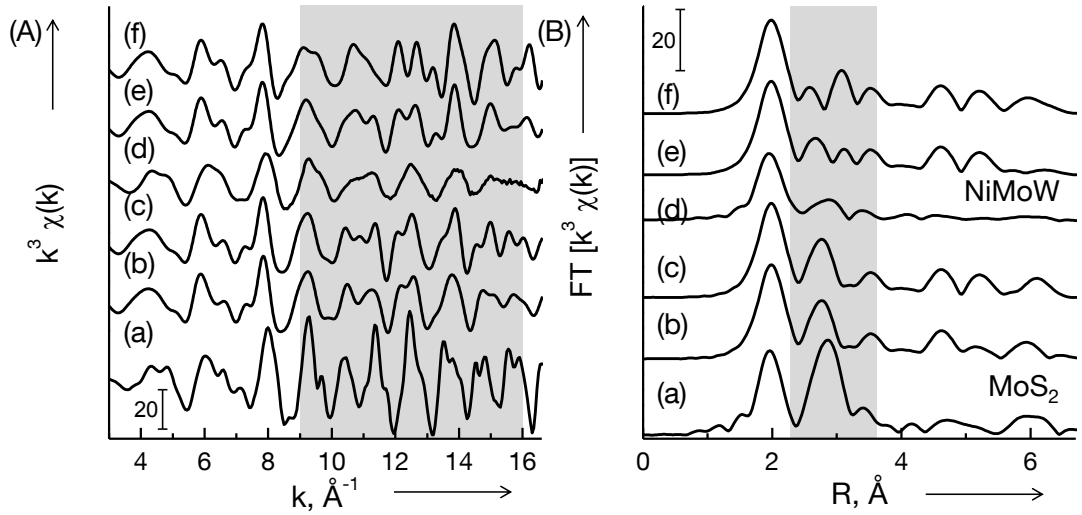

Figure 10. Experimental EXAFS of NiMoWS compared to EXAFS at the Mo K-edge (A) and the corresponding Fourier transforms (B) of model $MoWS_2$ with varying Mo-W coordination number N at 3.16 Å, namely MoS_2 bulk reference (a), $MoWS_2$ with $N_{Mo-W} = 2$ and $N_{W-Mo} = 6$ (b), $MoWS_2$ with $N_{Mo-W} = 2$ and $N_{W-Mo} = 2$ (c), NiMoWS catalyst (d), $MoWS_2$ with N = 3 (e) and $MoWS_2$ with N = 4 (f).

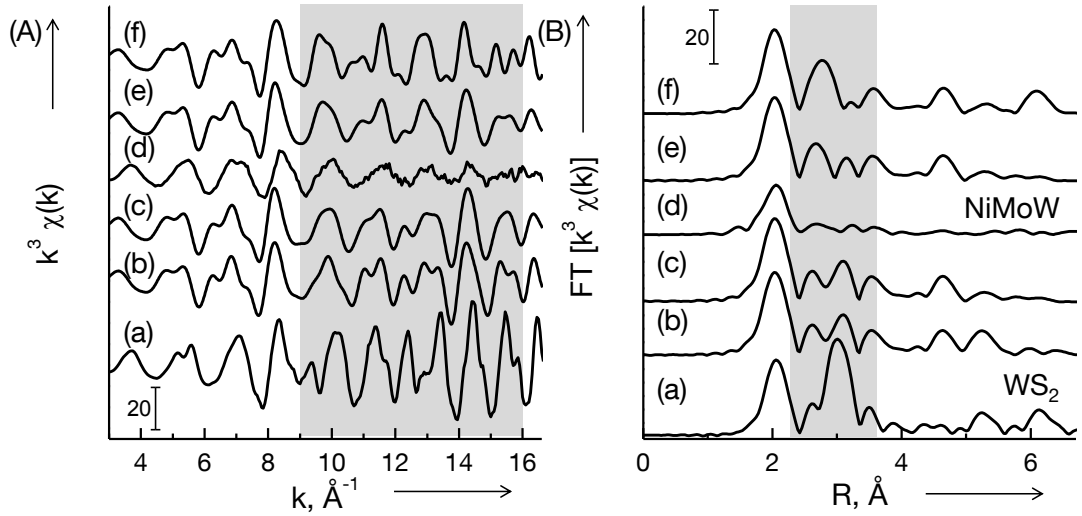

Figure 11. Experimental EXAFS of NiMoWS compared to the EXAFS at the W L_{III}-edge (A) and the corresponding Fourier transforms (B) of model $MoWS_2$ with varying W-Mo coordination number N at 3.16 Å, namely WS_2 bulk reference (a), $MoWS_2$ with $N_{W\text{-}Mo} = 2$ and $N_{Mo\text{-}W} = 6$ (b), $MoWS_2$ with $N_{W\text{-}Mo} = 2$ and $N_{Mo\text{-}W} = 2$ (c), NiMoWS catalyst (d), $MoWS_2$ with N = 3 (e) and $MoWS_2$ with N = 4 (f).

EXAFS analysis

In the discussion above, we have demonstrated that the X-ray spectra suggest the presence of intralayer $Mo_{1-x}W_xS_2$ clusters in NiMoWS in accordance with electron microscopy. As a final step of the XAS data analysis, a multi-edge, multi-scattering fitting procedure was applied to analyze the EXAFS of the sulfides at all metal edges simultaneously. The three references, MoS_2, WS_2 and Ni_3S_2 were fitted by using FEFF paths calculated from the crystallographic structure. The fit of the EXAFS and the corresponding Fourier transforms of the references are presented in Figures S12-S14 and Tables S3-S5. MoS_2 and WS_2 showed the expected trigonal-prismatic coordination environment with the maximum metal-sulfur and metal-metal coordination of six, respectively. Ni_3S_2 was difficult to fit, since the distanced to the 4 sulfur and the 4 Ni neighbors were very close. Moreover, the two distances for Ni-S neighbors at 2.26 and 2.27 Å could not be differentiated and were, therefore, fitted together resulting in an overall coordination number of 4.4. The most intense single scattering paths up to 4.1 Å were added to the analysis to obtain an appropriate fit.

Tables 2-4 summarize the best fit results for the k^3 weighted EXAFS data of the sulfided catalysts at the Mo K-edge, W L_{III}-edge, and Ni K-edge. For the sulfide NiMoS catalyst (Table 2), full Mo-S coordination environment was found at the Mo K-edge, and the bond distances match those corresponding to MoS_2 (Figures S15 and S16 show the experimental EXAFS data compared to the fit). The presence of Mo-O neighbors at short distances was not required during the fitting procedure. The $N_{Mo\text{-}Mo}$ in NiMoS was 5.1, which is below the

coordination number in the reference MoS_2 (N_{Mo-Mo} = 6). This implies that, although the metal was in a trigonal-prismatic environment, not all atoms have full coordination environment (i.e., metal atoms at the edges of the slabs). The value for N_{Ni-S} = 4.5 (Table 4) indicates that Ni is either tetrahedrally or pentagonally coordinated by sulfur, which fits to the observed pre-edge feature of the XANES (supporting information). The second contribution at r_{Ni-Ni} = 2.6 Å with N_{Ni-Ni} = 1.2, as well as the third contribution at r_{Ni-Ni} = 3.9 Å with N_{Ni-Ni} = 4.4 were smaller than those in Ni_3S_2. The metal-metal coordination numbers (Mo-Mo) and (Ni-Ni) smaller in NiMoS than in the references, which reflect lower crystallinity (smaller size of the MoS_2 slabs and Ni sulfide particles and large disorder). Moreover, other Ni sulfide phases than Ni_3S_2 are probably present as well. Additionally, a Ni-Mo contribution was observed at 2.7 Å with the coordination number of 0.2, which indicates that Ni is indeed associated with MoS_2. The quality of the fit was improved by 6.5 % after adding this contribution. The assumption of a Mo-Ni contribution and the associated constraints improved the fit further by 2 %.

Table 2. Best fit results for k^3 weighted EXAFS data of the sulfided catalysts at the Mo K-edge in k space.

Catalyst	Shell	r, Å	N	σ^2, Å^2	E_0, eV
NiMoS	Mo-S	2.40 (0.01)	6.2 (0.2)	0.0025 (0.0002)	0.74 (0.67)
R = 0.0013	Mo-Mo	3.17 (0.01)	5.1 (0.1)	0.0033 (0.0001)	
	Mo-Ni	2.68 (0.02)	0.3 (0.1)	0.0024 (0.0022)	
NiMoWS	Mo-S	2.40 (0.01)	5.2 (0.1)	0.0027 (0.0002)	1.52 (0.60)
R = 0.0055	Mo-Mo	3.16 (0.01)	3.1 (0.1)	0.0043 (0.0010)	
	Mo-W	3.17 (0.01)	1.6 (0.2)	0.0042 (0.0004)	
	Mo-Ni	2.68 (0.03)	0.6 (0.1)	0.0093 (0.0029)	

Abbreviations: r: distance, N: coordination number, σ^2: Debye-Waller like factor, E_0: inner potential; in parenthesis the absolute errors.

In NiWS, W-S and W-W contributions were found at the same distances as in the reference WS_2 structure. The experimental and fitted EXAFS and FT at the W and Ni edge, are shown in Figures S17 and S18, results of the fits are summarized in Table 3 and Table S5. The coordination numbers N_{W-S} and N_{W-W} were 4.5 and 3.1, respectively. Both are smaller than for the reference WS_2, which indicates smaller particle size and distortion in the catalyst. The addition of a W-O contribution at around 2 Å resulted in the degradation of the fit quality. Thus, its presence was excluded. The distances and coordination numbers of the

first Ni-S contribution match those of Ni_3S_2 (Table 4). The second and third Ni-Ni contributions appear at 2.57 Å (N_{Ni-Ni} = 0.5) and at 3.97 Å (N_{Ni-Ni} = 3.1), i.e., the coordination numbers are much smaller and a shift of the Ni-Ni contribution is observed compared to Ni_3S_2 and NiMoS. These observations also suggest smaller particle sizes of different Ni sulfide phases in NiWS. The fit was slightly improved by adding W-Ni and Ni-W contributions at 2.75 Å, which indicates that also in NiWS, Ni associates to the WS_2 slabs although probably to a minor extent compared to NiMoS.

Table 3. Best fit results for k^3 weighted EXAFS data of the sulfided catalysts at the W L_{III}-edge in k space.

Catalyst	Shell	r, Å	N	σ^2, Å^2	E_0, eV
NiWS	W-S	2.40 (0.01)	4.5 (0.2)	0.0037 (0.0002)	7.36 (0.44)
R = 0.0033	W-W	3.15 (0.01)	3.1 (0.4)	0.0045 (0.0005)	
	W-Ni	2.75 (0.05)	0.1 (0.1)	0.0033 (0.0030)	
NiMoWS	W-S	2.41 (0.01)	4.9 (0.2)	0.0044 (0.0006)	8.02 (1.23)
R = 0.0055	W-W	3.17 (0.02)	2.1 (0.3)	0.0042 (0.0006)	
	W-Mo	3.17 (0.01)	2.0 (0.2)	0.0042 (0.0004)	
	W-Ni	2.82 (0.04)	0.6 (0.2)	0.0030 (0.0021)	

Abbreviations: r: distance, N: coordination number, σ^2: Debye-Waller like factor, E_0: inner potential; in parenthesis the absolute errors.

The results of the EXAFS analysis and the corresponding FT of the trimetallic NiMoWS catalyst are summarized in Tables 2 to 4 and Figures S19, S20, and S21. The Mo-S and W-S coordination numbers were both around 5.0, lower than in NiMoS, but higher than in NiWS. This reflects an intermediate sulfidation (less complete sulfur coverage at the edges) state for the trimetallic catalyst. Furthermore, as predicted by the EXAFS of the model clusters, Mo-W and W-Mo contributions were found at 3.16 Å and 3.17 Å. The quality of the overall EXAFS fit improved by 25 % by using the FEFF-paths of the model $Mo_{1-x}W_xS_2$ cluster with N (Mo-W) of 3 (Particles 3(f) and 4 (f)) as a model to fit the experimental EXAFS. At the Mo K-edge, N_{Mo-Mo} = 3.1 and N_{Mo-W} = 1.6 were found, which leads to an average Mo-metal coordination number of 4.7 at around 3.2 Å. The average N_{Mo-Ni} in NiMoWS is 0.6, i.e., twice as high as in NiMoS. The coordination numbers at the W L_{III}-edge for NiMoWS were 2.0 for N_{W-Mo}, 2.1 for N_{W-W} and 0.6 for N_{W-Ni}. The latter two coordination numbers were higher than in the bimetallic NiWS catalyst. The finding of higher Mo-Ni and W-Ni coordination numbers in NiMoWS than in NiMoS and NiWS is important, because it indicates better interaction of Ni

on the sulfide slabs in the trimetallic than in the bimetallic sulfides. For this NiMoWS catalyst, N_{Mo-Mo} is higher than N_{W-W}, whereas N_{Mo-W} is lower than N_{W-Mo}. These observations suggest that the content of Mo and W within a sulfide slab is similar to that of the bulk (slightly more Mo than W, Table 1). Thus, most of the sulfide slabs must be $Mo_{1-x}W_xS_2$ particles containing both metals in one layer. N_{Ni-S} of 3.8 at r_{Ni-S} = 2.27 Å was found in NiMoWS, which is the lowest N_{Ni-S} value among all measured samples. N_{Ni-Ni} = 0.7 at 2.59 Å lies between the values compared to the bimetallic catalysts. The Ni-Mo contribution was found at a distance of 2.68 Å, which is the same as in NiMoS. A slightly longer distance was found for the Ni-W contribution in NiMoWS compared to that in NiWS (both are longer than the Ni-Mo distance). These mixed Ni-Mo and Ni-W contributions have higher coordination numbers than in the bimetallic catalyst, especially for Ni-W. The observations confirm that the Mo(W)-Ni incorporation was higher in the trimetallic than in both bimetallic catalysts.

Table 4. Best fit results for k^3 weighted EXAFS data of the sulfided catalysts at the Ni K-edge in k space.

Catalyst	Shell	r, Å	N	σ^2, Å^2	E_0, eV
NiMoS	Ni-S	2.27 (0.02)	4.5 (0.5)	0.0075 (0.0010)	3.00 (2.66)
R = 0.0013	Ni-Ni	2.60 (0.03)	1.2 (0.5)	0.0071 (0.0031)	
	Ni-Mo	2.68 (0.02)	0.2 (0.1)	0.0024 (0.0022)	
	Ni-Ni	3.88 (0.06)	4.4 (3.5)	0.0169 (0.0076)	
NiWS	Ni-S	2.26 (0.01)	4.4 (0.6)	0.0089 (0.0013)	2.35 (1.51)
R = 0.0033	Ni-Ni	2.57 (0.02)	0.5 (0.2)	0.0052 (0.0020)	
	Ni-W	2.75 (0.05)	0.1 (0.1)	0.0033 (0.0030)	
	Ni-Ni	3.97 (0.08)	3.1 (2.7)	0.0239 (0.0119)	
NiMoWS	Ni-S	2.27 (0.03)	3.8 (0.7)	0.0076 (0.0034)	2.85 (4.75)
R = 0.0055	Ni-Ni	2.59 (0.05)	0.7 (0.5)	0.0055 (0.0045)	
	Ni-Mo	2.68 (0.03)	0.3 (0.1)	0.0093 (0.0029)	
	Ni-W	2.82 (0.04)	0.2 (0.2)	0.0030 (0.0021)	

Abbreviations: r: distance, N: coordination number, σ^2: Debye-Waller like factor, E_0: inner potential; in parenthesis the absolute errors.

Catalytic activity

The kinetic data are compiled in the SI. Figure 12 summarizes the dependence of o-propylaniline (OPA) and dibenzothiophene (DBT) conversion rates on temperature. OPA is converted to propylbenzene (PB) via a C_{sp2}-N cleavage (direct denitrogenation route, DDN); and to propylcyclohexylamine (PCHA) via hydrogenation of the benzoic ring. This hydrogenation route (HYDN) continues with fast nitrogen removal to propylcyclohexene (PCHE) via Hoffman-elimination and hydrogenation to propylcyclohexane (PCH).[25] The HDS of DBT follows two pathways, direct desulfurization (DDS) and hydrogenation (HYDS). The former pathway has biphenyl (BiPh) as only product, whereas HYDS leads to tetrahydrodibenzothiophene (H-DBT), which is further hydrogenated to phenylcyclohexane (PhCH) or biphenyl (BiCH) via dodecahydrodibenzothiophene (DH-DBT).[109] The reaction networks for HDN and HDS are illustrated in Figs S22 and S23. All mentioned products were found for all three catalysts.

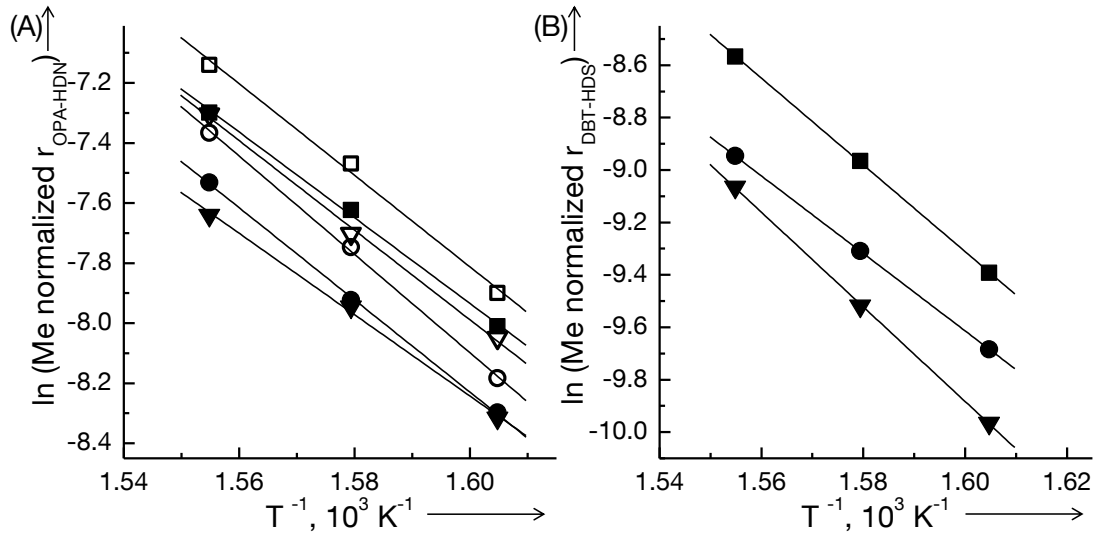

Figure 12. Hydrotreating activity. Presented are the metal content normalized reaction rates of the HDN of OPA (A) and HDS of DBT (B) of NiMoS (▾), NiMoWS (■) and NiWS (●). The HDN rates in absence of DBT are as well shown (open symbols ▿ □ ○). These plots are used for the determination of the apparent activation energies.

The rates normalized to the amount of metal atoms were identical for both HDN and HDS with the HDN rates being 4-5 times higher than rates of HDS (Figure 12). The nearly identical energy of activation for related reactions suggests that the differences are caused by differences in the concentrations of active sites. NiMoWS exhibited the highest conversion rates followed by the bimetallic NiWS and NiMoS, which had similar HDN rates. The presence of DBT decreased the HDN rates, especially on NiMoS, without showing impact on

the selectivity (Figure 13 for NiMoWS). The HDN rates in absence of DBT were higher for NiMoS than for NiWS, whereas NiWS had the higher HDN rates in the presence of DBT. In this regard, the HYDN route was faster than DDN by one order of magnitude.

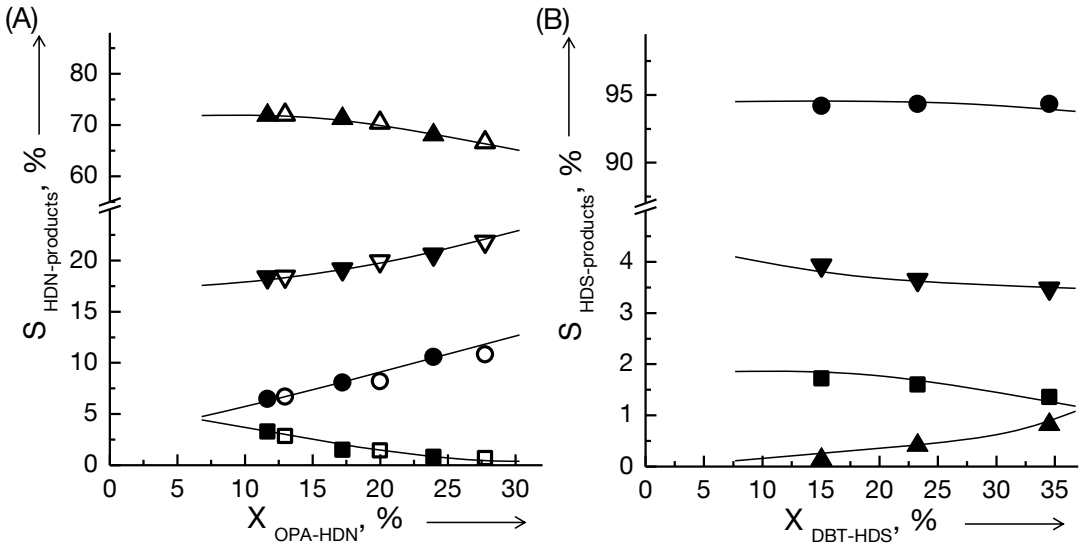

Figure 13. Selectivities along with conversion over NiMoWS for (A) OPA HDN and (B) DBT HDS. The products in (A) are PCHE (▲), PCH (▼), PB (●), and PCHA (■).The HDN selectivities are presented in the presence of DBT (black symbols ▲ ▼ ● ■) and in the absence of DBT (open symbols △ ▽ ○ □). The products in (B) are BiPh (●),BiCH (▼), H-DBT (■) and PhCH (▲).

In contrast, the HYDS route was slower than DDS also by one order of magnitude. The marked preference for DDS is illustrated by the selectivity towards BiPh, Figure 13(B). The apparent activation energies (E_a) for the DDN route were larger than those of the HYDN route. For instance, 191-230 kJ/mol (DDN) and 119-129 kJ/mol (HYDN), in the absence of DBT (Table S6). In general, the presence of DBT decreased the E_a values of both routes slightly, which is hypothesized to indicate that the adsorption of OPA becomes stronger in the presence of DBT (more negative adsorption enthalpies would decrease the apparent activation energies). The apparent activation energies for the DDS route of HDS were 137 kJ/mol for NiMoS, 139 kJ/mol for NiMoWS and 148 kJ/mol for NiWS. The E_a values of the HYDS route increased in the order NiWS < NiMoWS < NiMoS (the very low yields of the products of this route hinder quantitative discussion).

Structure activity correlations

Control experiment have shown that species of Ni sulfides are relatively unreactive for HDN and HDS, compared to Mo(W)S_2 phases. Therefore, in the following only Mo(W)S_2 species are discussed as catalytically active. All estimated rates in the HDS and HDN

reaction of the trimetallic NiMoWS sulfide catalyst were higher than those of bimetallic catalysts. The properties determining the activity of sulfide catalysts are the dispersion of the active phase and type of active sites, as both together control the concentration, availability, and its intrinsic activity. Especially, Lewis acidic sulfur vacancies (CUS) acting as adsorption sites and Brønsted acidic SH^- groups providing hydrogen are essential for hydrotreating.[3, 150] The SH^- groups are not only needed for the hydrogenation steps, but also to provide hydrogen during the cleavage of the carbon-heteroatom bonds and could act as weak adsorption site.[3, 25] The intrinsic activity is influenced by the nature of the active phase (WS_2 or MoS_2), the sulfidation degree and, the concentration of Ni. The dispersion is determined by the sulfide morphology and particle size. Therefore, the higher activity of NiMoWS suggests a higher concentration and/or availability of CUS and SH^- groups compared to the bimetallic sulfides.

The trimetallic sulfide has intralayer mixed $Mo_{1-x}W_xS_2$ slabs and an average metal-sulfur coordination number of 5, whereas the N_{W-S} was only 4.5 for WS_2 in NiWS. For NiMoS the N_{Mo-S} of 6 suggests fully coordinated Mo atoms in MoS_2. An average metal-sulfur coordination number lower than 6 for the W-containing sulfides suggest the presence of CUS (reduced edges) or to distorted sulfide structures. The metal-sulfur coordination is especially interesting to analyze for WS_2, since the sulfidation of W oxides is slower than of Mo oxides (W-O bond strength of 7.0 eV compared to 5.8 eV of Mo-O).[210] In turn, the activity of Ni-WS_2 has been correlated to its sulfidation degree.[246-247] The results demonstrate, however, that the contribution of oxide species is minor for both W containing catalysts as deduced from LCF and EXAFS, both pointing to a nearly complete sulfidation. Thus, the relatively low N_{W-S} values are attributed to the bent and less aligned morphology.

Differences in morphology and particle size were observed between the three unsupported catalysts. The highest stacking degree was observed for NiMoS, the largest sulfide slabs for NiMoWS, and the most disordered slabs for NiWS. Thus, we conclude that the low N_{W-S} value in NiWS is caused by distortion and bending of WS_2 slabs, which leads to variations in bond length and angles. Therefore, in the EXAFS not all sulfur neighbors were visible at the normal distance, leading to an underestimation of the sulfur coordination number.[245] The same is concluded to occur in NiMoWS as suggested by the strong sulfide slab bending. Such exposed sulfur atoms in a distorted environment are more labile and, hence, easier to remove to create CUS, which is connected to a formal reduction to W or Mo. Note that for the pure MoS_2 and WS_2 phases, the metal-S bond strength is 2.6 eV, and 2.9 eV, respectively [118], suggesting that only small differences in the reduction degree of MoS_2 and WS_2 are probable. However, the substitution of W by Ni might be more effective for WS_2 than for MoS_2, leading to higher CUS concentration than for promoted MoS_2.[33] In contrast, the well

ordered highly stacked slabs, i.e., high crystallinity, as observed for NiMoS influences the active site concentration negatively and, in turn, lowers the activity. Note in passing that increasing particle size and stacking degree increase are among the causes of deactivation. Thus, we conclude that both W containing catalysts have a higher CUS concentration, in line with their higher activity compared to NiMoS.

CUS and SH^- groups are located at the perimeter, i.e., at exposed edges of the Mo and W sulfide slabs. Considering hexagonal geometry, the number of Mo and W atoms at the edges of a sulfide particle derived from the average slab lengths, is 185 atoms for NiMoWS, 134 atoms for NiWS and 91 atoms for NiMoS per slab.[121] The trend for the edge atoms of the catalysts matches the found activity trend in HDS, i.e., the larger the slab the higher the HDS activity. However, the average fraction of Mo and W at the sulfide edge in relation to the total number of Mo and W atoms per sulfide slab[121] results in very low values for large particles such as in NiMoWS ($f_{Mo,W}$ = 0.06) and NiWS (f_W = 0.08). This fraction is used as a measure for the dispersion of supported sulfide systems, low dispersion accounts for low hydrotreating activity.[92, 109] This apparent contradiction is resolved by considering that the slabs of the catalysts are neither rigid nor straight. We speculate that the distortion of large sulfide slabs strongly increases the active site concentration.

Following the hypothesis that small, poorly crystalline sulfide particles are required for high catalytic activity, NiWS would be expected to be more active than NiMoWS based on its shorter sulfide slabs and the lower metal-sulfur coordination numbers. The question also arises as to why NiMoWS is more active than the strongly disordered NiWS, while at the same time the HDN rate on NiMoS was comparable to the HDN rate of NiWS. As discussed below the answer is related to the nature of the reactive perimeter and the way Ni influences it.

Hydrogenation has been found to scale with the concentration of SH^- groups, which are created by dissociative adsorption of H_2S and H_2 at CUS. The incorporation of Ni in MoS_2/Al_2O_3 increased the concentration of SH^- groups,[150] leading in turn to a correlation of the hydrogenation rates to the Ni concentration.[25, 248] The incorporation of Ni occurs on the edges of mixed sulfide phases, i.e., $Mo(W)S_2$ slabs.[144] All three materials contained large concentrations of Ni and Ni-promoted MoS_2 and WS_2 cations were identified by probe molecules (here not presented). In NiMoWS, the highest coordination numbers for Mo-Ni (Ni-Mo) and W-Ni (Ni-W) were observed as well as N_{Ni-S} of 3.8 (the lowest value in the series). The intermetallic coordination numbers in the bimetallic catalysts are low compared to NiMoWS with N_{Mo-Ni} and N_{W-Ni} of 0.3 and 0.1 in NiMoS and NiWS, respectively. Therefore, the interaction between the intralayer mixed $Mo_{1-x}W_xS_2$ phase in NiMoWS and the promoter Ni is concluded to be more effective than with the pure MoS_2 and WS_2 phase.

The formation of promoted sulfide phases has been demonstrated for Ni-W and bulk sulfides[33, 37, 46, 50] and is indicated by the significant mixed metallic coordination numbers (Mo-Ni or W-Ni). It is concluded that the concentration of Ni-promoted sulfide CUS was higher for NiMoWS than for NiMoS, which translates to an increased SH^- concentration. The interactions of Ni with WS_2 in NiWS are in contrast very weak.

It is hypothesized that the faster sulfidation rates for Mo species than for W increases the probability of incorporation of Ni. In addition to the Ni promoting species, the formation of a variety of Ni sulfide species is observed. The relatively low N_{Ni-Ni} values deduced from EXAFS compared to the reference Ni_3S_2 are attributed to the existence of several Ni-Ni distances and N_{Ni-Ni} values broadening the corresponding EXAFS. In line with this hypothesis, different Ni sulfide phases were observed by XRD and electron microscopy. Note, that in NiMoS, N_{Ni-Ni} at 2.6 Å is 1.2, whereas in NiWS and NiMoWS, N_{Ni-Ni} at around the same distance is 0.5 and 0.7, respectively. This indicates that the Ni_xS_y particles are, in average, smaller when interacting with WS_2 or $Mo_{1-x}W_xS_2$.[33]

Thus, the performance of unsupported NiMoS is dominated by the Ni promoted MoS_2 phase. Ni- and Mo-associated CUS are present, which act as adsorption and reaction sites for OPA, DBT and H_2. However, the overall concentration of active sites is lower compared to NiMoWS due to the morphology of NiMoS. Therefore, the reactants compete for fewer Ni-promoted sites, which is in line with the very low conversion rate for the HYDS route of DBT and the decrease of the conversion rate for the HYDN route in the presence of DBT. The DDN rates were hardly affected by DBT because the active sites for DDN are Mo associated sites instead of Ni-CUS.[25]

The morphology of WS_2 appears to be better suited to stabilize a high active site concentration. The fraction of Ni promoted WS_2 is relatively low compared to NiMoS, however, the high hydrogenation rates of DBT and OPA in presence of DBT (Figures S25-S26 and Table S6) might be due to higher intrinsic activity of the Ni-promoted W sites. This is consistent with the reported higher hydrogenation rates for Ni-W sulfides compared to Ni-Mo,[249] being more active for, e.g., HDS of substituted dibenzothiophenes (for which hydrogenation is critical in the reaction pathway).[250] [251] These sites are less active to convert OPA via the HYDN route in the absence of DBT compared to NiMoS. However, in the presence of DBT the HYDN rates decrease at most by 18 %, whereas in NiMoS a decrease of up to 43 % was observed. This suggests that the W associated sites are less affected by the presence of DBT.

The unsupported trimetallic NiMoWS catalyst exhibit a mixture of the sites and structural features found in NiMoS and NiWS. This is also indicated by the activation energies of the

catalytic routes being in between the values observed on NiMoS and NiWS. Moreover, this mixture results in a higher density of active sites. It is concluded that the intralayer mixture (Mo and W present in the same slab) is synergistic for the hydrotreating activity, stabilizing a concentration of Ni-promoted sites and a high concentration of SH^- groups. The intralayer $Mo_{1-x}W_xS_2$ phase enabled the growth of long slabs with a moderate stacking degree and a distortion providing a high edge area and, therefore, a higher CUS concentration than in NiWS. The higher concentration of Ni in the $Mo_{1-x}W_xS_2$ mixed phase compared to NiMoS is concluded to lead in turn to a higher SH^- group concentration.

5. Conclusions

All three mixed sulfide phases, i.e., NiMoS, NiWS, and NiMoWS offer interesting possibilities for hydrogenation, hydrodesulfurization as well as hydrodenitrogenation. The characterization suggests that all catalysts consist of mixtures of Ni containing $Mo(W)S_2$ and Ni sulfides (Ni_9S_8, Ni_3S_2, and Ni_3S_4). The $(Ni)Mo(W)S_2$ phase is formed by stacks of 4-6 sulfide slabs with some degree of bending and mismatch between the layers. Stacks of the sulfide particles agglomerate in random directions forming spheres with sizes in the submicron range on a mesoscopic level. The Ni sulfides show in contrast a broad distribution of particle sizes ranging from few microns, on which the $Mo(W)S_2$ agglomerates deposit, to small particles completely covered by the $Mo(W)S_2$ domains.

Microscopy images with atomic resolution showed metal (Mo or W) rich stacks of atoms with remarkable differences in Z-contrast in NiMoWS, which suggested the formation of intralayer $Mo_{1-x}W_xS_2$ particles (Mo and W in the same sulfide slabs), as well as the preference of alignment of homotopic cations in the projection direction of the STEM measurements. To confirm this hypothesis series of model clusters were constructed and the corresponding EXAFS were calculated. Models with interlayer $Mo_{1-x}W_xS_2$ particles (slabs of MoS_2 and WS_2 stacked in different sequences) and intralayer $Mo_{1-x}W_xS_2$ particles were considered. The analysis of the theoretical EXAFS showed that the presence of mixed Mo and W in different slabs did not influence the EXAFS and Fourier transforms of the Mo (K-edge). In contrast, the presence of W in close vicinity of Mo within a sulfide slab decreased the metal-metal (Mo-W or W-Mo) backscattering. This was caused by destructive interference between the Mo-W and Mo-Mo scattering pairs with opposite phases. The same effect was observed in the EXAFS and Fourier transforms of the NiMoWS catalyst, which suggested the formation of sulfides slabs with Mo and W.

The EXAFS fittings of bimetallic and the trimetallic sulfides confirms the presence of MoS_2, WS_2, in NiMoS and NiWS, respectively showing smaller coherent domains than the

reference materials. The EXAFS fitting of NiMoWS confirms the presence of intralayer $Mo_{1-x}W_xS_2$. The presence of Ni-Mo (Mo-Ni), and Ni-W (W-Ni) paths in all materials suggest that Ni is effectively interacting with MoS_2, WS_2 or $Mo_{1-x}W_xS_2$, allowing us to conclude that mixed Ni-Mo(W) sulfide phases were present in all catalysts. The values of the coordination numbers suggest that the most pronounced Mo(W)-Ni interaction occurs in the trimetallic NiMoWS. The nature of the promoting Ni species, i.e., single atoms (like in a classic Ni-Mo-S model[124]) or clusters[248] remains unresolved as evidence of Ni atoms at the edges of $Mo(W)S_2$ slabs and/or defined $Mo(W)S_2$ – Ni_xS_y phases[31] were not observed by microscopy. The small Ni-Ni coordination numbers suggest that a substantial fraction of Ni_xS_y consists of very small clusters or atomically dispersed Ni.

The catalytic properties (hydrodesulfurization of dibenzothiophene and hydrodenitrogenation of o-propylaniline) were governed by the concentration of accessible cations and the concentration of SH^- groups. The trimetallic catalyst had the highest concentration of active sites leading to the highest HDN and HDS rates. The trimetallic sulfide was, thus, concluded to have the largest specific perimeter. We conclude that the simultaneous presence of Mo and W in the same slab in NiMoWS retards the growth and favors nucleation of Ni promoting species, allowing so the largest fraction of Ni to be incorporated. The additional slow growth in z direction leads to a maximizing of the active sites at the perimeter of the particles.

Chapter 6

Physicochemical characterization and hydrotreating activity of unsupported Ni-Mo-W sulfide catalysts

Jennifer Hein, Oliver Y. Gutiérrez, Jinyi Han, Andreas Jentys, Johannes A. Lercher

A series of bimetallic and trimetallic Ni-Mo-W sulfide materials have been characterized and tested in the hydrodenitrogenation (HDN) of o-propylaniline and in the hydrodesulfurization (HDS) of dibenzothiophene. The bimetallic oxide precursors consisted of crystalline layered ammonium nickel molybdate and nickel tungstate. The addition of a third metal into the precursor led to the formation of oxides with structures depending on Mo to W ratio. The chemical environment of Mo, W, and Ni was similar in all precursors and the intermetallic interactions were retained during the gaseous sulfidation. Sulfide catalysts were comprised of mixtures between W(Mo)S_2 and Ni sulfides. Large Ni sulfide particles were covered by layered Mo(W)S_2 agglomerates with varying stacking degrees and lengths. Promotion of W(Mo)S_2 with Ni species and the formation of intralayer mixed $Mo_{1-x}W_xS_2$ in the trimetallic catalysts were evidenced by X-ray absorption spectroscopy. In a Ni-Mo-W sulfide catalyst, a high proportion of the $Mo_{1-x}W_xS_2$ phase resulted in a high Ni promotion, which was found to be more stable at high temperatures than Ni-W(Mo)S_2 in bimetallic catalysts. The activity of the catalysts is strongly influenced by the interaction of Mo and W with Ni and the accessibility of active sites determined by morphology. Accordingly, a bimetallic Ni-W, and a trimetallic Ni-Mo-W catalyst, with the highest proportions of exposed edges and Ni-promoted phases, respectively, exhibited the highest hydrotreating activities.

1. Introduction

The study of Mo and W sulfide catalysts (i.e., MoS_2, and WS_2) for hydroprocessing (hydrodefunctionalization and hydrogenation) is an active and attractive research field. Restrictive environmental regulations, rising demand for transportation fuels, and deteriorating quality of crude oils have driven the development of advanced catalytic formulations that are more active than the catalyst used few years ago.[7-8, 56, 252] A family of catalysts that stands out due to its high activity and stability in the most demanding hydrotreating conditions are bulk multimetallic sulfide catalysts.[2]

Hence, in recent years, many groups have studied the catalytic features of these systems in particular with respect to their exceptional activity. Special emphasis has been put on the role of the precursors,[51, 137, 253-255] sulfidation procedure, and concentration or interaction with the promoter.[31, 44, 239] On the fundamental side, the absence of a support has allowed to study the effect of the morphology on the performance of sulfide catalysts, e.g., stacking degree, and curvature of the sulfide layers.[93, 153, 256] However, the description of multimetallic bulk sulfide catalysts is challenging due to the formation of mixed sulfide phases, and the promotion mechanisms remain unclear.[31, 155, 235] On the other hand, most of reported studies focus on hydrodesulfurization (HDS), neglecting hydrodenitrogenation (HDN) despite of the high content of nitrogen in low quality feedstocks and its inhibition effects on the statutory removal of sulfur from crude oils.[155, 235, 254, 257]

Thus, in this work we perform the complete description of bulk sulfide catalysts (Ni-Mo, Ni-W, and Ni-Mo-W) and their corresponding oxide precursors by using X-ray diffraction, N_2-physisorption, electron microscopy, as well as Raman, UV-vis, and X-ray photoelectron and X-ray absorption spectroscopy. The physicochemical properties of the oxide precursors and sulfides are related to the catalytic performance in the HDN of o-propylaniline and HDS of dibenzothiophene. Our aim is to identify the properties required to obtain hydrotreating catalysts with high activity and stability for simultaneous HDN and HDS reactions.

2. Experimental Part

Catalyst preparation. Two bimetallic (Ni-Mo and Ni-W), and two trimetallic (Ni-Mo-W) catalyst precursors were synthesized by a pH controlled co-precipitation method in aqueous solution in accordance to Refs.[135, 235] For the Ni-Mo material, ammonium heptamolybdate (AHM), nickel nitrate, aqueous ammonia, and maleic acid were used, whereas for the NiW

catalyst, AHM was replaced by ammonium metatungstate (AMT). For the bimetallic materials, the molar ratio of the metals during the preparation step was 1:1 (Ni to Mo or W). Trimetallic materials were obtained by using AHM as well as AMT in the initial solutions with Ni:Mo:W molar ratios of 2:1:1 and 4:2:1, referred as NiWMo1 and NiMoW2, respectively. The sulfide catalysts were prepared by sulfidation of the precursors in 10 vol.-% H_2S in H_2 flow at 400 °C and 1.8 MPa for 12 hours. In the following, the precursors are denoted with the subscript "*Ox*" and the sulfide materials with no subscript.

Texture and elemental analysis. The BET surface areas were determined from the analysis of the N_2 adsorption isotherms at -196 °C. A PMI Automated BET Sorptomatic 1900 Series instrument (Thermo Finnigan) was used to carry out the experiments. Prior to the adsorption, the samples were evacuated at 120 °C for 4 hours. In the case of the oxide precursor, the pore size distributions were determined by recording the nitrogen desorption isotherms. Elemental analysis was carried out at the Microanalytical Laboratory of the TU München.

X-ray photoelectron spectroscopy (XPS). The XPS measurements of the sulfided catalysts were carried out with a Phi Quantera Scanning X-ray Microprobe instrument using Al K_α (hv = 1486.7 eV) radiation at Chevron Energy Technology Company in Richmond (CA), USA. The instrument is equipped with a hemispherical energy analyzer with multichannel detection and an energy resolution of 1.1 eV. The catalysts were mounted on double-sticky tape confining in an area approximately 0.8 cm x 0.8 cm. The tape was completely covered by the catalyst powder and the sample surface was carefully smoothed. For each catalyst, five analysis areas (1.2 mm x 100 micron) were selected for detailed spectral characterization. At each area, spectra were collected for C-1s, O-1s, S-2p, Ni-$2p^3$, Mo-3d and W-4f photoelectron peaks. Total spectral accumulation times were 100 minutes per analysis area while irradiating with 100 W of X-radiation. The binding energies (BE) were referenced to the C-1s peak (284.8 eV) to account for charging effects. The XPS spectra were de-convoluted using Gaussian/Lorentzian shaped curves and an iterative least square algorithm provided in Phi Multipak software. The areas of the peaks were computed following the fitting to quantify the Mo, W, and Ni species contents.

Powder X-Ray Diffraction (XRD). The crystal structures of the powdered samples were determined by X-ray diffraction using the X'Pert Pro PW 3040/60 (PANalytical). The Bragg-Brentano diffractometer was equipped with a copper X-ray tube (Cu-$K_{\alpha 1}$ radiation 0.154 nm), nickel K_β-filter and a solid state detector (X'Celerator). The measurements were carried out with a $10 \cdot 10^{-9}$ m slit mask in a range from 2θ = 5 ° to 2θ = 70 ° at 45 kV and 40 mA. Oxidic precursors and sulfide catalysts were measured for 1 h with a step size of 0.017 ° and scan

time of 115 s per step, whereas selected reference materials were measured for 5 min with a step size of 0.017 ° and 10 s per step. The crystallographic phases were identified by using the Inorganic Crystal Structure Database (ICSD).[69] The Scherrer equation, was used to determine the stacking degree of sulfide slabs in the catalyst, knowing that the diffraction at around 14° 2θ corresponds to the (002) plane with interplanar distance of 6.1 Å (distance between the molybdenum layers in MoS_2).

UV-vis Spectroscopy (DR UV-vis). The diffuse reflectance technique was applied to collect ultraviolet-visible-near infrared spectra using an Avantes AvaSpec-2048 fiber optic spectrometer equipped with a CCD detector array. The combined deuterium and halogen light source, Ava Light-DH-S-BAL, was used in combination with the optical fiber probe FCR-7UV400-2-SR-HT. Spectra of oxide precursors and reference materials were recorded under ambient conditions. The sample powders were placed in a Teflon sample holder providing 1 mm sample thickness. After normalization of the spectra in energy space, they were de-convoluted using a Levenberg-Marquardt algorithm implemented in the Fityk 9.7 software. The absorption bands were fitted by Gauss functions and an error function was used to describe the absorption edge. During the fitting procedure the FWHM of the Gauss functions were kept constants and reasonable limits for the peak positions were set. Each spectrum was de-convoluted with a minimum amount of parameter.

Raman Spectroscopy. Raman spectra were recorded with a Renishaw Raman Microscope (Type 1000, dispersive spectrometer) equipped with CCD detector and a Leica microscope DM LM. The used excitation wavelength of 514 nm was provided by a multi-line argon-ion gas laser (Stellar-Pro Select 150 of MODU-Laser) operating at 20 mW power. The wavenumber accuracy was within 1 cm^{-1}. All samples, oxide precursors, sulfided catalysts and reference materials, were analyzed under ambient conditions in the form of self-supported wafers.

Electron microscopy. The morphology and particle size of the different samples were visualized by different electron microscopic methods. The oxidic precursors were analyzed in the scanning mode (SEM) with the REM 5900 LV microscope (JEOL) with an accelerating voltage of 25 kV with a maximum magnification of $4.0 \cdot 10^4$ using secondary and backscatter electrons as well as energy-dispersive X-ray spectroscopy (EDX) mapping. The measurements of the sulfided catalysts were performed in transmission mode coupled with selective area electron diffraction (TEM-SAED) with the JEM-2011 (JEOL) operating at an accelerating voltage of 120 keV. The average length of the sulfide slabs in the catalysts was estimated by measuring around 200 different bundles of metal sulfide slabs from different sample spots. Additionally, studies using a scanning He ion microscope (SHIM) were carried

out at the Environmental Molecular Sciences Laboratory (EMSL) located at PNNL in Richland (WA), USA. The SHIM measurements were performed with a Zeiss Orion PLUS (Carl Zeiss SMT AG) instrument operating at 30 kV and with a beam current of 0.6 pA, the working distance was 10.6 mm.

X-ray absorption spectroscopy (XAS). The structural properties of the oxide precursor and sulfided catalysts were studied by X-ray absorption spectroscopy at the X1 beamline at Hasylab, DESY, Hamburg, Germany. The data set was completed with experiments performed on the BM 26A - DUBBLE, (dutch-belgian) beamline at the ESRF, Grenoble, France. Spectra were recorded in transmission mode at the Mo K-edge (20000 eV), W L_{III}-edge (10207 eV) and at the Ni K-edge (8333 eV). Prior to EXAFS measurements, the sulfide catalysts were resulfided in the stainless steel in situ flow XAS cell.

All spectra were analyzed with the Demeter- package (ATHENA and ARTEMIS, version 0.9.20) using FEFF6 and IFEFFIT.[199-200, 203] After background removal and normalization to the average post-edge height of one, the oscillations were weighted with k^3 and Fourier-transformed within the limit of k = 2.5 - 14.0 $Å^{-1}$. The local environments of the Mo, W and Ni atoms in the sulfide catalysts were determined in k-space from the EXAFS. Single and multiple scattering phase shifts and backscattering amplitudes were calculated with FEFF[203] based on crystallographic information files (cif files) of the ICSD.[69] Mixed metal Mo-W and W-Mo phase shifts and backscattering amplitudes were calculated by using self-created mixed $Mo_xW_yS_2$ cluster.[235] The EXAFS at the Mo K-edge, W L_{III}-edge and at the Ni K-edge were simultaneously fitted. The Debye-Waller factor σ^2 and the distance r between the metals A-B and B-A were constrained to be equal and the coordination numbers N for A-B and B-A were constrained by the molar ratio n of A and B in the catalysts ($N_{A\text{-}B} = n_B/n_A \cdot N_{B\text{-}A}$).

Kinetic studies. The kinetic hydrotreating studies were carried out in a continuous flow trickle bed reactor. The catalysts were loaded in their oxidic precursor state (0.025 g) and diluted with SiC (1 g). The hydrotreating reactions were carried out in excess of H_2 and with a mixture of hydrocarbons keeping a constant ratio of H_2 to liquid of 330 $Ndm^3 \cdot dm^{-3}$. The initial reactant concentrations were 1000 ppm N as o-propylaniline (OPA), 500 ppm S as dibenzothiophene (DBT) and 1000 ppm S as dimethyldisulfide (DMDS), in 4.94 wt.% hexadecane and 93.95 wt.-% tetradecane as solvent. The reactions were performed as temperature dependent experiments at constant space times of 43-48 $hg_{Cat}\,mol_{OPA}^{-1}$ and 191-250 $hg_{Cat}\,mol_{DBT}^{-1}$ at constant total pressure of 5 MPa. Prior to the activity tests, the materials were activated in situ in 10 vol.-% H_2S in H_2 at 400 °C and 1.8 MPa for 12 hours. After introducing the liquid-gas-mixture containing only OPA and DMDS, the pressure was

increased to the reaction pressure and the temperature was set to 350 °C. These conditions were kept for 60 hours. Afterwards, the liquid feed was changed to the OPA-DBT mixture and the simultaneous HDN and HDS reactions were performed at 350° C for 30 hours (steady state was reached after 20 hours time on stream). The temperature was subsequent lowered stepwise up to 310 °C with 6 hours reaction time at each temperature. At the end, the initial reaction conditions (350 °C) were applied to monitor deactivation. The same catalytic performance was observed at the beginning and the end of the experiments. The carbon mass balance was always closed with values higher than 98 % in OPA and DBT.

3. Results

Physicochemical characterization of sulfide catalysts

Details of the characterization for the two bimetallic ($NiMo_{Ox}$, and NiW_{Ox}) and two trimetallic oxide precursors ($NiWMo1_{Ox}$, and $NiMoW2_{Ox}$) are given in Chapter 4 and in the supporting information. Elemental composition, specific surface area, and stacking degree of the corresponding sulfide catalysts are summarized in Table 1. The surface areas of the sulfide catalysts resemble those of the corresponding oxide precursors with exception of NiMo that has a larger surface area than expected from its precursor $NiMo_{Ox}$ (Table S1). However, the surface areas were in general small and similar for the four sulfided catalysts, as well as the concentration of adsorbed NO were similar (i.e., 73 $\mu mol \cdot g^{-1}$ for NiW, and ~82 $\mu mol \cdot g^{-1}$ for the other sulfides).

The catalysts have different total metal contents between 8.3 mmol/g for NiMo and 5.3 mmol/g for NiW. NiMoW2 contains more Mo than W, whereas NiWMo1 contains more W than Mo (Table S5). Varying Mo and W contents in the materials were obtained by tunning the concentrations of the precursor salts during the precipitation procedure. The metal molar fraction for Ni was 0.55, with exception of NiW with a Ni molar fraction of 0.47 (Table 1). XPS indicated that the Ni molar fraction close to the surface is much higher than in the bulk (between 0.60 for NiW and 0.83 for NiWMo1). On the trimetallic samples the surface concentration of Mo was higher compare to W. In NiWMo1, the Mo/W molar ratio increased from 0.5 in the bulk to 3.8 close to the surface, whereas for NiMoW2 an increase of only 1.3 (bulk) to 1.6 (surface) was observed. The sulfur to total metal molar ratio in the range from 1.34 to 1.56 (Table S5) reflects the stoichiometry of the sulfides present in the catalysts (XRD characterization, Figure S19), i.e., $Mo(W)S_2$, Ni_9S_8 (in NiMo and NiMoW2), and Ni_3S_4 (in NiW and NiWMo1). The XRD signals of the hexagonal $Mo(W)S_2$ phases (14.2, 33, 40 and 60° 2θ) were broader for the catalysts than those of reference MoS_2 and WS_2, which points

to smaller crystalline domains. Furthermore, the (002) reflection on the catalysts around 14.2° 2θ shifted to smaller angles compared to the references, indicating that the lattice parameter *d,* i.e., the distance between the metal sulfide layers in z-direction is larger for the catalysts. An increased lattice parameter, the observed amorphous backgrounds, and the line broadening are attributed to disorder caused by e.g. bending of the metal sulfide layers, turbostratic displacement and uncorrelated single layers, which in turn, reduces the crystallinity.[2, 154, 235] According to the crystal sizes determined with the Scherrer equation, NiWMo1 and NiW have lower stacking degrees of the sulfide layers with 4.4 and 4.3, compared to NiMoW2, and NiMo with 5.1, and 5.7, respectively.

Table 1. Physicochemical properties including bulk and surface composition of the sulfided catalysts.

Catalyst		Metal molar fraction in the bulk (b) and near the surface (s), [mol/mol] [a]			Specific surface area, [m^2/g]	Stacking degree of the MoS_2 and WS_2 slabs[b]
		Ni	Mo	W		
NiMo	b	0.55	0.45	-	6.2	5.7
	s	0.75	0.25			
NiMoW2	b	0.56	0.25	0.20	7.4	5.1
	s	0.74	0.16	0.10		
NiWMo1	b	0.54	0.15	0.30	4.6	4.3
	s	0.81	0.15	0.04		
NiW	b	0.47	-	0.53	5.6	4.4
	s	0.60		0.40		

[a] Ratio of molar Ni, Mo and W concentration to the total metal concentration in the bulk (b) determined by elemental analysis after decomposition and near the surface by XPS measurements. The composition in mmol/g is presented in the SI. [b] Determined by applying the Scherrer-equation on the (002) reflection at 14.1 °2θ which corresponds to the interplanar distance of 6.1 Å.

The Raman spectra of sulfide catalysts and reference materials, as well as the assignment of the bands, are shown in the supporting information (Table S6 and Figure S20). A_{1g} and E^1_{2g} modes for Mo-S and W-S vibrations of sulfide species were observed in all materials. The corresponding bands exhibited red shifts compared to the reference materials, which is attributed to lower stacking degrees in the catalysts,[243] whereas the asymmetry and width of the bands can be attributed to highly bent slabs.[91] The spectra of the trimetallic catalysts (NiWMo1, NiMoW2) appear as combination of the spectra of the bimetallic catalysts, which points to the presence of Mo-W composite species[51] (confirmed by X-ray adsorption spectroscopy, vide infra). The shift and shape of the Raman bands, with respect to the references, were attributed to structural disorder of the sulfide slabs.[235] Especially, the A_{1g} band of NiWMo1 appeared broad and with a strong red shift compared to WS_2.

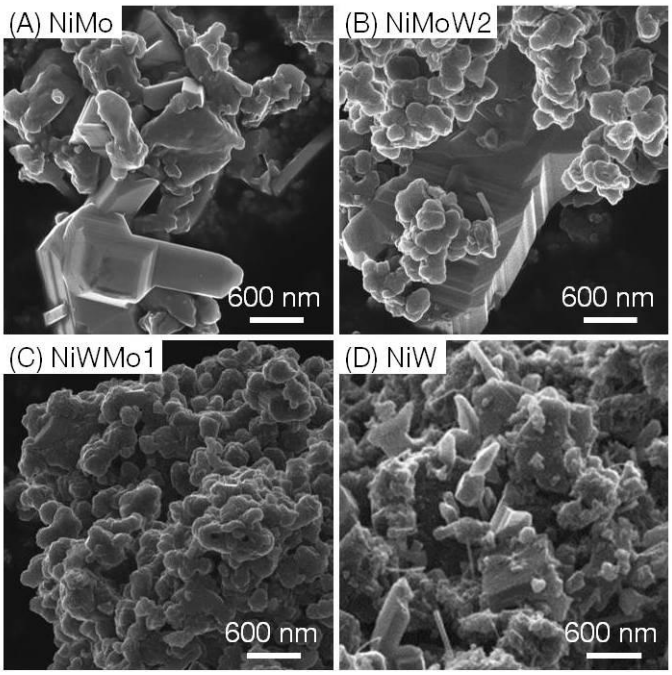

Figure 1. Representative He ion scanning micrographs of sulfided catalysts NiMo (A), NiMoW2 (B), NiWMo1 (C) and NiW (D). The larger smooth particles are identified as various Ni sulfides, whereas the uneven stacked pellets are $Mo(W)S_2$.

Figure 1 shows representative SHIM (scanning He ion microscopy) images of the sulfides (more images are shown in Figure S21). All catalysts consisted of large crystals with needle-like or cubic shape, identified as Ni_xS_y by EDX mapping.[155, 235] Stacked spherical particles, were identified as MoS_2 or WS_2, cover the larger Ni sulfides. Interestingly, Mo and W atoms were only detected in round pellets, whereas Ni was identified along the whole sample, which suggest that relatively small Ni_xS_y particles are occluded in the $Mo(W)S_2$ agglomerates. The trimetallic sulfides appear with similar morphologies and in average higher homogeneity compared to the bimetallic ones. For instance, the dominant texture in NiMoW2 and NiWMo1 were stacks of $Mo(W)S_2$ pellets with average diameters in a range of 100 to 300 nm, whereas in NiW a high variety of particle shapes, and in NiMo a large particle size distribution are present (Figure S21).

TEM shows (Figure 2) that the spherical agglomerates contain $Mo(W)S_2$ crystals with different degrees of crystallinity, i.e., varying lengths and stacking degrees in addition to structural disorder (bending, and random orientation of the crystalline domains). The averaged stacking degrees observed for the $Mo(W)S_2$ slabs are in good agreement with the values obtained from XRD (Table 1). The average slab lengths of $Mo(W)S_2$ increased in the order: NiMo (10 nm) < NiW (15 nm) < NiMoW2 (20 nm) < NiWMo1 (25 nm). A strong disorder was found for NiWMo1 with long curved sulfide slabs and an onion-like growth. The

presence of Ni_xS_y species next to $Mo(W)S_2$ was evidenced during TEM measurements by selected area electron diffraction (SAED, not shown).[155, 235]

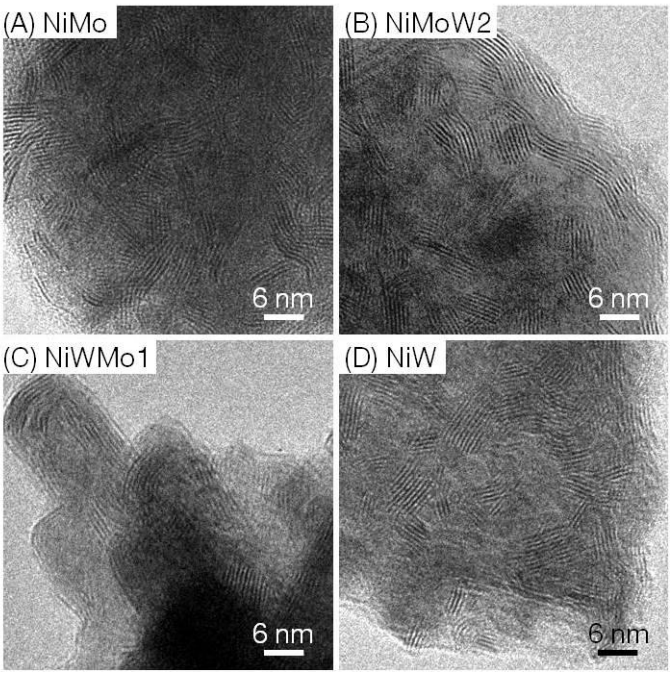

Figure 2. Representative transmission electron micrographs of sulfided catalysts NiMo (A), NiMoW2 (B), NiWMo1 (C) and NiW (D). The metal disulfide layers are visible as black fringes, which allows determination of stacking degree and slab length.

XAS characterization of sulfide catalysts

Oxide precursors, sulfide catalyst, and reference materials were investigated by X-ray absorption spectroscopy. The X-ray absorption near edge structure (XANES) and the Fourier transformed k^3 weighted extended X-ray absorption fine structures (FT-EXAFS) at the Ni K-edge, Mo K-edge and W L_{III}-edge are presented in Figures 3, 4, and 5, respectively.

In comparison to the XANES of the oxide precursors, all sulfide spectra had lower intensities and the absorption edges shifted to lower energies (Figures 3-5(A)). These observations point to lower oxidation states and higher population of the Ni-3p, Mo-4p and W-$5d_{3/2}$-orbitals in the sulfides, as expected for compounds with reduced states and covalent metal sulfur bonds.[38, 220, 222, 227-229] FT-EXAFS of the sulfides were more intense and the contributions were shifted to higher distances compared to the oxide precursors due to the stronger backscattering properties of sulfur, the presence of different structure types as well as the covalent metal-sulfur (M-S) bond character. We have presented a detailed analysis of the EXAFS of NiMo, NiW and NiMoW2 in a previous contribution[235] and therefore focus in the current work on the comparison of the two trimetallic sulfides in relation to the both

bimetallic catalysts. The analysis of the XANES by LCF is contained in the supporting information.

The XANES at the Ni K-edge (1s-3p electric dipole transition) of the oxide precursors are similar to the XANES of $NiMoO_4$ (Figure 3(A), grey lines) and NiO (Figure S11(A)). The absorption edges were observed at around 8347 eV and with a weak pre-edge feature (1s to 3d-4p-hybrid orbital electric dipole transition[220, 223]) at around 8334 eV (Figure S13). A more detailed analysis is reported in the supporting information. The absorption edges of the sulfides (Figure 3(A), black lines) are at 8339.0 eV for NiW, 8339.3 eV for NiMoW2 and at 8339.5 eV for NiMo and NiWMo1 (Ni_3S_2 is at 8338.0 eV). The white line intensity is the same for all sulfides and Ni_3S_2, although the white line of the sulfides is broader than for Ni_3S_2. A pre-edge feature was found at 8332.5 eV for all sulfides, which has a much higher intensity compared to the oxide precursors (Figure S13). The intensity of this feature increases in the order: Ni_3S_2 < NiMoW2 < NiMo = NiWMo1 < NiW. These observations indicate that in all sulfide catalysts Ni exhibits a strong distorted tetrahedral, square-pyramidal or trigonal-prismatic-like coordination with sulfur like in Ni_3S_2(ICSD #27521[69], R32 space group).[147, 258] Moreover, the fraction of covalent Ni-S bonds[38] is very high, whereas the presence of ionic Ni-O bonds is negligible. However, the oxidation states are higher and the symmetry of Ni is slightly different in the catalysts compared to Ni_3S_2.[221-222] The differences to Ni_3S_2 are especially pronounced in NiWMo1, whereas NiMoW2 appears as the most similar catalyst to Ni_3S_2 as confirmed by LCF (supporting information).

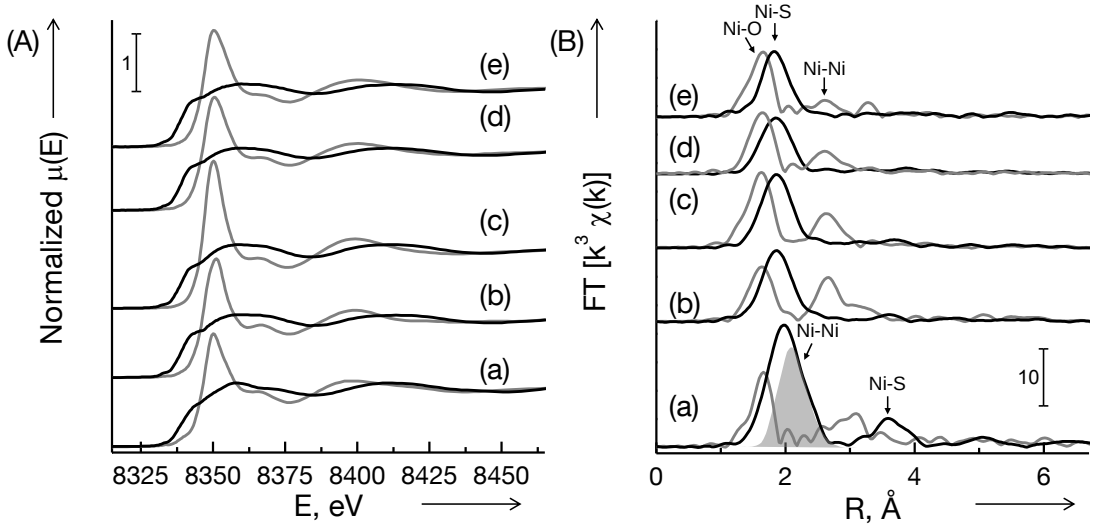

Figure 3. XANES at the Ni K-edge (A) and the corresponding Fourier transforms of k^3 weighted EXAFS (B) of Ni_3S_2 (a) and $NiMoO_4$ (a, grey) and of the oxide precursor (grey lines) and sulfide catalyst (black lines) of NiMo (b), NiMoW2 (c), NiWMo1 (d) and NiW (e).

The FT-EXAFS of the precursors at the Ni K-edge show a strong first contribution at around 1.6 Å (not phase corrected), which is assigned to Ni-O[33] backscattering (Figure 3(B), grey lines). The second contribution at around 2.6 Å (not phase corrected) results from Ni-Ni backscattering [33, 259] similar to NiO or $Ni(OH)_2$ (Figure S11(B)). The FT-EXAFS of the sulfides at the Ni K-edge exhibit broad and intense contributions at around 1.9 Å (not phase corrected), which includes Ni-S and Ni-Ni backscattering.[235] Its distance is shifted to lower values for the catalysts compared to Ni_3S_2. The more distant Ni-S and Ni-Ni contributions found in Ni_3S_2 were very weak and almost absent in NiWMo1 and NiW. Thus, in agreement with the semi-quantitative XANES analysis we can conclude that the local environment of Ni is different in both trimetallic sulfide catalysts.

The XANES at Mo K-edge (1s-5p electric dipole transition) of the oxide precursors are presented in Figure 4(A) (grey lines). All XANES were similar to that of $NiMoO_4$, with a remarkable pre-edge peak (1s to 4d-5p hybrid orbital transition[179, 220]) present at around 20004.5 eV. Both trimetallic precursor have almost the same intensity and white line shape, although the pre-edge peak intensity is slightly lower for $NiMoW2_{Ox}$, suggesting a different coordination symmetry (supporting information). The absorption edge of sulfide catalysts and reference MoS_2 is at 20007 eV. NiMo has the sharpest and highest white line and its XANES is almost identical to that of MoS_2. No pre-edge feature was observed in the Mo-XANES, which points to Mo^{4+} in a perfect octahedral site (like in MoS_2) since the presence of an inversion center hinders 4d-5p hybridization and a pure 1s-4d electronic transition is dipole forbidden.[220, 258]

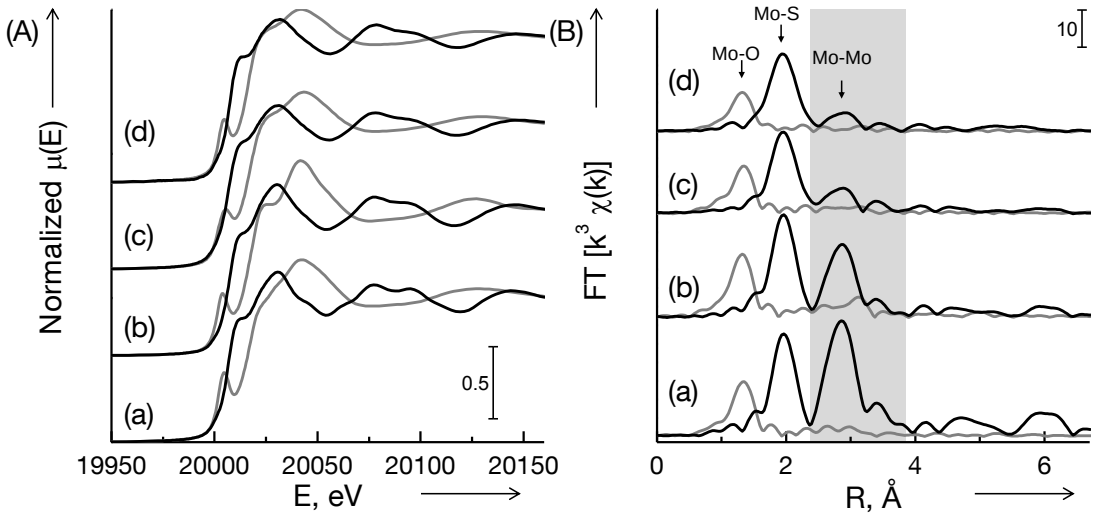

Figure 4. XANES at Mo K-edge (A) and the corresponding Fourier transforms of k^3 weighted EXAFS (B) of the references MoS_2 (a, black) and $NiMoO_4$ (a, grey) and of the oxide precursor (grey lines) and sulfide catalyst (black lines) of NiMo (b), NiMoW2 (c) and NiWMo1 (d).

The Mo FT-EXAFS of the oxide precursors are shown in Figures 4(B) (grey lines). A strong Mo-O[225-226] contribution at around 1.3 Å (not phase corrected) was observed for all precursors. The FT of $NiMo_{Ox}$ shows a weak contribution at 3.2 Å (not phase corrected), typical for Mo-Mo backscattering in polymolybdates like ammonium heptamolybdate (Figure S14(B)).[40] For the sulfide catalysts an intense Mo-S contribution at around 2.0 Å (not phase corrected) and a moderate Mo-Mo contribution at around 2.9 Å (not phase corrected) were identified (Figure 4(B), black lines).[235] The intensity of the Mo-S signal was the same for NiMo and MoS_2, whereas it is weaker for the trimetallic sulfides. The Mo-Mo contribution decreases in the following order: MoS_2 > NiMo >> NiMoW2 > NiWMo1; i.e., with decreasing Mo content. Moreover, the FT EXAFS of the sulfides shows no distinct contribution at the distance of a Mo-O backscatter (the FT of all sulfides looks the same at around 2.0 Å). Thus, presence of oxidized Mo or ionic Mo-O bonds can be neglected (also indicated by XANES).

At the W L_{III}-edge ($2p_{3/2}$-$5d_{3/2}$ electric dipole transition)[228] a very sharp onset at the adsorption edge at around 10212.0 eV was observed for all oxide precursors and their XANES were comparable to that of WO_3 (Figure 5(A), grey lines). Moreover, a white line splitting (d-orbital splitting) of 2.7 eV for $NiMoW2_{Ox}$ and 3.0 eV for the other precursors was determined by the second derivative of the XANES (Figure S17(B)). The split d-orbitals were identified as the t_{2g} and e_g orbitals of an octahedral ligand field and the observed energy splitting is characteristic for distorted $[WO_6]$-octahedons.[231]

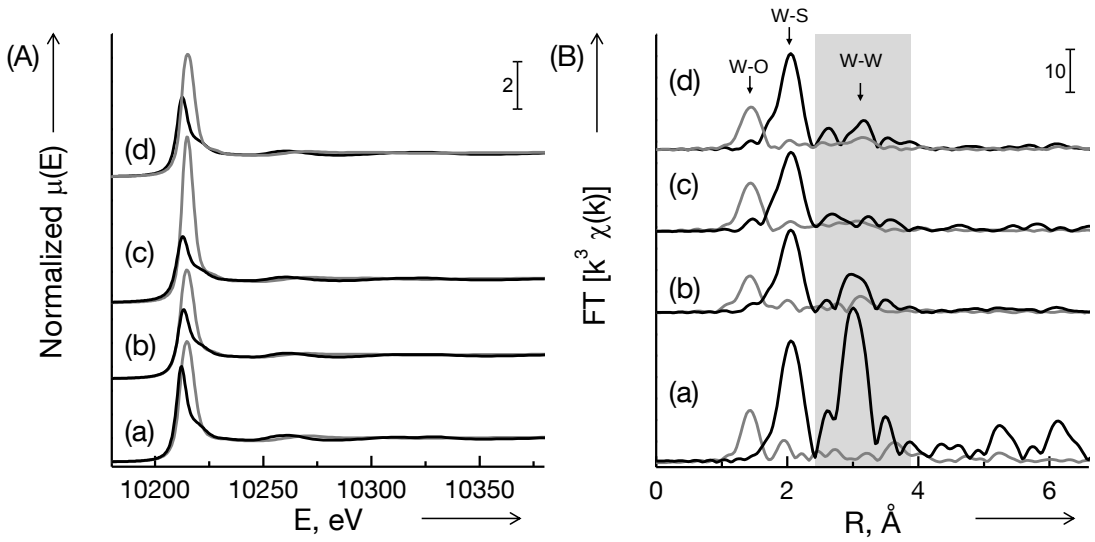

Figure 5. XANES at W L_{III}-edge (A) and the corresponding Fourier transforms of k^3 weighted EXAFS (B) of the references WS_2 (a, black) and WO_3 (a, grey) and of the oxide precursor (grey lines) and sulfide catalyst (black lines) of NiW (b), NiMoW2 (c) and NiWMo1 (d).

For the sulfide catalysts sharp white lines and absorption edges at 10210.2 eV for NiMoW2, 10210.4 eV for WS_2, 10210.5 eV for NiWMo1, and at 10210.7 eV for NiW catalyst were

observed. The white line intensity decreases in the following order: WS_2 > NiWMo1 > NiW > NiMoW2. Consequently, the lowest oxidation state and highest population of the 5d-orbitals is present on NiMoW2.[228-229] This 5d-population trend is in agreement with the results of the LCF (Table S7, Figure S24), which suggest a distorted octahedral W^{4+} coordination[230] (supporting information).

The FT-EXAFS at the W L_{III}-edge of the oxide precursors (Figure 5(B) (grey lines)) exhibit a strong W-O[33] contribution around 1.4 Å (not phase corrected). In NiW_{Ox}, an additional W-W contribution around 3.1 Å (not phase corrected)[33] is present, which is similar to the one in WO_3. However, in the FT-EXAFS of both trimetallic precursors the higher contributions are weaker compared to NiW_{Ox}. The sulfide materials (black lines in Figure 5(B)), show an intense W-S contribution at 2.0 Å (not phase corrected) and a moderate W-W contribution at 3.0 Å (not phase corrected)[235] with the following trends in intensity for the W-S signal: WS_2 > NiWMo1 > NiW = NiMoW2 and for the W-W signal: WS_2 > NiW >> NiWMo1 > NiMoW2. The intensity of the second W-W contribution decreases with decreasing W and increasing Mo content and a signal splitting is observed for the trimetallic materials.

Qualitative analysis of the XANES and FT-EXAFS revealed the presence of different Ni species, which are reflected in the intensities of the M-S contributions (M stands for Mo or W). The results of the LCF indicate a different population of the W 5d-orbitals between the two trimetallic sulfides. However, in both trimetallic catalysts unusually low M-M contributions were present. This feature was also observed for the oxidic precursors and could be caused by neighboring Mo and W atoms.[21, 50, 235] The phase functions for Mo-W absorber-backscatter pairs have a phase shift of π, which causes destructive interference and changes the EXAFS. Based on the findings for NiMoW2, intralayer mixed $Mo_{1-x}W_xS_2$ slabs are as well proposed for the second trimetallic catalyst NiWMo1.[235]

In order to prove this point, the k^3 weighted EXAFS at the Mo K-edge and W L_{III}-edge of all catalysts and references are presented In Figure 6. The oscillations of the sulfide catalysts are less intense and appear with a stronger noise compared to MoS_2 and WS_2. At the Mo K-edge, two separate features between 10-12 and 14-16 $Å^{-1}$ were found in the EXAFS of MoS_2 and NiMo, whereas only one broad feature was observed for both trimetallic sulfides. The same was observed at the W L_{III}-edge between 9-10 $Å^{-1}$ and 12-14 $Å^{-1}$ for the EXAFS of the trimetallic sulfides compared to NiW. These trends in the EXAFS of NiWMo1 (and NiWMo2) are the first indications for the presence of an intralayer mixed $Mo_{1-x}W_xS_2$ structure. Therefore, during EXAFS fitting, the structures of the reference compounds MoS_2, WS_2 and Ni_3S_2, as well as a model of $Mo_{1-x}W_xS_2$ (with x = 0.5 as starting parameter) were used. Based on the LCF analysis, which revealed the presence of other phases than the references and

the oxidic precursors, mixed Mo-Ni (Ni-Mo) and W-Ni (Ni-W) contribution were added during the multi-edge fitting procedure.[155, 235]

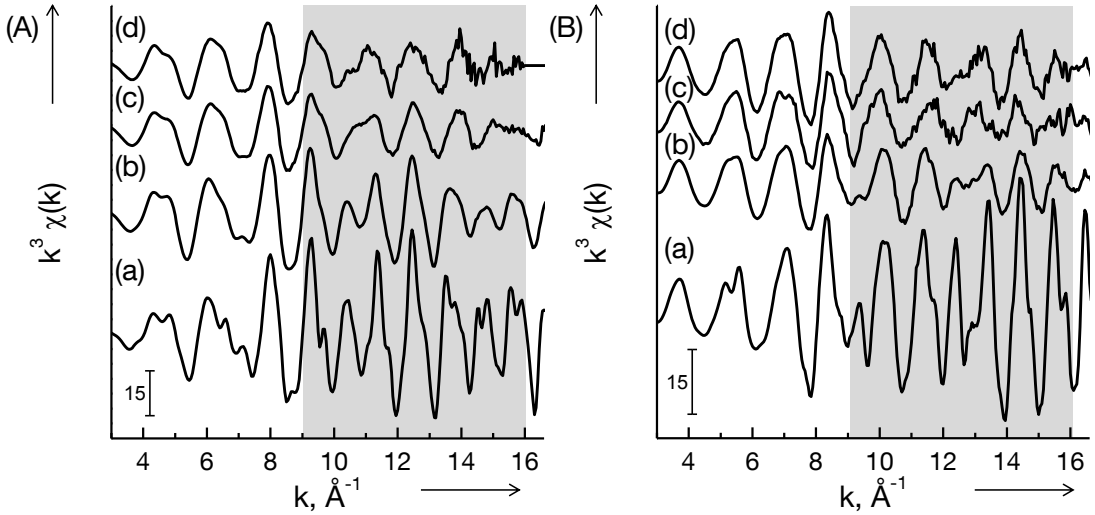

Figure 6. k^3 weighted EXAFS at the Mo K-edge (A) and at the W L_{III}-edge (B) of the references MoS_2 (A,a) and WS_2 (B,a) and of the sulfide catalysts NiMo (A,b), NiW (B,b), NiMoW2 (c) and NiWMo1 (d).

The fits of the EXAFS and all fit parameters of the sulfide catalysts and the references MoS_2, WS_2 and Ni_3S_2 are presented in the supporting information (Tables S8-S9, Figures S26-S28). Tables 2 and 3 summarize the results for the analysis of the EXAFS of the most relevant intermetallic contributions at the Mo K-edge and W L_{III}-edge.

In NiMo, the coordination number of the Mo-S contribution at 2.4 Å was $N_{Mo\text{-}S} = 6$ and for the Mo-Mo scattering $N_{Mo\text{-}Mo} = 5.1$ at 3.17 Å (Table S9 and 2). This indicates that the first sulfur shell was fully coordinated, whereas the coordination of the Mo atoms in the second shell was smaller compared to the coordination number of 6 in the reference MoS_2. The value of $N_{Ni\text{-}S} = 4.5$ (Table S8) is in line with the tetrahedral or pentagonal coordination indicated by the pre-edge feature of the XANES. The second and third contributions at the Ni K-edge ($N_{Ni\text{-}Ni} = 1.2$ at $r_{Ni\text{-}Ni} = 2.6$ Å, and $N_{Ni\text{-}Ni} = 4.4$ at $r_{Ni\text{-}Ni} = 3.9$ Å) were smaller than those in Ni_3S_2. These smaller intermetallic coordination numbers for NiMo compared to the references indicate the presence of smaller particle sizes of the MoS_2 and Ni sulfide species. Moreover, there is some interaction between Ni and Mo as indicated by the Mo-Ni contribution at 2.7 Å with $N_{Mo\text{-}Ni} = 0.3$ (Table 2).

In NiW, W-S and W-W contributions were identified at 2.4 and 3.15 Å (Table S9 and 3). The corresponding coordination numbers were $N_{W\text{-}S} = 4.5$, and $N_{W\text{-}W} = 3.1$. For the first Ni-S contribution a $N_{Ni\text{-}S} = 4.4$ at 2.26 Å was observed(Table S8), whereas Ni-Ni contributions were observed with $N_{Ni\text{-}Ni} = 0.5$ (r = 2.57 Å) and $N_{Ni\text{-}Ni} = 3.1$ (r = 3.97 Å). These Ni distances

and the smaller coordination numbers indicate the presence of smaller particles and of different Ni sulfide phases in NiW. Ni-W interactions are suggested by a weak contribution at 2.75 Å (N_{W-Ni} = 0.1; Table 3).

Table 2. Best fit results for k^3 weighted EXAFS data of the sulfided catalysts at the Mo K-edge in k space. Only the intermetallic contributions are shown (all data can be found in the SI).

Catalyst	Shell	r, Å	N	σ^2, Å^2	E_0, eV
NiMo	Mo-Mo	3.17 (0.01)	5.1 (0.1)	0.0033 (0.0001)	0.74 (0.67)
R = 0.0013	Mo-Ni	2.68 (0.02)	0.3 (0.1)	0.0024 (0.0022)	
NiMoW2	Mo-Mo	3.16 (0.01)	3.1 (0.1)	0.0043 (0.0010)	1.52 (0.60)
R = 0.0055	Mo-W	3.17 (0.01)	1.6 (0.2)	0.0042 (0.0004)	
	Mo-Ni	2.68 (0.03)	0.6 (0.1)	0.0093 (0.0029)	
NiWMo1	Mo-Mo	3.16 (0.01)	1.5 (0.1)	0.0010 (0.0002)	1.81 (1.12)
R = 0.0047	Mo-W	3.16 (0.01)	1.6 (0.1)	0.0020 (0.0002)	

Abbreviations: r: distance, N: coordination number, σ^2: Debye-Waller like factor, E_0: inner potential; in brackets the absolute errors.

Mo-W and W-Mo contributions were found at 3.16 Å and 3.17 Å in the EXAFS of the trimetallic sulfides, in agreement to the proposal of the formation of intralayer $Mo_{1-x}W_xS_2$ slabs. The Ni coordination numbers were small and Ni-Ni neighbors at higher distances could not be identified, which points to the presence of small particle sizes and diverse Ni sulfide phases.

In NiMoW2, N_{Mo-S} and N_{W-S} were around 5 (Table S9). At the Mo K-edge the coordination numbers for Mo were N_{Mo-Mo} = 3.1 and N_{Mo-W} = 1.6, which results in an overall coordination number N_{Mo-M} of 4.7 (Table 2). Additionally, another mixed metallic contribution was identified at 2.68 Å with the average N_{Mo-Ni} of 0.6. At the W L_{III}-edge, the observed coordination numbers for NiMoW2 were N_{W-W} = 2.1, N_{W-Mo} = 2, and N_{W-Ni} = 0.6.

In NiWMo1, N_{Mo-S} and N_{W-S} were 5.5 and 5.1, respectively, which points to a higher sulfidation degree than in NiMoW2 (Tables S9). At the Mo K-edge, an overall coordination number of N_{Mo-M} of 3.1 was determined with N_{Mo-Mo} = 1.5 and N_{Mo-W} = 1.6. At the W L_{III}-edge, the overall coordination number was N_{W-M} = 3.4 (N_{W-W} = 2.6 and N_{W-Mo} = 0.8). At both metal edges the M-M coordination numbers were lower compared to the other trimetallic catalyst (NiMoW2) suggesting a stronger distortion and a lower intralayer mixing of Mo and W

(smaller particles are excluded based on TEM). A satisfactory fit of the EXAFS of NiWMo1 does not require the addition of Mo-Ni or W-Ni contributions. In Table S10, an alternative fit is presented, where small Mo-Ni and W-Ni contributions were added while all other fit parameter except for the inner potential E_0 were fixed. The overall fit quality was not improved by these new parameters therefore their presence is uncertain.

Table 3. Best fit results for k^3 weighted EXAFS data of the sulfided catalysts at the W L_{III}-edge in k space. Only the intermetallic contributions are shown (all data can be found in the SI).

Catalyst	Shell	r, Å	N	σ^2, Å^2	E_0, eV
NiW	W-W	3.15 (0.01)	3.1 (0.4)	0.0045 (0.0005)	7.36 (0.44)
R = 0.0033	W-Ni	2.75 (0.05)	0.1 (0.1)	0.0033 (0.0030)	
NiMoW2	W-W	3.17 (0.02)	2.1 (0.3)	0.0042 (0.0006)	8.02 (1.23)
R = 0.0055	W-Mo	3.17 (0.01)	2.0 (0.2)	0.0042 (0.0004)	
	W-Ni	2.82 (0.04)	0.6 (0.2)	0.0030 (0.0021)	
NiWMo1	W-W	3.15 (0.01)	2.6 (0.2)	0.0034 (0.0003)	7.11 (0.87)
R = 0.0047	W-Mo	3.16 (0.01)	0.8 (0.1)	0.0020 (0.0002)	

Abbreviations: r: distance, N: coordination number, σ^2: Debye-Waller like factor, E_0: inner potential; in brackets the absolute errors.

Catalytic activity

Hydrodenitrogenation of o-propylaniline (OPA-HDN)

The catalytic activity of the sulfide catalysts was tested in the simultaneous hydrodenitrogenation of o-propylaniline (OPA-HDN) and hydrodesulfurization of dibenzothiophene (DBT-HDS) from 310 °C to 350 °C. The dependences of the conversions of OPA and DBT on temperature are shown in the supporting information. The normalized reaction rates of HDN and HDS on all catalysts at different temperatures are presented in the form of Arrhenius-type plots (Figure 7A and 7B). The activity rankings are the following: NiWMo1 < NiMoW2 < NiMo < NiW for HDN; and NiWMo1 < NiMo < NiW = NiMoW2, for HDS.

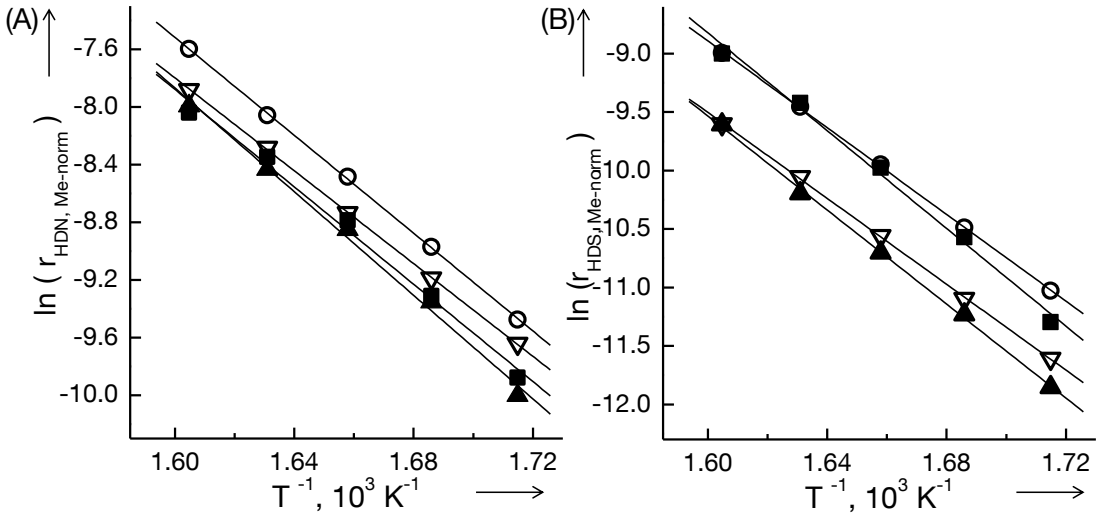

Figure 7. Catalytic activity in HDN of o-propylaniline (A), and HDS of dibenzothiophene (B) on the unsupported sulfide catalysts NiMo (▽), NiMoW2 (■), NiWMo1 (▲) and NiW (○). Presented are the normalized reaction rates (to the total metal content) at varying temperatures in an Arrhenius type plot.

The observed products in the OPA-HDN are propylbenzene (PB), propylcyclohexylamine (PCHA), propylcyclohexane (PCH), 1-propylcyclohexene, 3-propylcyclohexene, and propylidene cyclohexane. The latter three products are analyzed together as propylcyclohexene (PCHE). The yields of these products along with the OPA conversion are presented in Figure 8. The trends of the yields are well in line with the reaction network shown in Figure 9.[6, 155] PB is the primary product of the direct denitrogenation (DDN) pathway in the OPA-HDN, whereas PCHA is the primary product of the OPA hydrogenation pathway (HYDN). In a subsequent step, PCHA is denitrogenated to PCHE, which is subsequently hydrogenated to PCH. The DDN route has a minor contribution to the overall HDN as seen from the very low PB yields. On the other hand, the low concentrations of PCHA indicate that the hydrogenation of OPA is the rate determining step in the HYDN route. The yield of PB, and the sum of the yields of the other products are identical on all catalysts. This indicates that the selectivities for the HDN of OPA are very similar for all catalysts, although there are small differences for the specific steps within the HYDN.

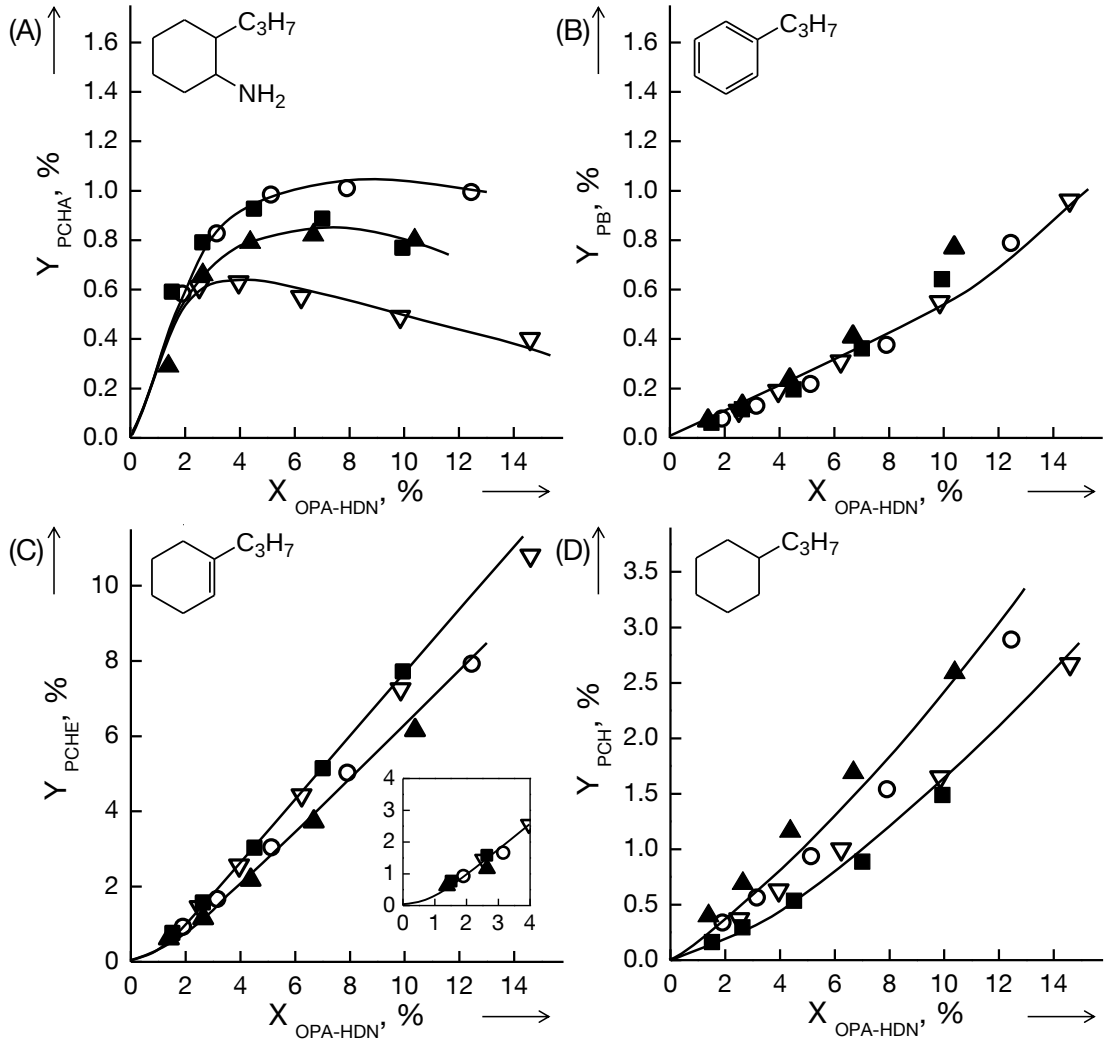

Figure 8. Yields along with OPA conversion, gained at different temperatures, of propylcyclohexylamine (A), propylbenzene (B), propylcyclohexene (C) and propylcyclohexane (D) on the sulfided catalysts NiMo (▽), NiMoW2 (■), NiWMo1 (▲) and NiW (○) (data are gained with a constant reactor loading for all catalyst; to guide the eyes the symbols are connected by trend curves).

Table 4 summarizes the rates of OPA-HDN and the individual reaction pathways, the corresponding rate ratios and apparent activation energies. In all cases the rates of the HYDN pathway are one order of magnitude higher than those of the DDN pathway, which leads to HYDN/DDN ratios from 25 to 12 with increasing temperature.

The decreasing ratio reflects the higher apparent activation energies of the DDN route compared to the HYDN route (161-177 kJ mol^{-1}, and 132-148 kJ mol^{-1}, respectively). The apparent activation energies of the HYDN route are very similar to those of the overall OPA-HDN because it is the dominant route. They increase in the order: NiMo (132 kJ mol^{-1}) < NiMoW2 (139 kJ mol^{-1}) = NiW (140 kJ mol^{-1}) < NiWMo1 (148 kJ mol^{-1}). The apparent

activation energies for the DDN route increase in the same order: NiMo (161 kJ mol^{-1}) < NiW (172 kJ mol^{-1}) = NiMoW2 (173 kJ mol^{-1}) < NiWMo1 (177 kJ mol^{-1}).

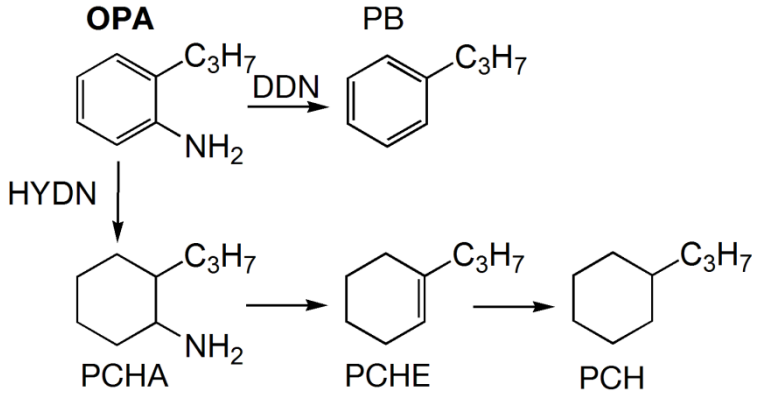

Figure 9. Reaction network of the hydrodenitrogenation of o-propylaniline (OPA). The products of the DDN (direct denitrogenation) route are propylbenzene (PB), and of the HYDN (hydrogenation) route propylcyclohexylamine (PCHA), propylcyclohexene (PCHE), and propylcyclohexane (PCH).

Table 4. Activity results for the HDN of o-propylaniline over the sulfide catalysts.

Catalyst	Reaction rates[a]	Temperature [°C]					$E_{A,app}$
	[10^{-4} mol·(h·mol_M)$^{-1}$]	350	340	330	320	310	[kJ·mol^{-1}]
NiMo	HDN	3.77	2.53	1.61	1.02	0.65	134
	HYDN	3.53	2.39	1.53	0.97	0.62	132
	DDN	0.25	0.14	0.08	0.05	0.03	161
	HYDN/DDN	14	17	19	20	22	
NiMoW2	HDN	3.22	2.37	1.53	0.90	0.51	140
	HYDN	3.03	2.25	1.46	0.87	0.49	139
	DDN	0.20	0.12	0.06	0.04	0.02	173
	HYDN/DDN	16	19	23	23	25	
NiWMo1	HDN	3.38	2.17	1.43	0.87	0.45	149
	HYDN	3.12	2.04	1.35	0.82	0.43	148
	DDN	0.25	0.13	0.08	0.04	0.02	177
	HYDN/DDN	12	15	18	19	18	
NiW	HDN	5.02	3.17	2.07	1.27	0.77	141
	HYDN	4.71	3.02	1.98	1.22	0.74	140
	DDN	0.31	0.15	0.09	0.05	0.03	172
	HYDN/DDN	15	20	23	24	24	

[a] The reaction rates are obtained from the conversions and yields of OPA-HDN and normalized to the total metal (M) content of the used catalysts (mol_M/g_{Cat}). The HYDN rates are determined from the sum of the production rates of PCHA, PCHE, and PCH and the DDN rates from the production rates of PB.

Hydrodesulfurization of dibenzothiophene (DBT-HDS)

The observed products in the DBT-HDS are biphenyl (BiPh), tetrahydrodibenzothiophene (H-DBT), and phenylcyclohexane (PhCH). Figure 10 shows the dependence of the product yields on DBT conversion. BiPh is the dominant product, having a yield almost 1 to 1 with DBT conversion. H-DBT and PhCH are detected in minor concentrations.

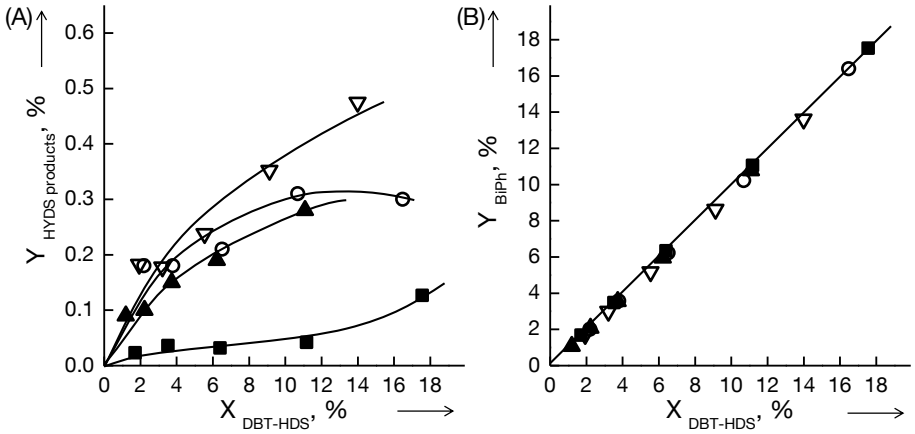

Figure 10. Yields along with DBT conversion, gained at different temperatures, of all hydrogenated DBT products (A), and biphenyl (B) on the sulfided catalysts NiMo (▽), NiMoW2 (■), NiWMo1 (▲) and NiW (○) (data are gained with a constant reactor loading for all catalyst). The yield of the HYDS products in (A) is the sum of tetrahydrodibenzothiophene and phenylcyclohexane (to guide the eyes the symbols are connected by trend curves).

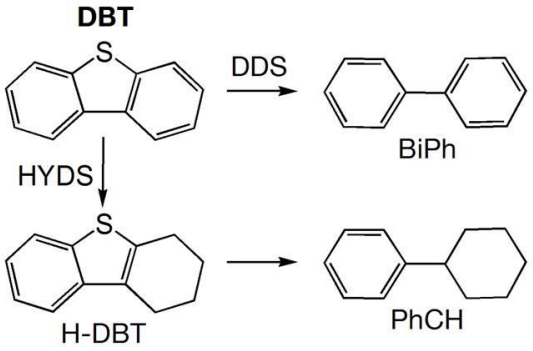

Figure 11. Reaction network of the hydrodesulfurization of dibenzothiophene (DBT). The products of the DDS (direct desulfurization) route are biphenyl (BiPh), and of the HYDS (hydrogenation) route are tetrahydrodibenzothiophene (H-DBT), and phenylcyclohexane (PhCH).

The product yields are in agreement with the expected reaction network presented in Figure 11.[109, 260] BiPh is the product of direct desulfurization (DDS) of DBT, whereas H-DBT and PhCH are the primary and secondary products, respectively, of the hydrogenation route (HYDS). The very low concentrations of the products of the HYDS route are in agreement with the observations that DBT is preferentially converted via DDS on Ni-promoted MoS_2 and

WS_2 catalysts in addition to the fact that the HYDS route is strongly suppressed by the presence of OPA.[109, 251]

The rate constants and activation energies for the HDS of DBT are summarized in Table 5. The HDS rates are lower than the HDN rates (Table 4), while the DDS rates are 3 to 7 times faster than the DDN, which reflects the strong preference of sulfides for direct desulfurization than direct denitrogenation.

The DDS rates are one to two orders of magnitude faster than those of HYDS. As a consequence, the rates and activation energies of the DDS route are almost identical to the overall rates and activation energies. The apparent activation energies for HDS are 153 kJ mol^{-1} for NiMo, 154 kJ mol^{-1} for NiW, 167 kJ mol^{-1} for NiWMo1, and 174 kJ mol^{-1} for NiMoW2. The rates and E_a values of the HYDS are not discussed because the very low yields of the HYDS products introduce a large error in the calculations.

Table 5. Activity results for the HDS of dibenzothiophene over the sulfide catalysts.

Catalyst	Reaction rates[a]	Temperature [°C]					$E_{A,app}$
	[10^{-5} mol·(h·mol_M)$^{-1}$]	350	340	330	320	310	[kJ·mol]
NiMo	HDS	6.75	4.30	2.60	1.52	0.91	153
	HYDS	0.23	0.17	0.11	0.09	0.09	
	DDS	6.52	4.13	2.48	1.43	0.82	
	DDS/DDN	28	24	23	16	9	
NiMoW2	HDS	12.35	8.09	4.64	2.56	1.24	174
	HYDS	0.07	0.03	0.02	0.03	0.02	
	DDS	12.29	8.06	4.62	2.54	1.22	
	DDS/DDN	175	269	231	84	61	
NiWMo1	HDS	6.73	3.74	2.25	1.33	0.71	167
	HYDS	0.17	0.11	0.09	0.06	0.06	
	DDS	6.56	3.62	2.16	1.27	0.66	
	DDS/DDN	39	33	24	21	11	
NiW	HDS	12.41	7.83	4.78	2.78	1.62	154
	HYDS	0.22	0.23	0.15	0.14	0.14	
	DDS	12.18	7.60	4.62	2.65	1.49	
	DDS/DDN	55	33	31	19	10	

[a] The reaction rates are obtained from the conversions and yields of DBT HDS and normalized to the total metal content of the used catalysts (mol_M/g_{Cat}). The HYDS rates are determined from the sum of the production rates of H-DBT, and PhCH and the DDS rates from the production rates of BiPh.

On the active phases and their properties in unsupported Ni-Mo, Ni-W, and Ni-Mo-W sulfide catalysts

The oxide catalysts precursors exhibit different coordination geometries for Ni, Mo and W within multimetallic oxide phases (supporting information). The bimetallic $NiMo_{Ox}$ precursor is mainly composed by a layered ammonium nickel molybdate $(NH_4)Ni_2(OH,H_2O)(MoO_4)_2$ with $[MoO_4]$-tetrahedra,[182] whereas the predominant phase in NiW_{Ox} is monoclinic closed packed $NiWO_4$ formed by $[WO_6]$-octahedra.[83] For the trimetallic oxide precursors, Mo-W mixed phases and structures similar to the bimetallic materials were observed. The Mo-W interaction is especially pronounced in the $NiMoW2_{Ox}$ precursor, for which a layered ammonium nickel metallate structure similar to $(NH_4)Ni_2(OH,H_2O)(Mo_{0.5}W_{0.5}O_4)_2$ with highly distorted $[MO_4]$-tetrahedra is concluded. The multimetallic structure contained in $NiWMo1_{Ox}$ can be better described with a distorted wolframite-type structure $NiMo_{0.33}W_{0.67}O_4$, which contains edge and corner connected distorted metal polyhedra.[80]

During sulfidation, a segregation of the metals takes place, which results in mixtures of $Mo(W)S_2$, and varying proportions of Ni_9S_8, and Ni_3S_4 in the sulfide catalysts. In the trimetallic catalysts a Mo-W mixed phase is retained and forms intralayer $Mo_{1-x}W_xS_2$ phases, where Mo and W are contained in the same sulfide slabs. The Mo-W coordination numbers showed a higher averaged Mo-W mixing ratio with N_{Mo-W} of 1.6 and N_{W-Mo} of 2.0 in NiMoW2 compared to N_{Mo-W} of 1.6 and N_{W-Mo} of 0.8 in NiWMo1, as already suggested for their oxidic counterparts. Additionally, Ni-containing bimetallic and trimetallic sulfide phases are present. Observing Ni-Mo(W) and Mo(W)-Ni contributions in the EXAFS analysis for most of the materials is a strong evidence the formation of promoted Ni-Mo-S and Ni-W-S mixed phases (the exception is discussed below). The formation of promoted $Mo(W)S_2$ species has been identified or inferred in unsupported materials by other techniques.[125, 189, 261-262] The most accepted model for promotion is the “Co-Mo-S” model, where promoter atoms substitute Mo atoms at edge positions of the sulfide slabs.[30, 32, 142, 148, 186] However, there are indications that Ni promotion or promotion of unsupported catalysts may also occur via interactions between $Mo(W)S_2$ and small Ni or Co sulfide clusters.[31, 248, 263-264] In EXAFS analysis, the distances of the M-Ni contributions of the studied catalysts are 2.68 Å for Ni-Mo in NiMo and NiMoW2, 2.75 Å for Ni-W in NiW, and 2.82 Å for Ni-W in NiMoW2. The latter distances are in good agreement to the structures proposed for “typical” Co(Ni)-Mo-S phases[42, 168], whereas the Ni-Mo distance is closer to the MoS_2–Co_9S_8 interface studied in reference compounds.[31] Therefore, we propose that a variety of Ni entities form at the edges of $Mo(W)S_2$, ranging from substituted mono-atomic Ni to small Ni_xS_y clusters.[248] This variety of small Ni sulfide species, in addition to segregated species observed by XRD, produces a broad distribution of particle sizes and interatomic distances which leads to rather low Ni-Ni coordination

numbers compared to the reference Ni_3S_2. In any case, the average Ni-Ni coordination number reflects the contribution of various Ni sulfide species to the overall catalyst composition.

The elemental composition of the catalysts is not homogeneous across the volume of the solids as seen by the differences in the metal molar fractions determined for the regions near the surface (XPS) and those corresponding to the bulk (Table 1). Interestingly, the catalyst NiWMo1, without Ni-Mo(W) contributions in the EXAFS, presented the largest difference between the Ni molar fraction in the bulk and near the surface (0.54, and 0.81, respectively). NiWMo1 exhibits a lower Mo-W contribution than NiMoW2, whereas the corresponding oxide precursors of both materials differ in their structures. It seems that the oxide precursors influences the properties of the active sulfide phase. During sulfidation, the open layered structure of $NiMoW2_{Ox}$ might induce strong intermetallic interactions enabling simultaneous sulfidation of the different metals. The predominant oxide phase in $NiWMo1_{Ox}$, however, crystallizes in a close packed wolframite structure, which is more difficult to sulfide and tends to produce segregated phases as reported for bulk $NiMoO_4$ and MoO_3.[215] Indeed, for NiMo, exhibiting as well a layered oxide precursor structure, a higher Ni promotion is found than in NiW, obtained by sulfidation of a $NiWO_4$-like oxide precursor. Thus, the large level of segregated Ni at the surface in NiWMo1 can be correlated to the lack of Ni-Mo(W) interactions. The rationale is that Ni, not incorporated to the Ni-promoted phases, segregates and forms bulk Ni sulfides.[125, 265] However, the presence of the Ni-Mo(W)-S phase in NiMoW1 is not discarded in view of the corresponding selectivity (see below). The phase must be present with much lower proportions compared to the segregated sulfides more evident by XAS and XRD. Based on these discussed findings as well as the TEM and EXAFS results, structural models for the sulfide catalysts are presented in Figure 12 and 13. Figure 12 presents the average distributions of Mo, and W within an hexagonal disulfide slab as well as the different degrees of edge decorations by Ni according to the EXAFS fitting. Figure 13 present visualizations of the metal edges of the sulfide catalysts according to the EXAFS fit results showing the local geometry, bond distances and neighbors.

On these sulfide catalysts, the active sites involved in hydrotreating (HDS and HDN) are coordinatively unsatured sites (CUS), where the heteroatom containing molecule adsorbs and hydrogenolytic C-S or C-N bond cleavage occurs.[7, 27, 126] The hydrogen needed for the reaction, as well as for hydrogenation, is provided by SH^- groups.[150, 266] Visualization of different sites in $Mo(W)S_2$ is shown in Figure 13. Control experiments allow us excluding any activity for Ni sulfides, therefore only $Mo(W)S_2$ phases are discussed as catalytically relevant. However, one of the roles of Ni as promoter is the increase of the concentration of both kinds of sites as demonstrated by site titration with several probe molecules.[25, 267-268] Ni also

modifies the intrinsic activity of the sites. Ni-associated vacancies are much more active for sulfur removal and C(sp^3)-N bond cleavage.[25] Moreover, Ni-containing sites are also more efficient than non-promoted sites for hydrogenation of aromatic structures.[109, 248] Thus, as the Ni-promoted Mo(W)S_2 phases are much more active than non-promoted phases, we consider that the proportion of promoted and non-promoted Mo(W)S_2 in a given catalyst determines its activity to a large extent. Accordingly, the least active catalyst for HDS and HDN in this study was NiMoW1, whit the lowest proportion of Ni-promoted Mo(W)S_2 phases.

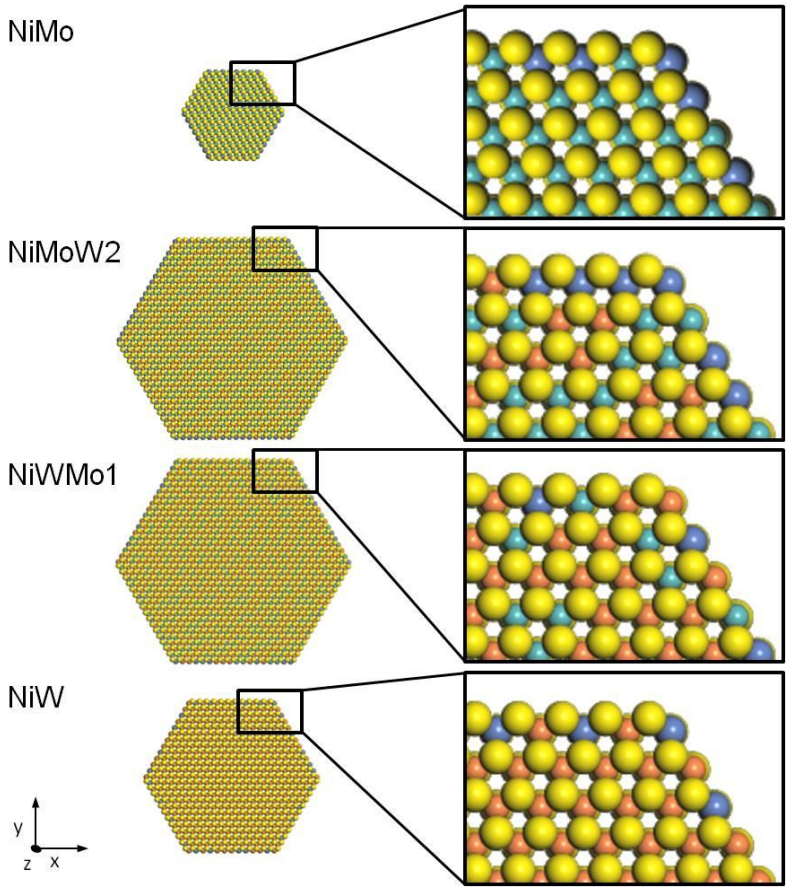

Figure 12. Top view of structural models for the four sulfide catalysts. These models consist of Mo(W)S_2 particles in the P 6_3/mmc space group with hexagonal shape and the van der Waals radii of Mo (light blue), W (orange), Ni (dark blue) and S (yellow). The models reflect the relative sulfide slab size within the catalysts based on the average particle size obtained by TEM (left) and probable atomic distributions of the metals according to EXAFS fit (right).

However, Mo(W)S_2 are anisotropic materials. The active sites of Mo(W)S_2, CUS and SH^- groups are located at the edges of the slabs, or regions of the basal planes near the edges, whereas the basal planes itself are considered as not reactive.[6-7] Metal-like sites, “brim” sites, attributed with hydrogenation functionality, are propose to exist on the basal plane near the edges.[25, 30, 129, 269] These potential active sites are schematically shown in Figure 13 for a Ni-promoted $Mo_{1-x}W_xS_2$ model slab. Thus, the morphology of Mo(W)S_2 (promoted or not) determines the concentration of exposed active sites, which is another key parameter for the

activity of the bulk sulfides (besides promotion). The concentration of accessible active sites is difficult to assess for the catalysts studied in this work because the surface area of these anisotropic materials does not necessarily correspond to the exposed active surface. Titration of NO, correlated to density of CUS on supported catalysts,[24-25, 109] is not informative for our materials because NO adsorbs as well on the inactive Ni sulfides.[248] Nevertheless, our materials have nearly the same surface areas, and concentration of adsorption sites for NO. In order to understand the activity trends, we assess structural differences on atomic and microstructural scales evidenced by EXAFS and TEM analysis.

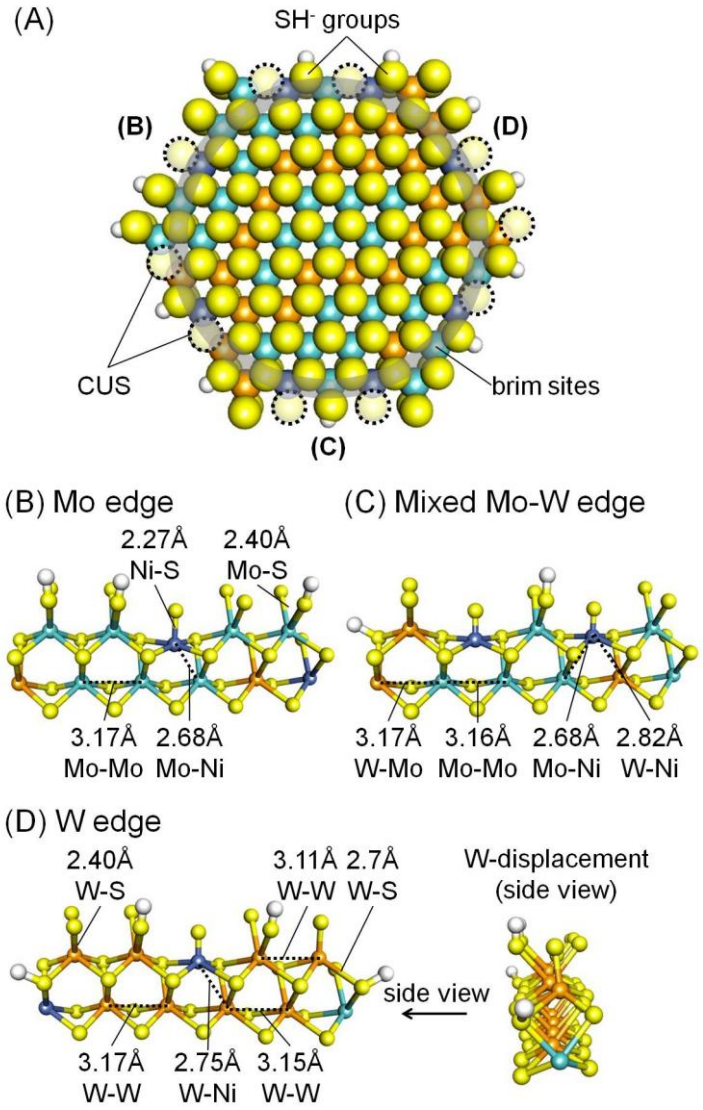

Figure 13. Model Ni-MoWS particle with the location of different active sites, (A): doted circles represent coordinatively unsaturated sites (CUS), white spheres (hydrogen atoms) on top of yellow spheres (sulfur atoms) represent SH^- groups (SH^-), and the greyish circle close to the edge represents the brim sites. The local geometry and the bond distances of the edge atoms according to the corresponding EXAFS fit, are shown in (B), (C), and (D). The edge (B) is representative of Ni in a Mo environment, therefore is the model for NiMo. The edge (C) contains Ni next to Mo and W, therefore is a model for NiMoW. Edge (D), containing only W and Ni, is the model for NiW. Additionally, the model structure (D) is bent in order to show the distribution of W-S and W-W bond distances produced by distorsion. Color code: Mo light blue, W orange, Ni dark blue and S yellow.

NiW was the most active catalyst in the DBT-HDS. This fact reflects that this material has the highest concentration of available CUS as schematically presented in Figure 13(A) and (D). The W-W coordination in NiW is 3.1, much smaller than the Mo-Mo coordination in NiMo (5.1) or the Mo-M/W-M coordination numbers of NiMoW2 (4.7 and 4.1, respectively). This indicates that the sulfide slabs in NiW are, in average, shorter and more distorted than the slabs in the other catalysts.[245] This difference is qualitatively supported by TEM and Raman characterization. Additionally, the modeled surface structure of NiW showed that slight bending of the sulfide slab has strong influence on the bond distances of the edge atoms and therefore on the average coordination number at a distinct distance, see Figure 13(D). As a consequence of those morphology features, larger fraction of edge sites is exposed in NiW than in, e.g., NiMo with a similar content of the Ni-Mo(W)-S phase (inferred from the Ni-Mo, and Ni-W coordination numbers by EXAFS analysis). In the case of NiMoW2, the sulfide slabs are longer than in NiW. These differences render higher fraction of exposed edge sites in NiW than in NiMoW2, which compensates the lower proportion Ni-promoted W in the former and results in similar DBT-HDS activity for both catalysts. In the case of NiMoW1, the low concentration of Ni-Mo(W)-S phases is not compensated by morphology because the $Mo(W)S_2$ slabs are very long (low M-M coordination numbers are caused by distortion instead of short sulfide slabs).

The trend of the OPA-HDN is different to that of DBT-HDS, which indicates that the sites for both processes are different. This is in line with the fact that most of DBT is converted by the direct desulfurization route, whereas hydrogenation dominates HDN. NiW remains as the most active catalyst likely due to its large proportion of exposed active site. However, NiMo, a catalyst with a relatively ordered MoS_2 structure and an apparently lower fraction of edge sites (highest N_{Mo-Mo} and straight, highly stacked slabs) is more active than NiMoW2. Thus we conclude that hydrogenation on bulk sulfides may depend more on structural features like stacking degree, and curvature than on dispersion of the active phase, or concentration of sulfur vacancies, in agreement with previous studies.[25, 153, 265] We speculate that, the ordered and short sulfide slabs in NiMo lead to relatively large concentrations of accessible basal planes compared those provided by large slabs like in NiMoW2 (Figure 12). The regions of the basal planes near the edges are associated to the hydrogenation function according to the “Rim-Edge” model for HDS[270], and are the location of postulated metal-like states (brim sites) acting as hydrogenation sites.[25, 30, 129, 269] Therefore, NiMo appears with a comparable high HDN activity than expected by its apparently low concentration of Ni-promoted sites.

Comparison of two temperature regimes: stability of the Ni-Mo(W)-S phase

Figure 14 presents a comparison of the rates of HDN and HDS (Arrhenius-type plots) over bulk sulfides under two different temperature regimes. That is, 310-350 °C as reported in this work, and 350-370 °C, as reported in a previous contribution.[235]

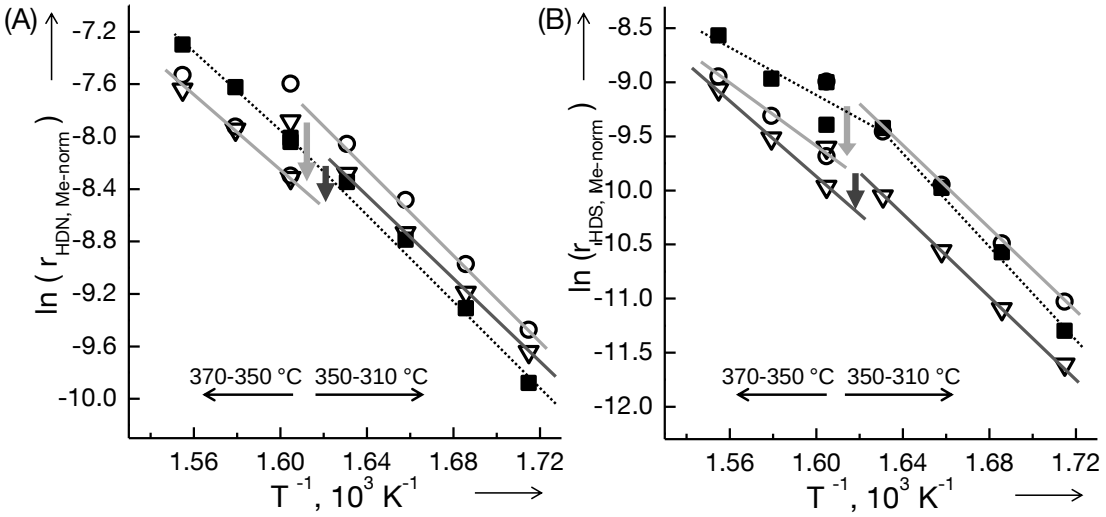

Figure 14. Variation of reaction rates of OPA HDN (A) and DBT HDS (B) with temperature over the sulfided catalysts NiMo (▿), NiMoW2 (■) and NiW (○) at two different regimes (the regime switches for NiW (➔) and NiMo (➔) are indicated).

The apparent activation energies in the high temperature regime are lower than in the low temperature regime. We have excluded transport limitations in both temperature regimes. Thus we attribute the differences in activation energies to structural changes of the sulfides. Moreover, the activity trends (350-370 °C: NiMo < NiW < NiMoW2 for HDS and HDN; 310-350 °C: NiMo < NiW = NiMoW2 for HDS and NiMoW2 < NiMo < NiW for HDN) are different in both regimes because of decreased activity of the bimetallic catalysts in the high temperature range compared to the low temperature regime. Note, that for each temperature regime shown in Figure 14, the catalysts were stabilized at the highest reaction temperature. At the end of the run, the temperature was adjusted as at the beginning of the experiment to verify deactivation, which was negligible, < 2 % over 135 h time on stream. Thus, the discrepancies of the trends in the two regimes are due to the differences in stability of the Ni-Mo(W)-S phase at high temperature, referring to the Ni-Mo(W)-S phase as key parameter for hydrotreating activity. In the high temperature range, NiMoW2 is the most active catalyst because it does not show activity losses likely keeping large contributions of the Ni-Mo(W)-S phase. In turn, we attribute the stability of the Ni-Mo(W)-S phase to the presence of Mo and W in the same sulfide slabs (intralayer $Mo_{1-x}W_xS_2$ particles). In line with this proposal,

supported and unsupported Ni-WS_2 has been found unstable under extreme conditions of temperature and sulfur concentration.[262, 271] In a comparative study, the Ni-Mo-S phase has resulted less stable than Ni-W-S.[272] The instability in both cases (significant losses in activity) was related to phase segregation favoring the formation of bulk Ni sulfides or the migration of Ni towards the support, decreasing so the promotion degree. Thus, it is hypothesized that the proportion of Ni-Mo(W)-S phases in the bimetallic catalysts studied in this work have further decreased at higher temperatures due to segregation of Ni_xS_y particles, which block the active sites at the perimeter of Mo(W)S_2.

4. Conclusions

This study focuses on the psychochemical and kinetic characterization of series of Ni-Mo(W) sulfide catalysts with varying compositions, i.e., Ni-Mo, Ni-W, and Ni-Mo-W. Ni-W and Ni-Mo precursors mainly consist of crystalline $NiWO_4$ and $(NH_4)Ni_2(OH,H_2O)_2(MoO_4)_2$, respectively. The addition of a third metal leads to amorphous materials, although the chemical environment of Ni, W, and Mo cations remained similar to that in the crystalline materials. The intermetallic interactions observed in the structure of the oxide precursors seem determining for the intermetallic interactions within the corresponding sulfides. The sulfide catalysts (NiMo, NiW, NiWMo1, and NiMoW2), obtained by sulfidation at 20 bar at 400 °C under H_2S/H_2 atmosphere, consisted of mixtures of MoS_2, WS_2, Ni_3S_4, and Ni_8S_9 phases according to XRD. The formation of $Mo_{1-x}W_xS_2$ intralayer phases was concluded in the trimetallic materials from analysis of the Raman spectra and the EXAFS. The latter technique also indicates the presence of Ni-promoted Ni-Mo(W)-S phases, with varying Ni-Mo, and Ni-W interactions. Different Ni-Mo and Ni-W distances and very small Ni-Ni coordination numbers hint to a distribution of different Ni entities promoting Mo(W)S_2, ranging from single Ni cations to small clusters. All formulations were tested in the simultaneous hydrodenitrogenation of o-propylaniline and the hydrodesulfurization of dibenzothiophene between 310 °C and 350 °C. The rates of HDN (dominated by hydrogenation prior to denitrogenation) are faster than those of HDS (dominated by direct desulfurization). The activity rankings are as follows NiWMo1 < NiMoW2 < NiMo < NiW for HDN; and NiWMo1 < NiMo < NiW = NiMoW2, for HDS. We conclude that the activity of all unsupported catalysts is determined by the proportion of the Ni-promoted phases and the morphology of the sulfide slabs. NiWMo1 (without Ni-Mo or Ni-W contributions gained by EXAFS fitting) is the least active catalyst in both reactions, whereas NiMoW2 (with the highest Ni-Mo and Ni-W coordination numbers) is among the most active ones in HDS. Morphology plays a crucial role for the bimetallic catalysts. NiW is the most active catalyst because that material

contains short slabs, which increase the concentration of exposed Ni-Mo(W) sites. In NiMo, a high proportion of accessible hydrogenation sites at the basal planes close to the sulfide edges is, in contrast, responsible for its high activity in HDN. Activity trends described for the temperature range of 310-350 °C do not hold in the temperature range of 350-370 °C due to losses in activity of the bimetallic catalysts. Hence, we conclude that the presence of Mo and W in the mixed $Mo_{1-x}W_xS_2$ phase stabilizes the highly active Ni-Mo(W)-S phases even at higher temperatures.

Chapter 7

Summary and Final Conclusions

1. Concluding Summary

In the current PhD thesis, mono-, bi-, and trimetallic oxides and sulfides containing Ni, Mo, and W, were investigated, extensively characterized and applied as heterogeneous catalysts in hydrotreating reactions of model compounds. The project was motivated by the industrial and academic relevance of transition metal sulfides caused by their unique structure and properties and by the ecological and economic importance of developing novel highly active sulfide catalysts for hydrotreating processes.

The emphasis was put on the structural features of unsupported NiMo, NiW and NiMoW sulfide formulations, and their activity in hydrodenitrogenation (HDN). The characterization included the standard methods, such as elemental analysis, nitrogen-physisorption, X-ray diffraction (XRD), DR-UV-vis and Raman spectroscopy, as well as the more advanced techniques electron microscopy, X-ray photoelectron and X-ray absorption spectroscopy (XAS). Scanning electron microscopy (SEM), transmission electron microscopy (TEM), scanning transmission electron microscopy (STEM) and scanning helium ion microscopy (SHIM) were applied to visualize the morphology of the different materials in microstructural and atomic scales. XAS allowed insight into the local environment, i.e., oxidation state and coordination geometry of the absorbing element as well as into the type, amount and distance of the neighboring atoms. X-ray absorption near edge structure (XANES), and extended X-ray absorption fine structure (EXAFS) were used to propose structural models from the analysis and multi-shell fitting procedures performed simultaneously at the Mo K-edge, W L_{III}-edge, and Ni K-edge. The catalytic tests comprised HDN of the model compounds quinoline (Q) and o-propylaniline (OPA) in the presence and absence of dibenzothiophene (DBT), which allowed the additional study of hydrodesulfurization (HDS) and the mutual influence of HDN and HDS. The hydrotreating reactions were performed as temperature dependent experiments at constant space time in a continuous flow trickle bed reactor at 5.0 MPa total pressure. Additionally, the conversion of Q was followed by space time dependent experiments at 370 °C for mechanistic studies.

In the first part of this work, industrial type alumina supported Ni promoted and unpromoted Mo based sulfides, $MoS_2/\gamma\text{-}Al_2O_3$ and $Ni\text{-}MoS_2/\gamma\text{-}Al_2O_3$, were studied and compared to an unsupported $Ni\text{-}MoS_2$ with the aim of gaining insight into the role of the promoter metal Ni and the support on the hydrotreating activity of MoS_2 and to identify the sites active in HDN. The performance of the catalysts was explored with respect to the HDN of Q in the presence of DBT. These kinetic investigations were combined with detailed physicochemical characterization of the sulfide catalysts.

Prior to sulfidation the oxide precursors were characterized by basic techniques. The supported Mo/γ-Al_2O_3 oxide precursor exhibited a well-dispersed amorphous polymolybdate structure. The oligomerization degree of the polymolybdate increased by addition of Ni caused by weakening of the interaction between the Mo species and the support. The NiMo/unsupported oxide precursor exhibited a mixture of nickel molybdate $NiMoO_4$, and an ammonium nickel molybdate $(NH_4)Ni_2(OH,H_2O)(MoO_4)_2$. The MoS_2 phase on alumina had high dispersions, average stacking degree of 2 and particle length of around 6 nm, while Ni-MoS_2/γ-Al_2O_3 exhibited in average shorter and higher stacked particles than MoS_2/γ-Al_2O_3. For the Ni-MoS_2/unsupported catalyst much larger stacking degrees and slab lengths were observed. The presence of Ni increased the concentration of coordinatively unsaturated sites (CUS) in the supported catalyst, whereas a higher agglomeration degree of the sulfide species in Ni-MoS_2/unsupported catalysts resulted in the lowest CUS concentration. Additionally, Mo-Ni interactions were identified, which pointed to the presence of Ni promoted MoS_2 structures in both Ni containing materials.

The hydrodenitrogenation and hydrodesulfurization activities followed the increasing trend: MoS_2/γ-Al_2O_3 < Ni-MoS_2/unsupported < Ni-MoS_2/γ-Al_2O_3. The observed mechanism for N removal in the quinoline HDN was the same on all three catalysts. The main conversion route for Q was identified as: Q → 1,2,3,4-tetrahydroquinoline (equilibrated step) → deca-hydroquinoline (DHQ, hydrogenation) → propylcyclohexylamine (ring opening via C(sp^3)-N bond cleavage) → propylcyclohexene (Hofmann-type elimination) → propylcyclohexane (hydrogenation). The ring opening of DHQ was rate determining in this sequence.

The high rates of Ni-MoS_2/γ-Al_2O_3 were caused by the high dispersion of the active phase on the support and by the promotion of Ni attributed to the formation of the Ni-Mo-S phase (Ni atoms decorating MoS_2). The higher intrinsic rates of Ni-MoS_2/unsupported than that of supported highly dispersed MoS_2/γ-Al_2O_3 was as well caused by a promotion mechanisms of Ni species. However, it was proposed that the promoter effect was mainly caused by formed Ni_xS_y particles at the MoS_2 edges, i.e., induced by the morphology of the unsupported material. This type of promoted sulfide structure exhibited an apparently weaker promoting effect than single Ni atom decoration suggested for Ni-MoS_2/γ-Al_2O_3.

In the second part of the PhD project, unsupported multimetallic materials were further investigated. The preparation and characterization of oxide precursors were addressed by improving the synthesis procedure, i.e., the preparation of a single phase NiMo material was achieved as well as the preparation of NiW and trimetallic NiMoW formulations. Thus, four unsupported multimetallic oxides were prepared, two bimetallic, $NiMo_{Ox}$ and NiW_{Ox}, and two

trimetallic, $NiWMo1_{Ox}$ and $NiMoW2_{Ox}$, precursors. The trimetallic materials had the Mo to W ratios of 1:2 in $NiWMo1_{Ox}$ and 1:1 in $NiMoW2_{Ox}$.

The four materials exhibited multimetallic oxide phases with different coordination geometries for Ni, Mo and W. For the bimetallic $NiMo_{Ox}$ a layered ammonium nickel molybdate $(NH_4)Ni_2(OH,H_2O)(MoO_4)_2$ phase was identified comprising corner connected $[MoO_4]$-tetrahedra and $[NiO_6]$-octahedra. The predominant phase in NiW_{Ox} was the monoclinic closed packed $NiWO_4$ with edge and corner connected $[WO_6]$- and $[NiO_6]$-octahedra. For the trimetallic oxides, X-ray amorphous Mo-W mixed phases were observed with structures dependent on their Mo to W ratio, although the chemical environment of Ni^{2+}, Mo^{6+}, and W^{6+} cations remained similar to that in the crystalline bimetallic materials. The Mo-W interaction was especially pronounced in the $NiMoW2_{Ox}$ precursor, for which a layered ammonium nickel metallate structure, similar to $(NH_4)Ni_2(OH,H_2O)(Mo_{0.5}W_{0.5}O_4)_2$, was concluded. Therefore, $NiMoW2_{Ox}$ contained highly distorted $[MO_4]$-tetrahedra and $[NiO_6]$-octahedra in a structure comparable to $NiMo_{Ox}$. In contrast, the multimetallic oxide structure of $NiWMo1_{Ox}$ was more similar to the one of NiW_{Ox}. A $NiMo_{0.33}W_{0.67}O_4$ phase with a distorted wolframite-type structure comprising edge and corner connected distorted metal polyhedra was proposed for $NiWMo1_{Ox}$.

The unsupported multimetallic sulfide catalysts were obtained after sulfidation of the oxide precursors under pressure in a H_2S/H_2 atmosphere, and an advanced characterization of NiMoS, NiWS, NiWMo1S and NiMoW2S was performed to investigate the structure, morphology, and local environment of the three metallic catalysts constituents. The distribution and interaction of Mo and W as well as the location and nature of the Ni species were of special interest. Therefore, a comprehensive STEM and EXAFS study of NiMoW2S at all three metallic absorption edges in combination with TEM, XRD, and Raman spectroscopy was used in order to elucidate atomic interactions.

The characterization of NiMoS, NiWS, NiWMo1S and NiMoW2S suggested that all catalysts consisted of mixtures of Ni containing $Mo(W)S_2$ slabs and different Ni sulfides (Ni_9S_8, Ni_3S_2, and Ni_3S_4). The $(Ni)Mo(W)S_2$ phases were formed by stacks of 4-6 sulfide slabs with different degree of bending, mismatch between the layers, and sulfide phase agglomeration in random directions. NiWMo1S had a complex morphology featured by strong bending and long slabs. Electron microscopy images with atomic resolution suggested the formation of intralayer $Mo_{1-x}W_xS_2$ particles with Mo and W in the same sulfide slabs in NiMoW2S. This hypothesis was confirmed by EXAFS measurements and fittings based on theoretical EXAFS of model clusters. The analysis of the theoretical EXAFS showed that only the close vicinity of Mo and W within a sulfide slab influences the EXAFS and corresponding Fourier transforms. It was proven that the backscattering functions of Mo and W present in interlayer

mixed $Mo_{1-x}W_xS_2$ particles with slabs of MoS_2 and WS_2 stacked in different sequences contribute to a minor extent to the overall EXAFS function. In NiWMo1S, the formation of $Mo_{1-x}W_xS_2$ intralayer phases was as well concluded, although to a lower concentration. The EXAFS fittings of bimetallic sulfides confirmed the presence of MoS_2 and WS_2, in NiMoS and NiWS, respectively. The formed Ni sulfides showed a broad distribution of particle sizes, on which the $Mo(W)S_2$ agglomerates deposited or which were completely covered by the $Mo(W)S_2$ domains. These covered small Ni species were either very small Ni_xS_y clusters or atomically dispersed Ni. Additionally, the presence of mixed Ni-Mo(W) sulfide phases was concluded in NiMoS and NiMoWS2 on the basis of Ni-Mo (Mo-Ni), and Ni-W (W-Ni) EXAFS contributions, while these contributions were weaker in NiWS and NiWMo1S. Consequently, the intermetallic interactions observed in the structure of the oxide precursors seem determining for the intermetallic interactions within the corresponding sulfides. The values of the Mo-Ni/W-Ni coordination numbers suggested a most pronounced Mo(W)-Ni interaction in the trimetallic NiMoW2S catalyst.

The impact of the physicochemical properties of unsupported sulfide catalysts on catalytic activity was explored for the simultaneous HDN of OPA and HDS of DBT. The formulations were tested in different temperature regimes. First, NiMoS, NiWS and NiMoW2S were tested between 350 °C to 370 °C. A second series of activity tests between 310 °C and 350 °C on all four catalysts were performed to explore the differential kinetic regime. The purpose of all activity studies was the identification of the required properties to obtain hydrotreating catalysts with high activity and stability for simultaneous HDN and HDS reactions.

All catalysts, i.e., NiMoS, NiWS, NiMoW2S, and NiWMo1S offered interesting possibilities for hydrodenitrogenation, hydrodesulfurization as well as hydrogenation reactions. The rates of HDN (dominated by hydrogenation prior to denitrogenation) were faster than those of HDS (dominated by direct desulfurization). The activity rankings in HDN were as follows, NiMoW2S > NiWS ≈ NiMoS at 370 °C and NiWS > NiMoS > NiMoW2S > NiWMo1S at 350 °C. And in HDS the following trends were observed NiMoW2S > NiWS > NiMoS at 370 °C and NiMoW2S ≈ NiWS > NiMoS > NiWMo1S at 350 °C. Thus, the trends observed at lower temperatures do not hold at higher temperatures due to losses in activity of the bimetallic catalysts. Overall, the trimetallic catalyst NiMoWS2 was the most active material in HDS and in HDN (at high temperatures), whereas the other trimetallic sulfide NiWMo1S had the lowest hydrotreating activities (between 310 °C and 350 °C).

The catalytic properties of the sulfides are governed by the interplay between the proportion of the Ni-promoted phases, the morphology of the $Mo(W)S_2$ slabs and the concentration of accessible cations (CUS) and SH^- groups. The low activity of NiWMo1S is explained by the lowest proportion of incorporated Ni and its long, curved slabs providing a low accessibility to

active sites. Morphology is as well crucial for the bimetallic catalysts. It is suggested that the high activity of NiWS is caused by its short slabs, which increase the concentration of exposed Ni promoted and unpromoted W-sites. And in NiMoS, a high proportion of accessible hydrogenation sites at the basal planes close to the sulfide edges is most probably responsible for its high activity in HDN. However, the morphology of NiWS and NiMoS apparently undergoes a restructuring at higher temperatures, which induces shifts to lower activity.

The highest proportion of Ni promoted Mo(W)S_2 phase accompanied by an intense interaction between Mo and W was observed for the trimetallic NiMoW2S catalyst. Furthermore, the intralayer mixed $Mo_{1-x}W_xS_2$ slabs exhibited medium values in length, stacking degree and only slight curvature as well as a large specific perimeter. These structural features resulted in the highest concentration of active sites leading to the highest HDN and HDS rates. It is proposed, that the simultaneous presence of Mo and W in the same slab favors nucleation of Ni promoting species and retards its further growth, allowing so the largest fraction of Ni to be incorporated into Ni-Mo(W)-S phases. And the additional slow growth of $Mo_{1-x}W_xS_2$ leads to a maximization of the active sites at the perimeter of the particles. Moreover, the mixed $Mo_{1-x}W_xS_2$ phase stabilizes the highly active Ni-Mo(W)-S phases at higher temperatures better than the pure metal sulfide phases.

In summary, in the framework of this PhD thesis it was possible to gain new insight into structural properties of unsupported multimetallic Ni-Mo-W sulfides, their hydrotreating activity and into active sites involved. The self-selected series of two bimetallic, NiMoS and NiWS, and two trimetallic, NiWMo1S and NiMoW2S, sulfide catalysts allowed the study and understanding of the structural and catalytic interaction of the consisting transition metals Ni, Mo, and W. Moreover, this study was complemented by a full characterization of the four unsupported oxide precursors as well as by a comparative investigation of an unsupported Ni-MoS_2 catalyst and commonly applied supported MoS_2 and Ni-MoS_2 catalysts. The distribution of Ni, Mo and W in the unsupported sulfides is identified. Ni is present in various phases, either in Ni sulfides exhibiting different composition and crystal sizes or in Ni-promoted Mo(W)S_2 phases. Trimetallic Ni-Mo-W sulfides form intralayer mixed $Mo_{1-x}W_xS_2$ phases whose promotion with Ni lead to higher fraction of incorporated Ni. All sulfide phases are in a close contact to each other and form complex morphologies, which are characterized by large crystalline domains with some structural disorder. All four unsupported sulfides exhibit excellent catalytic performance in N removal of OPA and S removal of DBT. The unsupported materials show high activities per volume of catalyst and similar selectivities, which are also comparable to supported catalysts.

Overall, this work demonstrates that Ni promotion and the morphology of unsupported $Mo(W)S_2$ are the key parameters for catalytic activity in hydrotreating. Both features are critical for the concentration and accessibility of active sites. It is further recognized that the composition and structure of the oxide precursors allow controlling to some extent the properties of the corresponding sulfides. Moreover, Ni promoting intralayer mixed $Mo_{1-x}W_xS_2$ phases are found to be more stable under hydrotreating conditions than Ni promoting pure MoS_2 or WS_2. Future work should, therefore, address the control of Mo-W alloying degree in mixed sulfides, the formation of Ni promoting species and the sulfide morphology during precursor preparation and sulfidation. Furthermore, it is important to focus on the unanswered questions, i.e., the exact structure of Ni promoting species and the correlation between this structure and the catalyst activity, in order to gain an even deeper understanding of these unique and highly interesting materials and to promote further developments in sulfide catalysts.

2. Abschließende Zusammenfassung

In der vorliegenden Doktorarbeit wurden mono-, bi- und trimetallische Oxide und Sulfide, welche die Elemente Nickel (Ni), Molybdän (Mo) und Wolfram (W) beinhalten, untersucht, ausführlich charakterisiert und als heterogene Katalysatoren in Hydrotreatingreaktionen von Modelverbindungen verwendet. Die allgemeine industrielle und akademische Bedeutung von Übergangsmetallsulfiden sowie die ökologische und ökonomische Notwendigkeit für besonders effektive sulfidische Hydrotreatingkatalysatoren waren die motivierenden Hintergründe für diese Dissertation.

Der Schwerpunkt der Arbeit lag auf den strukturellen Besonderheiten von ungeträgerten NiMo, NiW und NiMoW Sulfiden und ihrer katalytischen Aktivität in hydrierenden Entstickungsreaktionen (HDN) von organischen Modellverbindungen. Die hergestellten Materialien wurden sowohl mit den klassischen Standardmethoden, wie Elementaranalyse, Stickstoff-Adsorption, Röntgenbeugung, DR-UV-vis und Ramanspektroskopie, als auch mit den moderneren Verfahren der Elektronenmikroskopie, Röntgenphotoelektronen- und Röntgenabsorptionsspektroskopie (XAS) charakterisiert. Zu den angewendeten mikroskopischen Methoden zählten Rasterelektronenmikroskopie (SEM), Transmissions-elektronenmikroskopie (TEM), Rastertransmissionselektronenmikroskopie (STEM) und Raster-Heliumionenmikroskopie (SHIM). Diese Methoden wurden verwendet, um die Morphologie der unterschiedlichen Proben in verschiedenen Vergrößerungen darzustellen, welche von Mikrometern bis hin zur atomaren Auflösung reichten. XAS ermöglichte es die lokale Umgebung, d.h. den Oxidationszustand und die Koordinationsgeometrie des absorbierenden Metalls sowie die Art, Anzahl und den Abstand der Nachbaratome aufzuklären. Hierfür wurde der XANES (absorption near edge structure) Bereich analysiert und die experimentelle EXAFS (extended X-ray absorption fine structure) unter Verwendung von theoretischen EXAFS von möglichen Modellverbindung und einer Fitting-Prozedur beschrieben. Die Modelle beinhalteten mehrere Nachbarschalen, zudem wurden die verschiedenen Absorptionskanten der jeweils enthaltenen Elemente (Mo_K, W_{LIII} und Ni_K) gleichzeitig gefittet, um mögliche intermetallische Nachbarn zu identifizieren. Die katalytischen Aktivitätstests umfassten HDN Reaktionen der Modelverbindungen Chinolin (quinoline Q) und ortho-Propylanilin (OPA), die sowohl in der Gegenwart als auch in der Abwesenheit von Dibenzothiophen (DBT) durchgeführt wurden. Die Verwendung von DBT ermöglichte zudem die gleichzeitige Untersuchung der hydrierenden Entschweflungsreaktion (HDS) sowie den gegenseitigen Einfluss von HDN und HDS Reaktionen. Alle Reaktionen wurden in Abhängigkeit von der Temperatur bei konstanten Verweilzeiten (bzw. Raumgeschwindigkeit) und bei einem konstanten Druck von 5.0 MPa unter Verwendung

eines kontinuierlich durchströmten Rieselbettreaktors studiert. Zusätzlich wurde der Umsatz von Q auch in einem verweilzeitabhängigen Experiment bei 370 °C verfolgt, um den Reaktionsmechanismus aufzuklären.

In dem ersten Teil der vorliegenden Arbeit wurden Aluminiumoxid geträgerte Nickel promotierte und unpromotierte Mo Sulfide, $MoS_2/\gamma\text{-}Al_2O_3$ und $Ni\text{-}MoS_2/\gamma\text{-}Al_2O_3$, untersucht, welche vergleichbar zu industriell verwendeten Hydrotreatingkatalysatoren sind. Diese wurden dann mit einem ungeträgerten $Ni\text{-}MoS_2$ Katalysator verglichen, um einen Einblick in die Funktion und Bedeutung des Trägermaterials sowie des Promotermetals Ni für die katalytische Aktivität zu gewinnen und um HDN aktive Zentren zu identifizieren. Als Testreaktion für die katalytische Aktivität der Katalysatoren wurde die HDN von Q in Gegenwart von DBT verwendet. Diese kinetischen Untersuchen wurden dann mit der detaillierten Charakterisierung der sulfidischen Katalysatoren kombiniert. Vor der Sulfidierung der oxidischen Ausgangsmaterialien wurden diese zusätzlich charakterisiert. Das geträgerte oxidische $Mo/\gamma\text{-}Al_2O_3$ Material enthielt amorphe Polymolybdate, welche sich feinverteilt auf dem Al_2O_3 Träger befanden. Beim Hinzufügen des Promoters Ni wurde ein Anstieg des Polymerisationsgrades beobachtet als Folge der geschwächten Wechselwirkungskräfte zwischen den Polymolybdaten und Al_2O_3 durch Ni. Die oxidische NiMo/ungeträgert Probe war eine Mischung aus Nickelmolybdat $NiMoO_4$ und einem Ammoniumnickelmolybdat der Form $(NH_4)Ni_2(OH,H_2O)(MoO_4)_2$. Die sulfidischen MoS_2 Phasen der geträgerten Proben lagen mit einer sehr guten Verteilung auf Al_2O_3 vor und bestanden im Durchschnitt aus etwa 2 gestapelten MoS_2 Lagen mit einer Länge von ca. 6 nm. Der Ni promotierte Katalysator $Ni\text{-}MoS_2/\gamma\text{-}Al_2O_3$ besaß im Mittel kürzere Partikel mit einer höheren Anzahl an gestapelten MoS_2 Lagen als das unpromotierte Material. Für den sulfidischen Katalysator $Ni\text{-}MoS_2$/ungeträgert wurden hingegen viel größere Partikel mit deutlich mehr gestapelten MoS_2 Sulfidlagen beobachtet. Es wurde festgestellt, dass die Gegenwart von Ni in geträgerten Katalysatoren die Konzentration an ungesättigten Metallzentren/Lehrstellen (coordinatively unsaturated sites CUS) merklich erhöhte, wohingegen der hohe Agglomerationsgrad der sulfidischen Phasen in $Ni\text{-}MoS_2$/ungeträgert zu der geringsten CUS-Konzentration führte. Zusätzlich wurden in beiden Ni haltigen Katalysatoren Mo-Ni Wechselwirkungen identifiziert, welche auf die Ausbildung von Ni promotierte MoS_2 Strukturen hinwiesen.

Die HDN und HDS Aktivitäten zeigten den folgenden steigenden Trend: $MoS_2/\gamma\text{-}Al_2O_3$ < $Ni\text{-}MoS_2$/ungeträgert < $Ni\text{-}MoS_2/\gamma\text{-}Al_2O_3$. Der beobachtete Mechanismus für die Stickstoffentfernung aus Q war identisch für alle drei Katalysatoren. Die Umsetzung von Q erfolgte hauptsächlich gemäß folgender Sequenz: Q → 1,2,3,4-Tetrahydrochinolin (Gleichgewichtseinstellung) → Decahydrochinolin (DHQ, Hydrierung) → Propylcyclohexyl-

amin (Ringöffnung via C(sp^3)-N Bindungsbruch) → Propylcyclohexen (Hofmann-artige Eliminierung) → Propylcyclohexan (Hydrierung). Dabei war die Ringöffnung von DHQ der geschwindigkeitsbestimmende Schritt. Die hohen Raten von Ni-MoS_2/γ-Al_2O_3 wurden hauptsächlich zurückgeführt auf die hervorragende Verteilung der aktiven Phase auf dem Trägermaterial sowie auf die Ausbildung der Ni-Mo-S Phase, bei der sich Ni Atome an den Kanten der MoS_2 Kristalle befinden und auf deren Präsenz die nachgewiesenen Mo-Ni Wechselwirkungen hinweisen. Die höheren intrinsischen Raten von Ni-MoS_2/ungeträgert wurden ebenfalls der MoS_2 Promotion mit Ni zugeschrieben, welches einen größeren Effekt auf die Aktivität hatte als die für MoS_2/γ-Al_2O_3 beobachtete gute Verteilung der aktiven Spezies. Es wurde vorgeschlagen, dass der Promotereffekt in Ni-MoS_2/ungeträgert durch die Morphologie beeinflusst wurde und hauptsächlich durch kleine Ni_xS_y Partikel an den Kanten von MoS_2 verursacht wurde. Diese Art der Wechselwirkung zwischen Ni und MoS_2 resultiert scheinbar in einem schwächeren Promotionseffekt als die Kantendekoration von MoS_2 mit einzelnen Ni Atomen (vorgeschlagen für Ni-MoS_2/γ-Al_2O_3).

Im zweiten Teil des Dissertationsprojektes wurden die ungeträgerten multimetallischen Materialien weiterentwickelt und studiert. Zunächst wurde die Präparation und Charakterisierung der oxidischen Ausgangsmaterialen weitergeführt mit dem Ziel ein phasenreines bimetallisches Ni-Mo-Oxid sowie Ni-W- und trimetallische Ni-Mo-W-Oxide herzustellen. Das Resultat waren vier ungeträgerte Oxide, zwei bimetallische $NiMo_{Ox}$ und NiW_{Ox} und zwei trimetallische Materialen $NiWMo1_{Ox}$ und $NiMoW2_{Ox}$. Die beiden trimetallischen Oxide hatten unterschiedliche Mo zu W Verhältnisse mit 1:2 in $NiWMo1_{Ox}$ und 1:1 in $NiMoW2_{Ox}$.

Die vier Oxide bestanden aus multimetallischen oxidischen Phasen, in denen die Metalle Ni, Mo und W unterschiedliche Koordinationsgeometrien besaßen. Für $NiMo_{Ox}$ wurde eine annähernd phasenreine Schichtstruktur aus einem Ammoniumnickelmolybdat der Form $(NH_4)Ni_2(OH,H_2O)(MoO_4)_2$ bestimmt, in der eckenverknüpfte $[MoO_4]$-Tetraeder und $[NiO_6]$-Oktaeder vorliegen. Die vorherrschende Phase in NiW_{Ox} war das monokline dicht gepackte $NiWO_4$ mit kanten- und eckenverknüpften $[WO_6]$- und $[NiO_6]$-Oktaedern (Strukturtyp: Wolframit). In den trimetallischen Oxiden wurden röntgenamorphe gemischte Mo-W Oxidphasen gefunden, deren Strukturen von den Mo zu W Verhältnissen abhängig waren. Jedoch waren die chemischen Umgebungen der Ni^{2+}, Mo^{6+} und W^{6+} Kationen vergleichbar zu denen in den kristallinen bimetallischen Oxiden. Die gefundenen Mo-W Wechselwirkungen in den trimetallischen Oxiden waren besonders in $NiMoW2_{Ox}$ ausgeprägt, für welches eine schichtstrukturähnliche Phase der allgemeinen Form des Ammoniumnickelmetallats $(NH_4)Ni_2(OH,H_2O)(Mo_{0.5}W_{0.5}O_4)_2$ geschlussfolgert wurde. Dieser Strukturvorschlag beruhte auf der Tatsache, dass sich $NiMoW2_{Ox}$ sehr ähnlich zum $NiMo_{Ox}$

verhielt und ebenso [MO_4]-Tetraeder und [NiO_6]-Oktaeder nachgewiesen wurden, obgleich diese Polyeder sehr stark verzerrt vorlagen. Im Gegensatz dazu war das zweite trimetallische Oxid $NiWMo1_{Ox}$ eher vergleichbar mit NiW_{Ox}. Aus diesem Grund wurde für $NiWMo1_{Ox}$ eine $NiMo_{0.33}W_{0.67}O_4$ ähnliche Phase mit kanten- und eckenverknüpften verzerrten Metallpolyedern in einer verzerrten Wolframit-Struktur vorgeschlagen.

Nach der Hochdruck-Sulfidierung der multimetallischen Oxide in einem H_2S/H_2 Gasgemisch wurden die ungeträgerten sulfidischen Katalysatoren NiMoS, NiWS, NiWMo1S und NiMoW2S erhalten und diese umfassend und detailliert charakterisiert, um deren Morphologie, Struktur und Nahordnung der enthaltenen Metalle aufzuklären. Von besonderem Interesse waren die Verteilung und Wechselwirkungen von Mo und W sowie die Position und Struktur der Ni Spezies. Deswegen wurde eine neuartige komplementäre STEM und EXAFS Studie von NiMoW2S an allen drei metallischen Absorptionskanten durchgeführt und mit Messergebnissen der TEM, XRD, und Ramanspektroskopie kombiniert. Die Charakterisierung von NiMoS, NiWS, NiWMo1S und NiMoW2S ergab, dass alle Katalysatoren aus einem Gemisch aus Ni haltigen Mo(W)S_2 Phasen und unterschiedlichen Nickelsulfiden (Ni_9S_8, Ni_3S_2 und Ni_3S_4) bestanden. Die (Ni)Mo(W)S_2 Phasen wurden gebildet aus 4-6 gestapelten Mo(W)S_2 Sulfidschichten, die teilweise stark ungeordnet vorlagen. D. h., die (Ni)Mo(W)S_2 Schichten waren unterschiedlich stark gebogen, wiesen Stapelfehlordnungen auf und die Kristallite waren scheinbar willkürlich orientiert. In NiWMo1S war eine besonders komplexe Morphologie präsent, die sich durch eine starke Krümmung der zum Teil sehr langen Mo(W)S_2 Sulfidschichten auszeichnete. Elektronenmikroskopieaufnahmen von NiMoW2S wiesen auf die Ausbildung von gemischten $Mo_{1-x}W_xS_2$ Partikeln hin, in denen Mo und W in der gleichen Sulfidschicht vorlagen (intralamellare Mischung, sog. intralayer). Diese Vermutung konnte dann mittels EXAFS Messungen und mathematischen Fitting-Prozeduren basierend auf theoretischen selbstkreierten Modelclustern bestätigt werden. Die Analyse der theoretischen EXAFS zeigte, dass nur die direkte Nachbarschaft von Mo und W innerhalb der gleichen sulfidischen Schicht einen entscheidenden Einfluss auf die EXAFS und die dazugehörige Fourier transformierte Pseudo-Radialverteilungsfunktion hatte. Es wurde ferner gezeigt, dass die Rückstreufunktionen von Mo und W Nachbarn, die sich in unterschiedlichen Schichten eines interlamellaren Mischkristalls (Stapelung von phasenreinen [MoS_2]- und [WS_2] Schichten, sog. interlayer) befanden, nur geringfügig zur gemittelten EXAFS Funktion des gesamten $Mo_{1-x}W_xS_2$ Partikels beitrugen. Das bedeutet, dass die EXAFS Funktion eines interlayer $Mo_{1-x}W_xS_2$ Mischkristalls fast deckungsgleich war zu einem phasenreinem MoS_2 oder WS_2 Partikels. In NiWMo1S wurde die Ausbildung der intralayer $Mo_{1-x}W_xS_2$ Mischphase ebenfalls mit EXAFS nachgewiesen. Allerdings war diese Phase weniger stark ausgeprägt als in NiMoW2S, was auf eine höhere Konzentration von monometallischen Sulfidschichten und/oder auf starker Fehlordnung oder Kristallverzerrung

innerhalb von NiWMo1S hinwies. Die Ergebnisse des EXAFS Fittings für die bimetallischen Sulfide bestätigten die Ausbildung von MoS_2 und WS_2, in NiMoS bzw. NiWS. Die gebildeten Nickelsulfide traten in verschiedenen Größen auf, auf denen entweder kleine $Mo(W)S_2$ Agglomerate kristallisierten oder die vollständig von großen $Mo(W)S_2$ Kristallen bedeckt wurden. Diese kleinen Nickelspezies waren entweder Ni_xS_y Cluster oder atomar verteiltes Ni. Zusätzlich wurden Ni-Mo (Mo-Ni) und Ni-W (W-Ni) Beiträge mittels EXAFS in NiMoS und NiMoWS2 nachgewiesen, was auf die Bildung von gemischten Ni-Mo(W) Sulfidphasen schließen ließ. Diese gemischten Ni Beiträge wurden auch in NiWS und NiWMo1S gefunden jedoch mit kleineren Koordinationszahlen. Dementsprechend sind die intermetallischen Wechselwirkungen, die bereits in den Oxiden vermutet wurden, während der Sulfidierung bestehen geblieben und konnten letztendlich in den Sulfiden eindeutig nachgewiesen werden. Die bestimmten Koordinationszahlen für die Mo-Ni/W-Ni Beiträge lassen zudem im trimetallischen NiMoW2S Katalysator auf die stärksten Mo(W)-Ni Wechselwirkungen schließen.

Der Einfluss der physikochemischen Eigenschaften der ungeträgerten sulfidischen Katalysatoren auf ihre katalytische Aktivität wurde mittels der simultanen HDN von OPA und HDS von DBT untersucht. Die Katalysatoren wurden in unterschiedlichen Temperaturbereichen getestet. Zunächst wurden NiMoS, NiWS und NiMoW2S zwischen 350 °C bis 370 °C untersucht und anschließend erfolgten katalytische Aktivitätstest zwischen 310 °C und 350 °C für alle vier sulfidischen Katalysatoren, um den differentialen kinetischen Bereich genauer zu studieren. Mit diesen Aktivitätsstudien sollten die notwendigen Eigenschaften von Hydrotreatingkatalysatoren für eine hohe Aktivität und Stabilität während der simultan ablaufenden HDN und HDS Reaktionen identifiziert werden. Alle Katalysatoren, d. h., NiMoS, NiWS, NiMoW2S und NiWMo1S, boten interessante Anwendungsmöglichkeiten für die hydrierende Entstickung und Entschwefelung als auch für Hydrierungen. Die bestimmten HDN Raten, welche von Hydrierreaktionen vor der eigentlichen Entstickung dominiert wurden, waren größer als die HDS Raten (geprägt von der direkten Entschwefelung). Die HDN Aktivitätstrends waren wie folgt: bei 370 °C, NiMoW2S > NiWS ≈ NiMoS und bei 350 °C NiWS > NiMoS > NiMoW2S > NiWMo1S. Bei der HDS Reaktion wurden folgende Trends beobachtet: NiMoW2S > NiWS > NiMoS bei 370 °C und NiMoW2S ≈ NiWS > NiMoS > NiWMo1S bei 350 °C. Dementsprechend wurden unterschiedliche Trends in den untersuchten Temperaturbereichen gefunden, die auf Aktivitätsverluste der bimetallischen Sulfide bei höheren Temperaturen zurückzuführen waren. Im Allgemeinen zeigte der trimetallische NiMoWS2 Katalysator die höchste Aktivität in HDS und in HDN (bei hohen Temperaturen), wohingegen der zweite trimetallische NiWMo1S Katalysator die geringsten Hydrotreatingaktivitäten besaß (zwischen 310 °C und 350 °C).

Die katalytischen Eigenschaften der ungeträgerten Sulfide wird beherrscht von dem Zusammenspiel der Morphologie der $Mo(W)S_2$ Schichten, dem Anteil der Ni promotierten Phasen sowie der Konzentrationen der erreichbaren metallischen Lehrstellen (CUS) und SH^- Gruppen. Die geringe Aktivität von NiWMo1S kann erklärt werden mit dem im Vergleich zu den anderen Katalysatoren geringsten Anteil an inkorporierten Ni in $Mo(W)S_2$ und dessen langen, stark gekrümmten $Mo(W)S_2$ Schichten, die eine nur sehr geringe Erreichbarkeit der aktiven Zentren ermöglichen. Die Morphologie ist auch ausschlaggebend für die bimetallischen Katalysatoren. Die hohe Aktivität von NiWS wird zurückgeführt auf dessen kurze WS_2 Schichten, die die Konzentration der exponierten Ni promotierten und unpromotierten Wolframlehrstellen erhöhen. Während in NiMoS höchstwahrscheinlich der hohe Anteil an den gut erreichbaren hydrieraktiven Zentren auf den Basalflächen nahe der Kanten der MoS_2 Partikel verantwortlich sind für dessen hohe HDN Aktivität. Jedoch durchlaufen NiWS und NiMoS scheinbar einen Restrukturierungsprozess bei höheren Temperaturen, der deren Morphologie und damit ihre Aktivität negativ verändert. Der höchste Anteil der Ni promotierten $Mo(W)S_2$ Phase wurde für NiMoW2S beobachtet und zusätzlich bestand eine intensive Wechselwirkung zwischen Mo und W. Des Weiteren besaßen dessen $Mo_{1-x}W_xS_2$ Schichten im Verhältnis zu den anderen ungeträgerten Katalysatoren eine mittlere Länge, eine mittlere Anzahl an gestapelten Sulfidschichten und nur eine geringfügige Krümmung sowie den größten spezifischen Umfang, d. h. den höchsten Anteil an erreichbaren Kanten der sulfidischen Schichten. Diese strukturellen Besonderheiten führten zu der höchsten Konzentration an aktiven Zentren und somit zu den höchsten HDN und HDS Raten. Aufgrund dieser Beobachtungen wird vermutet, dass die simultane Gegenwart von Mo und W in den gleichen sulfidischen Schicht die Kristallisation von Ni promotierten Spezies induziert und zeitgleich dessen weiteres Wachstum verzögert, so dass ein sehr großer Anteil an Ni in der Ni-Mo(W)-S Phase vorliegen kann. Zeitgleich führt ein verlangsamtes Kristallwachstum von $Mo_{1-x}W_xS_2$ zu einer Maximierung der aktiven Zentren an den Kanten der Sulfidpartikel. Des Weiteren stabilisiert die intralayer $Mo_{1-x}W_xS_2$ Mischkristallphase die hoch aktive Ni-Mo(W)-S Phase bei höheren Temperaturen besser als die reinen Metallsulfide.

Abschließend ist festzustellen, dass es im Rahmen der vorliegenden Doktorarbeit möglich war, einen neuen Einblick in die strukturellen Eigenschaften von ungeträgerten multi-metallischen Ni-Mo-W Sulfiden sowie in deren Hydrotreatingaktivität und den involvierten aktiven Zentren zu erhalten. Die selbstgewählte Serie von zwei bimetallischen, NiMoS und NiWS, und zwei trimetallischen, NiWMo1S und NiMoW2S, sulfidischen Katalysatoren erlaubte die Analyse und das Verständnis der strukturellen und katalytischen Wechselwirkungen der enthaltenen Übergangsmetalle Ni, Mo und W. Die Studie über die ungeträgerten Sulfide wurde komplettiert um die vollständige Charakterisierung der vier

oxidischen Ausgangsmaterialien sowie um die vergleichende Untersuchung eines ungeträgerten Ni-MoS_2 Katalysators mit Aluminiumoxid geträgerten MoS_2 und Ni-MoS_2 Katalysatoren. Die Verteilung von Ni, Mo und W in den ungeträgerten Sulfiden ist aufgeklärt worden. Nickel ist in unterschiedlichen Phasen präsent. Es liegt entweder in Nickelsulfiden mit unterschiedlicher Zusammensatzung und in verschiedenen Kristallitgrößen vor oder in Ni promotierten Mo(W)S_2 Phasen. Trimetallische Ni-Mo-W Sulfide bilden intralayer $Mo_{1-x}W_xS_2$ Mischkristallphasen, deren Promotierung mit Ni zu einer höheren Konzentration von inkorporierten Ni führen. Alle enthaltenen sulfidischen Phasen liegen in einem dichtem Kontakt zueinander vor und bilden komplexe Morphologien, die sich durch große kristalline Agglomerate mit zum Teil stark ausgeprägter Fehlordnung auszeichnen. Alle vier ungeträgerten Sulfide besitzen eine exzellente katalytische Wirkung während der hydrierenden Entstickung von OPA und Entschwefelung von DBT. Sie verfügen über hohe Aktivitäten pro Katalysatorvolumen und ähnlichen Produktselektivitäten, die zudem vergleichbar sind mit denen von geträgerten Katalysatoren.

Insgesamt betrachtet, demonstriert diese Arbeit auf anschaulicher Weise, dass Ni promotierte Mo(W)S_2 Phasen sowie die Morphologie von ungeträgerten Sulfiden die entscheidenden Parameter für die katalytische Hydrotreatingaktivität sind. Beide Materialeigenschaften sind ausschlaggebend für die Konzentration und Erreichbarkeit der aktiven Zentren. Zudem stellte sich heraus, dass die Zusammensetzung und Struktur der oxidischen Ausgangsmaterialien bedeutsam sind, da sie zu einem bestimmten Umfang die Eigenschaften der entsprechenden Sulfide beeinflussen. Es wurde ferner erkannt, dass Ni promotierte intralayer $Mo_{1-x}W_xS_2$ Mischphasen unter Hydrotreatingbedingungen stabiler sind als Ni promotiertes reines MoS_2 oder WS_2. Aus diesen Gründen wird empfohlen sich in zukünftige Studien mit der Kontrolle des Mo-W Legierungsgrades in Sulfiden, der Ausbildung der Ni promotierten Spezies und der Sulfidmorphologie während der Präparation der Ausgangsmaterialien sowie während der Sulfidierung zu beschäftigen. Letztendlich wäre es zudem wichtig, die in der vorliegenden Arbeit unbeantworteten Fragen über die exakte Struktur der Ni promotierten Spezies und über die Beziehung zwischen dieser Struktur und der Katalysatoraktivität anzugehen, um ein noch tieferes Verständnis für diese speziellen und interessanten Materialien zu generieren und somit die Entwicklung sulfidischer Katalysatoren weiter voranzutreiben.

References

[1] O. V. Yazyev, Y. P. Chen, *Nat Nano* **2014**, *9*, 755-767.
[2] S. Eijsbouts, S. W. Mayo, K. Fujita, *Appl. Catal. A* **2007**, *322*, 58-66.
[3] O. Y. Gutiérrez, A. Hrabar, J. Hein, Y. Yu, J. Han, J. A. Lercher, *J. Catal.* **2012**, *295*, 155-168.
[4] B. Radisavljevic, A. Radenovic, J. Brivio, V. Giacometti, A. Kis, *Nat. Nano.* **2011**, *6*, 147-150.
[5] J. N. Coleman, M. Lotya, A. O'Neill, S. D. Bergin, P. J. King, U. Khan, K. Young, A. Gaucher, S. De, R. J. Smith, I. V. Shvets, S. K. Arora, G. Stanton, H. Y. Kim, K. Lee, G. T. Kim, G. S. Duesberg, T. Hallam, J. J. Boland, J. J. Wang, J. F. Donegan, J. C. Grunlan, G. Moriarty, A. Shmeliov, R. J. Nicholls, J. M. Perkins, E. M. Grieveson, K. Theuwissen, D. W. McComb, P. D. Nellist, V. Nicolosi, *Science* **2011**, *331*, 568-571.
[6] R. Prins, *Adv. Catal.* **2001**, *46*, 399-464.
[7] W. Bensch, in *Comprehensive Inorganic Chemistry II (Second Edition)* (Eds.: J. Reedijk, K. Poeppelmeier), Elsevier, Amsterdam, **2013**, pp. 287-321.
[8] R. R. Chianelli, G. Berhault, B. Torres, *Catal. Today* **2009**, *147*, 275-286.
[9] P. M. Mortensen, J. D. Grunwaldt, P. A. Jensen, K. G. Knudsen, A. D. Jensen, *Appl. Catal. A* **2011**, *407*, 1-19.
[10] W. Wang, K. Zhang, Z. Qiao, L. Li, P. Liu, Y. Yang, *Catal. Comm.* **2014**, *56*, 17-22.
[11] U. Maitra, U. Gupta, M. De, R. Datta, A. Govindaraj, C. N. R. Rao, *Angew. Chem. Int. Ed.* **2013**, *52*, 13057-13061.
[12] J. P. Wilcoxon, T. R. Thurston, J. E. Martin, *Nanostruct. Mater.* **1999**, *12*, 993-997.
[13] T. F. Jaramillo, K. P. Jørgensen, J. Bonde, J. H. Nielsen, S. Horch, I. Chorkendorff, *Science* **2007**, *317*, 100-102.
[14] J. M. Martin, C. Donnet, T. Le Mogne, T. Epicier, *Phys. Rev. B* **1993**, *48*, 10583-10586.
[15] K. F. Mak, C. Lee, J. Hone, J. Shan, T. F. Heinz, *Phys. Rev. Lett.* **2010**, *105*, 136805.
[16] Y. Zhu, Q. M. Ramasse, M. Brorson, P. G. Moses, L. P. Hansen, C. F. Kisielowski, S. Helveg, *Angew. Chem.* **2014**, *53*, 1-6.
[17] P. R. Bonneau, R. B. Kaner, *Inorg. Chem.* **1993**, *32*, 6084-6087.
[18] C. H. Ho, C. S. Wu, Y. S. Huang, P. C. Liao, K. K. Tiong, *J. Phys.: Condens. Matter* **1998**, *10*, 9317-9328.
[19] S. Srivastava, D. Palit, *Solid State Ion.* **2005**, *176*, 513-521.
[20] D. O. Dumcenco, Y.-C. Su, Y.-P. Wang, K.-Y. Chen, Y.-S. Huang, C.-H. Ho, K.-K. Tiong, *Solid State Phen.* **2011**, *170*, 55-59.
[21] C. Thomazeau, C. Geantet, M. Lacroix, V. Harlé, S. Benazeth, C. Marhic, M. Danot, *J. Solid State Chem.* **2001**, *160*, 147-155.
[22] D. O. Dumcenco, H. Kobayashi, Z. Liu, Y.-S. Huang, K. Suenaga, *Nat. Commun.* **2013**, *4*, 1351.
[23] J. L. García-Gutiérrez, G. C. Laredo, G. A. Fuentes, P. García-Gutiérrez, F. Jiménez-Cruz, *Fuel* **2014**, *138*, 98-103.
[24] O. Y. Gutiérrez, T. Klimova, *J. Catal.* **2011**, *281*, 50-62.
[25] A. Hrabar, J. Hein, O. Y. Gutiérrez, J. A. Lercher, *J. Catal.* **2011**, *281*, 325-338.
[26] M. Egorova, R. Prins, *J. Catal.* **2006**, *241*, 162-172.
[27] S. Eijsbouts, *Appl. Catal. A* **1997**, *158*, 53-92.
[28] N.-Y. Topsøe, A. Tuxen, B. Hinnemann, J. V. Lauritsen, K. G. Knudsen, F. Besenbacher, H. Topsøe, *J. Catal.* **2011**, *279*, 337-351.
[29] F. Besenbacher, M. Brorson, B. S. Clausen, S. Helveg, B. Hinnemann, J. Kibsgaard, J. V. Lauritsen, P. G. Moses, J. K. Nørskov, H. Topsøe, *Catal. Today* **2008**, *130*, 86-96.
[30] J. V. Lauritsen, J. Kibsgaard, G. H. Olesen, P. G. Moses, B. Hinnemann, S. Helveg, J. K. Nørskov, B. S. Clausen, H. Topsøe, E. Lægsgaard, F. Besenbacher, *J. Catal.* **2007**, *249*, 220-233.
[31] M. Ramos, G. Berhault, D. A. Ferrer, B. Torres, R. R. Chianelli, *Catal. Sci. Technol.* **2012**, *2*, 164-178.

[32] F. L. Deepak, R. Esparza, B. Borges, X. Lopez-Lozano, M. Jose-Yacaman, *ACS Catal.* **2011**, *1*, 537-543.
[33] E. J. M. Hensen, Y. van der Meer, J. A. R. van Veen, J. W. Niemantsverdriet, *Appl. Catal. A* **2007**, *322*, 16-32.
[34] J. N. Díaz de León, T. A. Zepeda, G. Alonso-Nuñez, D. H. Galván, B. Pawelec, S. Fuentes, *J. Catal.* **2015**, *321*, 51-61.
[35] P. Moses, L. Grabow, E. Fernandez, B. Hinnemann, H. Topsøe, K. Knudsen, J. Nørskov, *Catal. Lett.* **2014**, *144*, 1425-1432.
[36] M. Girleanu, T. Alphazan, Z. Boudene, A. Bonduelle-Skrzypczak, C. Legens, A.-S. Gay, C. Copéret, O. Ersen, P. Raybaud, *ChemCatChem* **2014**, *6*, 1594-1598.
[37] S. D. Kelly, N. Yang, G. E. Mickelson, N. Greenlay, E. Karapetrova, W. Sinkler, S. R. Bare, *J. Catal.* **2009**, *263*, 16-33.
[38] V. Schwartz, M. Sun, R. Prins, *J. Phys. Chem. B* **2002**, *106*, 2597-2605.
[39] M. Sun, T. Bürgi, R. Cattaneo, D. van Langeveld, R. Prins, *J. Catal.* **2001**, *201*, 258-269.
[40] R. Cattaneo, F. Rota, R. Prins, *J. Catal.* **2001**, *199*, 318-327.
[41] N. Koizumi, Y. Hamabe, S. Jung, Y. Suzuki, S. Yoshida, M. Yamada, *J. Synchrotron Rad.* **2010**, *17*, 414-424.
[42] S. P. A. Louwers, R. Prins, *J. Catal.* **1992**, *133*, 94-111.
[43] L. Wang, Y. Zhang, Y. Zhang, P. Liu, H. Han, M. Yang, Z. Jiang, C. Li, *Appl. Catal. A* **2011**, *394*, 18-24.
[44] J. Bocarando, R. Huirache-Acuña, W. Bensch, Z. D. Huang, V. Petranovskii, S. Fuentes, G. Alonso-Núñez, *Appl. Catal. A* **2009**, *363*, 45-51.
[45] B. S. Zhang, Y. J. Yi, W. Zhang, C. H. Liang, D. S. Su, *Mater. Charact.* **2011**, *62*, 684-690.
[46] A. Olivas, D. H. Galván, G. Alonso, S. Fuentes, *Appl. Catal. A* **2009**, *352*, 10-16.
[47] S. L. Amaya, G. Alonso-Núñez, J. Cruz-Reyes, S. Fuentes, A. Echavarría, *Fuel* **2015**, *139*, 575-583.
[48] R. Huirache-Acuña, G. Alonso-Núñez, F. Paraguay-Delgado, J. Lara-Romero, G. Berhault, E. M. Rivera-Muñoz, *Catal. Today* **2014**.
[49] R. Huirache-Acuña, M. A. Albiter, J. Espino, C. Ornelas, G. Alonso-Nuñez, F. Paraguay-Delgado, J. L. Rico, R. Martínez-Sánchez, *Appl. Catal. A* **2006**, *304*, 124-130.
[50] C. Thomazeau, C. Geantet, M. Lacroix, M. Danot, V. Harle, *Oil & Gas Sci. Techn. - Rev. IFP* **2005**, *60*, 781-790.
[51] L. Wang, Y. Zhang, Y. Zhang, Z. Jiang, C. Li, *Chem.- Eur. J.* **2009**, *15*, 12571-12575.
[52] J. Ancheyta, J. G. Speight, *Hydroprocessing of Heavy Oils and Residua*, CRC Press, Taylor & Francis Group, Boca Raton, **2007**.
[53] T. Kuznicki, J. H. Masliyah, S. Bhattacharjee, *Energy Fuels* **2008**, *22*, 2379-2389.
[54] UNEP, in *Diesel Sulphur Levels: Global Status*, United Nations Environment Programme, www.unep.org/pcfv **2015**.
[55] K. O. Blumberg, M. Walsh, C. Pera, in *Low-Sulfur Gasoline and Diesel: The Key to Lower Vehicle Emissions* (Ed.: ICCT), **2003**, p. 66.
[56] J. D. Miller, C. Façanha, International Council on Clean Transportation (ICCT), Washington DC (USA), **2014**.
[57] BP, *Statistical Review of World Energy 2015, Vol. 64*, BP, London, **2015**.
[58] OECD/IEA, *World Energy Outlook 2012*, IEA Publishing, **2012**.
[59] M. Nic, J. Jirat, B. Kosata, A. Jenkins, in *Gold Book* (Eds.: A. D. McNaught, A. Wilkinson), IUPAC, **2014**.
[60] A. F. Holleman, E. Wiberg, N. Wiberg, *Lehrbuch der Anorganischen Chemie, Vol. 101., verb. und stark erw. Aufl.*, Walter de Gruyter, Berlin, New York, **1995**.
[61] C. Housecroft, A. G. Sharpe, *Inorganic Chemistry, Vol. 2*, Pearson Education Limited, Prentice Hall, **2005**.
[62] E. Riedel, C. Janiak, *Anorganische Chemie, Vol. 6*, de Gruyter, **2004**.
[63] H. Bode, K. Dehmelt, J. Witte, *Z. Anorg. Allg. Chem.* **1969**, *366*, 1-21.
[64] R. T. Downs, M. Hall-Wallace, *Am. Mineral.* **2003**, *88*, 247-250.

[65] W. B. Pearson, P. Villars, L. D. Calvert, *Pearson's handbook of crystallographic data for intermetallic phases*, American Society for Metals, Metals Park, Ohio, **1985**.
[66] H. Baker*, Vol. 3*, ASM International, **1992**.
[67] H. Okamoto, *J. Phase Equilib. Diffus.* **2009**, *30*, 123-123.
[68] T. Weber, R. Prins, R. A. van Santen, (eds.), *Transition Metal Sulphides, Chemistry and Catalysis, Vol. 60*, Springer Netherlands, Kluwer Academic Publishers, Dordrecht, **1998**.
[69] A. Belsky, M. Hellenbrandt, V. L. Karen, P. Luksch, *Acta Crystallogr., Sect. B: Struct. Sci.* **2002**, *58*, 364-369.
[70] M. Dieterle, G. Weinberg, G. Mestl, *Phys. Chem. Chem. Phys.* **2002**, *4*, 812-821.
[71] E. Salje, R. Gehlig, K. Viswanathan, *J. Solid State Chem.* **1978**, *25*, 239-250.
[72] S. Morandi, G. Ghiotti, A. Chiorino, B. Bonelli, E. Comini, G. Sberveglieri, *Sens. Actuators B: Chemical* **2005**, *111-112*, 28-35.
[73] O. Bock, U. Müller, *Z. Anorg. Allg. Chem.* **2002**, *628*, 987-992.
[74] T. Ekström, E. Salje, R. J. D. Tilley, *J. Solid State Chem.* **1981**, *40*, 75-84.
[75] G. Mestl, *J. Raman Spectrosc.* **2002**, *33*, 333-347.
[76] B. O. Loopstra, H. M. Rietveld, *Acta Crystallogr. Sect. B* **1969**, *25*, 1420-1421.
[77] J. F. Keggin, in *Proc. Royal Soc. London, Ser. A, Vol. 144*, London, **1934**, pp. 75-100.
[78] G. Mestl, T. K. K. Srinivasan, *Catal. Rev. - Sci. Eng.* **1998**, *40*, 451-570.
[79] E. I. Ross-Medgaarden, I. E. Wachs, *J. Phys. Chem. C* **2007**, *111*, 15089-15099.
[80] M. Daturi, G. Busca, M. M. Borel, A. Leclaire, P. Piaggio, *J. Phys. Chem. B* **1997**, *101*, 4358-4369.
[81] S. F. Matar, A. Largeteau, G. Demazeau, *Solid State Sci.* **2010**, *12*, 1779-1785.
[82] S. C. Abrahams, J. M. Reddy, *J. Chem. Phys.* **1965**, *43*, 2533-2543.
[83] R. Keeling, *Acta Crystallogr.* **1957**, *10*, 209-213.
[84] J. B. Christian, M. S. Whittingham, *J. Solid State Chem.* **2008**, *181*, 1782-1791.
[85] M. J. G. Fait, H. J. Lunk, M. Feist, M. Schneider, J. N. Dann, T. A. Frisk, *Thermoc. Acta* **2008**, *469*, 12-22.
[86] G. Busca, *J. Raman Spectrosc.* **2002**, *33*, 348-358.
[87] P. Ehrlich, *Z. anorg. Chemie* **1948**, *257*, 247-253.
[88] L. Brewer, R. H. Lamoreaux, *Bull. Alloy Ph. Diagrams* **1980**, *1*, 93-95.
[89] H. Jehn, S. Gmünd, G. Bär, E. Best, E. Koch, in *Gmelin Handbook of Inorganic and Organometallic Chemistry - 8th Edition, Vol. W Tungsten / A-B / A / 5 / b* (Eds.: J. von Jouanne, E. Koch, E. Koch), Springer Berlin Heidelberg, **1993**, pp. 110-116.
[90] R. Alsfasser, C. Janiak, T. M. Klapötke, H.-J. Meyer, *Riedel Moderne Anorganische Chemie, Vol. 3. Aufl.*, Walter de Gruyter, Berlin, New York, **2007**.
[91] J. W. Chung, A. Adib, Z. R. Dai, K. Adib, F. S. Ohuchi, *Th. Sol. Films* **1998**, *335*, 106-111.
[92] E. J. M. Hensen, P. J. Kooyman, Y. van der Meer, A. M. van der Kraan, V. H. J. de Beer, J. A. R. van Veen, R. A. van Santen, *J. Catal.* **2001**, *199*, 224-235.
[93] Y. Iwata, K. Sato, T. Yoneda, Y. Miki, Y. Sugimoto, A. Nishijima, H. Shimada, *Catal. Today* **1998**, *45*, 353-359.
[94] F. Pedraza, J. Cruz-Reyes, D. Acosta, M. J. Yanez, M. Avalos-Borja, S. Fuentes, *J. Phys.: Condens. Matter* **1993**, *5*, A219.
[95] J. A. Wilson, A. D. Yoffe, *Adv. in Physics* **1969**, *18*, 193-335.
[96] W. Bensch, *Nachrichten der Chemie* **2012**, *60*, 422-425.
[97] S. K. Srivastava, T. K. Mandal, B. K. Samantaray, *Syn. Metals* **1997**, *90*, 135-142.
[98] L. Zhang, X. Long, D. Li, X. Gao, *Catal. Comm.* **2011**, *12*, 927-931.
[99] C. E. Scott, M. J. Perez-Zurita, L. A. Carbognani, H. Molero, G. Vitale, H. J. Guzmán, P. Pereira-Almao, *Catal. Today* **2015**, *250*, 21-27.
[100] M. Cattenot, J.-L. Portefaix, J. Afonso, M. Breysse, M. Lacroix, G. Perot, *J. Catal.* **1998**, *173*, 366-373.
[101] R. Prins, in *Handbook of Heterogeneous Catalysis*, Wiley-VCH Verlag GmbH & Co. KGaA, **2008**.
[102] V. La Vopa, C. N. Satterfield, *J. Catal.* **1988**, *110*, 375-387.
[103] T. C. Ho, *Catal. Rev. - Sci. Eng.* **1988**, *30*, 117-160.

[104] C. N. Satterfield, M. Modell, R. A. Hites, C. J. Declerck, *Ind. Eng. Chem. Proc. Des. Dev.* **1978**, *17*, 141-148.
[105] M. Jian, R. Prins, *J. Catal.* **1998**, *179*, 18-27.
[106] F. E. Massoth, S. C. Kim, *Ind. Eng. Chem. Res.* **2003**, *42*, 1011-1022.
[107] C. N. Satterfield, S. H. Yang, *Ind. Eng. Chem. Proc. Des. Dev.* **1984**, *23*, 11-19.
[108] H. Farag, *Appl. Catal. A* **2007**, *331*, 51-59.
[109] O. Y. Gutiérrez, S. Singh, E. Schachtl, J. Kim, E. Kondratieva, J. Hein, J. A. Lercher, *ACS Catal.* **2014**, *4*, 1487-1499.
[110] Z. D. Huang, W. Bensch, A. Lotnyk, L. Kienle, S. Fuentes, J. Bocarando, G. Alonso, C. Ornelas, *J. Mol. Catal. A: Chem.* **2010**, *323*, 45-51.
[111] I. V. Babich, J. A. Moulijn, *Fuel* **2003**, *82*, 607-631.
[112] M. Egorova, R. Prins, *J. Catal.* **2004**, *225*, 417-427.
[113] N. Kagami, B. M. Vogelaar, A. D. v. Langeveld, J. A. Moulijn, *Appl. Catal. A* **2005**, *293*, 11-23.
[114] M. Egorova, R. Prins, *J. Catal.* **2004**, *221*, 11-19.
[115] M. Egorova, R. Prins, *J. Catal.* **2004**, *224*, 278-287.
[116] Á. Logadóttir, P. G. Moses, B. Hinnemann, N.-Y. Topsøe, K. G. Knudsen, H. Topsøe, J. K. Nørskov, *Catal. Today* **2006**, *111*, 44-51.
[117] T. A. Pecoraro, R. R. Chianelli, *J. Catal.* **1981**, *67*, 430-445.
[118] H. Toulhoat, P. Raybaud, S. Kasztelan, G. Kresse, J. Hafner, *Catal. Today* **1999**, *50*, 629-636.
[119] S. P. Ahuja, M. L. Derrien, J. F. Le Page, *Ind. Eng. Chem. Prod. Res. Develop.* **1970**, *9*, 272-281.
[120] R. Candia, B. S. Clausen, H. Topsøe, *J. Catal.* **1982**, *77*, 564-566.
[121] S. Kasztelan, H. Toulhoat, J. Grimblot, J. P. Bonnelle, *Appl. Catal.* **1984**, *13*, 127-159.
[122] S. M. A. M. Bouwens, D. C. Koningsberger, V. H. J. de Beer, R. Prins, *Catal. Lett.* **1988**, *1*, 55-59.
[123] S. Eijsbouts, C. Sudhakar, V. H. J. De Beer, R. Prins, *J. Catal.* **1991**, *127*, 605-618.
[124] M. W. J. Craje, S. P. A. Louwers, V. H. J. De Beer, R. Prins, A. M. Van der Kraan, *J. Phys. Chem.* **1992**, *96*, 5445-5452.
[125] K. Inamura, R. Prins, *J. Catal.* **1994**, *147*, 515-524.
[126] J. Grimblot, *Catal. Today* **1998**, *41*, 111-128.
[127] L. Byskov, J. Nørskov, B. Clausen, H. Topsøe, *Catal. Lett.* **2000**, *64*, 95-99.
[128] M. Brorson, A. Carlsson, H. Topsøe, *Catal. Today* **2007**, *123*, 31-36.
[129] P. Moses, B. Hinnemann, H. Topsoe, J. Norskov, *J. Catal.* **2007**, *248*, 188-203.
[130] M. A. Domínguez-Crespo, A. M. Torres-Huerta, L. Díaz-García, E. M. Arce-Estrada, E. Ramírez-Meneses, *Fuel Proc. Techn.* **2008**, *89*, 788-796.
[131] F. L. Plantenga, R. Cerfontain, S. Eijsbouts, F. van Houtert, G. H. Anderson, S. Miseo, S. Soled, K. Riley, K. Fujita, Y. Inoue, in *Stud. Surf. Sci. Catal., Vol. 145* (Eds.: M. O. Masakazu Anpo, Y. Hiromi), Elsevier, **2003**, pp. 407-410.
[132] C. Thomazeau, C. Geantet, M. Lacroix, M. Danot, V. Harlé, P. Raybaud, *Appl. Catal. A* **2007**, *322*, 92-97.
[133] J. C. Duchet, E. M. van Oers, V. H. J. de Beer, R. Prins, *J. Catal.* **1983**, *80*, 386-402.
[134] L. Dixit, D. L. Gerrard, H. J. Bowley, *Appl. Spectrosc. Rev.* **1986**, *22*, 189-249.
[135] T. Maesen, A. E. Kuperman, US 2009/007883 Chevron Cooperation, **2008**.
[136] L. Zhang, P. Afanasiev, D. Li, X. Long, M. Vrinat, *Catal. Comm.* **2007**, *8*, 2232-2237.
[137] R. Huirache-Acuña, M. A. Albiter, C. Ornelas, F. Paraguay-Delgado, R. Martínez-Sánchez, G. Alonso-Nuñez, *Appl. Catal. A* **2006**, *308*, 134-142.
[138] E. Furimsky, *Appl. Catal. A* **2001**, *208*, 251-257.
[139] D. Genuit, P. Afanasiev, M. Vrinat, *J. Catal.* **2005**, *235*, 302-317.
[140] R. R. Chianelli, T. A. Pecoraro, T. R. Halbert, W. H. Pan, E. I. Stiefel, *J. Catal.* **1984**, *86*, 226-230.
[141] R. R. Chianelli, G. Berhault, *Catal. Today* **1999**, *53*, 357-366.
[142] B. S. Clausen, H. Topsoe, R. Candia, J. Villadsen, B. Lengeler, J. Als-Nielsen, F. Christensen, *J. Phys. Chem.* **1981**, *85*, 3868-3872.

[143] H. Topsøe, B. S. Clausen, R. Candia, C. Wivel, S. Mørup, *J. Catal.* **1981**, *68*, 433-452.
[144] H. Topsoe, B. S. Clausen, *Catal. Rev. - Sci. Eng.* **1984**, *26*, 395-420.
[145] Z. Le, P. Afanasiev, D. Li, X. Long, M. Vrinat, *Catal. Today* **2008**, *130*, 24-31.
[146] A. Olivas, G. Alonso, S. Fuentes, *Top. Catal.* **2006**, *39*, 175-179.
[147] W. Niemann, B. Clausen, H. Topsøe, *Catal. Lett.* **1990**, *4*, 355-363.
[148] L. S. Byskov, J. K. Nørskov, B. S. Clausen, H. Topsøe, *J. Catal.* **1999**, *187*, 109-122.
[149] P. Raybaud, J. Hafner, G. Kresse, S. Kasztelan, H. Toulhoat, *J. Catal.* **2000**, *190*, 128-143.
[150] E. Schachtl, E. Kondratieva, O. Y. Gutiérrez Tinoco, J. A. Lercher, *J. Phys. Chem. Lett.* **2015**, *6*, 2929-2932.
[151] S. Helveg, J. V. Lauritsen, E. Lægsgaard, I. Stensgaard, J. K. Nørskov, B. S. Clausen, H. Topsøe, F. Besenbacher, *Phys. Rev. Lett.* **2000**, *84*, 951-954.
[152] M. Daage, R. R. Chianelli, *J. Catal.* **1994**, *149*, 414-427.
[153] Y. Iwata, Y. Araki, K. Honna, Y. Miki, K. Sato, H. Shimada, *Catal. Today* **2001**, *65*, 335-341.
[154] D. Yang, R. F. Frindt, *Mol. Cryst. Liq. Cryst.* **1994**, *244*, 355-360.
[155] J. Hein, A. Hrabar, A. Jentys, O. Y. Gutiérrez, J. A. Lercher, *ChemCatChem* **2014**, *6*, 485-499.
[156] R. Prins, V. H. J. De Beer, G. A. Somorjai, *Catal. Rev. - Sci. Eng.* **1989**, *31*, 1-41.
[157] H. Topsøe, *Appl. Catal. A* **2007**, *322*, 3-8.
[158] G. Berhault, M. Perez De la Rosa, A. Mehta, M. J. Yácaman, R. R. Chianelli, *Appl. Catal. A* **2008**, *345*, 80-88.
[159] S. Eijsbouts, L. C. A. van den Oetelaar, R. R. van Puijenbroek, *J. Catal.* **2005**, *229*, 352-364.
[160] M. Jian, R. Prins, *Catal. Today* **1996**, *30*, 127-134.
[161] G. Perot, *Catal. Today* **1991**, *10*, 447-472.
[162] L. Qu, R. Prins, *Appl. Catal. A* **2003**, *250*, 105-115.
[163] J. van Gestel, J. Leglise, J. C. Duchet, *Appl. Catal. A* **1992**, *92*, 143-154.
[164] F. Maugé, J. Lamotte, N. S. Nesterenko, O. Manoilova, A. A. Tsyganenko, *Catal. Today* **2001**, *70*, 271-284.
[165] R. W. G. Wyckoff, *Crystal Structures, Vol. 1*, 2nd ed., Interscience, New York, **1963**.
[166] J. L. Verble, T. J. Wieting, *Phys. Rev. Lett.* **1970**, *25*, 362-365.
[167] T. J. Wieting, J. L. Verble, *Phys. Rev. B* **1971**, *3*, 4286-4292.
[168] S. M. A. M. Bouwens, R. Prins, V. H. J. De Beer, D. C. Koningsberger, *J. Phys. Chem.* **1990**, *94*, 3711-3718.
[169] T. C. Ho, *Appl. Catal. A* **2010**, *378*, 52-58.
[170] P. Afanasiev, *J. Catal.* **2010**, *269*, 269-280.
[171] C. N. Satterfield, J. F. Cocchetto, *Ind. Eng. Chem. Proc. Des. Dev.* **1981**, *20*, 53-62.
[172] J. F. Cocchetto, C. N. Satterfield, *Ind. Eng. Chem. Proc. Des. Dev.* **1976**, *15*, 272-277.
[173] I. E. Wachs, *Catal. Today* **1996**, *27*, 437-455.
[174] C. P. Cheng, G. L. Schrader, *J. Catal.* **1979**, *60*, 276-294.
[175] H. Hu, I. E. Wachs, S. R. Bare, *J. Phys. Chem.* **1995**, *99*, 10897-10910.
[176] N. F. D. Verbruggen, G. Mestl, L. M. J. von Hippel, B. Lengeler, H. Knoezinger, *Langmuir* **1994**, *10*, 3063-3072.
[177] H. Jeziorowski, H. Knoezinger, *J. Phys. Chem.* **1979**, *83*, 1166-1173.
[178] H. Knoezinger, H. Jeziorowski, *J. Phys. Chem.* **1978**, *82*, 2002-2005.
[179] H. Aritani, T. Tanaka, T. Funabiki, S. Yoshida, M. Kudo, S. Hasegawa, *J. Phys. Chem.* **1996**, *100*, 5440-5446.
[180] M. Breysse, B. A. Bennett, D. Chadwick, M. Vrinat, *Bull. Soc. Chim. Belg.* **1981**, *90*, 1271-1278.
[181] E. Payen, J. Grimblot, S. Kasztelan, *J. Phys. Chem.* **1987**, *91*, 6642-6648.
[182] D. Levin, S. L. Soled, J. Y. Ying, *Inorg. Chem.* **1996**, *35*, 4191-4197.
[183] R. Cattaneo, T. Weber, T. Shido, R. Prins, *J. Catal.* **2000**, *191*, 225-236.

[184] H. Topsøe, B. Clausen, F. Massoth, *Hydrotreating Catalysis, Vol. 11*, Springer Berlin Heidelberg, **1996**.
[185] J. V. Lauritsen, M. Nyberg, J. K. Nørskov, B. S. Clausen, H. Topsøe, E. Lægsgaard, F. Besenbacher, *J. Catal.* **2004**, *224*, 94-106.
[186] T. G. Parham, R. P. Merrill, *J. Catal.* **1984**, *85*, 295-310.
[187] J. V. Lauritsen, S. Helveg, E. Lægsgaard, I. Stensgaard, B. S. Clausen, H. Topsøe, F. Besenbacher, *J. Catal.* **2001**, *197*, 1-5.
[188] H. Topsøe, B. S. Clausen, *Appl. Catal.* **1986**, *25*, 273-293.
[189] C. Wivel, B. S. Clausen, R. Candia, S. Mørup, H. Topsøe, *J. Catal.* **1984**, *87*, 497-513.
[190] B. Yoosuk, J. H. Kim, C. Song, C. Ngamcharussrivichai, P. Prasassarakich, *Catal. Today* **2008**, *130*, 14-23.
[191] R. Chianelli, R., *Oil & Gas Sci. Techn. - Rev. IFP* **2006**, *61*, 503-513.
[192] Y. Okamoto, H. Okamoto, T. Kubota, H. Kobayashi, O. Terasaki, *J. Phys. Chem. B* **1999**, *103*, 7160-7166.
[193] M. Breysse, E. Furimsky, S. Kasztelan, M. Lacroix, G. Perot, *Catal. Rev. - Sci. Eng.* **2002**, *44*, 651-735.
[194] P. Clark, X. Wang, P. Deck, S. T. Oyama, *J. Catal.* **2002**, *210*, 116-126.
[195] A. N. Startsev, *Catal. Rev. - Sci. Eng.* **1995**, *37*, 353-423.
[196] F. E. Massoth, G. Muralidhar, J. Shabtai, *J. Catal.* **1984**, *85*, 53-62.
[197] J. Shabtai, Q. Guohe, K. Balusami, N. K. Nag, F. E. Massoth, *J. Catal.* **1988**, *113*, 206-219.
[198] K. V. Klementiev, VIPERfreeware, K. V. Klementev, *J. Phys. D: Appl. Phys.* **2001**, *34*, 209.
[199] B. Ravel, M. Newville, *J. Synchrotron Rad.* **2005**, *12*, 537-541.
[200] M. Newville, *J. Synchrotron Rad.* **2001**, *8*, 322-324.
[201] A. L. Ankudinov, J. J. Rehr, *Phys. Rev. B* **2000**, *62*, 2437-2445.
[202] R. S. Weber, *J. Catal.* **1995**, *151*, 470-474.
[203] S. I. Zabinsky, J. J. Rehr, A. Ankudinov, R. C. Albers, M. J. Eller, *Phys. Rev. B* **1995**, *52*, 2995-3009.
[204] A. V. Neimark, K. S. W. Sing, M. Thommes, in *Handbook of Heterogeneous Catalysis*, Wiley-VCH Verlag GmbH & Co. KGaA, **2008**.
[205] D. Levin, J. Ying, *J. Electroceramics* **1999**, *3*, 25-36.
[206] F. D. Hardcastle, I. E. Wachs, *J. Raman Spectrosc.* **1990**, *21*, 683-691.
[207] S. Deabate, F. Fourgeot, F. Henn, *J. Power Sources* **2000**, *87*, 125-136.
[208] I. Kanesaka, H. Hashiba, I. Matsuura, *J. Raman Spectrosc.* **1988**, *19*, 213-218.
[209] S.-H. Lee, H. M. Cheong, N.-G. Park, E. Tracy, A. Mascarenhas, D. K. Benson, S. K. Deb, *Solid State Ion.* **2001**, *140*, 135-139.
[210] *CRC Handbook of Chemistry and Physics, Vol. 90th Ed., Internet Version*, CRC Press, Boca Raton, FL, **2010**.
[211] J. A. Horsley, I. E. Wachs, J. M. Brown, G. H. Via, F. D. Hardcastle, *J. Phys. Chem.* **1987**, *91*, 4014-4020.
[212] T. E. Johnson, W. Martens, R. L. Frost, Z. Ding, J. Theo Kloprogge, *J. Raman Spectrosc.* **2002**, *33*, 604-609.
[213] J. Wright, M. M. Barsan, I. S. Butler, D. F. R. Gilson, M. O. Adebajo, R. L. Frost, *J. Raman Spectrosc.* **2011**, *42*, 1562-1566.
[214] M. Fournier, C. Louis, M. Che, P. Chaquin, D. Masure, *J. Catal.* **1989**, *119*, 400-414.
[215] A. Guevara-Lara, R. Bacaud, M. Vrinat, *Appl. Catal. A* **2007**, *328*, 99-108.
[216] B. Scheffer, J. J. Heijeinga, J. A. Moulijn, *J. Phys. Chem.* **1987**, *91*, 4752-4759.
[217] Y. Qi, H. Qi, J. Li, C. Lu, *J. Cryst. Growth* **2008**, *310*, 4221-4225.
[218] S. Morandi, G. Ghiotti, A. Chiorino, E. Comini, *Th. Solid Films* **2005**, *490*, 74-80.
[219] C. C. Williams, J. G. Ekerdt, J. M. Jehng, F. D. Hardcastle, A. M. Turek, I. E. Wachs, *J. Phys. Chem.* **1991**, *95*, 8781-8791.
[220] M. Bauer, H. Bertagnolli, in *Methods in Physical Chemistry* (Eds.: P. R. Schäfer, P. P. C. Schmid), Wiley-VCH Verlag GmbH & Co. KGaA, **2012**, pp. 231-269.
[221] P. Glatzel, U. Bergmann, *Coord. Chem. Rev.* **2005**, *249*, 65-95.

[222] M. J. Ward, P. A. Rupar, M. W. Murphy, Y.-M. Yiu, K. M. Baines, T. K. Sham, *Chem. Commun. (Cambridge, U. K.)* **2010**, *46*, 7016-7018.
[223] T. Yamamoto, *X-Ray Spectrom.* **2008**, *37*, 572-584.
[224] F. Farges, G. E. Brown Jr, P.-E. Petit, M. Munoz, *Geochim. Cosmochim. Acta* **2001**, *65*, 1665-1678.
[225] B. S. Clausen, B. Lengeler, H. Topsøe, *Polyhedron* **1986**, *5*, 199-202.
[226] R. Radhakrishnan, C. Reed, S. T. Oyama, M. Seman, J. N. Kondo, K. Domen, Y. Ohminami, K. Asakura, *J. Phys. Chem. B* **2001**, *105*, 8519-8530.
[227] B. K. Teo, P. A. Lee, *J. Am. Chem. Soc.* **1979**, *101*, 2815-2832.
[228] G. N. George, W. E. Cleland, J. H. Enemark, B. E. Smith, C. A. Kipke, S. A. Roberts, S. P. Cramer, *J. Am. Chem. Soc.* **1990**, *112*, 2541-2548.
[229] F. W. Lytle, P. S. P. Wei, R. B. Greegor, G. H. Via, J. H. Sinfelt, *J. Chem. Phys.* **1979**, *70*, 4849-4855.
[230] S. R. Bare, G. E. Mitchell, J. J. Maj, G. E. Vrieland, J. L. Gland, *J. Phys. Chem.* **1993**, *97*, 6048-6053.
[231] S. Yamazoe, Y. Hitomi, T. Shishido, T. Tanaka, *J. Phys. Chem. C* **2008**, *112*, 6869-6879.
[232] R. Thomas, J. Kas, P. Glatzel, M. Al Samarai, F. M. F. de Groot, R. Alonso Mori, M. Kavčič, M. Zitnik, K. Bucar, J. J. Rehr, M. Tromp, *J. Phys. Chem. C* **2015**, *119*, 2419-2426.
[233] J. Evans, J. F. W. Mosselmans, *J. Phys. Chem.* **1991**, *95*, 9673-9676.
[234] E. J. Lede, F. G. Requejo, B. Pawelec, J. L. G. Fierro, *J. Phys. Chem. B* **2002**, *106*, 7824-7831.
[235] J. Hein, O. Y. Gutiérrez, E. Schachtl, P. Xu, N. D. Browning, A. Jentys, J. A. Lercher, *ChemCatChem* **2015**, *accepted*.
[236] L. A. Palacio, A. Echavarría, D. Á. Hoyos, C. Saldarriaga, *Solid State Sci.* **2005**, *7*, 1043-1048.
[237] F. D. Hardcastle, I. E. Wachs, *J. Raman Spectrosc.* **1995**, *26*, 397-405.
[238] J. A. Mendoza-Nieto, F. Robles-Méndez, T. E. Klimova, *Catal. Today* **2015**, *250*, 47-59.
[239] Y. Gochi, C. Ornelas, F. Paraguay, S. Fuentes, L. Alvarez, J. L. Rico, G. Alonso-Núñez, *Catal. Today* **2005**, *107–108*, 531-536.
[240] B. T. Yonemoto, G. S. Hutchings, F. Jiao, *J. Am. Chem. Soc.* **2014**, *136*, 8895-8898.
[241] J. J. Rehr, J. J. Kas, F. D. Vila, M. P. Prange, K. Jorissen, *Phys. Chem. Chem. Phys.* **2010**, *12*, 5503-5513.
[242] J. Moser, F. Lévy, *Th. Solid Films* **1994**, *240*, 56-59.
[243] C. Lee, H. Yan, L. E. Brus, T. F. Heinz, J. Hone, S. Ryu, *ACS Nano* **2010**, *4*, 2695-2700.
[244] L. P. Hansen, Q. M. Ramasse, C. Kisielowski, M. Brorson, E. Johnson, H. Topsoe, S. Helveg, *Angew. Chem. Int. Ed.* **2011**, *50*, 10153-10156.
[245] T. Shido, R. Prins, *J. Phys. Chem. B* **1998**, *102*, 8426-8435.
[246] H. R. Reinhoudt, R. Troost, A. D. van Langeveld, J. A. R. van Veen, S. T. Sie, J. A. Moulijn, *J. Catal.* **2001**, *203*, 509-515.
[247] M. J. Vissenberg, Y. van der Meer, E. J. M. Hensen, V. H. J. de Beer, A. M. van der Kraan, R. A. van Santen, J. A. R. van Veen, *J. Catal.* **2001**, *198*, 151-163.
[248] E. Schachtl, E. Kondratieva, L. Zhong, J. Hein, O. Y. Gutiérrez, A. Jentys, J. A. Lercher, *ChemCatChem* **2015**, *accepted*.
[249] J. A. R. van Veen, in *Zeolites for Cleaner Technologies* (Eds.: M. Guisnet, J.-P. Gilson), Imperial College Press, **2002**, pp. 131-152.
[250] W. R. A. M. Robinson, J. A. R. v. Veen, V. H. J. d. Beer, R. A. v. Santen, *Fuel Energy Abstr.* **2000**, *41*, 79-80.
[251] T. Kabe, Y. Aoyama, D. Wang, A. Ishihara, W. Qian, M. Hosoya, Q. Zhang, *Appl. Catal. A* **2001**, *209*, 237-247.
[252] H. Topsøe, R. G. Egeberg, K. G. Knudsen, *Prepr. Pap.-Am. Chem. Soc., Div. Fuel Chem* **2004**, *49*, 569.

[253] Y. Chen, L. Wang, Y. Zhang, T. Liu, X. Liu, Z. Jiang, C. Li, *Appl. Catal. A* **2014**, *474*, 69-77.
[254] T. C. Ho, *Catal. Today* **2008**, *130*, 206-220.
[255] C. Larabi, P. K. Nielsen, S. Helveg, C. Thieuleux, F. B. Johansson, M. Brorson, E. A. Quadrelli, *ACS Catal.* **2012**, *2*, 695-700.
[256] M. Kouzu, K. Uchida, Y. Kuriki, F. Ikazaki, *Appl. Catal. A* **2004**, *276*, 241-249.
[257] H. Farag, M. Kishida, H. Al-Megren, *Appl. Catal. A* **2014**, *469*, 173-182.
[258] S. M. A. M. Bouwens, J. A. R. Van Veen, D. C. Koningsberger, V. H. J. De Beer, R. Prins, *J. Phys. Chem.* **1991**, *95*, 123-134.
[259] S. Chaturvedi, J. Rodriguez, J. Brito, *Catal. Lett.* **1998**, *51*, 85-93.
[260] H. Wang, R. Prins, *J. Catal.* **2008**, *258*, 153-164.
[261] E. G. Derouane, E. Pedersen, B. S. Clausen, Z. Gabelica, R. Candia, H. Topsøe, *J. Catal.* **1986**, *99*, 253-261.
[262] M. Lacroix, M. Vrinat, M. Breysse, *Appl. Catal.* **1986**, *21*, 73-83.
[263] B. Delmon, in *Stud. Surf. Sci. Catal., Vol. Volume 53* (Eds.: S. A. M. A.-H. D.L. Trimm, A. Bishara), Elsevier, **1989**, pp. 1-40.
[264] M. W. J. Craje, E. Gerkema, V. H. J. D. Beer, A. M. V. D. Kraan, in *Stud. Surf. Sci. Catal., Vol. Volume 50* (Eds.: M. L. Occelli, R. G. Anthony), Elsevier, **1989**, pp. 165-179.
[265] F. B. Garreau, H. Toulhoat, S. Kasztelan, R. Paulus, *Polyhedron* **1986**, *5*, 211-217.
[266] N. Y. Topsoe, H. Topsoe, *J. Catal.* **1993**, *139*, 641-651.
[267] C. Dujardin, M. A. Lélias, J. van Gestel, A. Travert, J. C. Duchet, F. Maugé, *Appl. Catal. A* **2007**, *322*, 46-57.
[268] Y. Okamoto, *Appl. Catal. A* **2002**, *226*, 115-127.
[269] M. V. Bollinger, J. V. Lauritsen, K. W. Jacobsen, J. K. Nørskov, S. Helveg, F. Besenbacher, *Phys. Rev. Lett.* **2001**, *87*, 196803.
[270] M. Daage, R. R. Chianelli, A. F. Ruppert, in *10th Intern. Congress on Catal., Vol. 75*, Budapest, **1992**, pp. 571-584.
[271] L. Coulier, G. Kishan, J. A. R. van Veen, J. W. Niemantsverdriet, *J. Phys. Chem. B* **2002**, *106*, 5897-5906.
[272] H. Yasuda, M. Higo, S. Yoshitomi, T. Sato, M. Imamura, H. Matsubayashi, H. Shimada, A. Nishijima, Y. Yoshimura, *Catal. Today* **1997**, *39*, 77-87.
[273] A. Hrabar, PhD thesis at TU München (München, Germany), **2011**.
[274] X. Cai, Z. Ren, T. Hu, Y. Xie, *Surf. Interface Anal.* **2001**, *32*, 293-295.
[275] T. Sekine, T. Nakashizu, K. Toyoda, K. Uchinokura, E. Matsuura, *Solid State Commun.* **1980**, *35*, 371-373.
[276] C. Sourisseau, F. Cruege, M. Fouassier, M. Alba, *Chem. Phys.* **1991**, *150*, 281-293.
[277] J. J. Rehr, A. L. Ankudinov, *Coord. Chem. Rev.* **2005**, *249*, 131-140.

Appendices

1. A 1 - Support Chapter 3

Supporting Information

Characterization and sulfidation of oxide precursors

The characterization and the sulfidation of the oxide precursor were performed by Dr. Ana Hrabar and Jennifer Hein at the TU München. Therefore, the interested reader is referred to the PhD thesis of Dr. Ana Hrabar[273] or to the Supporting Information of DOI 10.1002/cctc.201300856[155], available on www.chemcatchem.org. However, the XANES and FT-EXAFS investigation of the oxide precursors are in the following described.

The XANES of the catalyst precursors and reference materials at the Mo K-edge are shown in Figure S4(A) and at the Ni K-edge in Figure S5(A). The XANES at the Mo K-edge of the three precursors exhibit characteristic pre-edge peaks at around 20005 eV. Absorption peaks before the K-edge originate from the electronic 1s→4d transition,[179] which is symmetry-forbidden in centrosymmetric structures. Therefore, Mo^{6+} is either present in a tetrahedral or in a distorted octahedral coordination. The XANES of the tetrahedral Mo^{6+} in $NiMoO_4$ reference exhibited the highest intensity of the pre-edge peak, whereas the XANES of the distorted octahedral Mo^{6+} in MoO_3 (pre-edge at 20007 eV) showed only a very weak pre-edge peak. In the XANES of MoO_2 a pre-edge signal was not observed due to the presence of Mo^{4+} in a centrosymmetric structure.[176]

The FT-EXAFS at the Mo K-edge of the catalyst precursors and reference materials are shown in Figure S4(B). The oxide precursors exhibited only one strong contribution at around 1.4 Å (not phase corrected) assigned to Mo-O backscattering.[40, 225] Furthermore, the shape of the Mo-O peak could be caused by distinct oxygen shells in different distances, indicating that Mo^{6+} is in a distorted octahedral coordination. Mo-Mo and Mo-O contributions at lager distances were not observed, which is (in agreement with XRD) an indication for only a short range order. In the precursor of the unsupported catalyst the increasing metal concentration led to an increase of the Mo-O contribution as well as of a signal at around 3.2 Å (not phase corrected), which is assigned to Mo-Mo backscattering.[40, 176] Moreover, the presence of a Mo-Ni contribution at around 3 Å (not phase corrected) is plausible by comparing the FT-EXAFS of NiMo/unsupported to the $NiMoO_4$ reference.

The XANES at the Ni K-edge of both Ni-containing catalyst precursors are comparable to the XANES of $NiMoO_4$ reference with absorption edge energy of 8347 eV, whereas for the reference $NiAl_2O_4$ spinel absorption edge energy of 8345 eV was observed. The FT-EXAFS

at the Ni K-edge of the catalyst precursors and reference materials are shown in Figure S5 (B). Both catalyst precursors showed a broad signal at 1.6 Å and one at around 2.5 Å (not phase corrected) due to Ni-O and Ni-Ni backscattering, respectively.[259, 274] In comparison to the highly crystalline NiO reference compound, the contribution of Ni-Ni is much weaker in the catalyst precursors and, therefore, the formation of large NiO crystals can be excluded. Additionally, a Ni-Mo back scattering contribution at around 3.0 Å (not phase corrected) was identified through comparison with the FT-EXAFS of the $NiMoO_4$ reference.

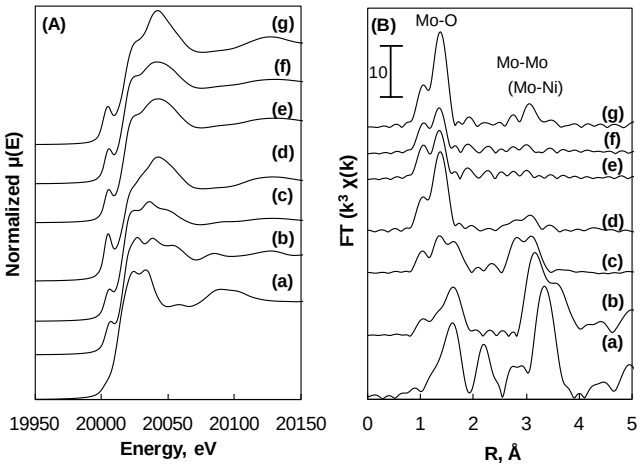

Figure S4. Mo K-edge XANES (A) and FT-EXAFS (B) of references and oxide catalyst precursors: (a) MoO_2, (b) MoO_3, (c) $(NH_4)_6Mo_7O_{24} \cdot 6H_2O$, (d) $NiMoO_4$ (e) Mo/γ-Al_2O_3, (f) NiMo/γ-Al_2O_3, and (g) NiMo/unsupported.

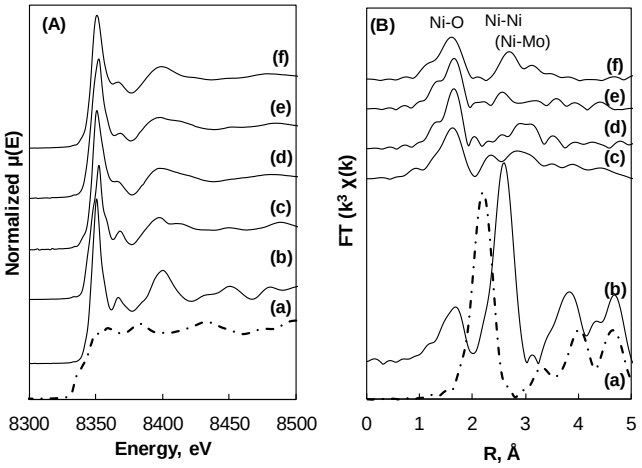

Figure S5. Ni K-edge XANES (A) and FT-EXAFS (B) of references and oxidic catalyst precursors: (a) Ni foil, (b) NiO, (c) $NiAl_2O_4$, (d) $NiMoO_4$, (e) NiMo/γ-Al_2O_3, and (f) NiMo/unsupported.

Characterization of the sulfide catalysts

Table S4. Linear combination fitting (LCF) results for XANES at Mo K-edge and Ni K-edge of the sulfided catalysts. R-factor: the goodness of LCF, integrated area of the residual: area under the difference spectra (difference between the measured and the modeled XANES).

Catalyst	Absorber metal	Weight of the used XANES, %			R factor	Integrated area of the residual
		Oxidic precursor	MoS_2	Ni_3S_2		
$MoS_2/\gamma\text{-}Al_2O_3$	Mo	7.3	92.7		0.0005	- 0.1414
$Ni\text{-}MoS_2/\gamma\text{-}Al_2O_3$	Mo	6.0	94.0		0.0008	- 0.1475
	Ni	14.7		85.3	0.0031	2.5967
$Ni\text{-}MoS_2$/unsupported	Mo	2.1	97.9		0.0004	0.0247
	Ni	5.3		94.7	0.0020	4.7936

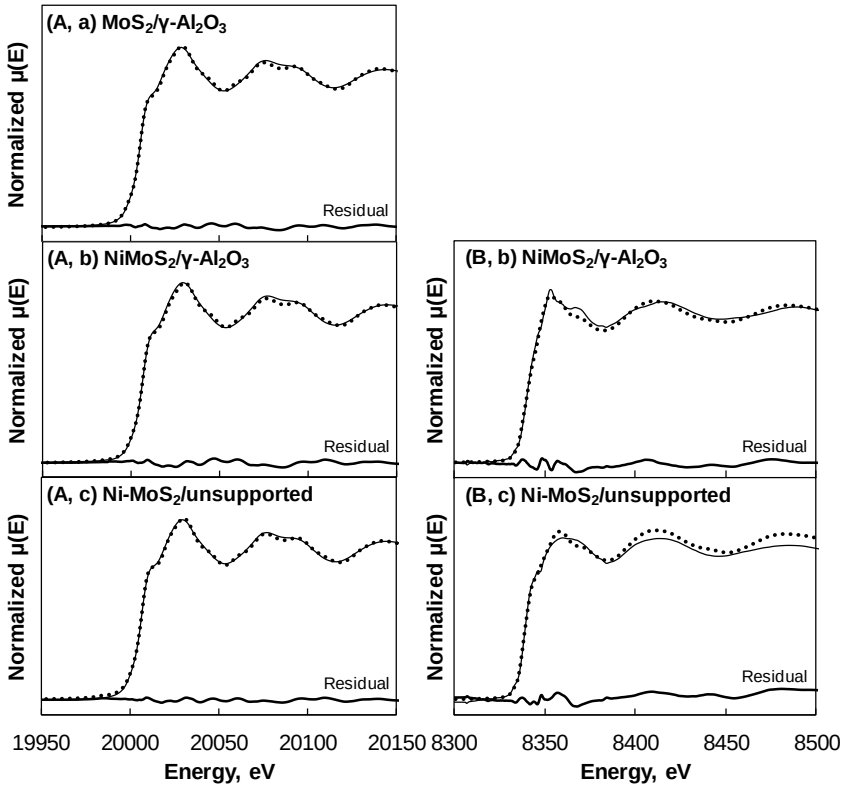

Figure S10. XANES at the Mo K-edge (A) and Ni K-edge (B) of the sulfided catalysts (solid line) and of the modeled XANES (dashed line) obtained by LCF using the XANES of the reference bulk materials MoS_2 and Ni_3S_2 and the corresponding oxidic precursors. The bottom solid line represents the difference spectra between the measured and the modeled XANES (residual).

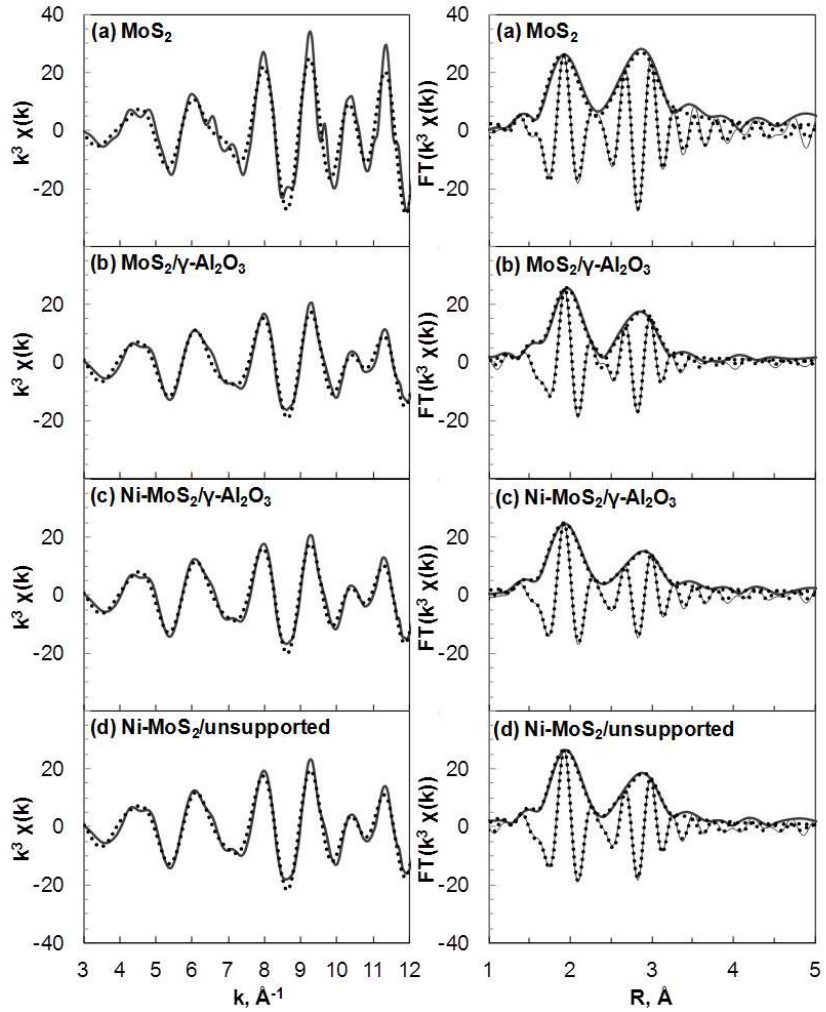

Figure S11. k^3 weighted EXAFS (left) at the Mo K-edge and the corresponding Fourier transforms, magnitudes and imaginary part (right) of the sulfided catalysts (solid lines) and of the best models (dashed line) obtained by multi-edge fitting of the k^3 weighted EXAFS in k-space.

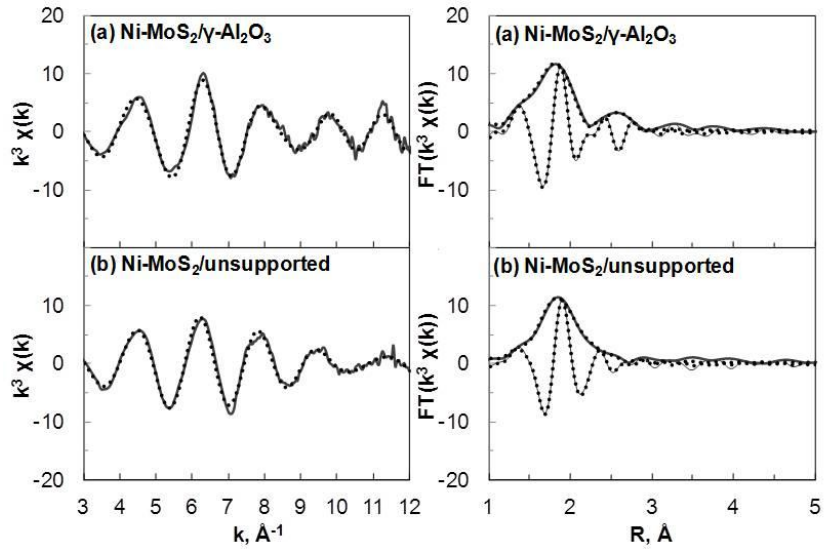

Figure S12. k^3 weighted EXAFS (left) at the Ni K-edge and the corresponding Fourier transforms, magnitudes and imaginary part (right) of the sulfided catalysts (solid lines) and of the best models (dashed line) obtained by multi-edge fitting of the k^3 weighted EXAFS in k-space.

On the equilibration of quinoline and 1,2,3,4-tetrahydroquinoline

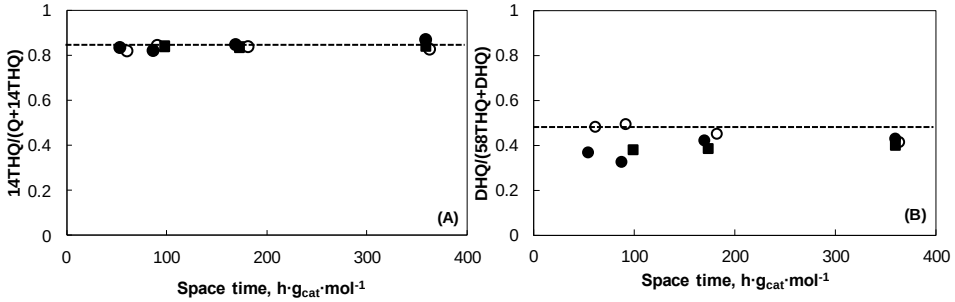

Figure S13. Equilibrium (dotted line) between: quinoline and 14THQ (A) and DHQ and 58THQ (B), when quinoline HDN is carried out at 370 °C and 5 MPa on $MoS_2/\gamma\text{-}Al_2O_3$ (■), Ni-$MoS_2/\gamma\text{-}Al_2O_3$ (●), and Ni-MoS_2/unsupported (○) in the presence of 3.4 kPa DBT.

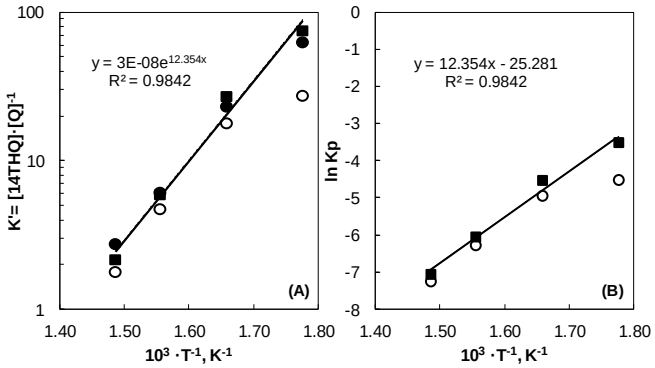

Figure S14. The ratio of 14THQ and quinoline (A) and the natural logarithm of the Kp (B) as a function of the reciprocal of the temperature at 5 MPa. Different assignments were used for the reactions carried out on $MoS_2/\gamma\text{-}Al_2O_3$ (■), Ni-$MoS_2/\gamma\text{-}Al_2O_3$ (●), and Ni-MoS_2/unsupported (○).

The thermodynamic equilibrium between quinoline and 14THQ was reached at all temperatures studied, as seen in Figure S13 (A), where quinoline is favored at higher temperatures. The equilibrium constant ($K' = K_p \cdot p_{H2}^2$), is shown as the reciprocal function of the temperature for all three catalysts, Figure S14 (A). Applying the Van't Hoff equation:

$$\frac{d\ln K_p}{d(1/T)} = -\frac{\Delta H}{R}$$

$$\ln K_p = -\frac{\Delta H}{RT} + \frac{\Delta S}{R}$$

where K_p is the conventional equilibrium constant, T is the temperature (K), ΔH is the heat of the reaction in (J·mol^{-1}), ΔS is the entropy of the reaction (J·(mol K)$^{-1}$), and R is the gas constant (8.314 J·(mol K)$^{-1}$), a linear correlation was obtained, as shown in Figure S14 (B):

$$K_p = \frac{12354}{T} - 25.28$$

The heat of the reaction was calculated to be 102.7 kJ·mol^{-1}.

John Wiley and Sons License

JOHN WILEY AND SONS LICENSE
TERMS AND CONDITIONS

Aug 19, 2015

This Agreement between Oliver Y Gutiérrez ("You") and John Wiley and Sons ("John Wiley and Sons") consists of your license details and the terms and conditions provided by John Wiley and Sons and Copyright Clearance Center.

License Number	3681850593025
License date	Aug 04, 2015
Licensed Content Publisher	John Wiley and Sons
Licensed Content Publication	ChemCatChem
Licensed Content Title	γ-Al2O3-Supported and Unsupported (Ni)MoS2 for the Hydrodenitrogenation of Quinoline in the Presence of Dibenzothiophene
Licensed Content Author	Jennifer Hein, Ana Hrabar, Andreas Jentys, Oliver Y. Gutiérrez, Johannes A. Lercher
Licensed Content Date	Jan 16, 2014
Pages	15
Type of use	Dissertation/Thesis
Requestor type	Author of this Wiley article
Format	Print and electronic
Portion	Full article
Will you be translating?	No
Title of your thesis / dissertation	Investigation and understanding of unsupported NiMoW sulfides for hydrotreating
Expected completion date	Oct 2015
Expected size (number of pages)	200
Requestor Location	Oliver Y Gutiérrez Lichtenbergstr. 4; Garching, Germany D-85747 Attn: Oliver Y Gutiérrez
Billing Type	Invoice
Billing Address	Oliver Y Gutiérrez Lichtenbergstr. 4, Garching, Germany D-85747 Attn: Oliver Y Gutiérrez
Total	0.00 EUR

Terms and Conditions

This copyrighted material is owned by or exclusively licensed to John Wiley & Sons, Inc. or one of its group companies (each a"Wiley Company") or handled on behalf of a society with which a Wiley Company has exclusive publishing rights in relation to a particular work (collectively "WILEY"). By clicking "accept" in connection with completing this licensing transaction, you agree that the following terms and conditions apply to this transaction (along with the billing and payment terms and conditions established by the Copyright Clearance Center Inc., ("CCC's Billing and Payment terms and conditions"), at the time that you opened your Rightslink account (these are available at any time at http://myaccount.copyright.com).

The materials you have requested permission to reproduce or reuse (the "Wiley Materials") are protected by copyright.

Questions? customercare@copyright.com or +1-855-239-3415 (toll free in the US) or +1-978-646-2777.

2. A 2 - Support Chapter 5

Raman spectroscopy

In accordance to the group theory for MoS_2 and WS_2 (Figure 2 (b) and (c)), the most pronounced first-order Raman active modes are observed as follows.[167, 275] The S displacement along the z-axis is found at 409 cm^{-1} for MoS_2 and at 421 cm^{-1} for WS_2 (the A_{1g} mode). The second strong mode is the asymmetric metal-S vibration along the basal plane, namely E^1_{2g} (MoS_2: 384 cm^{-1}; WS_2: 353 cm^{-1}). The third Raman active mode is the E_{1g} (S displacement along the basal plane), which is dependent on the orientation of the back-scattering surface to the incident light. For MoS_2, a weak E_{1g} mode is found at 288 cm^{-1} whereas for WS_2 it is not observed. The Raman band at 325 cm^{-1} of WS_2 can be assigned as a higher-order Raman mode caused by phonon coupling.[276]

Table S1. The measured Raman scattering bands in cm^{-1} and their assignments (λ_{ex} = 514 nm).

Sample	Frequencies of the Raman active modes in cm^{-1} (involved atoms and direction of vibration) [a]		
	A_{1g} (S along z axis)	E^1_{2g} (Mo/W and S along the basal plane)	
MoS_2	409	384	288 (E_{1g}; S along the basal plane)
WS_2	421	353	325 (higher order Raman band)
NiMoS	405	381	
NiMoWS	410	374; 349	
NiWS	413	347	

[a] The irreducible representations of the Raman active modes are given and in parentheses the direction of vibration and the involved atoms are indicated according to Ref. [167, 275-276].

Electron microscopy

Figure S1. Transmission electron micrographs of the sulfided catalysts NiMoS (A), NiMoWS (B) and NiWS(C).

Figure S2. He ion electron micrographs of the sulfided catalysts NiMoS (A), NiMoWS (B) and NiWS(C).

The TEM and SHIM pictures of these three sulfide catalysts are included in **Figure 1** and **2** of **Ch. 6**.

Description of the XANES and linear combination fitting

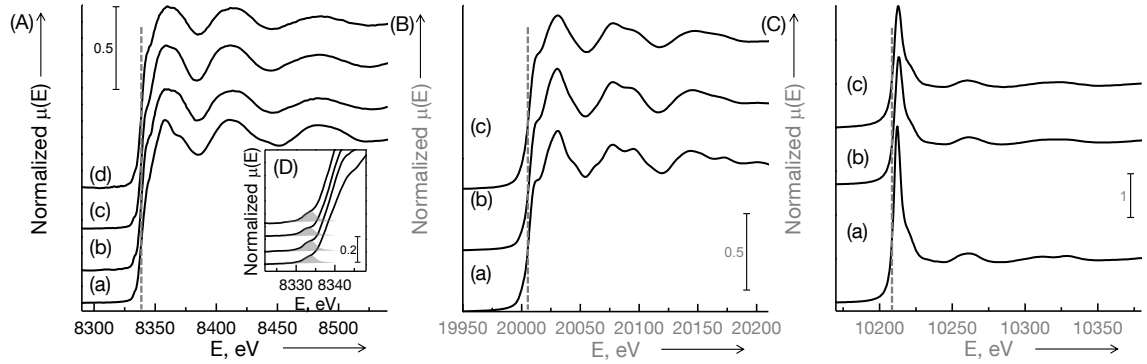

Figure S3. XANES at the Ni K-edge (A), Mo K-edge (B) and W LIII-edge (C) of the references Ni_3S_2 (A,a), MoS_2 (B,a) and WS_2 (C,a) as well as of the catalysts NiMoS (A,b and B,b), NiMoWS (c) and NiWS (A,d and C,b). In (A) the pre-edge area is additionally presented in the inset (D).

The analysis of difference spectra and linear combination fitting (LCF) revealed that the best fits for the XANES of the sulfide catalysts are combinations of the XANES of sulfide reference materials with a small portion of the oxidic precursor (not presented) of the relevant catalyst (less than 4 %). However, the estimated residual between the measured and the modeled XANES indicates that other phases with different short-range geometry parameters are present than the ones used for XANES modeling. At all three metal edges, the FT of the EXAFS of all references and all catalyst exhibit a strong feature at around 2 Å (not phase-shift corrected), which can be assigned to a metal-sulfur contribution.[155] The second pronounced contribution in the FT, usually assigned to metal-metal (Mo-Mo or W-W) contributions,[155] is different at the different metal edges and for the different samples. Therefore, all metals in all catalysts exhibit high coordination with sulfur with reduction states similar to those in the reference sulfides, whereas having important differences at the second coordination sphere. In the following, the observations at the different edges are described more in detail.

At the Ni K-edge, the absorption edge of Ni_3S_2 appears at 8338.0 eV (Figure S3(A, a)). The bimetallic catalyst NiWS exhibits a higher absorption edge at 8339.0 eV, followed by NiMoWS at 8339.3 eV and the highest is found for NiMoS at 8339.5 eV. The edge position is influenced by the attraction of core electrons to the absorber metal, i.e., the edge energy increases with increasing oxidation state of the absorber.[220] Thus, the lowest oxidation state is found for Ni_3S_2 followed by NiWS, NiMoWS, and the highest Ni oxidation state is that in NiMoS. The white line intensity of Ni_3S_2, NiMoS, NiWS, and NiMoWS are very similar, which points to the same covalent Ni-S bonding in all samples and the absence of ionic Ni-O bonds.[38] However, the white line shapes of the catalysts are broader than that of Ni_3S_2. This broadening is associated with a symmetry change of 4p orbitals[222] and points to the

presence of atomic neighbors different than in Ni_3S_2. A pre-edge feature is found at 8332.8 eV in the XANES of all samples, which is caused by a dipole forbidden 1s-3d electronic transition enabled by hybridization of the d-orbitals.[220] This pre-edge indicates a trigonal-prismatic, square-pyramidal or tetrahedral coordination site for Ni in Ni_3S_2 as well as in the catalysts.[147, 258] Ni_3S_2 crystallizes in a trigonal space group, where Ni is in a distorted tetrahedral coordination with four sulfur atoms (ICSD #27521[69]). The distortion is the reason for the less intense pre-edge in Ni_3S_2. The best LCF reproduction of the XANES of NiMoWS is obtained by the XANES of Ni_3S_2 to 99.4 % and the XANES of the oxide NiMoW precursor to the other 0.6 %. The XANES of NiWS is best described by 98.2 % of the Ni_3S_2 spectra and 1.8 % of the catalyst precursor. The highest value for the oxidic precursor portion in the modeled XANES has the XANES of NiMoS with 3.8 % (Table S2 and Figure S4).

At the Mo K-edge, the same absorption edge is observed for the reference MoS_2 and the catalysts NiMoS and NiMoWS (20007 eV) without any pre-edge feature in the XANES (Figure S3). These observations point to Mo^{4+} in an octahedral site, where the 1s-4d electronic transition is not allowed due to the presence of an inversion center.[220, 258] The LCF of the XANES of NiMoWS contains 3.9 % of the XANES of the corresponding oxidic precursor and 96.1 % of the one of MoS_2 (Figure S5). The XANES of the bimetallic NiMoS catalysts is best represented by 99.6% of MoS_2 and only 0.4% of the oxide precursor. The R factor of the LCF and the integrated area of the residuals indicate a very good match between the experimental and modeled XANES (Table S2). However, the intensity and shape of the white line of NiMoWS indicated the interaction of Mo with neighbors different to those present in MoS_2 or in the bimetallic NiMoS catalyst.

At the W L_{III}-edge, the XANES is caused by the electronic dipole transition of a $2p_{3/2}$ electron to the unoccupied $5d_{3/2}$ electronic state, i.e., the unoccupied d-orbitals are probed. The XANES of the bulk reference WS_2 and of the catalysts NiWS and NiMoWS are presented in Figure S3. The W L_{III}-edge XANES of all sulfided samples exhibit a sharp 2p-5d electronic transition at the onset of the adsorption edge. The absorption edge positions of the samples differ only slightly being at 10210.2 for NiMoWS, at 10210.4 for reference WS_2 and at 10210.7 eV for the sulfided NiWS catalyst. Thus, NiMoWS has the lowest oxidation state. Additionally, the least intense white line is observed for NiMoWS, which suggests the highest population of the 5d-orbitals. The linear combination fitting obtained by combining only the XANES of WS_2 and the oxidic precursors were not satisfactory. Therefore, the XANES of the metal W foil used for calibration was additionally added during the LCF (Table S2 and Figure S6). In this way, the XANES of NiMoWS is best described by 61.5 % of WS_2, 37.5 % of the W metal foil and 1.0 % of the oxidic precursor. During the LCF of NiWS, 66.6 % of WS_2 is found as well as 31.2 % of the W metal foil and 2.2 % of the oxidic precursor.

Figure S4. XANES at the Ni K-edge of NiMoS (A), NiMoWS (B) and NiWS (C). The sulfided catalysts (solid line) and the modeled XANES (dotted line) obtained by LCF using the XANES of the references bulk material Ni_3S_2 and the corresponding oxidic precursor. The bottom solid line represents the difference spectra between the measured and the modeled XANES (residual).

See Figure S26 in A 3, support of Chapter 6.

Figure S5. XANES at the Mo K-edge of NiMoS (A) and NiMoWS (B). The sulfided catalysts (solid line) and the modeled XANES (dotted line) obtained by LCF using the XANES of the references bulk material MoS_2 and the corresponding oxidic precursor. The bottom solid line represents the difference spectra between the measured and the modeled XANES (residual).

See Figure S27 in A 3, support of Chapter 6.

Figure S6. XANES at the W L_{III}-edge of NiWS (A) and NiMoWS (B). The sulfided catalysts (solid line) and the modeled XANES (dotted line) obtained by LCF using the XANES of the references bulk material WS_2, W metal foil and the corresponding oxidic precursor. The bottom solid line represents the difference spectra between the measured and the modeled XANES (residual).

See Figure S28 in A 3, support of Chapter 6.

Table S2. Results of the modeled XANES by LCF.

Contained in Table S7 in A 3, support of Chapter 6.

The EXAFS at the Ni K-edge of the reference and the sulfide catalysts

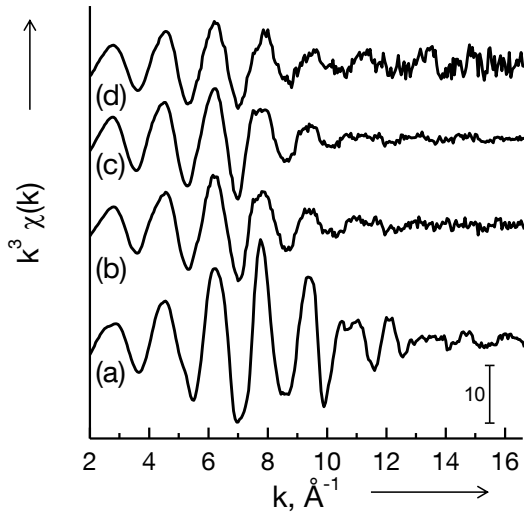

Figure S7. k^3 weighted EXAFS of Ni_3S_2 (a) and of the catalysts NiMoS (b), NiMoWS (c) and NiWS (d).

Theoretical EXAFS and FT transforms of model clusters

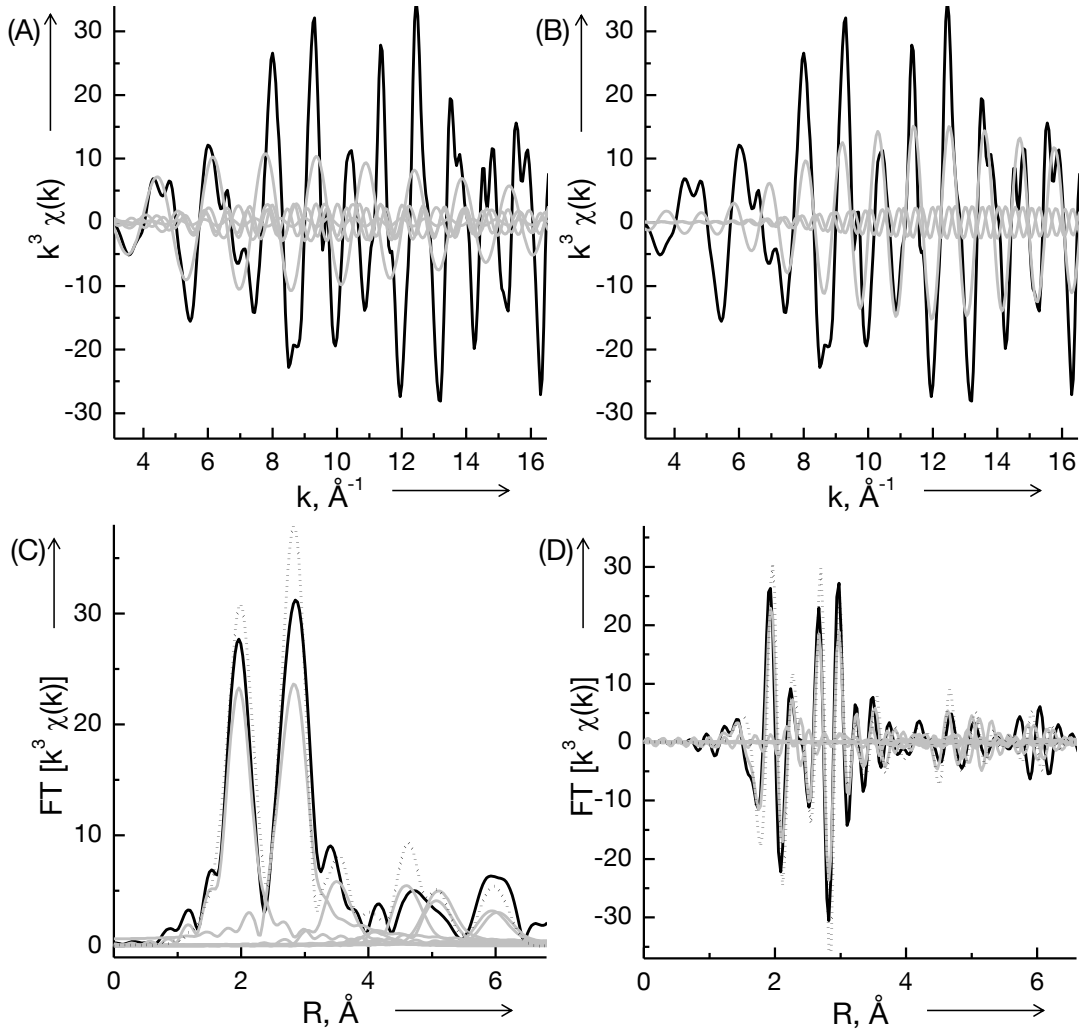

Figure S8. k^3 weighted EXAFS of simulated MoS_2 (A, B black line) and of the relevant feff-paths of S (A, grey line) and Mo (B, grey line) and the corresponding Fourier transforms of the magnitude (C) and of the imaginary part (D) at the Mo K-edge. Additionally, the modeled Fourier transforms are displayed (dotted line in C and D). The particle used for simulation is shown in the picture Particles 1 (model clusters).

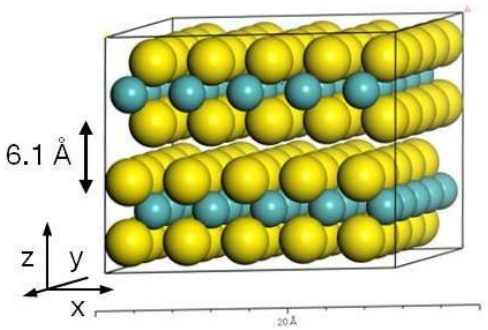

Particle 1. Pure MoS_2, 5x5 Mo atoms (blue) and S (yellow), particle used for feff-creation and simulation of 2H-MoS_2 The structural information were taken from ISCD # 644245 and the supercell was created by using 5 hexagonal unit cells in a- and b-direction (a = b 15.8 Å, c = 12.3 Å).

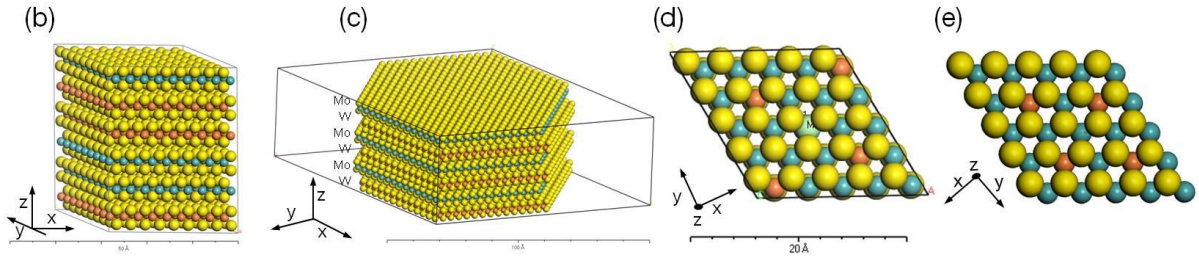

Particle 2. Particles corresponding to Figure 8 for simulation of k^3 weighted EXAFS at the Mo K-edge of $MoWS_2$ with Mo-W = 3 at 6.42 Å, stacking sequence abbaab (b), $MoWS_2$ with Mo-W = 6 at 6.42 Å, stacking sequence abababab (c), $MoWS_2$ with Mo-W = 2 at 5.48 Å (d), $MoWS_2$ with Mo-W = 2 at 3.16 Å (e). Pure MoS_2 (a) was already presented as Particle 1. (Color code: blue = Mo, orange = W, yellow = S).

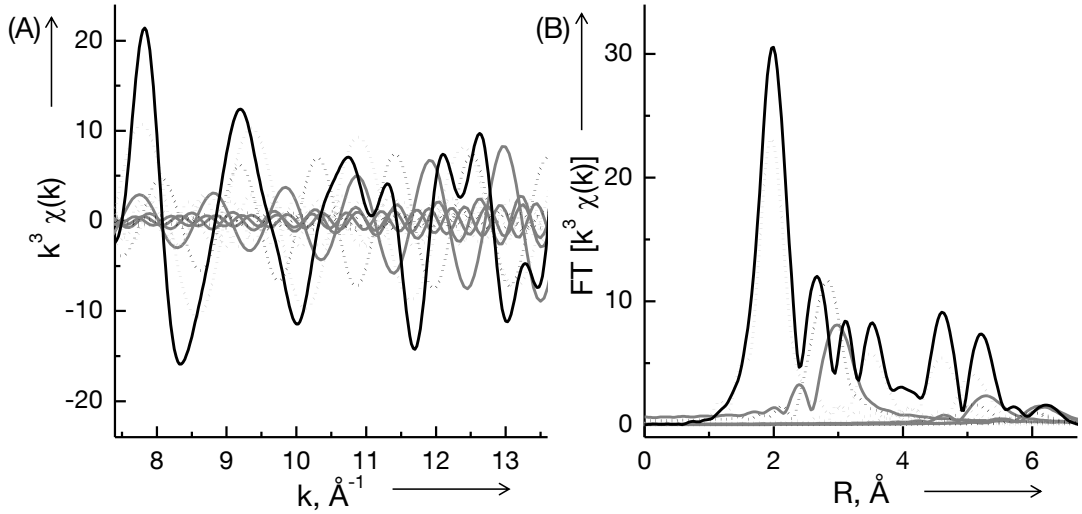

Figure S9. Simulated k^3 weighted EXAFS at the Mo K-edge (A) and the corresponding Fourier transforms (B) of $MoWS_2$ with the N(Mo-W) = 3 at 3.16 Å. Additionally, all single-scattering Mo-S (light grey dotted line), Mo-Mo (black dotted line) and Mo-W (grey solid line) feff-paths are shown next to the simulated overall EXAFS (black solid line).

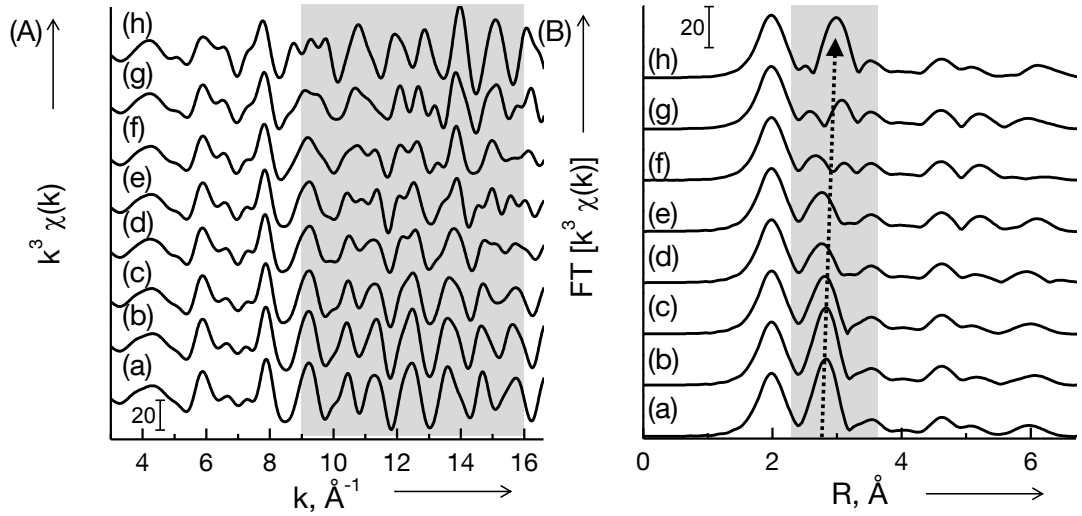

Figure S10. Simulated k^3 weighted EXAFS at the Mo K-edge (A) and the corresponding Fourier transforms (B) of constructed mixed $MoWS_2$ with varying Mo-W coordination number N at 3.16 Å as shown in the picture Particles 3; namely simulated MoS_2 with N = 0 (a), $MoWS_2$ with N (3.16 Å) = 0 and N (5.48 Å) = 2 (b), N = 1 (c), $MoWS_2$ with N (Mo-W) = 2 and N (W-Mo) = 6 (d), $MoWS_2$ with N (Mo-W) = 2 and N (W-Mo) = 2 (e), N = 3 (f), N = 4 (g), and N = 6 (h).

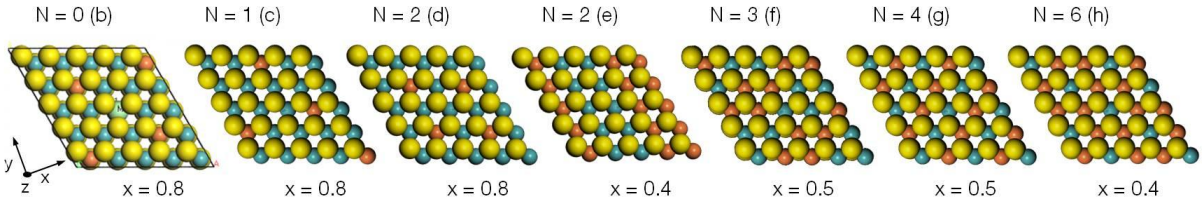

Particle 3. Particles for simulation of k^3 weighted EXAFS at the Mo K-edge of mixed $MoWS_2$ with varying Mo-W coordination number N at 3.16 Å, namely $MoWS_2$ with N (3.16 Å) = 0 and N (5.48 Å) = 2 (b), N = 1 (c), $MoWS_2$ with N (Mo-W) = 2 and N (W-Mo) = 6 (d), $MoWS_2$ with N (Mo-W) = 2 and N (W-Mo) = 2 (e), N = 3 (f), N = 4 (g), and N = 6 (h). (Color code: blue = Mo, orange = W, yellow = S).

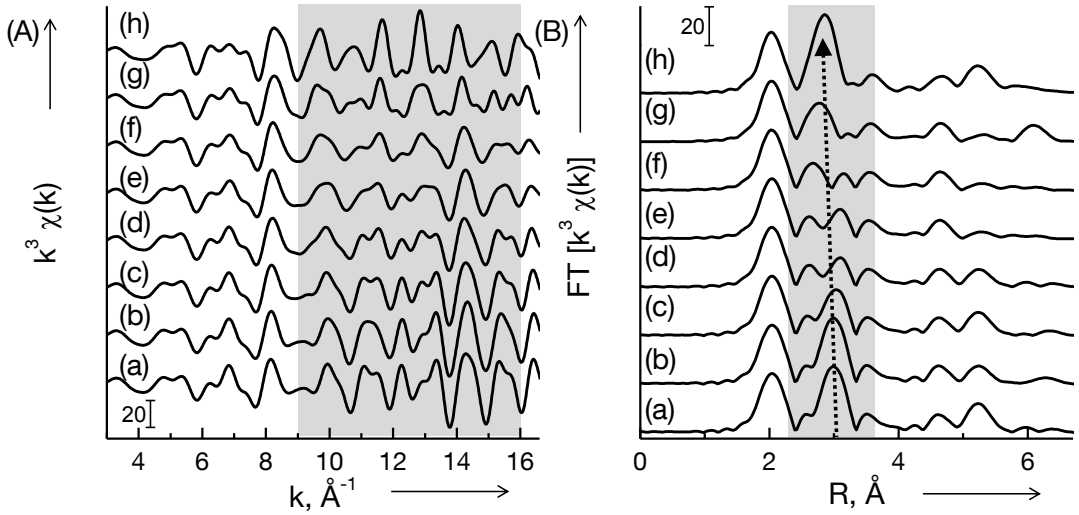

Figure S11. Simulated k^3 weighted EXAFS at the W L_{III}-edge (A) and the corresponding Fourier transforms (B) of constructed mixed $MoWS_2$ with varying W-Mo coordination number N at 3.16 Å as shown in the picture Particles 4; namely simulated WS_2 with N = 0 (a), $MoWS_2$ with N (3.16 Å) = 0 and N (5.48 Å) = 2 (b), N = 1 (c), $MoWS_2$ with N (W-Mo) = 2 and N (Mo-W) = 6 (d), $MoWS_2$ with N (W-Mo) = 2 and N (Mo-W) = 2 (e), N = 3 (f), N = 4 (g), and N = 6 (h).

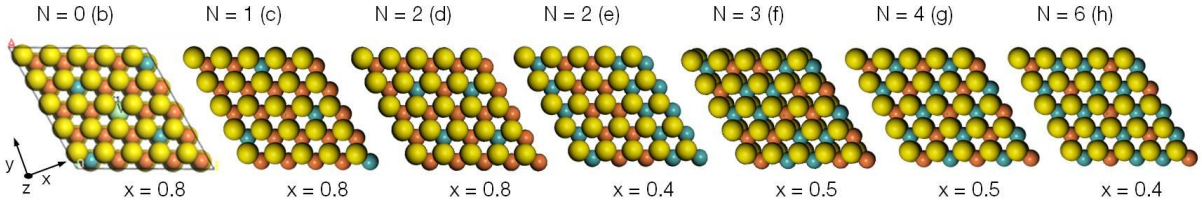

Particle 4. Particles for simulation of k^3 weighted EXAFS at the W L_{III}-edge of mixed $MoWS_2$ with varying W-Mo coordination number N at 3.16 Å, namely $MoWS_2$ with N (3.16 Å) = 0 and N (5.48 Å) = 2 (b), N = 1 (c), $MoWS_2$ with N (W-Mo) = 2 and N (Mo-W) = 6 (d), $MoWS_2$ with N (W-Mo) = 2 and N (Mo-W) = 2 (e), N = 3 (f), N = 4 (g), and N = 6 (h). (Color code: blue = Mo, orange = W, yellow = S).

Fitting results of the k^3 weighted EXAFS

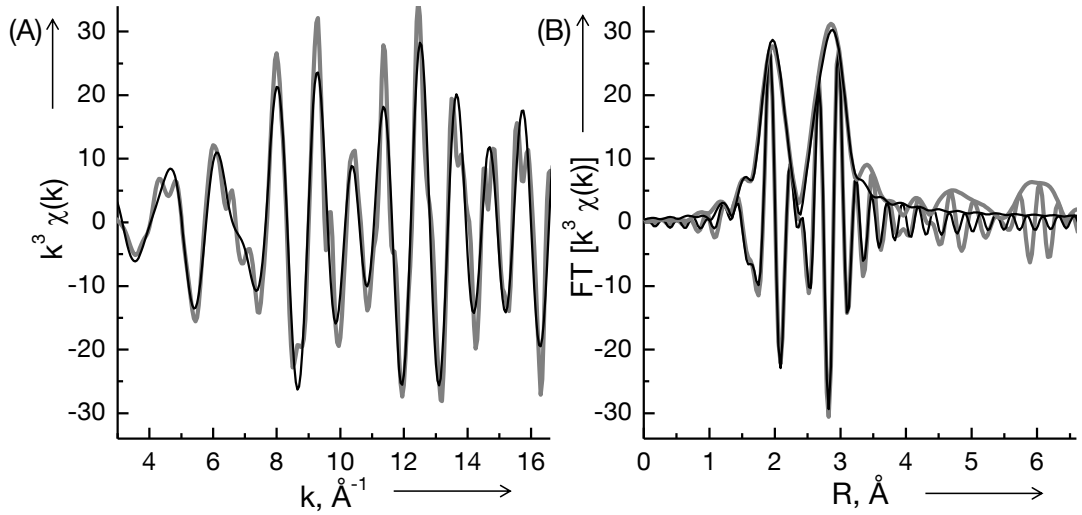

Figure S12. k^3 weighted EXAFS (A) at the Mo K-edge and the corresponding Fourier transforms, magnitudes and imaginary part (B) of MoS_2 (grey lines) and of the best models (black lines) obtained by fitting of the k^3 weighted EXAFS in k-space.

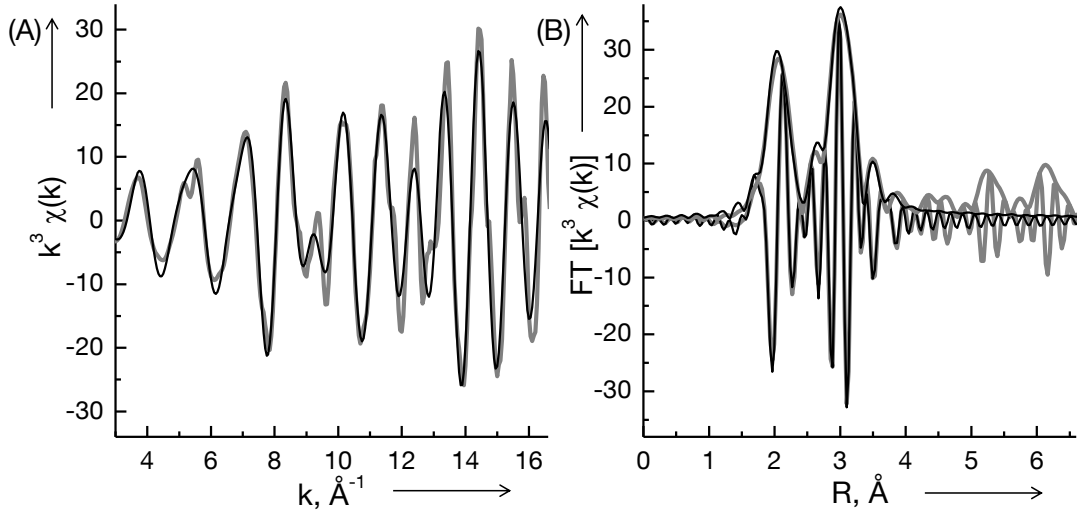

Figure S13. k^3 weighted EXAFS (A) at the W L^{III}-edge and the corresponding Fourier transforms, magnitudes and imaginary part (B) of WS_2 (grey lines) and of the best models (black lines) obtained by fitting of the k^3 weighted EXAFS in k-space.

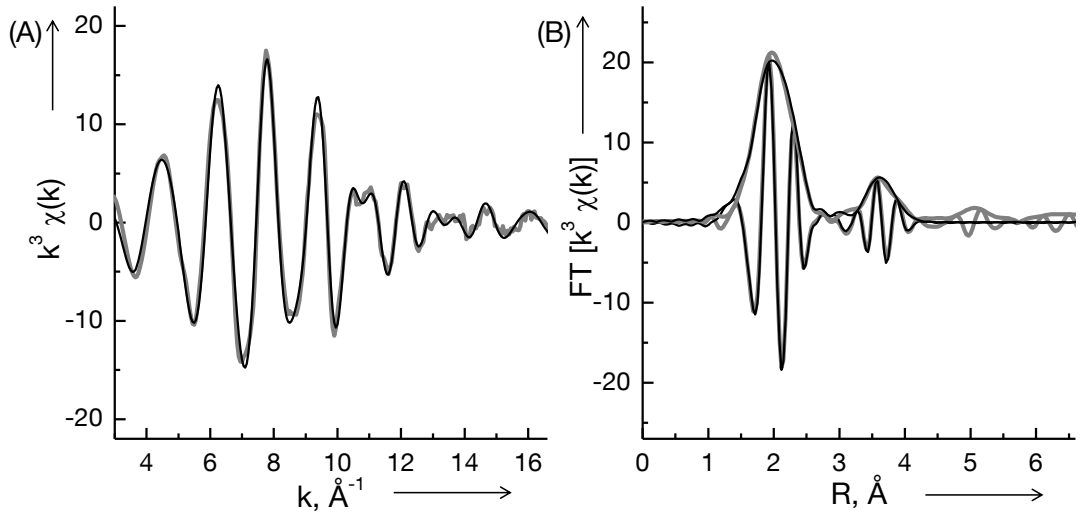

Figure S14. k^3 weighted EXAFS (A) at the Ni K-edge and the corresponding Fourier transforms, magnitudes and imaginary part (B) of Ni_3S_2 (grey lines) and of the best models (black lines) obtained by fitting of the k^3 weighted EXAFS in k-space.

EXAFS fitting results of NiMoS sulfide catalyst

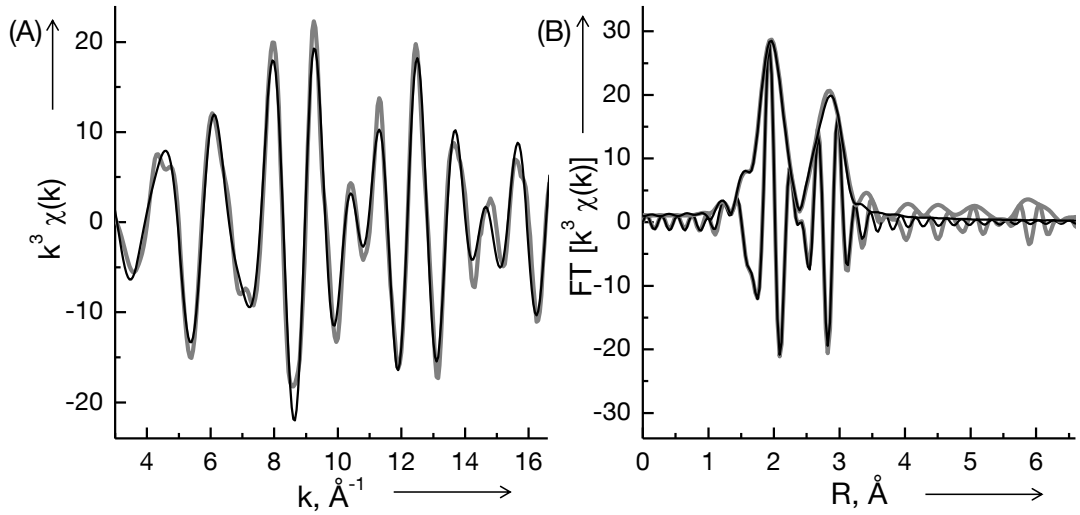

Figure S15. k^3 weighted EXAFS (A) at the Mo K-edge and the corresponding Fourier transforms, magnitudes and imaginary part (B) of the sulfided NiMoS catalyst (grey lines) and of the best models (black lines) obtained by multi-edge fitting of the k^3 weighted EXAFS in k-space.

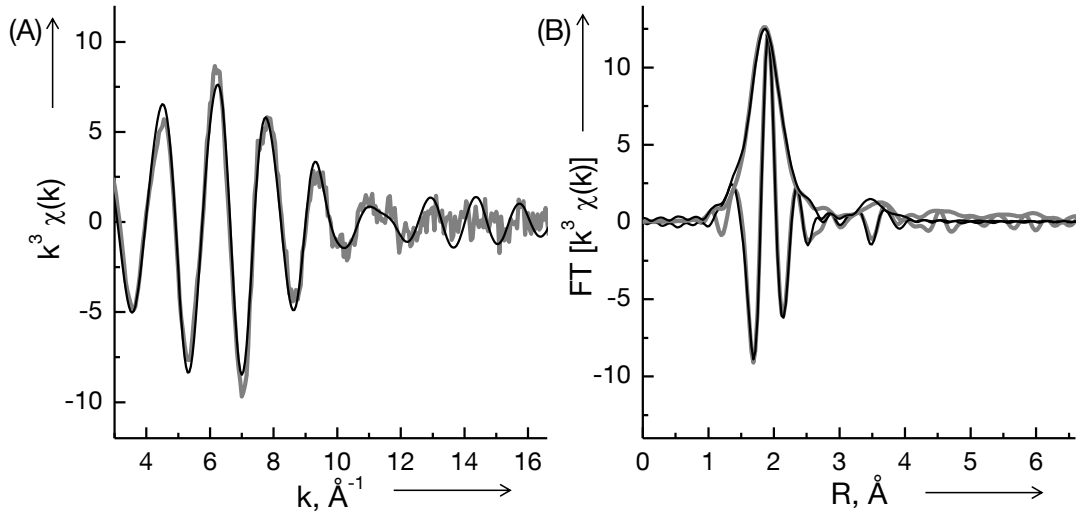

Figure S16. k^3 weighted EXAFS (A) at the Ni K-edge and the corresponding Fourier transforms, magnitudes and imaginary part (B) of the sulfided NiMoS catalyst (grey lines) and of the best models (black lines) obtained by multi-edge fitting of the k^3 weighted EXAFS in k-space.

Table S3. Best fit results for k^3 weighted EXAFS of sulfided catalysts at the Mo K-edge in k space.

Catalyst	Shell	r, Å	N	σ^2, Å^2	E_0, eV
MoS_2 S_0^2 = 1.16	Mo-S	2.41 (0.01)	5.9 (0.5)	0.0024 (0.0005)	3.51 (2.55)
(0.20) R = 0.0094	Mo-Mo	3.17 (0.01)	6.0 (0.4)	0.0018 (0.0003)	
NiMoS	Mo-S	2.40 (0.01)	6.2 (0.2)	0.0025 (0.0002)	0.74 (0.67)
R = 0.0013	Mo-Mo	3.17 (0.01)	5.1 (0.1)	0.0033 (0.0001)	
	Mo-Ni	2.68 (0.02)	0.3 (0.1)	0.0024 (0.0022)	
NiMoWS	Mo-S	2.40 (0.01)	5.2 (0.1)	0.0027 (0.0002)	1.52 (0.60)
R = 0.0055	Mo-Mo	3.16 (0.01)	3.1 (0.1)	0.0043 (0.0010)	
	Mo-W	3.17 (0.01)	1.6 (0.2)	0.0042 (0.0004)	
	Mo-Ni	2.68 (0.03)	0.6 (0.1)	0.0093 (0.0029)	

Abbreviations: r: distance, N: coordination number, σ^2: Debye-Waller like factor, E_0: inner potential, S_0^2: amplitude reduction factor; in parenthesis the absolute errors are shown.

EXAFS fitting results of NiWS sulfide catalyst

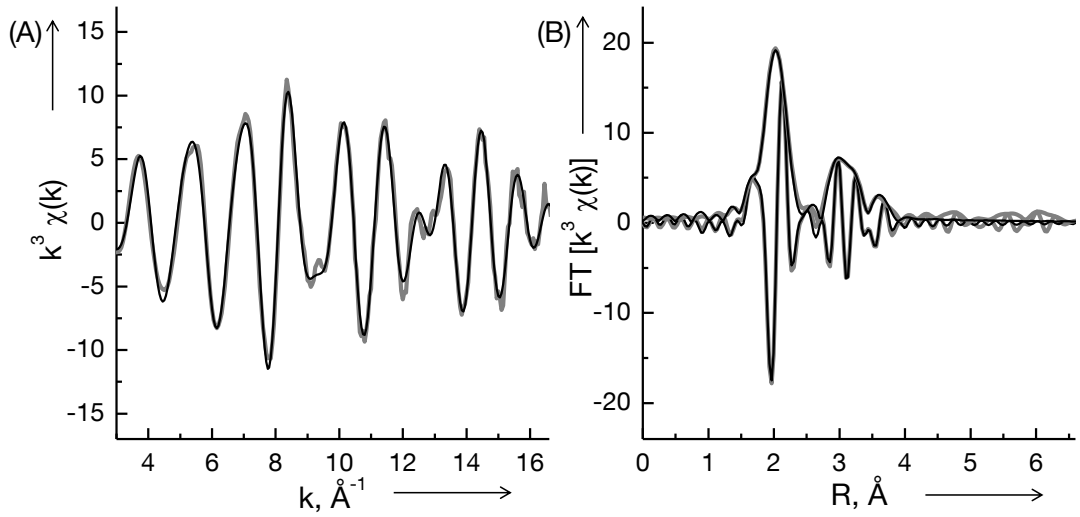

Figure S17. k^3 weighted EXAFS (A) at the W L_{III}-edge and the corresponding Fourier transforms, magnitudes and imaginary part (B) of the sulfided NiWS catalyst (grey lines) and of the best models (black lines) obtained by multi-edge fitting of the k^3 weighted EXAFS in k-space.

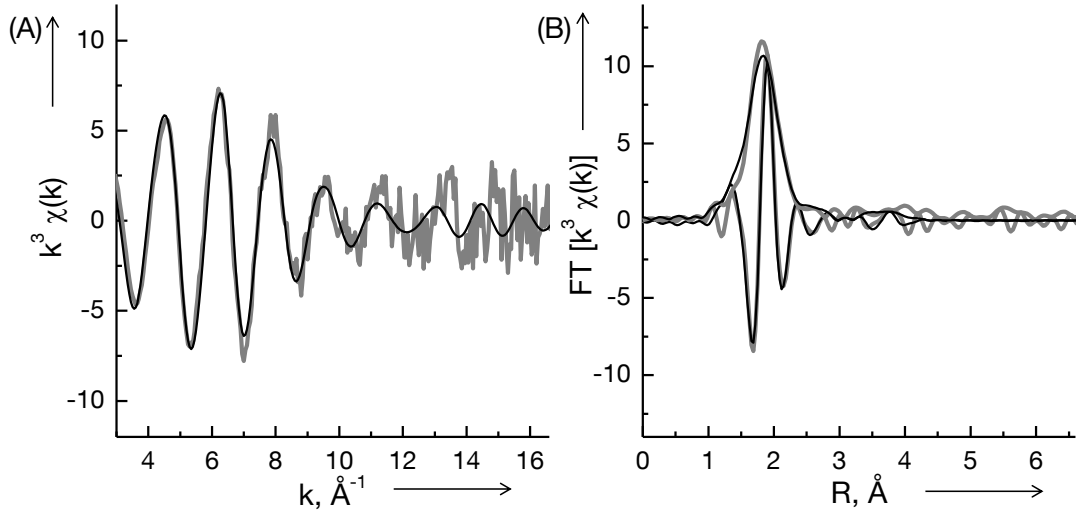

Figure S18. k^3 weighted EXAFS (A) at the Ni K-edge and the corresponding Fourier transforms, magnitudes and imaginary part (B) of the sulfided NiWS catalyst (grey lines) and of the best models (black lines) obtained by multi-edge fitting of the k^3 weighted EXAFS in k-space.

Table S4. Best fit results for k^3 weighted EXAFS of sulfided catalysts at the W L_{III}-edge in k space.

Catalyst	Shell	r, Å	N	σ^2, Å^2	E_0, eV
WS_2 S_0^2 = 1.18	W-S	2.40 (0.01)	5.8 (0.5)	0.0027 (0.0005)	7.83 (1.93)
(0.20) R = 0.0092	W-W	3.16 (0.01)	6.1 (0.5)	0.0024 (0.0003)	
NiWS	W-S	2.40 (0.01)	4.5 (0.2)	0.0037 (0.0002)	7.36 (0.44)
R = 0.0033	W-W	3.15 (0.01)	3.1 (0.4)	0.0045 (0.0005)	
	W-Ni	2.75 (0.05)	0.1 (0.1)	0.0033 (0.0030)	
NiMoWS	W-S	2.41 (0.01)	4.9 (0.2)	0.0044 (0.0006)	8.02 (1.23)
R = 0.0055	W-W	3.17 (0.02)	2.1 (0.3)	0.0042 (0.0006)	
	W-Mo	3.17 (0.01)	2.0 (0.2)	0.0042 (0.0004)	
	W-Ni	2.82 (0.04)	0.6 (0.2)	0.0030 (0.0021)	

Abbreviations: r: distance, N: coordination number, σ^2: Debye-Waller like factor, E_0: inner potential, S_0^2: amplitude reduction factor; in parenthesis the absolute errors are shown.

EXAFS fitting results of NiMoW2S sulfide catalyst

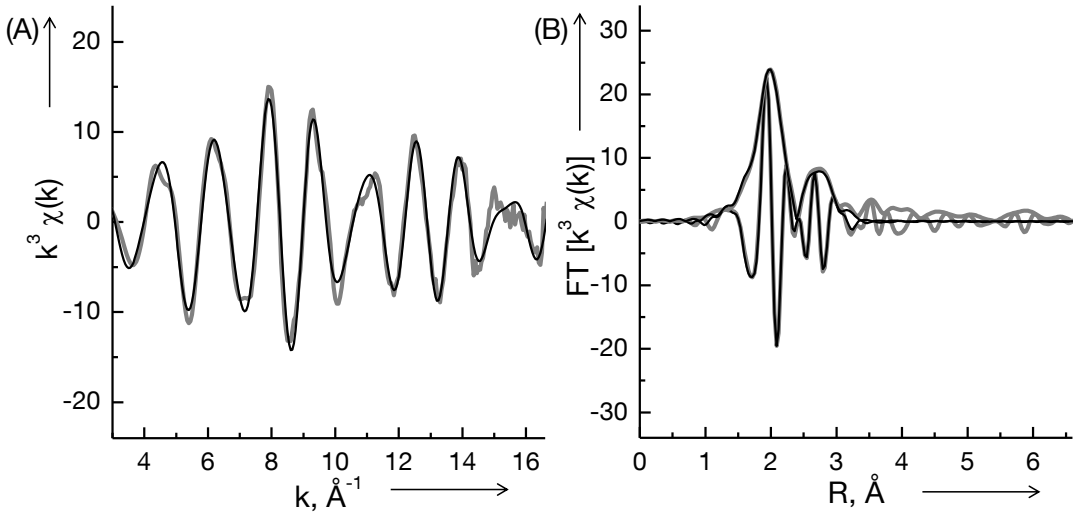

Figure S19. k^3 weighted EXAFS (A) at the Mo K-edge and the corresponding Fourier transforms, magnitudes and imaginary part (B) of the sulfided NiMoWS catalyst (grey lines) and of the best models (black lines) obtained by multi-edge fitting of the k^3 weighted EXAFS in k-space.

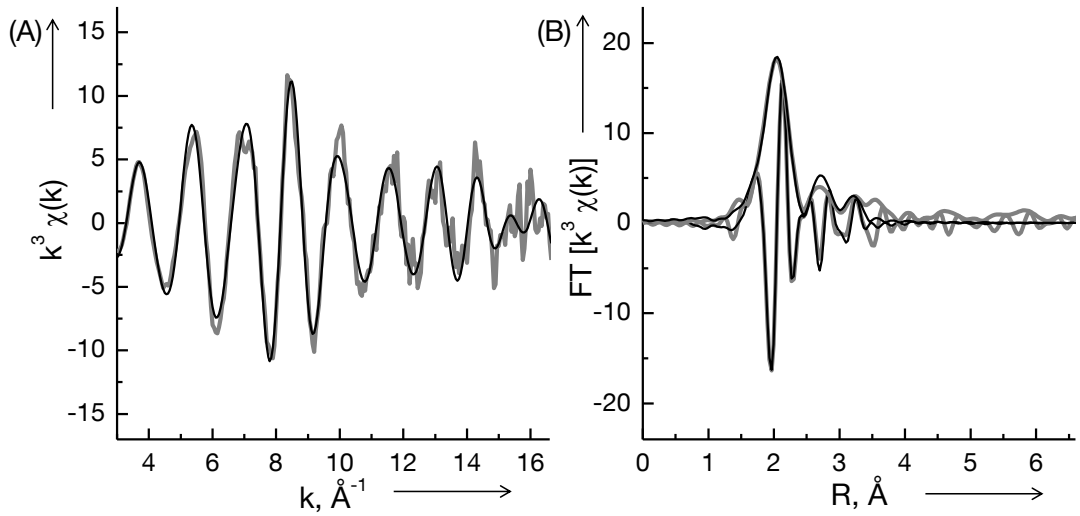

Figure S20. k^3 weighted EXAFS (A) at the W L_{III}-edge and the corresponding Fourier transforms, magnitudes and imaginary part (B) of the sulfided NiMoWS catalyst (grey lines) and of the best models (black lines) obtained by multi-edge fitting of the k^3 weighted EXAFS in k-space.

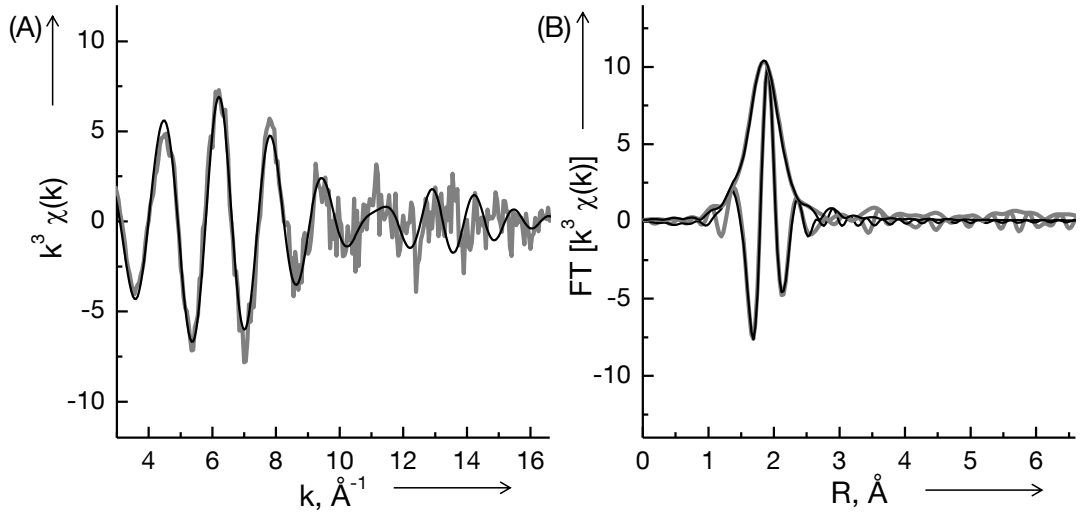

Figure S21. k^3 weighted EXAFS (A) at the Ni K-edge and the corresponding Fourier transforms, magnitudes and imaginary part (B) of the sulfided NiMoWS catalyst (grey lines) and of the best models (black lines) obtained by multi-edge fitting of the k^3 weighted EXAFS in k-space.

Table S5. Best fit results for k^3 weighted EXAFS of sulfided catalysts at the Ni K-edge in k space.

Catalyst	Shell	r, Å	N	σ^2, Å^2	E_0, eV
Ni_3S_2	Ni-S	2.27 (0.01)	4.4 (0.4)	0.0057 (0.0009)	1.68 (0.68)
S_0^2 = 0.98 (0.20)	Ni-Ni	2.52 (0.01)	3.7 (0.4)	0.0055 (0.0008)	
R = 0.0060	Ni-S	3.71 (0.01)	4.5 (0.9)	0.0068 (0.0023)	
	Ni-Ni	3.78 (0.01)	8.0 (1.1)	0.0090 (0.0016)	
	Ni-Ni	4.06 (0.01)	5.6 (0.9)	0.0085 (0.0013)	
NiMoS	Ni-S	2.27 (0.02)	4.5 (0.5)	0.0075 (0.0010)	3.00 (2.66)
R = 0.0013	Ni-Ni	2.60 (0.03)	1.2 (0.5)	0.0071 (0.0031)	
	Ni-Mo	2.68 (0.02)	0.2 (0.1)	0.0024 (0.0022)	
	Ni-Ni	3.88 (0.06)	4.4 (3.5)	0.0169 (0.0076)	
NiWS	Ni-S	2.26 (0.01)	4.4 (0.6)	0.0089 (0.0013)	2.35 (1.51)
R = 0.0033	Ni-Ni	2.57 (0.02)	0.5 (0.2)	0.0052 (0.0020)	
	Ni-W	2.75 (0.05)	0.1 (0.1)	0.0033 (0.0030)	
	Ni-Ni	3.97 (0.08)	3.1 (2.7)	0.0239 (0.0119)	
NiMoWS	Ni-S	2.27 (0.03)	3.8 (0.7)	0.0076 (0.0034)	2.85 (4.75)
R = 0.0055	Ni-Ni	2.59 (0.05)	0.7 (0.5)	0.0055 (0.0045)	
	Ni-Mo	2.68 (0.03)	0.3 (0.1)	0.0093 (0.0029)	
	Ni-W	2.82 (0.04)	0.2 (0.2)	0.0030 (0.0021)	

Abbreviations: r: distance, N: coordination number, σ^2: Debye-Waller like factor, E_0: inner potential, S_0^2: amplitude reduction factor; in parenthesis the absolute errors are shown.

Calculation of the phase function

The characteristic phase shifts are tabled for every element in function on the wavenumber k. Lee and Teo formulated a simplified equation to calculate the phase function for different atom-backscatter pairs at different absorption edges.[227]

With absorbing atom A and backscattering atom B, follows for the phase function ϕ that:

for K and L_I-edges (l = 1) : $\varphi_{AB}(k) = \varphi_A^l(k) + \varphi_B(k) - \pi$

for $L_{II, III}$ - edges (l = 2,0): $\varphi_{AB}(k) = \varphi_A^l(k) + \varphi_B(k)$

where $\varphi_A^l(k)$ is the phase shift of the central atom A and $\varphi_B(k)$ is the phase shift of the neighboring atom B. Thus, in the concrete case of mixed $Mo_{1-x}W_xS_2$, for a k of 11.3384, the following phase functions are calculated for the different absorber-backscatter pairs at both metal edges.

Mo K-edge:

1. $\varphi_{Mo-Mo}(11.3384) = \varphi_{Mo}^1(k) + \varphi_{Mo}(k) - \pi = 0.4160 + 7.1972 - \pi = 4.4716 = 1.4234 * \pi$

2. $\varphi_{Mo-W}(11.3384) = \varphi_{Mo}^1(k) + \varphi_W(k) - \pi = 0.4160 + 10.2952 - \pi = 7.5696 = 2.4095 * \pi$

W L_{III}-edge:

1. $\varphi_{W-W}(11.3384) = \varphi_W^0(k) + \varphi_W(k) = 3.4588 + 10.2952 = 13.754 = 4.3780 * \pi$

2. $\varphi_{W-Mo}(11.3384) = \varphi_W^0(k) + \varphi_{Mo}(k) = 3.4588 + 7.1972 = 10.6560 = 3.3919 * \pi$

Additional figures and table referring to catalytic activity

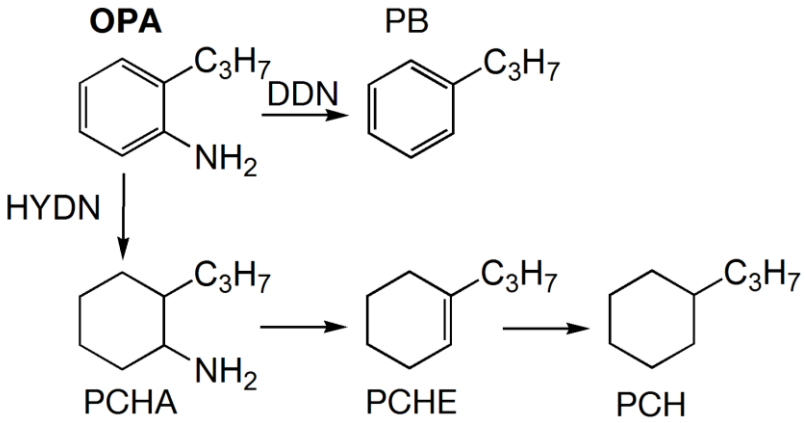

Figure S22. Reaction network for hydrodenitrogenation (HDN) of o-propylaniline (OPA) showing the direct denitrogenation (DDN) and hydrogenation (HYDN) routes and the products propylbenzene (PB), propylcyclohexylamine (PCHA), propylcyclohexene (PCHE) and propylcyclohexane (PCH).[25]

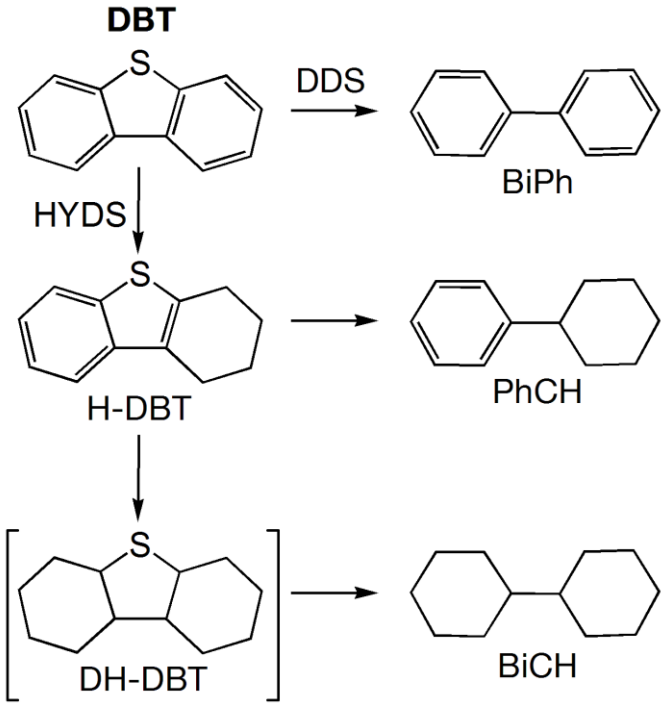

Figure S23. Reaction network for hydrodesulfurization (HDS) of dibenzothiophene (DBT) showing the direct desulfurization (DDS) and hydrogenation (HYDS) routes and the products biphenyl (BiPh), tetrahydrodibenzothiophene (H-DBT), phenylcyclohexane (PhCH), dodecahydrodibenzothiophene (DH-DBT) and bicyclohexane (BiCH).[109]

Table S6. Activity results for the simultaneous HDN of o-propylaniline and HDS of dibenzothiophene over the sulfided catalysts.

Rates, * 10^{-5} $mol_{Educt}/(h*mol_{Metal})$	T, °C	NiMoS	NiMoWS	NiWS
HDN rate (without DBT)[a]	350	24.5 (31.9)	33.2 (37.1)	24.9 (27.9)
	360	35.4 (45.2)	48.9 (57.1)	36.2 (43.2)
	370	48.1 (67.2)	67.6 (79.3)	53.6 (63.2)
HYDN rate (without DBT)[b]	350	23.0 (30.4)	31.1 (34.6)	23.6 (26.4)
	360	32.9 (42.4)	45.0 (52.4)	34.2 (40.4)
	370	43.6 (62.3)	60.6 (70.7)	49.1 (57.5)
DDN rate (without DBT)[b]	350	1.4 (1.6)	2.2 (2.5)	1.1 (1.3)
	360	2.5 (2.8)	3.9 (4.7)	2.3 (2.8)
	370	4.5 (4.9)	7.2 (8.6)	4.5 (5.5)
HDS rate[a]	350	4.7	8.3	6.2
	360	7.3	12.8	9.1
	370	11.6	19.0	13.0
DDS rate (HYDS rate)[c]	350	4.2 (0.4)	7.8 (0.5)	4.3 (1.9)
	360	6.6 (0.7)	12.1 (0.7)	6.8 (2.3)
	370	9.6 (1.9)	17.9 (1.1)	10.6 (2.6)
Apparent activation energy, kJ/mol	HDN with DBT (without DBT)	113 (124)	119 (127)	128 (136)
	HYDN with DBT (without DBT)	107 (119)	111 (119)	122 (129)
	DDN with DBT (without DBT)	185 (191)	200 (207)	227 (230)
	HDS	150	139	124
	DDS	137	139	148
	HYDS	242	134	50

[a] The reaction rates are obtained by the conversions of OPA (in presence and absence of DBT) and DBT divided by the space time and normalized on the total metal content. [b] The HYDN rate determined from the sum of the HDN yields of PCHA+PCHE+PCH and the DDN rate by the yield of PB. [c] The DDS rate is determined by the yield of BiPh and the HYDS rate by the sum of the HDS yields of H-DBT+PhCH+BiCH.

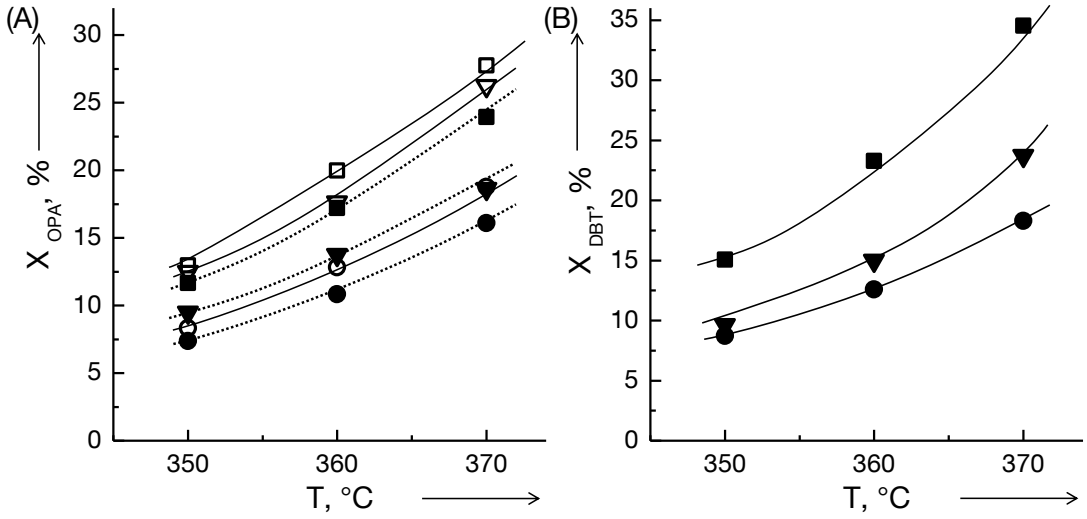

Figure S24. Hydrotreating activity; conversion of OPA (A) and DBT (B) over NiMoS (▾), NiMoWS (■) and NiWS (●). Additionally, HDN activity is determined in the absence of DBT (open symbols ▿ □ ○).

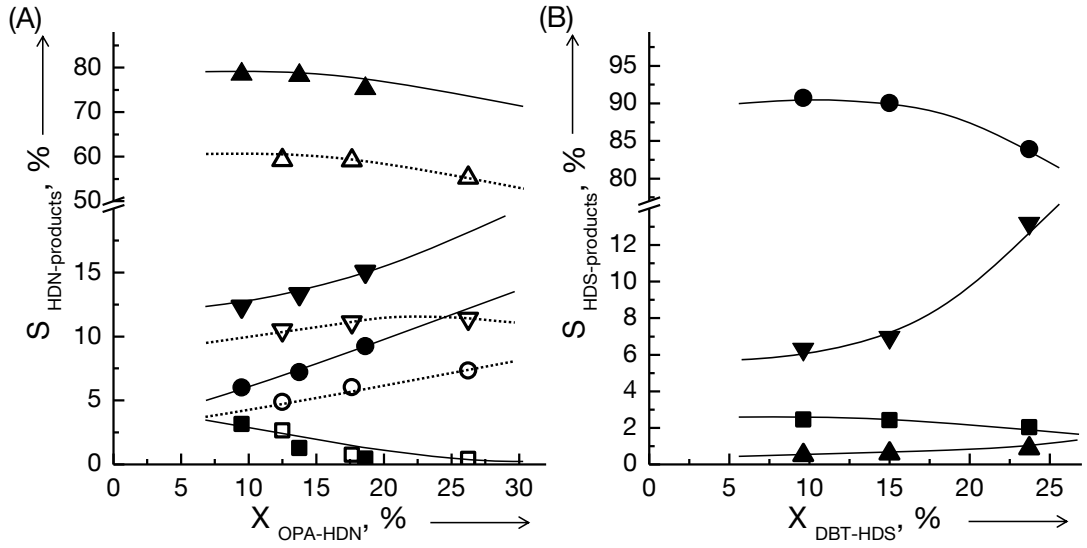

Figure S25. Selectivities versus conversion over NiMoS for (A) OPA HDN products PCHE (▲), PCH (▾), PB (●) and PCHA (■) and for (B) DBT HDS products BiPh (●),BiCH (▾), H-DBT (■) and PhCH (▲). The HDN selectivities in absence of DBT are as well presented (open symbols △ ▿ ○ □).

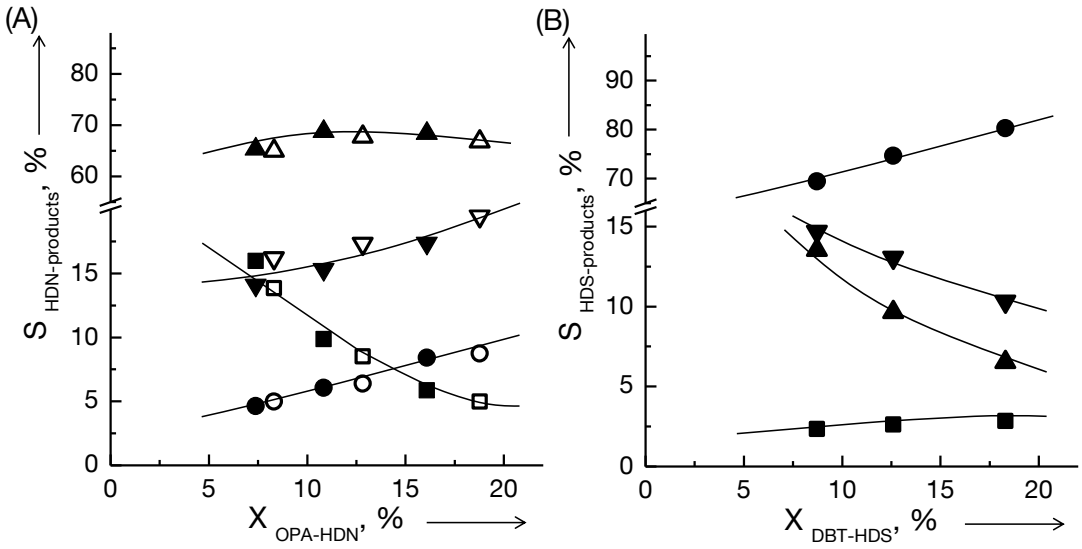

Figure S26. Selectivities versus conversion over NiWS for (A) OPA HDN products PCHE (▲), PCH (▼), PB (●) and PCHA (■) and for (B) DBT HDS products BiPh (●),BiCH (▼), H-DBT (■) and PhCH (▲). The HDN selectivities in absence of DBT are as well presented (open symbols △ ▽ ○ □).

3. A 3 - Support Chapter 6

The full characterization of the oxide precursors is described in Chapter 4 (Figure S1-S22). In this supporting information, additional results regarding the sulfide catalysts are presented, including Figure S13 showing the pre-edge of the Ni K-edge XANES of oxides and sulfides.

Additional data of the characterization of the sulfided catalysts

Table S5. Physicochemical properties of the sulfided catalysts.

Catalyst	Composition, [mmol/g]				Specific surface area, [m^2/g]	Stacking degree of the MoS_2 and WS_2 slabs[b]
	Ni	Mo	W	S		
NiMo	4.6	3.7		11.8	6.2	5.7
NiMoW2	4.0	1.8	1.4	9.7	7.4	5.1
NiWMo1	3.6	1.0	2.0	9.1	4.6	4.3
NiW	2.5		2.8	8.3	5.6	4.4

[a] Determined by passing pulses of NO on in-situ sulfided samples of the catalysts at room temperature. [b] Determined by applying the Scherrer-equation on the (002) reflection at 14.1 °2θ which corresponds to the interplanar distance of 6.1 Å.

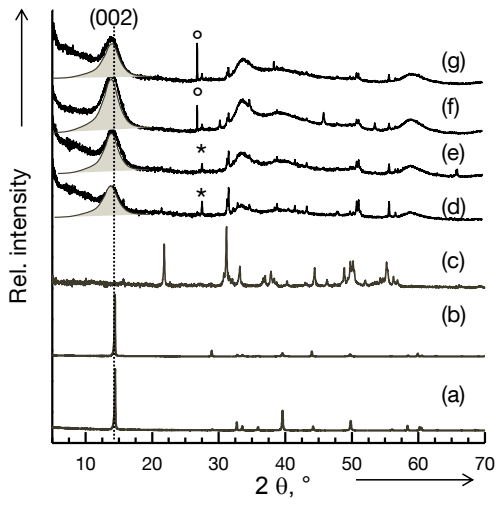

Figure S23. XRD pattern (Cu-K_α) of the reference bulk materials MoS_2 (a), WS_2 (b) and Ni_3S_2 (c), and of the unsupported sulfide catalysts NiMo (d), NiMoW2 (e), NiWMo1 (f) and NiW (g). The fitted profile functions under the (002) reflection at around 14.2 °2θ (grey filled) are used to determine the stacking degree of the MoS_2 and WS_2 slabs. The most important reflection of Ni_9S_8 (*) and Ni_3S_4 (°) are indicated.

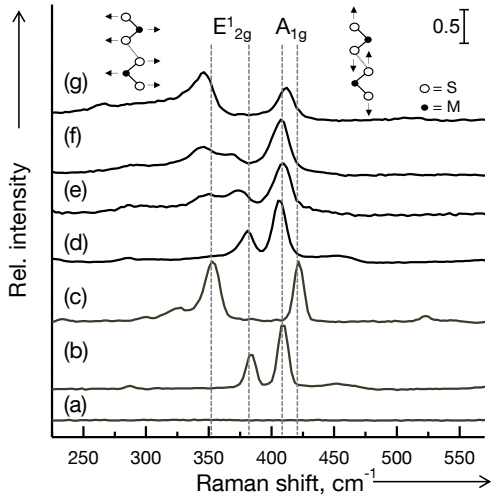

Figure S24. Raman spectra (λ_{ex} = 514 nm) of the reference Ni_3S_2 (a; no Raman bands), MoS_2 (b) and WS_2 (c), and of the unsupported sulfided catalysts NiMo (d), NiMoW2 (e), NiWMo1 (f) and NiW (g). The shift of the most intense Raman bands of the references are indicated by the dotted vertical lines and the corresponding atomic displacement of the E^1_{2g} (left) and A_{1g} (right) mode is illustrated.

Table S6. The measured Raman scattering bands in cm^{-1} and their assignments (λ_{ex} = 514 nm).

Sample	Frequencies of the Raman active modes in cm^{-1} (involved atoms and direction of vibration) [a]		
	A_{1g} (S along z axis)	E^1_{2g} (Mo/W and S along the basal plane)	
MoS_2	409	384	288 (E_{1g}; S along the basal plane)
WS_2	421	353	325 (higher order Raman band)
NiMo	405	381	
NiMoW2	410	374; 349	
NiWMo1	408	369, 345	
NiW	413	346	

[a] The irreducible representations of the Raman active modes are given and in parentheses the direction of vibration and the involved atoms are indicated according to Ref. [167, 275-276].

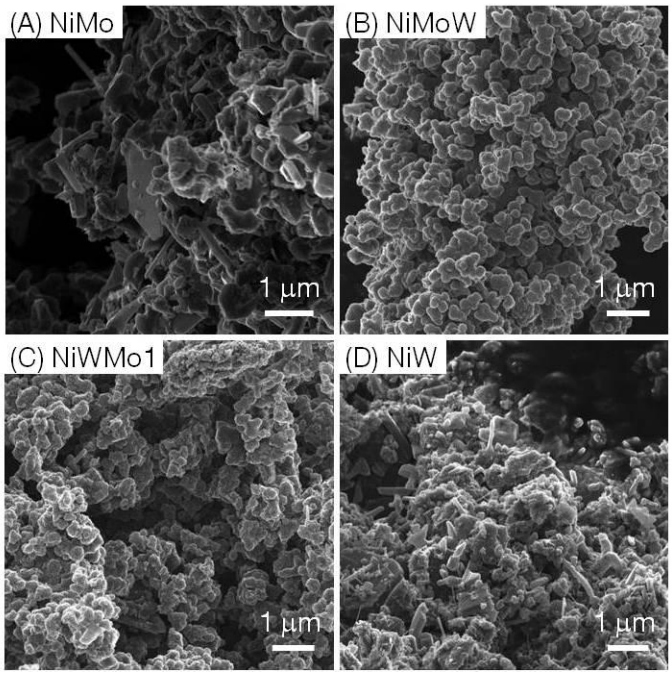

Figure S25. Additional He ion scanning micrographs of sulfided catalysts NiMo (A), NiMoW2 (B), NiWMo1 (C) and NiW (D). The images show the typical morphology over a wide range of 7.5 x 7.5 µm.

XANES analysis and linear combination fitting (LCF)

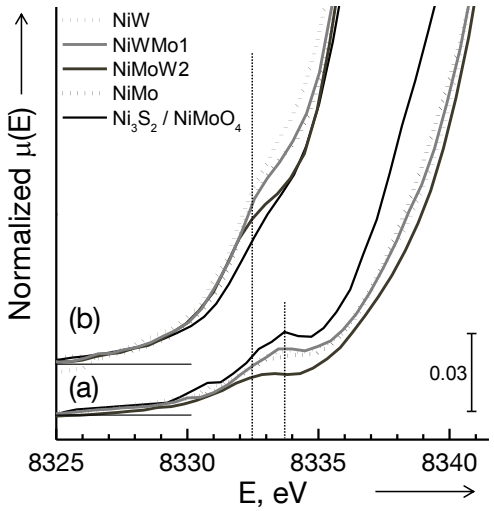

Figure S13. The pre-edge region of the XANES at the Ni K-edge of the oxides (a, for comparison) and sulfides (b) presented in Figure 3 is shown. The pre-edge position of the references Ni_3S_2 and $NiMoO_4$ (—) is indicated by the dotted vertical line (the following lines are used for the samples: $NiMo_{Ox}$ and NiMo (···), $NiMoW2_{Ox}$ and NiMoW2 (—), $NiWMo1_{Ox}$ and NiWMo (—) and NiW_{Ox} and NiW (···)).

The LCF results of the XANES at the Ni K-edge are shown in Table S7 and Figure S26. The content of Ni_3S_2 to reproduce the XANES of the sulfide catalysts decreases from NiMoW2 (99.4 %) over NiW (98.2 %) and NiMo (96.2 %) to NiWMo1 (93.6 %). The

performed LCF analysis was only based on the combination of the XANES of the oxidic precursors and the spectra of Ni_3S_2, accordingly, the highest fraction of the oxidic precursor was contained in NiWMo1 with 6.4 %. The best LCF was obtained for NiWMo1. However, the quality of the fits showed that a combination of these both spectra was not sufficient and that other phases (structural or electronic properties) are needed to determine the XANES of the sulfide catalysts.

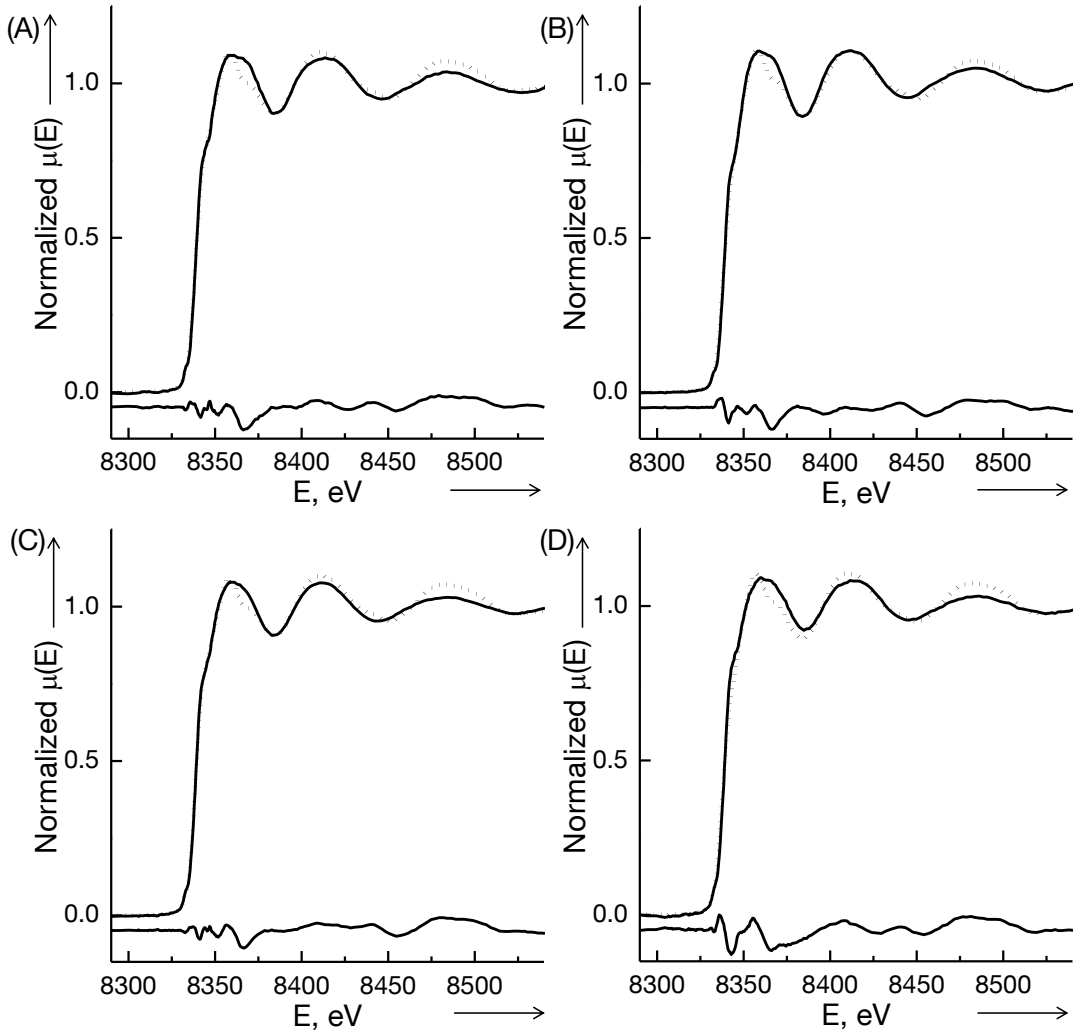

Figure S26. XANES (solid line) and modeled XANES by LCF (dotted line) at the Ni K-edge of the sulfide catalysts NiMo (A), NiMoW2 (B), NiWMo1 (C) and NiW (D). Additionally, the residual is presented in the bottom

At the Mo K-edge, a very good LCF was obtained for NiMo including 99.6 % of the XANES of MoS_2. (Table S7, Figure S27). The fraction of the oxidic precursor XANES in the XANES of the trimetallic sulfides was 1.1 % for NiWMo1 and 3.9 % for NiMoW2, i.e. the oxide proportions were higher for the trimetallic catalysts. However, the observed absorption edge position and white line intensity in the XANES as well as the FT-EXAFS indicate the absence of oxidized Mo or ionic Mo-O bonds. The intensity of the modeled XANES of the

trimetallic sulfides by LCF was higher than the measured one (Figure S27), which points to a higher density of the Mo-5p states in the experimental data than predicted by the fitting.

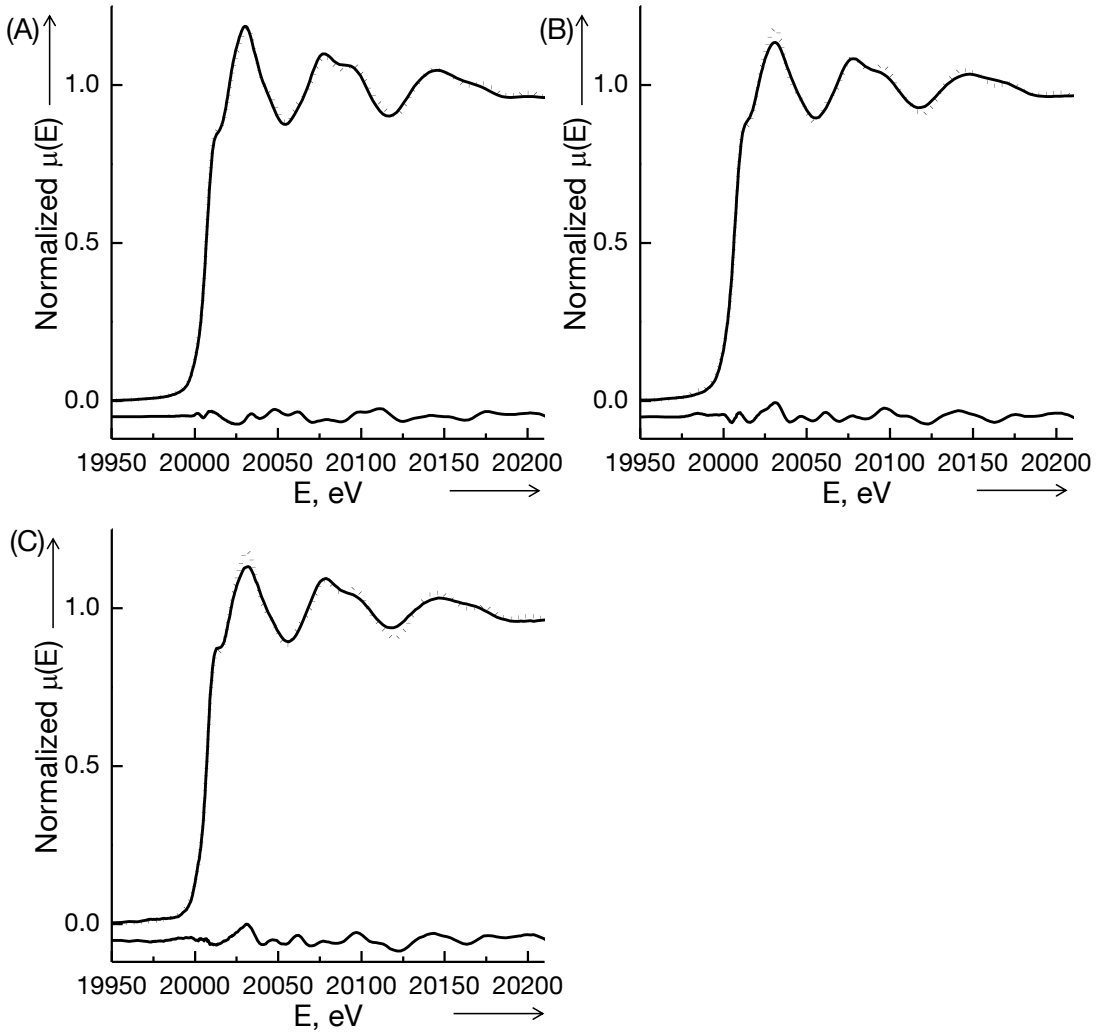

Figure S27. XANES (solid line) and modeled XANES by LCF (dotted line) at the Mo K-edge of the sulfide catalysts NiMo (A), NiMoW2 (B) and NiWMo1 (C). Additionally, the residual is presented in the bottom.

It is known that XANES is the result of many different parameters and not only caused by the oxidation state and coordination number in the first shell. For instance, the symmetry, electronic structure and multiple scattering processes (more distant neighbors and the whole long range order) influence the XANES.[221, 277] Therefore, it is proposed that the good agreement with the modeled XANES is not gained by the addition of oxidized Mo, but by the contribution of other species contained in the precursors, like Ni and W. This modified environment of Mo is apparently more pronounced in NiMoW2 than in NiWMo1 (having higher percentage of oxidic precursor included in modeled XANES). However, the difference spectra presented in the bottom of the diagrams in Figure S27 pointed, in general, to the

presence of additional compounds not contained in the precursors (e.g. sulfided Ni and W), also in the bimetallic NiMo.

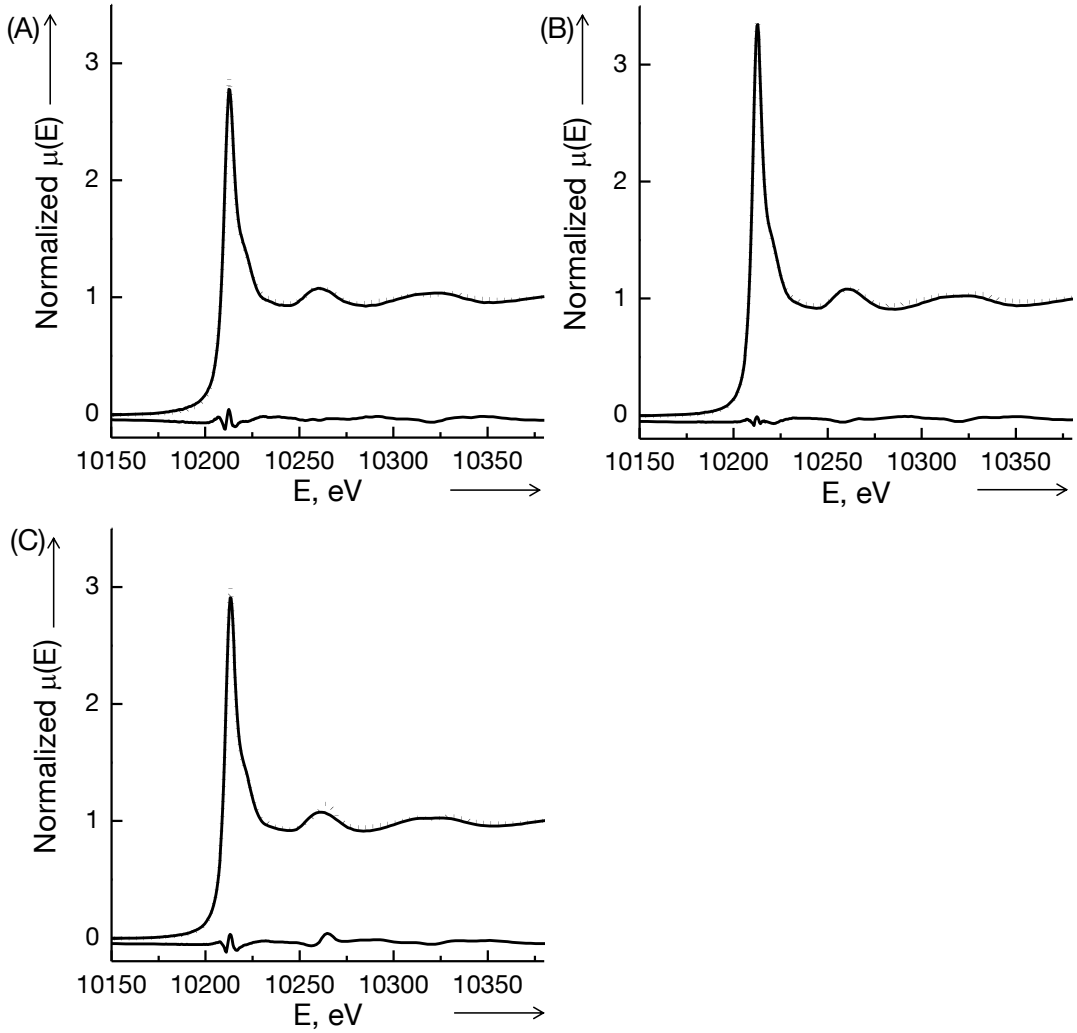

Figure S28. XANES (solid line) and modeled XANES by LCF (dotted line) at the W LI_{II}-edge of the sulfide catalysts NiMoW2 (A), NiWMo1 (B) and NiW (C). Additionally, the residual is presented in the bottom

The XANES of all sulfide catalysts at the W L_{III}-edge could not be modeled by using the XANES of WS_2 and the oxidic precursors only (Table S7, Figure S28). To accommodate the high density of states, the XANES of the W metal foil was added, which improved the fits remarkably. The lowest fraction of W foil (23 %) and therefore the highest fraction of WS_2 (73 %) and oxidic precursor (5 %) was used to model the XANES of NiWMo1. And in the case of the LCF of NiMoW2, the highest fraction of W foil (38 %) and the lowest of WS_2 (62 %) and oxidic precursor (1 %) was required. Additionally, it has to be considered that the white line intensity and shape of a L_{III}-edge depends as well on the structure of the compound including the absorber atom since d-orbitals are involved in the bonding.[230] For instance, a tetrahedrally coordinated absorber has a less intense white line since their

symmetry causes a high mixing ratio of the 6p-orbitals into the 5d-orbitals, which reduces the transition probability at a L_{III}-edge due to the dipole forbidden p-p electronic transition. A distorted octahedral W^{4+} coordination, which allows a higher pd-mixing ratio is present in the sulfide catalysts indicated by their less intense white lines than observed for the perfect octahedral coordinated W in WS_2.

Table S7. LCF results of the modeled XANES for the catalyst sulfides.

Catalyst	Absorber metal	Weight of used XANES, %		R factor [a]	Integrated area of the residual [b]
		Oxidic precursor	Sulfide reference		
NiMo	Ni	3.8	96.2	0.0025	3.842
	Mo	0.4	99.6	0.0008	0.161
NiMoW2	Ni	0.6	99.4	0.0026	4.384
	Mo	3.9	96.1	0.0013	0.064
	W	1.0	61.5 37.5 % W foil	0.0016	2.324
NiWMo1	Ni	6.4	93.6	0.0014	0.447
	Mo	1.1	98.9	0.0013	0.259
	W	4.6	72.6 22.8 % W foil	0.0004	0.370
NiW	Ni	1.8	98.2	0.0067	4.053
	W	2.2	66.6 31.2 % W foil	0.0011	2.321

[a] The godness of the LCF. [b] The left area between the measured and modeled XANES (residual).

EXAFS fitting results of the reference materials

The EXAFS of measured references MoS_2 (Figure S29 = Figure S12 and Table S3 in A2, Support Ch.5), WS_2 (Figure S30 = Figure S13 and Table S4 in A2, Support Ch.5) and Ni_3S_2 (Figure S31 = Figure S14 and Table S5 in A2, Support Ch.5) were fitted to estimate the amplitude reduction factor S_0^2 and for comparison with the sulfide catalysts. MoS_2 and WS_2 exhibit the expected hexagonal coordination geometry with $N_{M-S} = 6$ and $N_{M-M} = 6$ (N stands for coordination number and M for Mo or W). The Ni-S coordination number for Ni_3S_2 was 4.4 fitted by two different kinds of S neighbors at 2.26 and 2.27 Å and N_{Ni-Ni} was 3.7 at 2.52 Å.

EXAFS fitting results of the sulfide catalysts

EXAFS fitting of sulfided **NiMo catalyst** (Figures S32-S33 and Tables S8-S9):
In Appendix **A2** - Support of Chapter 5: **Figures S15-S16, Tables S3-S5**

EXAFS fitting of sulfided **NiW catalyst** (Figures S34-S35 and Tables S8-S9):
In Appendix **A2** - Support of Chapter 5: **Figures S17-S18, Tables S3-S5**

EXAFS fitting of sulfided **NiMoW2 catalyst** (Figures S36-S38 and Tables S8-S9):
In Appendix **A2** - Support of Chapter 5: **Figures S19-S21, Tables S3-S5**

EXAFS fitting results of NiWMo1 sulfide catalyst

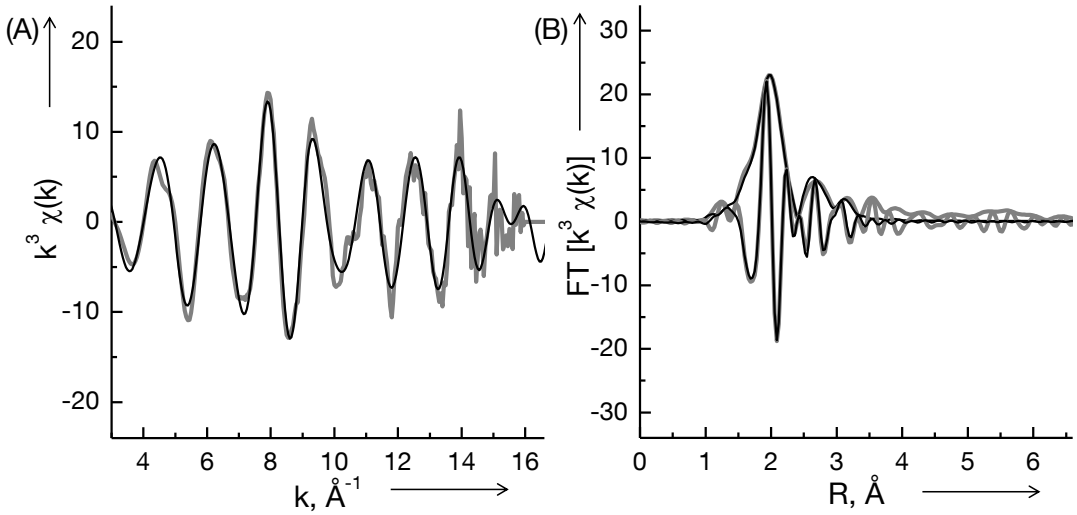

Figure S39. k^3 weighted EXAFS (A) at the Mo K-edge and the corresponding Fourier transforms, magnitudes and imaginary part (B) of the sulfided NiWMo1 catalyst (grey lines) and of the best models (black lines) obtained by multi-edge fitting of the k^3 weighted EXAFS in k-space.

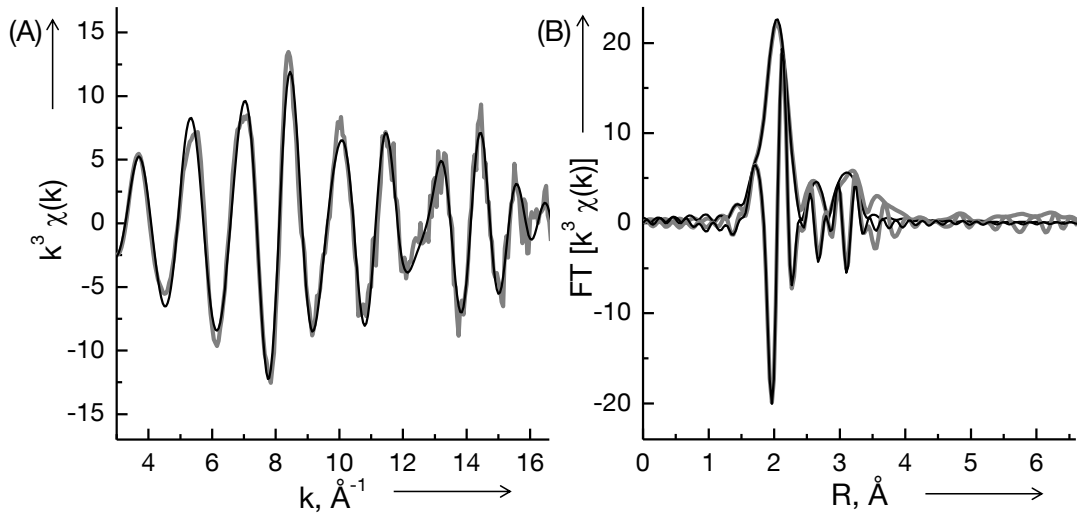

Figure S40. k^3 weighted EXAFS (A) at the W L_{III}-edge and the corresponding Fourier transforms, magnitudes and imaginary part (B) of the sulfided NiWMo1 catalyst (grey lines) and of the best models (black lines) obtained by multi-edge fitting of the k^3 weighted EXAFS in k-space.

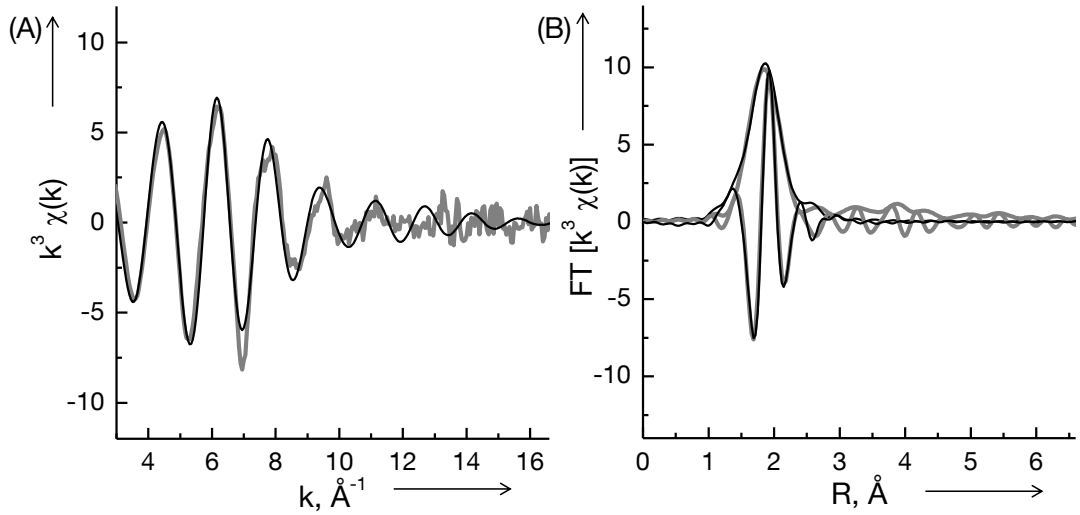

Figure S41. k^3 weighted EXAFS (A) at the Ni K-edge and the corresponding Fourier transforms, magnitudes and imaginary part (B) of the sulfided NiWMo1 catalyst (grey lines) and of the best models (black lines) obtained by multi-edge fitting of the k^3 weighted EXAFS in k-space.

TableS8. Best fit results for k^3 weighted EXAFS data of the sulfided catalysts at the Ni K-edge in k space. The results of the other catalysts are in Table S5 of A2 - support Ch.5.

Catalyst	Shell	r, Å	N	σ^2, Å^2	E_0, eV
Ni_3S_2	Ni-S	2.27 (0.01)	4.4 (0.4)	0.0057 (0.0009)	1.68 (0.68)
A = 0.98 (0.20)	Ni-Ni	2.52 (0.01)	3.7 (0.4)	0.0055 (0.0008)	
R = 0.0060	Ni-S	3.71 (0.01)	4.5 (0.9)	0.0068 (0.0023)	
	Ni-Ni	3.78 (0.01)	8.0 (1.1)	0.0090 (0.0016)	
	Ni-Ni	4.06 (0.01)	5.6 (0.9)	0.0085 (0.0013)	
NiWMo1	Ni-S	2.28 (0.01)	4.3 (0.2)	0.0088 (0.0005)	2.72 (1.14)
R = 0.0047	Ni-Ni	2.61 (0.02)	0.8 (0.2)	0.0083 (0.0018)	

Abbreviations: r: distance, N: coordination number, σ^2: Debye-Waller like factor, E_0: inner potential; in brackets the absolute errors.

Table S9. Best fit results for k^3 weighted EXAFS data of the sulfided catalysts at the Mo K-edge and W L_{III}-edge in k space. The results of the other catalysts are in Table S3-S4 of A2 - support Ch.5.

Catalyst	Shell	r, Å	N	σ^2, Å^2	E_0, eV
MoS_2 A = 1.16	Mo-S	2.41 (0.01)	5.9 (0.5)	0.0024 (0.0005)	3.51 (2.55)
(0.20) R = 0.0094	Mo-Mo	3.17 (0.01)	6.0 (0.4)	0.0018 (0.0003)	
NiWMo1	Mo-S	2.40 (0.01)	5.5 (0.2)	0.0030 (0.0002)	1.81 (1.12)
R = 0.0047	Mo-Mo	3.16 (0.01)	1.5 (0.1)	0.0010 (0.0002)	
	Mo-W	3.16 (0.01)	1.6 (0.1)	0.0020 (0.0002)	
Catalyst	Shell	r, Å	N	σ^2, Å^2	E_0, eV
WS_2 A = 1.18	W-S	2.40 (0.01)	5.8 (0.5)	0.0027 (0.0005)	7.83 (1.93)
(0.20) R = 0.0092	W-W	3.16 (0.01)	6.1 (0.5)	0.0024 (0.0003)	
NiWMo1	W-S	2.40 (0.01)	5.1 (0.2)	0.0036 (0.0002)	7.11 (0.87)
R = 0.0047	W-W	3.15 (0.01)	2.6 (0.2)	0.0034 (0.0003)	
	W-Mo	3.16 (0.01)	0.8 (0.1)	0.0020 (0.0002)	

Abbreviations: r: distance, N: coordination number, σ^2: Debye-Waller like factor, E_0: inner potential; in brackets the absolute errors.

Alternative fitting for NiWMo1 with Mo-Ni (Ni-Mo) and WNi (Ni-W) contributions

Table S10. Best fit results for k^3 weighted EXAFS data of the sulfided catalysts at the W L_{III}-edge in k space including Mo-Ni and W-Ni.

Catalyst	Shell	r, Å	N	σ^2, Å^2	E_0, eV
NiWMo1	Mo-S	2.40 (0.01)	5.5 (0.2)	0.0030 (0.0002)	1.77 (1.12)
R = 0.0047	Mo-Mo	3.16 (0.01)	1.5 (0.1)	0.0010 (0.0002)	
	Mo-W	3.16 (0.01)	1.6 (0.1)	0.0020 (0.0002)	
	Mo-Ni	2.68 (0.03)	0.2 (0.1)	0.0200 (0.0050)	
NiWMo1	W-S	2.40 (0.01)	5.1 (0.2)	0.0036 (0.0002)	7.12 (0.87)
R = 0.0047	W-W	3.15 (0.01)	2.6 (0.2)	0.0034 (0.0003)	
	W-Mo	3.16 (0.01)	0.8 (0.1)	0.0020 (0.0002)	
	W-Ni	2.77 (0.11)	0.2 (0.1)	0.0200 (0.0050)	
NiWMo1	Ni-Ss	2.28 (0.01)	4.3 (0.2)	0.0088 (0.0005)	2.64 (1.14)
R = 0.0047	Ni-Ni	2.61 (0.02)	0.8 (0.2)	0.0083 (0.0018)	
	Ni-Mo	2.68 (0.01)	0.1 (0.1)	0.0200 (0.0050)	
	Ni-W	2.77 (0.11)	0.1 (0.1)	0.0200 (0.0050)	

Abbreviations: r: distance, N: coordination number, σ^2: Debye-Waller like factor, E_0: inner potential; in brackets the absolute errors.

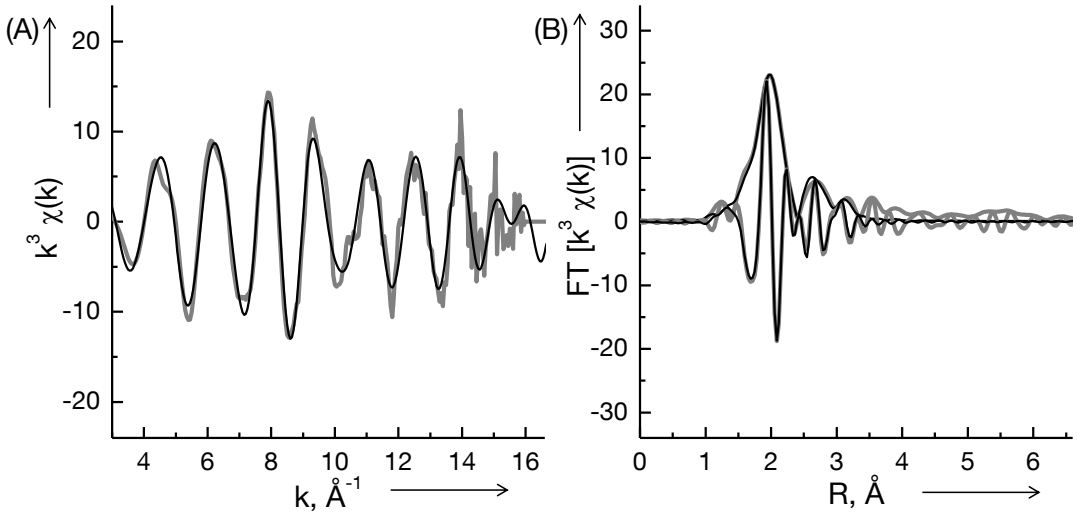

Figure S42. k^3 weighted EXAFS (A) at the Mo K-edge and the corresponding Fourier transforms, magnitudes and imaginary part (B) of the sulfided NiWMo1 catalyst (grey lines) and of the best models (black lines) obtained by multi-edge fitting of the k^3 weighted EXAFS in k-space.

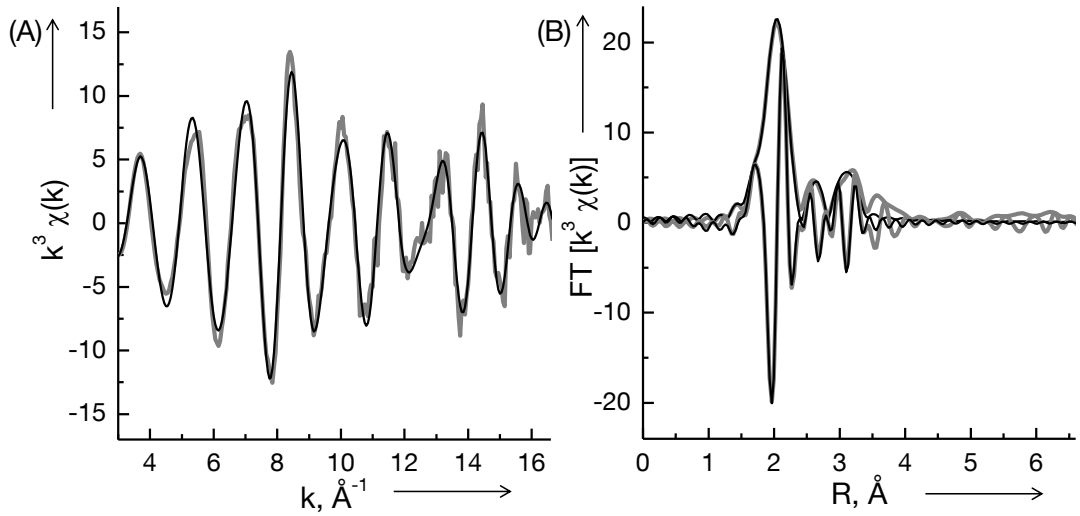

Figure S43. k^3 weighted EXAFS (A) at the W L_{III}-edge and the corresponding Fourier transforms, magnitudes and imaginary part (B) of the sulfided NiWMo1 catalyst (grey lines) and of the best models (black lines) obtained by multi-edge fitting of the k^3 weighted EXAFS in k-space.

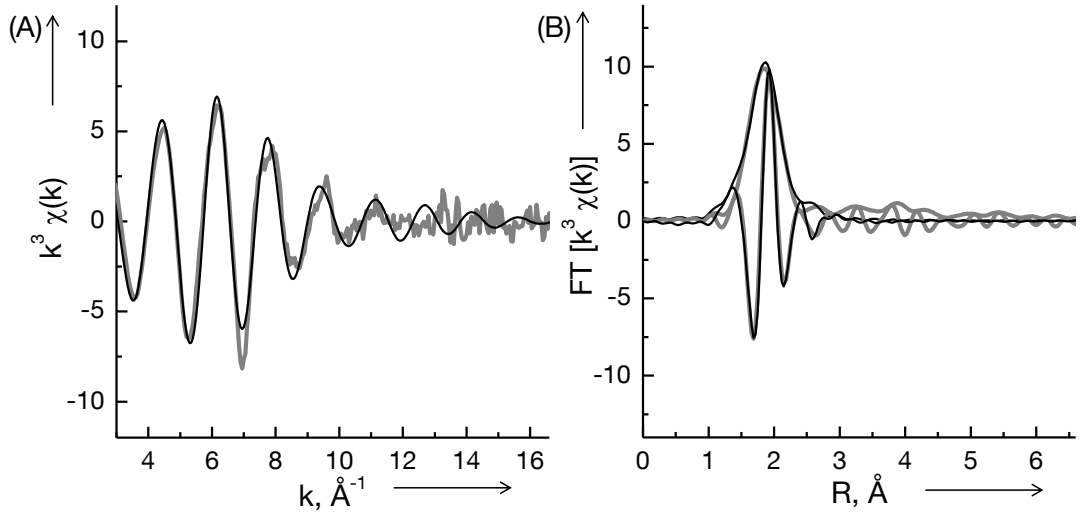

Figure S44. k^3 weighted EXAFS (A) at the Ni K-edge and the corresponding Fourier transforms, magnitudes and imaginary part (B) of the sulfided NiWMo1 catalyst (grey lines) and of the best models (black lines) obtained by multi-edge fitting of the k^3 weighted EXAFS in k-space.

Hydrodenitrogenation and hydrodesulfurization activities

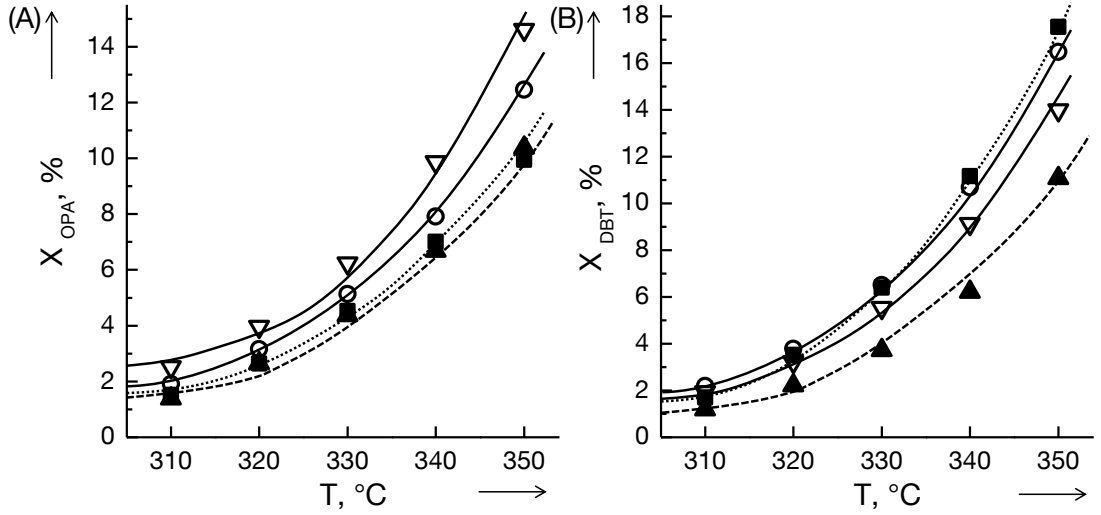

Figure S45. Conversions of the simultaneous hydrodenitrogenation (A) of o-propylaniline (OPA), and hydrodesulfurization (B) of dibenzothiophene (DBT) over the unsupported sulfide catalysts NiMo (▽), NiMoW2 (■), NiWMo1 (▲) and NiW (○).

Short Curriculum Vitae of Jennifer Hein

Education

10/2010 – 09/2014	PhD studies at Technische Universität München, Germany in the group of Prof. Dr. J. A. Lercher
02/2010 – 08/2010	Diploma thesis under supervision of Prof. Dr. T. Ressler (Technische Universität Berlin, Germany) and Prof. Dr. J. A. Lercher (Technische Universität München, Germany)
10/2005 – 08/2010	Studies of chemistry at Technische Universität Berlin, Germany specialization: analytical chemistry; (grading "very good")
09/2002 – 01/2005	Apprenticeship as chemical laboratory assistant at Helmholtz-Zentrum Potsdam, Deutsches GeoForschungsZentrum (GFZ), Germany in the group of Prof. Dr. J. Erzinger
09/1995 – 06/2002	Gymnasium Gransee, (Degree: German Abitur)

Trainings

06/2009 – 07/2009	Research internship at Technische Universität Berlin, Germany in the group of Prof. Dr. T. Ressler.
03/2006	Research internship at Helmholtz-Zentrum Berlin für Materialien und Energie, Germany (HMI Berlin) in the group of Dr. A. Kyriakopoulos

Work Experiences

10/2014 – 06/2015	Assessed internship in the field of catalyst development at Shell Global Solutions International B.V., Amsterdam, The Netherlands
08/2006 – 02/2009	Student research assistant at the Technische University Berlin in the groups of Prof. Dr. A. Grohmann and Prof. Dr. M. Drieß (Dr. S. Kohl)
02/2005 – 08/2005	Chemical laboratory assistant at Helmholtz-Zentrum Potsdam, Deutsches GeoForschungsZentrum (GFZ), Germany in the group of Prof. Dr. J. Erzinger

International Experience

08/2008 – 10/2008	IAESTE-internship in the field of chemical engineering at CPQ INGENIEROS, S. L. in Barcelona, Spain

Scholarships

03/2013	Travel grant of German Catalysis Society (GeCatS) for the 23th North American Catalysis Society Meeting in Louisville, Kentucky/USA
12/2008	Klaus-Koch-Scholarship of Technische Universität Berlin, Germany

Memberships

Gesellschaft Deutscher Chemiker e.V. (GDCh)
Deutsche Wissenschaftliche Gesellschaft für Erdöl, Erdgas und Kohle e.V. (DGMK)
German Catalysis Society (GeCats)
TUM Graduate School

Publications and Conference Contributions

List of Publications

J. Hein, O. Y. Gutiérrez, J. Han, A. Jentys, J. A. Lercher; *“Physicochemical characterization and hydrotreating activity of unsupported Ni-Mo-W sulfide catalysts” (2015)*, in preparation.

J. Hein, O. Y. Gutiérrez, E. Schachtl, P. Xu, N. D. Browning, A. Jentys, J. A. Lercher; *"Distribution of metal cations in Ni-Mo-W sulfide catalysts” ChemCatChem (2015)*, accepted.

E. Schachtl, E. Kondratieva, L. Zhong, J. Hein, O. Y. Gutiérrez, A. Jentys, J. A. Lercher; *"Understanding Ni promotion of MoS_2/γ-Al_2O_3 and its implications for the hydrogenation of phenanthrene", ChemCatChem (2015)*, accepted.

O.Y. Gutiérrez, S. Singh, E. Schachtl, J. Kim, E. Kondratieva, J. Hein, J.A. Lercher, *ACS Catal.* 4, 5 *(2014),* 1487.

J. Hein, A. Hrabar, A. Jentys, O.Y. Gutiérrez, J.A. Lercher, *ChemCatChem* 6, 2 *(2014)*, 485-499. Distinguished with an inside cover.

O.Y. Gutiérrez, A. Hrabar, J. Hein, Y. Yu, J. Han, J.A. Lercher, *J. Catal.* 295 *(2012)*, 155.

J. Hein, A. Hrabar, O.Y. Gutiérrez, J.A. Lercher, *DGMK Tagungsbericht 2012-3.* (2012), 241. DGMK Fachbereichstagung "Reducing the Carbon Footprint of Fuels and Petrochemicals".

A. Hrabar, J. Hein, O.Y. Gutiérrez, J.A. Lercher, *J. Catal.* 281 *(2011)*, 325.

J. Hein, A. Hrabar, O.Y. Gutiérrez, J.A. Lercher, *DGMK Tagungsbericht 2011-2.* (2011), 47. DGMK Fachbereichstagung "Catalysis – Innovative Applications in Petrochemistry and Refining".

Conference Contributions

1st STCA Symposium on Hydrotreating Catalysis, 2014, Amsterdam (The Netherlands); Talk.

47. Jahrestreffen Deutscher Katalytiker, 2014, Weimar (Germany); Poster.

XI. European Congress on Catalysis, 2013, Lyon (France); Poster.

23rd North American Catalysis Society Meeting, 2013, Louisville (USA, KY); Talk.

46. Jahrestreffen Deutscher Katalytiker, 2013, Weimar(Germany); Poster.

6th IDECAT/ERIC-JCAT Conference on Catalysis (6th IEJCat), 2013, Brixen (Italy); Poster.

DGMK Konferenz, 2012, Berlin (Germany); Poster.

15th International Congress on Catalysis, 2012, München (Germany); Poster Symposium.

45. Jahrestreffen Deutscher Katalytiker, 2012, Weimar (Germany); Poster.

DGMK Konferenz, 2011, Dresden (Germany); Talk.

Catalysis Research Center Symposium (TU München), 2011, München (Germany); Poster.